

Université du Québec
Institut National de la Recherche Scientifique
Centre Énergie, Matériaux et Télécommunications

Carbon Nanomaterials for Dye-Sensitized Solar Cells

by
Mahyar Mohammadnezhad

Dissertation submitted for the partial fulfillment of the requirements of the degree,
Doctor of Philosophy, Ph.D.
in Energy and Materials Science

Evaluation Juries

Research supervisor	Prof. Federico Rosei, INRS-EMT
Internal examiner and president of the Jury	Prof. Fiorenzo Vetrone, INRS-EMT
External examiner	Prof. Fabio Cicoira, Polytechnique Montreal
External examiner	Prof. Rafik Naccache, Concordia University

ABSTRACT

According to the late Nobel Laureate Richard E. Smalley, energy is one of the biggest problems to be faced by humanity over the next 50 years. At the dawn of the 21st century, with the rapid development of industrialization and globalization, worldwide energy demands have rapidly increased. Different forms of fossil fuels represent over 80% of the world's energy use. However, the limited availability of fossil fuels, together with climate change and environmental pollution dictates a transition towards sustainable, clean and carbon-neutral energy sources, including wind power, hydroelectric and solar energy. Amongst different sources of renewable energy, solar energy is one of the cleanest energy resources to be considered as a viable alternative to fossil fuels since sunlight is the most abundant of all available carbon-free energy sources. A solar cell is an optoelectronic device that directly converts the energy of light into electricity by the photovoltaic (PV) effect. Silicon (Si) solar cells currently constitute the most widespread commercial product in this field due to their high conversion efficiency and relatively long-term stability compared to other solar cell technologies. However, their high production cost and environmental impact are restricted to the terrestrial PV market. In recent years, dye-sensitized solar cells (DSSCs) have been regarded as a promising alternative to Si solar cells. DSSCs are considered as a promising future technology due to their appealing features, including a simple fabrication process, eco-friendly materials, colour choice and transparency. DSSCs must pass three main filters for large-scale commercialization: power conversion efficiency (PCE); long-term stability; and production cost. Although the design of new and modified devices that are structured to fabricate highly efficient cells are widely investigated, thus far the long-term stability and production costs have rarely been investigated and reported in the field of DSSCs.

The first part of this thesis demonstrates the effect of adding carbonaceous materials, in particular multi-wall carbon nanotubes (MWCNTs), on the stability of DSSCs under continuous simulated sunlight, indoor and ultraviolet (UV) light irradiation. After light aging, DSSCs are characterized by different techniques, to document the degradation mechanisms. The results indicate that MWCNTs can act as a strong conductive support and reinforcement of the titanium dioxide (TiO₂) matrix, which is able to significantly

improve the long-term stability of DSSCs under continuous simulated one sun and indoor light by 22% and 42%, respectively. Based on UV stability measurements, MWCNTs, as an efficient absorbing and blocking agent for UV light, can successfully stabilize DSSCs for long-term operation with a 24% improvement in UV stability.

The second part of this work describes an investigation into the effect of incorporating MWCNTs in the thermal stability of DSSCs. Under identical measurement conditions (aging at 80°C for 240 h in the dark), standard DSSCs present a significant loss in PCE, dropping to 59% of their initial value, while a composited device with MWCNTs attained a promising thermal stability with only a 20% reduction. This loss in cell performance in standard DSSCs is mainly associated with a dramatic reduction in short circuit current density (J_{sc}). The composite anode exhibited excellent microstructure stability due to the bonding between MWCNTs and TiO₂ nanoparticles. Furthermore, transient photovoltage decay and electrochemical impedance spectroscopy (EIS) measurements confirm the higher electron lifetime and reduction in charge recombination in the composite network due to the excellent conductivity of MWCNTs.

The final part of this work describes a simple and low-cost approach to preparing a nanocomposite film of copper sulfide-graphene (CuS-G) as a transparent conducting oxide (TCO) and platinum (Pt)-free counter electrodes (CEs) for DSSCs. Different measurements verified the structure and the composition of a nanocomposite of CuS-G with uniform distribution of graphene between the CuS particles. The results demonstrated that the addition of graphene improves the PCE of the DSSCs (~12%) compared to the DSSCs based on CEs made of pristine CuS. The prepared CuS-G nanocomposite thin films that exhibit good catalytic performance towards the reduction of the tri-iodide electrolyte exhibited an impressive PCE of 4.83%, which is comparable to that of using the Pt CE (5.14%).

ACKNOWLEDGEMENT

The present study was established in the NanoFemtoLab (NFL), Centre of Energy, Materials and Telecommunications (EMT), Institut National de la Recherche Scientifique (INRS) University of Quebec, under the direction of Prof. Federico Rosei.

First and foremost, I gratefully acknowledge Prof. Federico Rosei for having given me the great opportunity to accomplish my PhD thesis in Photovoltaics in his prestigious research group. Prof. Rosei, being a member of this group is one of the most valuable experiences in my academic life.

I would like to express my gratitude to Prof. Barry Stansfield for his generous support throughout my PhD studies.

I would also like to offer my appreciation to Prof. Haiguang Zhao and Dr. Gurpreet Singh Selopal for their patience, motivation, enthusiasm, and immense knowledge. Haiguang, I wish to give special thanks to you for the avenues you have opened up for me in PhD research. Gurpreet, you have supported me not only by providing a wealth of knowledge on solar cell and solar energy, but also by being a close friend whenever I needed help.

I am also grateful to all the group members from NFL, the departmental and technical staff at INRS-EMT and all my friends as well as other collaborators for their help throughout the work. I also highly appreciate the Fonds de Recherche du Québec-Nature et Technologies (FRQNT) for their financial support of my research.

Last but not the least, I thank my family who have given me true love and unwavering support from the first to the last day of my PhD. I am honored to dedicate my thesis to them.

TABLE OF CONTENTS

Abstract.....	iii
Acknowledgement.....	v
Table of Contents	vii
List of Figures	xi
List of Tables	xix
List of Acronyms	xxi
Introduction	1
CHAPTER 1	4
Solar energy and solar cells.....	4
1.1 Photovoltaics.....	6
1.2 Classification of solar cells	7
1.2.1 First generation.....	7
1.2.2 Second generation.....	8
1.2.3 Third generation.....	9
1.3 Dye-sensitized solar cells (DSSCs)	10
1.3.1 Brief history.....	10
1.3.2 Cell architecture.....	11
1.3.3 Basic Operating Principle of DSSCs	12
1.4 Characterizations of photovoltaic performance	15
1.4.1 Short circuit photocurrent density.....	16
1.4.2 Open circuit voltage	16
1.4.3 Fill Factor.....	17
1.4.4 Efficiency	18
1.4.5 Incident photon to current conversion efficiency.....	18

1.4.6	Standard test conditions	19
1.4.7	Electrochemical impedance spectroscopy	20
CHAPTER 2.....		25
2	Materials and experimental techniques	25
2.1	Materials	25
2.1.1	Transparent conductive oxide electrode	25
2.1.2	Anode	27
2.1.3	Sensitizers	30
2.1.4	Electrolytes	32
2.1.5	Counter electrode	33
2.1.6	Sealant	34
2.1.7	Carbon nanomaterials.....	34
2.2	Device Fabrication	38
2.3	Characterization methods	39
2.3.1	X-ray diffraction.....	39
2.3.2	Scanning electron microscope	40
2.3.3	Transmission electron microscopy.....	41
2.3.4	Atomic force microscopy.....	41
2.3.5	X-ray Photoemission spectroscopy	42
2.3.6	Raman spectroscopy	43
2.3.7	UV-visible (UV-vis) Spectroscopy	44
2.3.8	Electrochemical impedance spectroscopy	45
2.3.9	Cyclic voltammetry.....	45
2.3.10	Photovoltaic characterization	45
2.3.11	External quantum efficiency	46
CHAPTER 3.....		48
3	Role of carbon nanotubes to enhance the long-term stability of dye-sensitized solar cells.....	48
3.1	Introduction	49

3.2	Experimental	52
3.3	Results and discussion	53
3.3.1	Long-term stability under simulated sunlight illumination.....	54
3.3.2	Long-term stability under indoor light illumination.....	60
3.3.3	Long-term stability under UV light	63
3.3.4	Microstructure evaluation	66
3.3.5	Raman spectroscopy measurements.....	68
3.3.6	EIS analyses.....	70
3.4	Conclusions and Perspectives	75
CHAPTER 4.....		77
4 Incorporation of multi-wall carbon nanotubes to boost the long-term thermal stability of dye sensitized solar cells		77
4.1	Introduction	78
4.2	Experimental	80
4.3	Results and discussion	81
4.3.1	Stability under different aging temperatures.....	82
4.3.2	Long-term thermal stability.....	84
4.3.3	Microstructural evaluation	86
4.3.4	Electron lifetime evaluation	89
4.3.5	Electrochemical characterization	90
4.3.6	Raman spectroscopy analysis	93
4.3.7	Chemical analysis.....	95
4.4	Conclusions and Perspectives	97
CHAPTER 5.....		99
5 CuS-graphene nanocomposite as a transparent conducting oxide and Pt-free counter electrode for dye-sensitized solar cells		99
5.1	Introduction	100
5.2	Experimental	103

5.3	Results and discussion	105
5.3.1	Microstructure evaluation.....	105
5.3.2	Surface characterizations of CuS-3G nanocomposite.....	108
5.3.3	PV performance of the DSSC fabricated CuS-G nanocomposite CEs	110
5.3.4	DSSCs based on Pt and optimized CuS-3G CEs.....	114
5.4	Conclusions and Perspectives	119
6	Conclusions and perspectives	121
6.1	Conclusions	121
6.2	Perspectives	123
7	References.....	124
8	Appendix B: Résumé (in French).....	145

LIST OF FIGURES

Figure 1.1 Solar irradiance spectrum (yellow: at the top of the Earth's atmosphere; red: after passing through the atmosphere) comparison with spectrum of black body radiation at 5250°C (grey line) [32].	5
Figure 1.2 Schematic of p-n junction based solar cell [32].	6
Figure 1.3 Efficiency and production cost projections for three generations of solar cells [40].	7
Figure 1.4 Best research-cell reported by the National Renewable Energy laboratory [43].	9
Figure 1.5 Selected PCE landmarks in DSSCs [49].	11
Figure 1.6 Schematic of the working principle of a DSSC and time scale of the processes within a device [54].	12
Figure 1.7 Typical current-voltage curve of a photovoltaic cell.	16
Figure 1.8 Evolution of simulated J-V curves with the change of (a) overall series resistance and (b) parallel shunt resistance [59].	17
Figure 1.9 Typical illustration of air mass.	19
Figure 1.10 (a) General transmission line model of DSSCs and (b) simplified model at high illumination intensities [59].	21
Figure 1.11 Typical impedance spectra (Nyquist plot) of a complete DSSC.	22
Figure 1.12 Typical Bode plots of a complete DSSC.	23
Figure 2.1 General structure of DSSCs [55].	26
Figure 2.2 SEM image of FTO glass substrate.	27
Figure 2.3 Band positions of different semiconductors in contact with aqueous electrolyte at pH 1. The conduction band (red colour) and the valence band (green colour) are presented along with the band gap in electron volts (eV) [7].	28
Figure 2.4 TEM image of TiO ₂ anatase nanoparticles.	29
Figure 2.5 EDS spectra of the TiO ₂ anatase nanoparticles.	29
Figure 2.6 XPS spectra of the TiO ₂ anatase nanoparticles.	30

Figure 2.7 Cross-sectional SEM image of mesoporous and scattering TiO ₂ layer: (a) low and (b) high magnification.	30
Figure 2.8 Various binding modes for a carboxylate unit on the TiO ₂ surface as an example of a metal oxide semiconductor: (a) monodentate (b) bidentate chelating (c) bidentate bridging [67].	31
Figure 2.9 UV-visible absorption of N719 dye molecule photosensitizers for DSSCs.	31
Figure 2.10 Molecular structures of different dye molecule photosensitizers for DSSCs [55].	32
Figure 2.11 SEM image of Pt thin film layer on an FTO substrate.	34
Figure 2.12 Polymorphs of carbon materials [80].	35
Figure 2.13 Electron transport across nanostructured semiconductor films: (a) and (c) CNT and (b) and (d) graphene composite electrodes [19].	37
Figure 2.14 TEM images of the MWCNTs: (a) low and (b) high magnifications.	38
Figure 2.15 (a) DSSC fabrication steps and (b) a complete DSSC [83].	39
Figure 2.16 Schematics of diffraction of X-rays [84].	40
Figure 2.17 Electrons interact with a sample's atoms in the SEM [85].	40
Figure 2.18 Electron beams interact with a sample's atoms in the TEM [86].	41
Figure 2.19 Experimental setup for a typical AFM [91].	42
Figure 2.20 Experimental setup for a typical XPS [93].	43
Figure 2.21 "Jablonski" style diagrams of different forms of energetic transitions in Raman scattering.	44
Figure 3.1 Current density-voltage curves of solar cells under simulated one sun at AM 1.5G (100 mW cm ⁻²) fabricated using TiO ₂ mesoporous films with (red circles) and without MWCNTs (black squares).	54
Figure 3.2 Functional properties of DSSCs in cases with and without MWCNTs under a continuous one sun light irradiation as a function of soaking time: (a) J-V curves of DSSCs without MWCNTs; (b) J-V curves of DSSCs with MWCNTs; (c) J _{sc} (mA cm ⁻²); (d) V _{oc} (V); (e) FF (%); and (f) PCE (%).	57

Figure 3.3 Transient V_{oc} decay and obtained electron lifetime (τ_e): for cells without MWCNTs (a) and (b) and cells with MWCNTs (c) and (d), measured at different times under one sun irradiation.59

Figure 3.4 Schematic of: (a) and (b) enhanced dispersion of TiO_2 particles and preventing agglomerating with MWCNT addition; (c) and (d) greater quantity of dye molecules are adsorbed to the highly porous morphology; (e) MWCNTs act as act good support and reinforcement for TiO_2 ; (f) micro-crack formation in the photoanode because of intense light soaking and thermal stress; (g) MWCNTs act as a strong conductive network, preventing charge recombination; (h) loss of electrical contact between the TiO_2 particles and decrease in electron lifetime and recombination resistance.60

Figure 3.5 Functional properties of DSSCs in cases with and without MWCNTs under a continuous indoor light irradiation as a function of soaking time: (a) J-V curves of DSSCs without MWCNTs; (b) J-V curves of DSSCs with MWCNTs; (c) J_{sc} ($mA\ cm^{-2}$); (d) V_{oc} (V); (e) FF (%); and (f) PCE (%).62

Figure 3.6 Functional properties of DSSCs in cases with and without MWCNTs under a continuous UV light irradiation as a function of soaking time: (a) J-V curves of DSSCs without MWCNTs; (b) J-V curves of DSSCs with MWCNTs; (c) J_{sc} ($mA\ cm^{-2}$); (d) V_{oc} (V); (e) FF (%); and (f) PCE (%).64

Figure 3.7 Schematic illustration of the band structure model for the TiO_2 that forms deep electronic traps. Under UV light illumination, the injected and photogenerated electron can be adsorbed through deep electron-donating sites. The electron in this site can then undergo direct recombination with a hole in the electrolyte.66

Figure 3.8 FESEM images of synthesized photoanodes: (a) without MWCNTs and (b) with MWCNTs at different magnifications before aging. Solid and dashed ovals highlight the agglomeration and porosity of the TiO_2 particles, respectively. (c) Photoanode without MWCNTs and (d) photoanode with MWCNTs after aging.67

Figure 3.9 (a) Schematic overview of a DSSC under Raman setup for Raman characterization; (b) a complete fabricated DSSC for Raman measurement; and (c) Raman spectra of cells in cases with and without MWCNTs at 514.5 nm before and after aging.70

Figure 3.10 (a)-(d): Electrochemical impedance spectroscopy analysis of fresh and aged cells without MWCNTs as a function of applied biases; (e) Bode phase of fresh and aged cells without MWCNTs; and (f) equivalent circuit of the transmission model.72

Figure 3.11 (a)-(d) Electrochemical impedance spectroscopy analysis of fresh and aged cells with MWCNTs as a function of applied biases; (e) Bode phase of the fresh and aged cells with MWCNTs; and (f) equivalent circuit of the transmission model.....73

Figure 3.12 (a) Electrochemical impedance spectroscopy analysis of fresh and aged cells without MWCNTs and with MWCNTs for a bias of 450 mV; (b) charge-transfer resistance (R_{ct}) as a function of applied bias in samples with and without MWCNTs, before and after aging; (c) and (d) Bode phase of fresh and aged cells in cases without and with MWCNTs, respectively; and (e) electron lifetime (τ_e) for cells without and with MWCNTs.74

Figure 4.1 Current density-voltage curves of solar cells under simulated one sun at AM 1.5G (100 $mW\ cm^{-2}$) fabricated using TiO_2 mesoporous films with (red circles) and without MWCNTs (black squares).....82

Figure 4.2 PCE reduction (%) as a function of the thermal aging temperature of the two devices: TiO_2 (black square) and TiO_2 -MWCNTs (red circle).83

Figure 4.3 Functional properties of DSSCs in cases with and without MWCNTs as a function of thermal aging time: (a) J-V curves of DSSCs without MWCNTs; (b) J-V curves of DSSCs with MWCNTs; (c) J_{sc} ($mA\ cm^{-2}$); (d) V_{oc} (V); (e) FF (%); and (f) PCE (%).85

Figure 4.4 FESEM images of the photoanodes without MWCNTs in different magnifications after thermal aging. Red arrows indicate cracks in the photoanode.....87

Figure 4.5 FESEM images of the photoanodes with MWCNTs in different magnifications after thermal aging.88

Figure 4.6 High magnification FESEM images of the photoanodes with (a) 0.01 % wt and (b) 0.03 % wt of MWCNTs. Red arrows indicate MWCNTs.88

Figure 4.7 Transient V_{oc} decay and obtained electron lifetime (τ_e): for cells without MWCNTs (a) and (b) and cells with MWCNTs (c) and (d), measured after different thermal stress times.90

Figure 4.8 (a) and (b) EIS analysis of the fresh and aged cells without and with MWCNTs in biases at 300 and 450 mV respectively; (c) charge-transfer resistance as a function of applied biases before and after thermal aging; (d) Bode phase of the fresh and aged cells; (e) Mott-Schottky plots for fresh and aged cells without and with MWCNTs; and (f) equivalent circuit of the transmission model.....92

Figure 4.9 Raman spectra of cells with and without MWCNTs at 514.5 nm before and after thermal aging. The insert shows a schematic overview of a DSSC under setup for Raman measurement.94

Figure 4.10 High-resolution XPS spectra of (a) TiO₂ mesoporous films with and without MWCNTs, before and after dye sensitization; (b) TiO₂ mesoporous film before dye sensitization in the C 1s region; (c) and (d) dye sensitized mesoporous film without and with MWCNTs in the C 1s region, respectively; (e) and (f) dye sensitized mesoporous film without and with MWCNTs in the N 1s region, respectively; (g) and (h) dye sensitized mesoporous film without and with MWCNTs in the S 2p region.96

Figure 5.1 (a) Photograph of the CuS-3G composite film. SEM images of CuS film with various concentrations of graphene at different magnifications: (b)-(c) bare CuS-0G; (d)-(e) CuS-3G; (f)-(g) CuS-10G. Red arrows indicate the microcrack areas..... 106

Figure 5.2 EDS mapping of as-prepared CEs, (a) CuS and (b) CuS-3G nanocomposites. EDS spectra and measurement of chemical composition are taken from the red squared zones. ... 107

Figure 5.3 XRD pattern of as-prepared CuS-3G nanocomposites..... 108

Figure 5.4 XPS plots of the CuS-3G composite film: (a) Survey; (b) Carbon; (c) Cu; (d) Auger Cu; and (e) Sulfur. 109

Figure 5.5 (a) Current density-voltage curves of the DSSCs under one sun simulated sunlight at AM 1.5G (100 mW cm⁻²) fabricated using different CEs. Variation of the photovoltaic parameters of the corresponding devices: (b) PCE (%) and J_{sc} (mA cm⁻²); (c) V_{oc} (mV) and FF (%). 111

Figure 5.6 (a) Transient V_{oc} decay and (b) obtained electron lifetime (τ_e) for DSSCs fabricated using different CEs..... 112

Figure 5.7 Cyclic voltammogram for the standard three-electrode system using different CEs. 113

Figure 5.8 Current density-voltage curves of solar cells under one sun simulated sunlight at AM 1.5G (100 mW cm⁻²) fabricated using Pt and CuS-3G composite CEs. 114

Figure 5.9 Cyclic voltammogram of Pt and CuS-3G composite CEs. 115

Figure 5.10 Electrochemical impedance spectroscopy analysis of the Pt and CuS-3G composite CEs..... 116

Figure 5.11 AFM images of: (a) Pt/FTO and (b) CuS-3G/Glass composite film. 118

Figure 5.12 Statistics (a) J_{sc} (mA cm^{-2}); (b) V_{oc} (mV); (c) FF (%); and (d) PCE (%) of 12 devices as collected over 6 different batches.	119
Figure 1 Schéma d'une cellule solaire à jonction p-n [32].	147
Figure 2 Sélection de points de repère PCE dans les DSSC [49].	148
Figure 3 Schéma du principe de fonctionnement d'un DSSC et échelle de temps des processus au sein d'un appareil [54].	150
Figure 4 Courbes densité / tension actuelles de cellules solaires sous un soleil simulé à AM 1,5G (100 mW cm^{-2}) fabriquées à l'aide de films mésoporeux de TiO_2 avec (cercles rouges) et sans MWCNT (carrés noirs).	153
Figure 5 Propriétés fonctionnelles des DSSC dans les cas avec et sans MWCNT sous irradiation continue d'un rayonnement solaire en fonction du temps de trempage (a) Courbes J-V des DSSC sans MWCNT, (b) Courbes J-V des DSSC avec MWCNT, (c) J_{sc} (mA cm^{-2}); (d) V_{oc} (V); (e) FF (%) and (f) PCE (%).	154
Figure 6 Images FESEM de photoanodes synthétisées: (a) sans MWCNT et (b) avec des MWCNT à un grossissement différent avant vieillissement. Les ovales solides et en pointillés mettent en évidence l'agglomération et la porosité des particules de TiO_2 , respectivement. (c) photoanode sans MWCNT et (d) photoanode avec MWCNT après vieillissement.	156
Figure 7 Illustration schématique du modèle de structure de bande du TiO_2 formant des pièges électroniques profonds. Sous illumination UV, les électrons injectés et photogénérés peuvent être adsorbés via des sites de donneurs d'électrons profonds. Ensuite, l'électron dans ce site peut subir une recombinaison directe avec un trou dans l'électrolyte.	158
Figure 8 Propriétés fonctionnelles des DSSC dans les cas avec et sans MWCNT en fonction du temps de vieillissement thermique (a) courbes J-V des DSSC sans MWCNT, (b) courbes J-V des DSSC avec MWCNT, (c) J_{sc} (mA cm^{-2}); (d) V_{oc} (V); (e) FF (%) and (f) PCE (%).	160
Figure 9 Décomposition transitoire de V_{oc} et durée de vie électronique obtenue (τ_e): pour les cellules sans MWCNT (a et b) et les cellules avec MWCNT (c et d) mesurées après différents temps de contrainte thermique.	162
Figure 10 (a) Photographie du film composite CuS-3G. Images au MEB d'un film de CuS avec diverses concentrations de graphène à différents grossissements: (b)-(c) CuS-0G; (d)-(e) CuS-3G; (f)-(g) CuS-10G. Les flèches rouges indiquent les zones de microfissures.	164

Figure 11 Courbes densité / tension actuelles de cellules solaires sous une lumière solaire simulée à une AM 1,5G (100 mW cm^{-2}) simulées à l'aide de CE composites Pt et CuS-3G.... 165

Figure 12 Voltamogramme cyclique de CE composites Pt et CuS-3G. 166

LIST OF TABLES

Table 2.1. Properties of carbon allotropes [80].	36
Table 3.1. Functional parameters of DSSCs with and without MWCNTs.	54
Table 4.1. Functional parameters of DSSCs with and without MWCNTs.	82
Table 5.1. Functional parameters of DSSCs fabricated using different CuS-G nanocomposite CEs.	111
Table 5.2. Functional parameters of DSSCs with different Pt and CuS-3G CEs.	115
Table 5.3. Comparison of R_s (Ω) and R_{ct} (Ω) calculated from EIS measurements of symmetric cell configuration of spin coated CuS-3G composite and Platinum CEs.	117

LIST OF ACRONYMS

PV	Photovoltaic
DSSCs	Dye sensitized solar cells
PCE	Photo conversion efficiency
UV	Ultraviolet
CE	Counter electrode
Pt	Platinum
TCO	Transparent conductive oxide
MWCNTs	Multi-wall carbon nanotubes
SWCNTs	Single-walled nanotubes
G	Graphene
IEA	International Energy Agency
c-Si	Crystalline silicon
a-Si	Amorphous silicon
CIGS	Copper indium gallium selenide
CIS	Copper indium selenide
CdTe	Cadmium telluride
QDSSCs	Quantum dot sensitized solar cells
a-Si	Amorphous silicon
CuS	Copper sulfide
FTO	Fluorine doped tin oxide
LUMO	Lowest unoccupied molecular orbital
HOMO	Highest occupied orbital

ITO	Indium-tin oxide
J-V	Current-Voltage
J_{sc}	Short circuit photocurrent density
V_{oc}	Open circuit voltage
FF	Fill factor
MPP	Maximum power point
R_s	Series resistance
R_p	Parallel shunt resistance
P_{out}	Maximum obtainable power
P_{in}	Power of the incident light
V	Voltage
J	Current
ZnO	Zinc oxide
SnO_2	Tin(IV) oxide
TiO_2	Titanium dioxide
CNTs	Carbon nanotubes
η_{LHE}	Light harvesting efficiency
η_{inj}	Electron injection efficiency
η_{reg}	Efficiency of dye molecules regeneration
η_{col}	Charge collection efficiency
IPCE	Incident photon to current efficiency
AM	Air mass
EIS	Electrochemical impedance spectroscopy
R_{ct}	Electron transport resistance

C_{Pt}	Interfacial capacitance
C_{μ}	Chemical capacitance
R_{TCO}	Charge-transfer resistance at the TCO and electrolyte interface
C_{TCO}	Capacitance at the TCO and electrolyte interface
C_{CO}	Capacitance at the semiconductor layer and TCO contact
R_{CO}	Resistance at the contact of the TCO and semiconductor
Z_d	Impedance of the electrolyte
R_d	Diffusion resistance of the redox species in the electrolyte
C_{μ}	Chemical capacitance
τ_e	Electron lifetime
CB	Conduction band
VB	Valence band
XRD	X-ray diffraction
SEM	Scanning electron microscope
FESEM	Field emission scanning electron microscopy
EDS	Energy-dispersive X-ray spectrometer
TEM	Transmission electron microscopy
SAED	Selected area electron diffraction
AFM	Atomic force microscopy
XPS	X-ray Photoelectron Spectroscopy
$E_{binding}$	Binding energy
E_{photon}	Photon energy
ϕ	Spectrometer work function
UV-vis	Ultraviolet-visible

CV	Cyclic voltammetry
QE	Quantum efficiency
EQE	External quantum efficiency
IQE	Internal Quantum Efficiency
MS	Mott-Schottky
TMS	Transition metal sulfides
eV	Electron volt
MS	Metal sulfides
CNTH	Copper nitrate trihydrate
TAA	Thioacetamide
WF	Work function

"To truly transform our economy, protect our security, and save our planet from the ravages of climate change, we need to ultimately make clean, renewable energy the profitable kind of energy."

Barack Obama

Introduction

In 2007, the Norwegian Nobel prize committee awarded for the first time the Nobel Prize for Peace to an important scientific consortium, the aim of which is to investigate and prove the rapid environmental and economic change in the earth's climate, namely so-called "Global Warming". The increase in the world's energy demand due to the rapid growth of population has not only accelerated the depletion of the earth's oil reserves, but has also resulted in environmental contamination and the greenhouse effect. Thus, the development of renewable and green energy sources is crucial towards a sustainable future. The American Recovery and Reinvestment Act in the United States has set a goal that greenhouse gas emissions should be reduced by 28% by 2020 [1]. In this context, the PV device that converts solar energy into electricity is a clean and renewable technology with considerable potential. However, this technology is not yet widely deployed; optimization of PV efficiency, long-term stability and cost reduction are the major challenges that hinder its widespread use [2–4]. Breakthrough developments in materials are needed to address these challenges. Since Gratzel and O'Regan first reported this new type of solar cell in 1991 [5], DSSCs have represented a promising solar technology due to appealing features such as a simple fabrication process, eco-friendly production, low production costs, colour choice and transparency [1,6]. Since then, this field of research has made considerable progress and is beginning to make significant inroads into solar energy [1,6].

DSSCs possess the ability to surpass the above mentioned challenges, in particular efficiency, stability and production cost for large-scale commercialization. During recent years, the research community has made significant advances on different components of DSSC including the anode, dye, electrolyte, and cathode, to improve PCE [1,6,7]. Progress in the design of device architecture has enabled the production of stable, reproducible cells and contributed to boosting the PCE up to ~ 14.7% [8]. However, there is still room for improvement, such as achieving long-term stability and decreasing production cost, both of which are crucial challenges for large-scale commercialization.

Various stability issues are generally associated with DSSCs, such as thermal stability as well as UV and visible light stability [9–13]. There are already interesting reports on improvement in the PV performance of DSSCs with the addition of carbon nano materials [14–19]. However, questions have been raised about whether this composite of carbon materials has any effect on the stability of DSSCs.

The CE, which is another important component in DSSCs, is generally made of Pt coated FTO [20–24]. While the overall fabrication cost of DSSCs is comparatively low, Pt and the TCO glass account for more than 40% of the total device cost [25–27]. Therefore, design and fabrication of TCO and Pt-free CEs for DSSCs without reducing electrocatalytic activity is the subject of much current interest in the field of DSSC research.

Objectives of the thesis

In the framework of this PhD project, DSSCs were fabricated in different configurations incorporating carbon nanomaterial composite structures in order to improve stability and decrease the production cost of the device.

Chapter 1, entitled 'Solar energy and solar cells', is useful for understanding the basic concepts related to capturing solar energy and transforming it into electricity. The basic operational principle of PV is then discussed. An in-depth discussion on device structure and a theoretical description of the phenomena within the cell are also presented. The last section of this chapter provides the necessary foundations for the device's investigation methods.

In Chapter 2, materials and experimental techniques, together with all of the used materials and experimental techniques for device fabrication and characterization, are described in detail.

The contribution of MWCNTs to the TiO₂ anode is investigated in Chapter 3. The focus of this section is a comparison of the long-term stability of two devices made of (i) bare nanocrystalline TiO₂ and (ii) MWCNTs-TiO₂ composite anode, exposed to continuous visible and UV light irradiation.

The focus of Chapter 4 is directed to long-term thermal stability, as a major challenge that needs to be addressed for this technology to become commercially viable. The main

subject of this section focuses on the effect on the thermal stability of DSSCs of incorporating MWCNTs.

Chapter 5 describes a simple, low temperature and solution-processable approach to preparing a composite film of CuS-G as a TCO and Pt-free CE for DSSCs.

CHAPTER 1

Solar energy and solar cells

During the last two decades, as a result of rapid development and industrialization, worldwide energy demands have shown a remarkable increase. All predictions indicate that this growth will continue by over 50% before 2030 [3,4]. According to the International Energy Agency (IEA) report, energy usage by nations with emerging economies, such as those in Southeast Asia, the Middle East, South America and Africa, will increase at an average annual rate of 3.2% while developed countries, including North America, Western Europe, Japan, Australia and New Zealand, will grow at an average rate of 1.1% [28,29]. Different forms of fossil fuels, including coal, oil and natural gas, contribute up to 80% of the world's energy use [3]. A series of measurements of atmospheric CO₂ levels demonstrate a relentless increase, year after year. The atmospheric CO₂ concentration has risen from 300 to 380 ppm in the past 50 years. This unacceptable rise in the atmospheric CO₂ level increases the earth's temperature, with effects on global climate such as higher levels of atmospheric water vapor, changing weather patterns and rising sea levels from the melting of polar icecaps [30,31].

As a consequence, the limited availability of fossil fuels as a non-renewable energy source requires societies to make changes to their current energy management for sustainable living [3,4]. Energy management has led policy makers and industrialists to identify efficient means of energy shift to the utilization of new energy sources. Renewable energy sources have several advantages, such as being sustainable and nature friendly as well as their ability to reduce carbon emissions to the atmosphere [3,4]. An important decision faced by governments and businesses concerns which renewable energy source is the best choice since future generations are dependent on today's decision. In this sense, different factors have to be evaluated and compared, including: the availability and type of renewable sources; the efficiency of energy conversion; land requirements; water

consumption; and social impact [3,4]. Amongst various renewable energy sources, including solar, wind, hydroelectric, biomass, geothermal, hydrogen and ocean energy, solar energy is one of the cleanest and most abundant [2,28]. The amount of solar energy reaching the earth's surface per second is more than the total energy that people have used since the beginning of time [28].

Solar energy is directly related to the light and heat generated by the Sun. The Sun can be considered as a black-body emitting radiation at 5500 K with a broad spectrum, stretching out from UV up to radio waves with a peak at 525 nm (2.36 eV), as shown in Figure 1.1 [32]. As can be observed, half of the solar spectrum falls in the infrared region (responsible for warming the Earth), 40% is in the visible region while the remaining 10% is in the UV region.

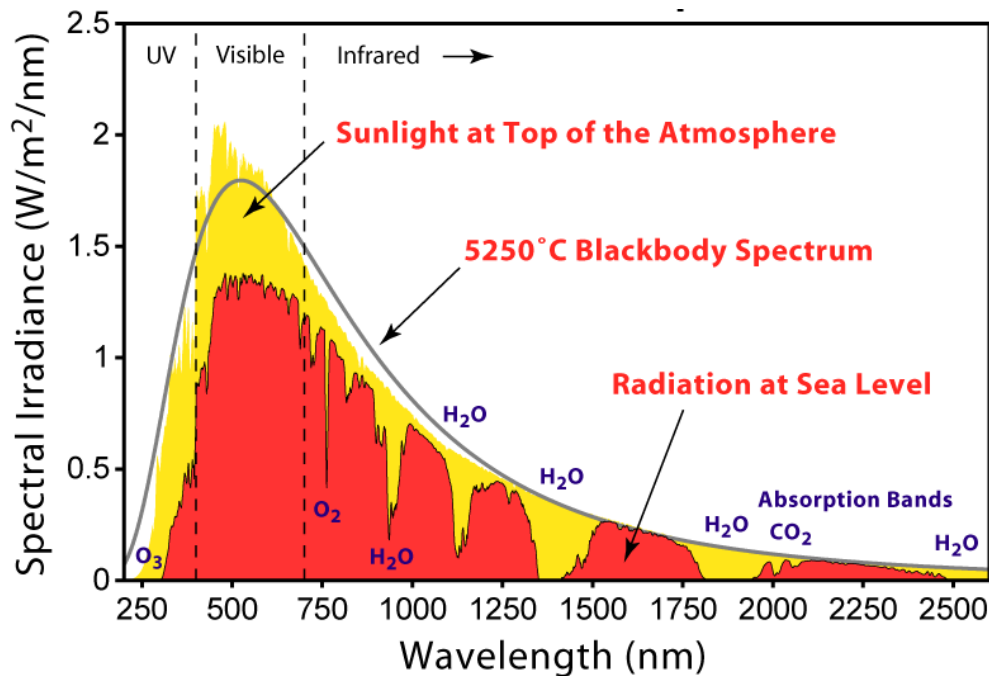


Figure 1.1 Solar irradiance spectrum (yellow: at the top of the Earth's atmosphere; red: after passing through the atmosphere) comparison with spectrum of black body radiation at 5250°C (grey line) [32].

Solar energy can be captured through passive and active solar systems. Passive solar system merely collects the Sun's energy without converting it into other forms: for example, maximizing the use of light and heat through green building design. Active solar

energy technology refers to the converting of solar energy into other forms of energy that can be classified into three groups: (i) solar cell; (ii) chemical energy; and (iii) solar thermal [2,28,33].

1.1 Photovoltaics

The French scientist, Edmond Becquerel, first discovered the PV effect in 1839 [34]. The solar cell is an electrical device that converts the energy of sunlight directly into electricity. This subject has created a new road for renewable energy sources with the potential to replace a significant percentage of fossil fuels. The conversion of solar energy into electricity by a solar cell is based on three primary mechanisms: (i) the absorption of a photon and generation of a charge-carrier; (ii) charge-carrier separation; and (iii) charge-carrier collection [35,36].

PV devices mainly exploit a semiconductor material that works as a light absorber. As can be seen from Figure 1.1, the region between 400 and 1100 nm has the highest photon density in the solar spectrum. Therefore, an ideal light absorber (semiconductor) is a material that can absorb sunlight between 400 and 1100 nm. Upon absorption of photons with energy equal or greater than the band gap of the semiconductor ($h\nu \geq E_g$), an electron/hole pair is generated. The electron and hole can then be effectively separated and diffused toward the n-type semiconductor and the p-type semiconductor, respectively (Figure 1.2) [32]. Electrons flow through an external circuit and generate an electric current.

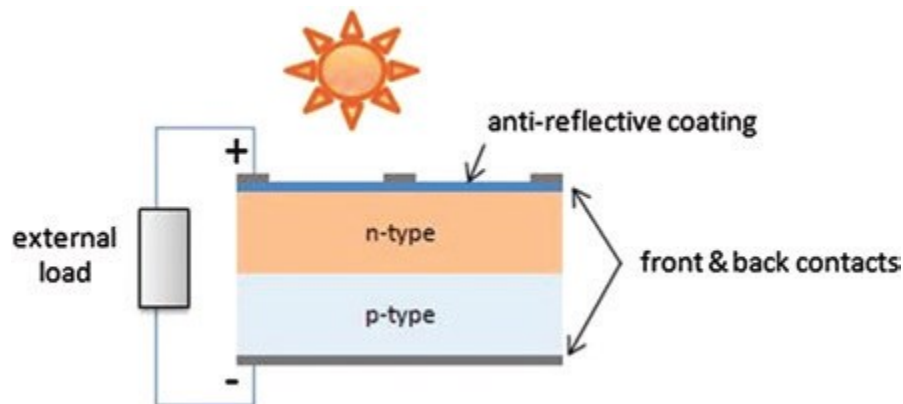


Figure 1.2 Schematic of p-n junction based solar cell [32].

1.2 Classification of solar cells

In 1883, Charles Fritts first reported the fabrication of a complete solar cell by a sandwich structure, consisting of selenium and gold, whose PCE reached less than 1% [37]. In 1954, Daryl Chapin, Calvin Fuller and Gerald Pearson built the first silicon-based solar cell at the Bell Telephone Laboratories, reporting a PCE as high as 6% [38]. From that time until now, researchers have been trying to develop a simple structure and low cost technology by applying new materials, approaches and concepts. Martin Green categorized solar cells in three different generations based on the nature of the material, PCE, and cost effectiveness [39]. Figure 1.3 graphically shows energy conversion efficiency ranges and possible module production costs per unit area for the three generations of technology [39].

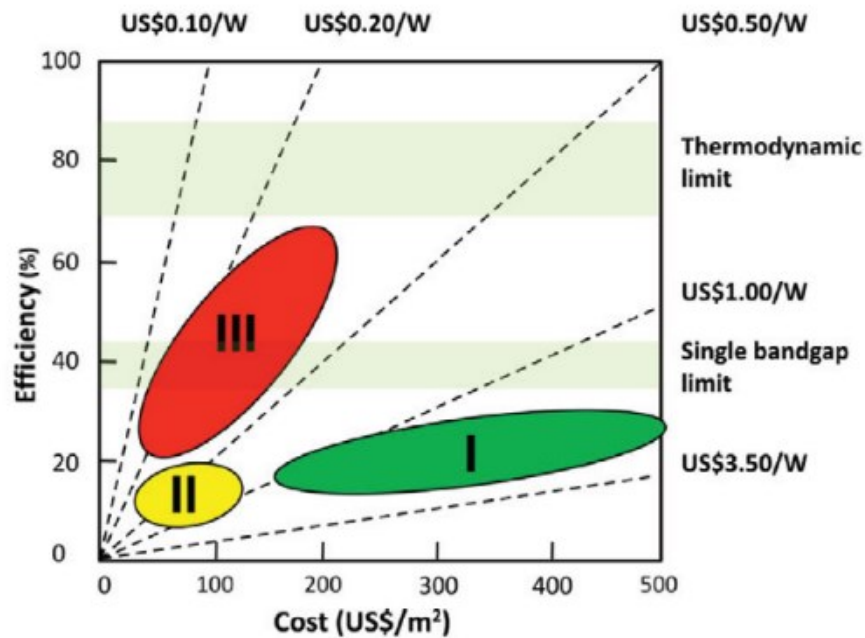


Figure 1.3 Efficiency and production cost projections for three generations of solar cells [40].

1.2.1 First generation

First generation PV is based on extremely purified crystalline silicon (c-Si). This generation features a quite high conversion efficiency (~24%) thanks to a broad absorption spectral range. Unfortunately, manufacturing processes that are applied to

growing highly pure c-Si are inherently expensive, thus raising the cost of devices. Thus, first generation is characterized by high production costs as well as moderate efficiency [32,39]. The first generation of solar cells consists of monocrystalline and polycrystalline silicon solar cells. The value of conversion efficiency for monocrystalline (~ 24%) is higher than polycrystalline silicon (~ 20%) solar cells, due to high rate exciton recombination at the grain boundaries [32,39]. However, production of a multicrystal wafer is easier and cheaper compared with polycrystalline.

First generation solar cells are also known as conventional and traditional cells. Solar cells based on the II-IV and III-V groups are also classified under the first generation category. First generation PVs account for 86% of account for 86% of the solar cell market due to high conversion efficiency and a large amount of purified Si production by well-developed semiconductor industries.

1.2.2 Second generation

Second-generation solar cells, which were introduced to reduce the production cost of first generation whilst maintaining the PCE, are based on thin film technology. There is no doubt that, while second generation PVs certainly address the high production cost issue of first generation PVs, their efficiencies are lower than first generation [32,39]. Second generation are more applicable to purposes such as windows, cars, and building integrations because there are no fingers in front. As an advantage of solar cells, these thin films can also be grown on flexible substrates and in large areas, up to 6 m² [41]. The most common second generation solar cells available on the market are [41]:

- Amorphous silicon (a-Si), with 10.1% conversion efficiency
- Copper indium gallium selenide (CIGS), with 19.9% conversion efficiency
- Copper indium selenide (CIS) , with 12.5% conversion efficiency
- Cadmium telluride (CdTe), with 16.7% conversion efficiency.

- Much lower investment costs compared with conventional and traditional PV technologies
- Low production cost (short energy payback time [<1 year])
- Relatively better performance than competitors under real outdoor conditions at diffused light and higher temperatures
- Design options, such as transparency and multicolor opportunities
- Ability to outperform competitors for indoor applications
- Flexibility and light weight.

1.3 Dye-sensitized solar cells (DSSCs)

1.3.1 Brief history

The dye-sensitization process on wide band gap semiconductors, including ZnO and SnO₂, was reported in the late 1960s [44,45]. Gerischer studied the effect of dye adsorption on the stability of large band gap semiconductors under a visible region [44]. Most of these works reported fundamental concepts and novel materials used in DSSCs, such as dye-sensitization of semiconductors, electrolyte redox chemistry and electron-transfer processes [46,47]. The obtained cells were characterized with low conversion efficiencies (1-2%) due to the poor dye anchorage on the semiconductor surface and weak light absorption [45,48].

Since 1991, DSSCs have attracted great attention in the solar cell field, following the breakthrough work by O'Regan and Gratzel who introduced the mesoporous structure of the TiO₂ and a tris (2, 2'-bipyridyl 4, 4'-carboxylate) ruthenium (II) dye as a light harvester, and reported a record PCE of around 8% [5]. Subsequent to this pioneering work, researchers have been racing to further improve both the PCE and stability of DSSCs for large scale commercialization by optimizing the different components (metal oxide, dye, electrolyte and CE) of the device (Figure 1.5) [49]. Recently, a PCE greater than 14% has been reported for DSSCs [8]. Although this is still lower than the PCE of the Si based solar cells (~25%) [2], it has an edge over them at some points: (i) DSSCs show high

efficiency in diffuse sunlight or cloudy conditions; and (ii) performance is less sensitive to the incident angle of light radiation [6,42].

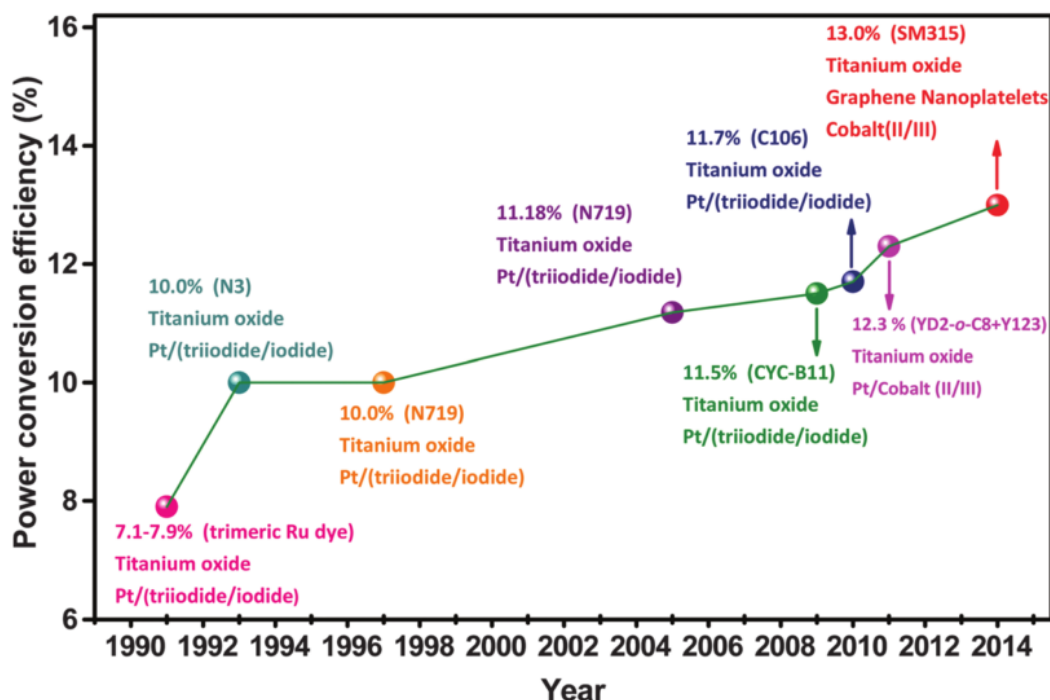


Figure 1.5 Selected PCE landmarks in DSSCs [49].

1.3.2 Cell architecture

DSSCs are made in a sandwich configuration of different materials that are trapped between two pieces of conducting glass. A schematic of a complete cell is presented in Figure 1.6. The main components of the DSSC are: a semiconductor, dye, transparent electrode, an electrolyte and a CE. The photoanode is constituted of a 10-20 μm thick layer of a wide band gap metal oxide semiconductor (usually TiO_2 , ZnO and SnO_2) deposited on a transparent conducting oxide substrate. Among different types of semiconductors, TiO_2 nanostructure is the most efficient material to be used as a photoanode. A TiO_2 photoanode is composed of two different layers: (i) an 8-14 μm mesoporous film of 20 nm sized TiO_2 nanoparticles called the “active layer”; and (ii) a 4-6 μm layer of 200-400 nm sized nanoparticles called the “scattering layer”. Dye molecules serve as antennae to harvest the sunlight (photons). The light enters the device from the photoanode side, so that good transparency of the substrate is necessary. The CE is

typically made with a platinized (5-10 nm Pt thin layer) transparent conducting glass. The space between the dye sensitized photoanode and the CE is filled by a liquid electrolyte [5,50–52].

1.3.3 Basic Operating Principle of DSSCs

DSSCs are quite different from conventional p-n junction solar cells by their basic construction and the physical processes behind their operation. The typical configuration of DSSCs combines two solid and liquid phases, while other solar cells are based on the solid phase [5,6,36,50–52]. All the components and a complete cycle to conversion of light into electrons in DSSCs are shown in Figure 1.6. The overall PCE of DSSCs can be evaluated based on three factors: ($\eta = \eta_{\text{abs}} + \eta_{\text{inj}} + \eta_{\text{coll}}$) [53]. One cycle of a DSSC operation is completed in five steps, as described below:

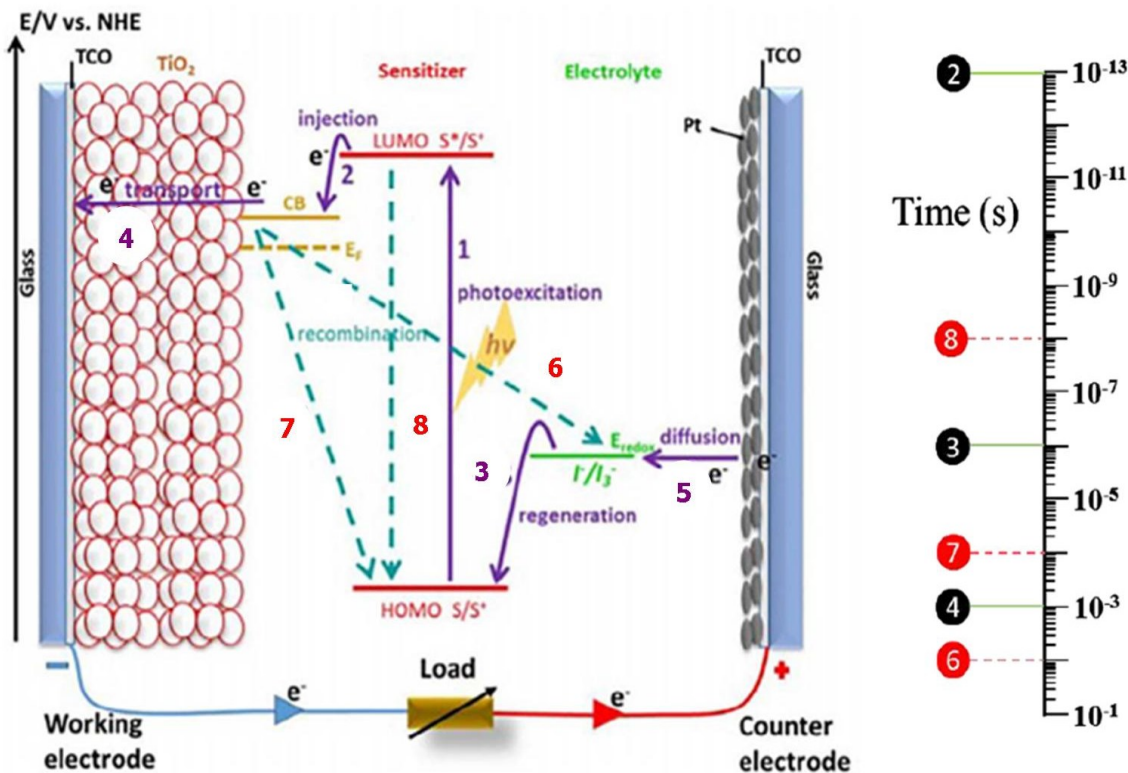


Figure 1.6 Schematic of the working principle of a DSSC and time scale of the processes within a device [54].

Light Absorption

In DSSCs, sensitizer molecules are adsorbed on the surface of metal oxide semiconductors (e.g., TiO₂ and ZnO) and act as light harvesters. The ideal sensitizer should meet several requirements. These include: (i) the sensitizer should be able to harvest more light of the solar spectrum; (ii) the sensitizer must carry a carboxylate or phosphonate group to make a chemical bounding to the surface of the semiconductor; (iii) the lowest unoccupied molecular orbital (LUMO) of the sensitizer must be higher than the conduction band of the semiconductor; (iv) the highest occupied orbital (HOMO) of the sensitizer must be sufficiently low to accept electron donation from an electrolyte; and (v) there should be chemical and thermal stability in the electrolyte media and during exposure to solar radiation [6]. Due to the absorption of light, the dye molecule is excited from the ground state (S) to the excited state (S*). In this condition, an electron jumps from the HOMO to the LUMO of the dye molecule (Step 1) [6,36,42].

Charge separation

Charge separation in DSSCs is fundamentally different from the p-n junction solar cell. Due to the concentration difference between the p and n type semiconductor in a conventional photovoltaic built on a p-n junction, the holes move to the n region and the electrons to the p region. In DSSCs, the excited electron must successfully inject from the LUMO of the dye molecule to the conduction band of the semiconductor (Step 2). The electron injection typically occurs on a time scale of femtoseconds. The next step for charge separation is hole transfer from the HOMO to the electrolyte (Step 3) [6,36,42]. After transferring the hole from dye to electrolyte (reducing the dye), the positive charge is now moved to the redox couple and the negative charge, or electron, is injected into the conduction band of the semiconductor, which creates a charge separation between the hole and the electron [36,50,55].

In metal based dyes, the electron excitation occurs via a metal to ligand charge transfer mechanism. Under the absorption of photons, electrons are shifted from the metal part of the dye molecules to the ligand. This shifting of the electron leads to oxidation of the metal and a reduction of ligands. The dye molecules are covalently bonded to the surface atom of the metal oxide (e.g. TiO₂, ZnO, SnO₂) via carboxylic groups in the ligand species. This

bonding leads to significant overlapping between the LUMO level of the dye and the conduction band of the metal oxide that is necessary for electron injection from the LUMO level of the excited dye molecules to the conduction band of the metal oxide semiconductor [56,57].

Charge-carrier transport

After charge separation, the hole and the electron travel through the electrolyte (Step 3) and mesoporous metal oxide layer (Step 4), respectively. DSSCs are majority carrier devices where electrons and holes are separated into two chemical phases. Although many theoretical and experimental investigations have been carried out to understand the exact mechanism of electron transport through the mesoporous metal oxide, diffusion via a trapping/detrapping mechanism along localized energy levels below the conduction band edge seems the most realistic [36,50,55]. Under illumination, the injected electrons to the conduction band of metal oxide particles generates a potential gradient within the particles and appears to be the main driving force for transport in the mesoporous film [42]. After diffusing in the nanocrystalline semiconductor network to the conductive coating of the substrate, electrons can be transferred to an external circuit.

After the injection of the electron from the LUMO of the excited dye molecule to the conduction band of the semiconductor, the hole is left in the HOMO of the oxidized dye molecules. For current generation, the dye must be reduced by taking the electron from the redox couple electrolyte. The oxidized electrolyte then diffuses to the CE and is reduced back to the iodide by the collected electrons from the external circuit (Step 5) [36,50,55].

Recombination processes

The main source of the losses in the performance of DSSCs is non-radiative carrier recombination [42]. This reaction can occur via two channels: in the conduction band of mesoporous metal oxide and in the LUMO of the excited dye. The first process is the recombination of electrons in the conduction band of the semiconductor with acceptors in the electrolyte (Step 6). The probability of occurrence of this process is higher compared with other existing recombination processes because the liquid electrolyte has good penetration inside the mesoporous film, which leads to intimate contact with the metal

oxide nanoparticles. Recombination can occur both at the semiconductor/electrolyte interface and at the part of the conducting substrate that is exposed to the electrolyte [42,55]. However, electron back reaction at the conducting substrate/electrolyte interface can be suppressed by deposition of a compact blocking layer [42]. Recombination of electrons with oxidized dye molecules is another possible reaction (Step 7). This reaction competes with the regeneration process of dye molecules with electron transfer from the conduction band of the semiconductor to oxidized dye molecules, which usually occurs on a time scale of about 1 μ s [42]. The last recombination process takes place in excited dye molecules by re-combining of the electron in the LUMO with a hole in the HOMO of the dye molecules (step 8). This recombination process competes with the process of electron injection into the conduction band of the semiconductor that occurs in the femtosecond time range and which is much faster than the electron recombination [6,42,50,55].

1.4 Characterizations of photovoltaic performance

The most important measurement of a solar cell is the current density-voltage (J-V) characterization curve under standard conditions (temperature, spectral irradiance, total irradiance) to report the performance of the cells [36]. In order to be able to compare performances of solar cells, the J-V curve is measured under standard illumination conditions (see the standard test conditions section). The J-V characteristics are monitored under illumination or dark conditions by applying an external potential (altered from J_{sc} to V_{oc}) between two electrodes. Since no oxidized dye is present in dark conditions, the dark current gives information about the electrons moving in reverse, from the semiconductor nanoparticles to the oxidized species of the redox couple, which is a recombination of the oxidized redox species [1,6,36]. An example of a J-V curve under illumination is shown in Figure 1.7.

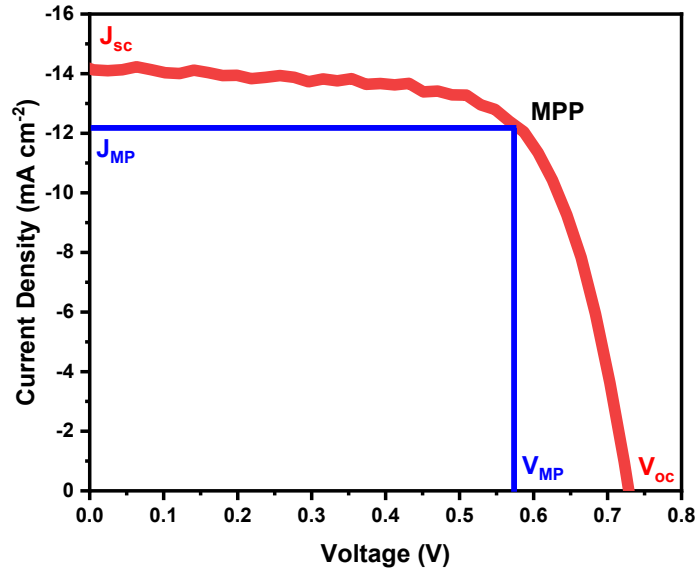


Figure 1.7 Typical current-voltage curve of a photovoltaic cell.

1.4.1 Short circuit photocurrent density

Short circuit photocurrent density (J_{sc}) is the photocurrent divided by the active area of the device (mA cm^{-2}) when the device is short-circuited or, in other words, when the external output voltage is zero. In DSSCs, J_{sc} depends on several factors such as: the light intensity; electron generation and injection efficiency; recombination resistance; and the efficiency of charge transport [35,36]. Graphically, J_{sc} is determined by the intersection with the y-axis (when $V = 0$), as shown by the J-V curve.

1.4.2 Open circuit voltage

The open circuit voltage (V_{oc}) is the maximum voltage obtained from a solar cell under open circuit conditions when no external load is connected. Graphically, V_{oc} is determined by the intersection with the x-axis (when $J = 0$). For DSSCs, the V_{oc} is given by the difference between the Fermi level of the semiconductor and the redox potential of the electrolyte [58].

$$V_{oc} = \frac{E_{CB}}{q} + \beta \frac{kT}{q} \ln \left[\frac{n}{N_{CB}} \right] - \frac{E_{redox}}{q} \quad \text{(Equation 1.1)}$$

where E_{CB} is the conduction band edge energy level, N_{CB} is the effective density of states in the semiconductor, and q is the elementary charge of the electrons. For a defect-free semiconductor material $\beta=1$ [58]. n is the number of electrons in the conduction band of the semiconductor that is determined by the balance between electron injection and electron recombination [58].

1.4.3 Fill Factor

The fill factor (FF), which is a parameter related to the maximum power point (MPP), is often described as a measure of the “squareness” of the J-V curve. The general formula for electric power is $P = J \times V$. The FF value is determined by the ratio of the current and voltage at the MPP ($J_{MP}-V_{MP}$) and the parameter of the cell ($J_{sc}-V_{oc}$), with a value between 0 and 1 [1,6].

$$FF = \frac{J_{MP} \times V_{MP}}{J_{sc} \times V_{oc}} \quad \text{(Equation 1.2)}$$

The FF is dependent on the R_s and R_p of the solar cell. R_s in a solar cell is the result of contact resistance and charge transfer resistance that reduces the FF affecting the maximum power output. To obtain a higher FF, an improvement in the R_p is required (Figure 1.8) [1,6,59].

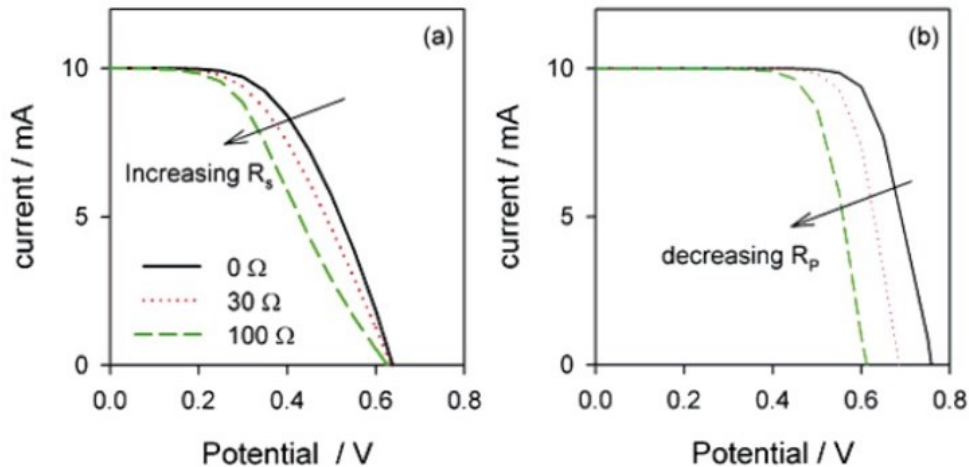


Figure 1.8 Evolution of simulated J-V curves with the change of (a) overall series resistance and (b) parallel shunt resistance [59].

1.4.4 Efficiency

The overall performance of a solar cell is evaluated by the solar-to-electrical energy conversion efficiency (η), which is determined by the ratio of the maximum obtainable power (P_{out}) to the power of the incident light (P_{in}) [1,6,36].

$$\eta = \frac{P_{out}}{P_{in}} = \frac{J_{sc} \times V_{oc} \times FF}{P_{in}} \quad \text{(Equation 1.3)}$$

1.4.5 Incident photon to current conversion efficiency

The incident photon to current conversion efficiency (IPCE) gives information about the efficiency of the solar cell in converting sunlight at a particular wavelength into an electrical current. In DSSCs, the IPCE factorized into different parameters such as light harvesting efficiency (η_{LHE}), electron injection efficiency (η_{inj}), the efficiency of dye molecule regeneration (η_{reg}), and photo-generated charge collection efficiency (η_{col}) [60].

$$\eta_{IPCE} = \eta_{LHE} \times \eta_{inj} \times \eta_{reg} \times \eta_{col} \quad \text{(Equation 1.4)}$$

The IPCE is also defined as the ratio of the output electrons to the incident photons at a particular wavelength (λ):

$$\eta = \frac{\text{Output electrons } (\lambda)}{\text{Incident photons } (\lambda)} = \frac{1240 \times J_{sc} \left(\frac{\text{mA}}{\text{cm}^2}\right)}{\lambda \text{ (nm)} \times P_{in} \left(\frac{\text{mW}}{\text{cm}^2}\right)} \quad \text{(Equation 1.5)}$$

where P_{in} is the input power and λ is the illumination wavelength [1,60].

The IPCE can be used as a useful technique to cross-check the result obtained with the J-V measurements. The J_{sc} is the integrated sum of the IPCE (λ) measured over the entire solar spectrum:

$$J_{sc}(\lambda) = \int_0^{\infty} IPCE(\lambda) I_{sun}(\lambda) d\lambda \quad \text{(Equation 1.6)}$$

where $I_{sun}(\lambda)$ is the incident irradiance as a function of the wavelength.

1.4.6 Standard test conditions

To compare photovoltaic performance, solar cells are measured under a set of standard test conditions: (i) the temperature of the cell should be 25°C; (ii) the total input power density of solar radiation must be 100 mW cm⁻² [35,36]. All the photovoltaic parameters (PCE, FF, J_{sc}, and V_{oc}) depend on the temperature and the intensity of illumination light. The sun's spectral power distribution is characterized as air mass (AM), which measures the reduction in the spectral content and intensity of solar radiation as it passes through the atmosphere, mainly caused by the scattering and absorption of the light by air molecules and dust particles. The air mass number is given by [35,36]:

$$\text{Air mass} = \frac{1}{\cos \theta} \quad (\text{Equation 1.7})$$

where θ is the angle of incidence (Figure 1.9).

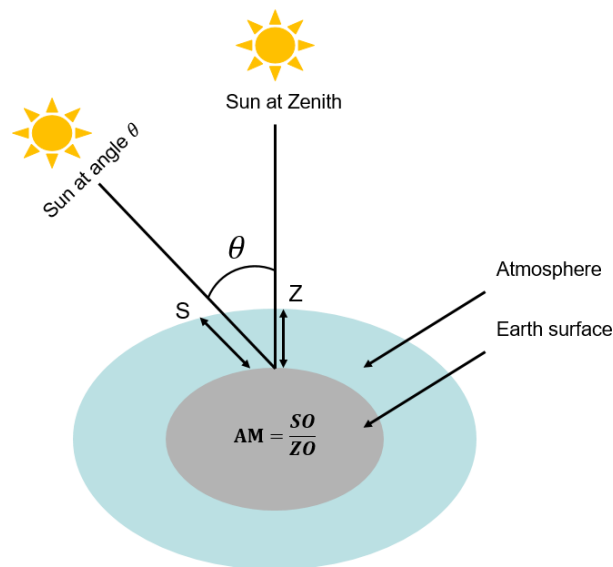


Figure 1.9 Typical illustration of air mass.

The standard for comparing solar cell performance is a spectrum normalized to a total power density of 100 mW cm⁻², AM1.5 at $\theta = 48.2^\circ$. AM0 is then the value for the solar irradiation just above the Earth's atmosphere where the radiation intensity is about 130 mW cm⁻². AM1 corresponds to the shortest possible path length when the sun radiation is coming at an angle of 0° [35,36].

1.4.7 Electrochemical impedance spectroscopy

Electrochemical impedance spectroscopy (EIS) is a powerful tool for investigating the kinetics of charge transport and recombination in DSSCs. EIS is widely used in these fields because of its sensitivity to electron diffusion and recombination at the interfaces of the metal oxide/electrolyte, CE/electrolyte and TCO/electrolyte interface [61,62]. Moreover, EIS is a non-destructive technique for analyzing the degradation mechanisms of DSSCs, including electron transport resistance in the different interfaces [63].

The equivalent circuit of a complete DSSC is represented in Figure 1.10 (a) [59]. The key parameters of the equivalent circuit are:

- Mesoporous TiO_2 film is the most characteristic element of the transmission line; its electron transport resistance is $R_t = r_t L$ (L as the thickness of the nanoporous TiO_2). The interfacial charge recombination resistance and the chemical capacitance in the nanoporous film are $R_{ct} = r_{ct}/L$ and $C_\mu = c_\mu L$, respectively.
- Charge-transfer resistance R_{ct} and the interfacial capacitance C_{Pt} at the Pt CE and the electrolyte interface are other important elements in the DSSC model.
- R_{TCO} is the charge-transfer resistance at the TCO and the electrolyte interface.
- C_{TCO} is the capacitance at the exposed TCO and the electrolyte interface.
- R_s is the sheet resistance of the TCO.
- The capacitance of the semiconductor layer and the TCO contact is C_{CO} .
- R_{CO} is the resistance at the contact of the TCO and the semiconductor layer.
- Z_d and R_d are the impedance and diffusion resistance of the redox species in the electrolyte.

Under high-illumination intensity, due to the electron excitation and injection from dye molecules to the semiconductor nanoparticles, the transport resistance becomes negligible and the equivalent circuit can be simplified (Figure 1.10b) [59].

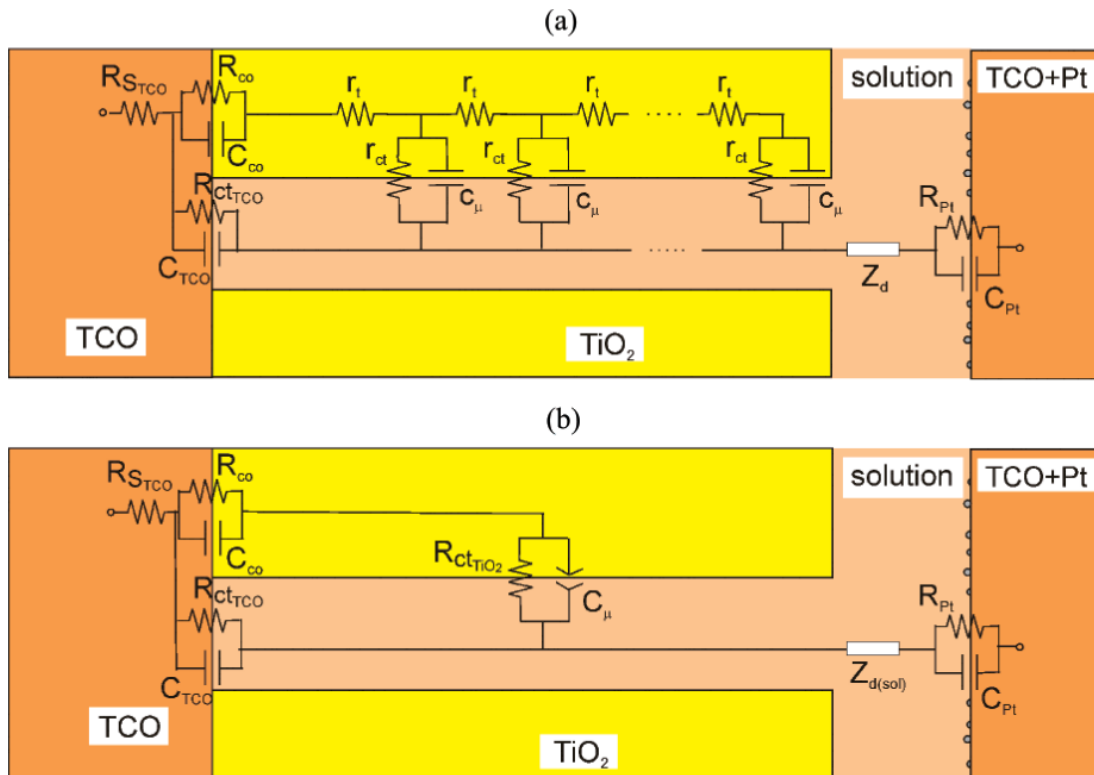


Figure 1.10 (a) General transmission line model of DSSCs and (b) simplified model at high illumination intensities [59].

The Nyquist plots of the complete DSSC can be represented in three semi-circles, as shown in Figure 1.11.

- The semi-circle that appears at high-applied potentials is related to the charge transfer resistance at the CE/electrolyte interface.
- The second semi-circle at medium-applied potentials represents the behaviour of the charge carrier at the metal oxide/dye/electrolyte interface.
- The third semi-circle at low-applied potentials reports information that represents the response of the diffusion resistance of the electrolyte.
- Information can be obtained about the R_s of the complete cell from the distance between the origin and the first semi-circle.

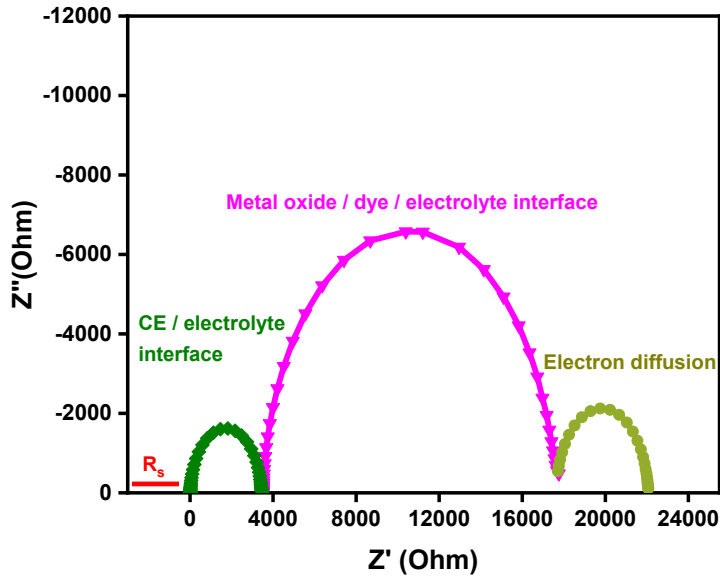


Figure 1.11 Typical impedance spectra (Nyquist plot) of a complete DSSC.

EIS is a well-established electrochemical method designed to study the electron lifetime (τ_e) of DSSCs. This measurement can be performed by two different methods:

- The second semi-circle of the Nyquist plots reports some information about the chemical capacitance, charge transfer and recombination resistance of the injected electron to the conduction band of the semiconductor. Based on Equation 1.7, these parameters allow the calculation of the electron lifetime at each applied bias [59,61,64].

$$\tau_e = R_{ct} \times C_{\mu} \quad \text{(Equation 1.8)}$$

- The EIS results can also be represented in Bode plots in terms of phase angle versus frequency (Figure 1.12). The electron lifetime can be evaluated with Bode plots by using the following equation [65]:

$$\tau_e = \frac{1}{2 \times \pi \times f_{max}} \quad \text{(Equation 1.9)}$$

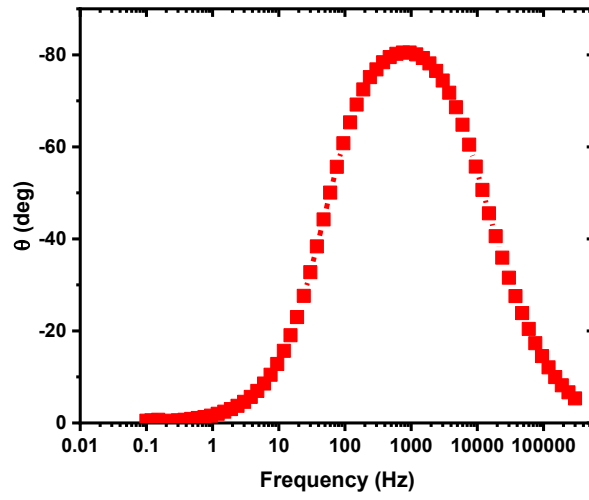


Figure 1.12 Typical Bode plots of a complete DSSC.

*“Experiments are the only means of knowledge at our disposal.
The rest is poetry, imagination.”*

Max Planck

Materials and experimental techniques

This chapter includes a description of the materials, cell fabrication procedures and device characterization by various techniques.

2.1 Materials

2.1.1 Transparent conductive oxide electrode

A schematic representation of the structure of DSSC is shown in Figure 2.1 [55]. In the case of the front side, the substrate should be highly transparent in the visible-IR region, but blocking the UV light. On the other hand, the backside of the substrate should have a high reflection to enhance light absorption by reflecting back the transmitted light into the dye. Moreover, other requirements for a good DSSC substrate are low sheet resistance, high transparency, thermal stability up to 450-500 °C, and ability to prevent impurities such as water and oxygen from entering into the cell. TCO-coated glass is generally used as the substrate for DSSCs. Indium doped-tin oxide (ITO) is one of the most well-known TCO materials for solar cell application, but it has a low thermal stability (ITO's sheet resistance also increases with temperature). Fluorine-doped tin oxide (FTO)-coated glass is commonly used as the TCO substrate for DSSCs (around $10 \Omega \text{ cm}^{-2}$). Other materials developed for working as a substrate for DSSCs include plastic foils and metal sheets to overcome some of the disadvantages of glass, such as fragility, rigidity, heavy weight and a high price. Conductive plastics are lightweight and flexible but they have low temperature tolerance, high R_s (around $60 \Omega \text{ cm}^{-2}$), and uncertainties considering the oxygen and water penetration. While metals are also mechanically robust, their main problem is corrosion behavior when in contact with an electrolyte. Stainless steel and

titanium have shown enough chemical stability in the iodine electrolyte, but their price is higher than glass [32,35,36,66].

In the present work, FTO glass substrate has been used for solar cell fabrication with sheet resistance in the range of $10\text{-}15 \Omega \text{ cm}^{-2}$ (Figure 2.2).

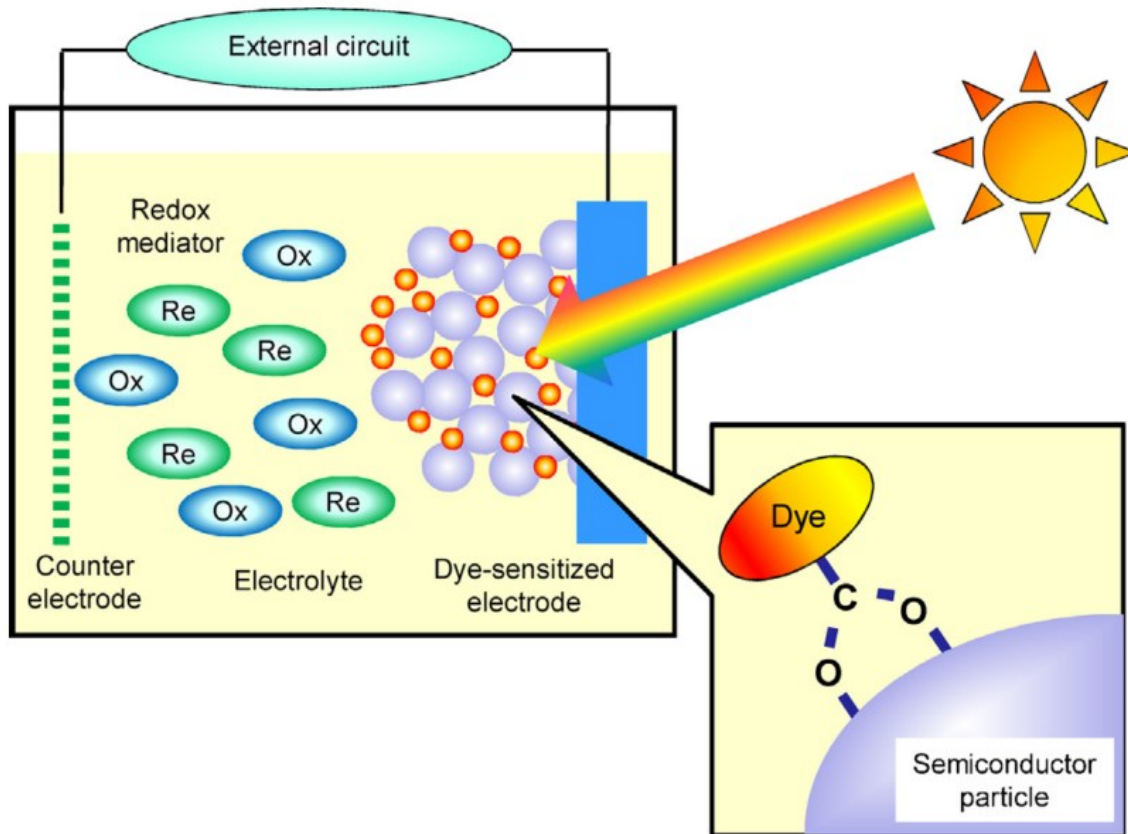


Figure 2.1 General structure of DSSCs [55].

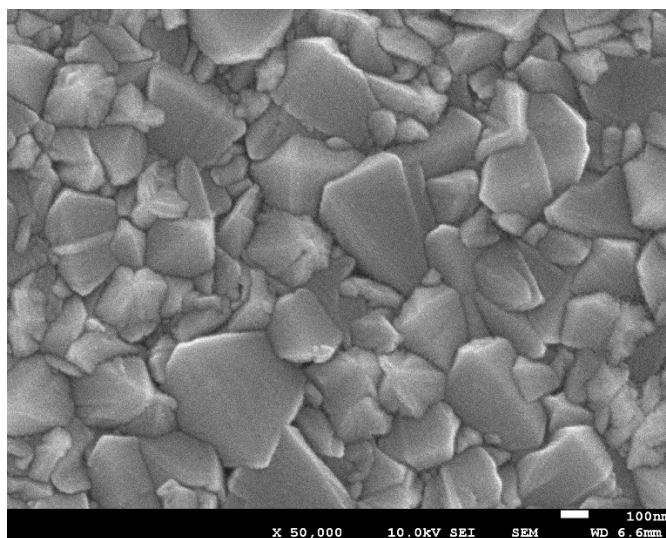


Figure 2.2 SEM image of FTO glass substrate.

2.1.2 Anode

The DSSC revolution actually started from the application of a mesoporous anode with a high surface area. The primary role of the mesoporous layer is to provide adequate surface area for loading sufficient amounts of dye molecules since monolayers of semiconductors lead to an intrinsic limitation. A monolayer of dye bound to the surface can inject electrons into the semiconductor. During the last few years, different semiconductors have been used for the working electrode of DSSCs. Figure 2.3 illustrates the band positions of several semiconductors [7]. The conduction band edge of the metal oxide semiconductor should be below the LUMO level of the dye. Metal oxide semiconductor must be chemically stable when in contact with the electrolyte, has a lattice structure suitable for dye bonding and be available in nanostructured form to enable high enough dye loading [6,50,55].

TiO₂ is the most efficient material to be used as photoanode, with a large band gap (3-3.2 eV). The thickness of the electrode is determined by the absorption coefficients of the dye molecules and electron diffusion length of the electrodes. To produce high-performance DSSCs, electrodes are prepared from small nanoparticles (10-25 nm, 10-18 micron thickness) and a scattering layer consisting of large nanocrystalline TiO₂ particles (250-300 nm, 5-10 micron thickness) [6,7,32,50].

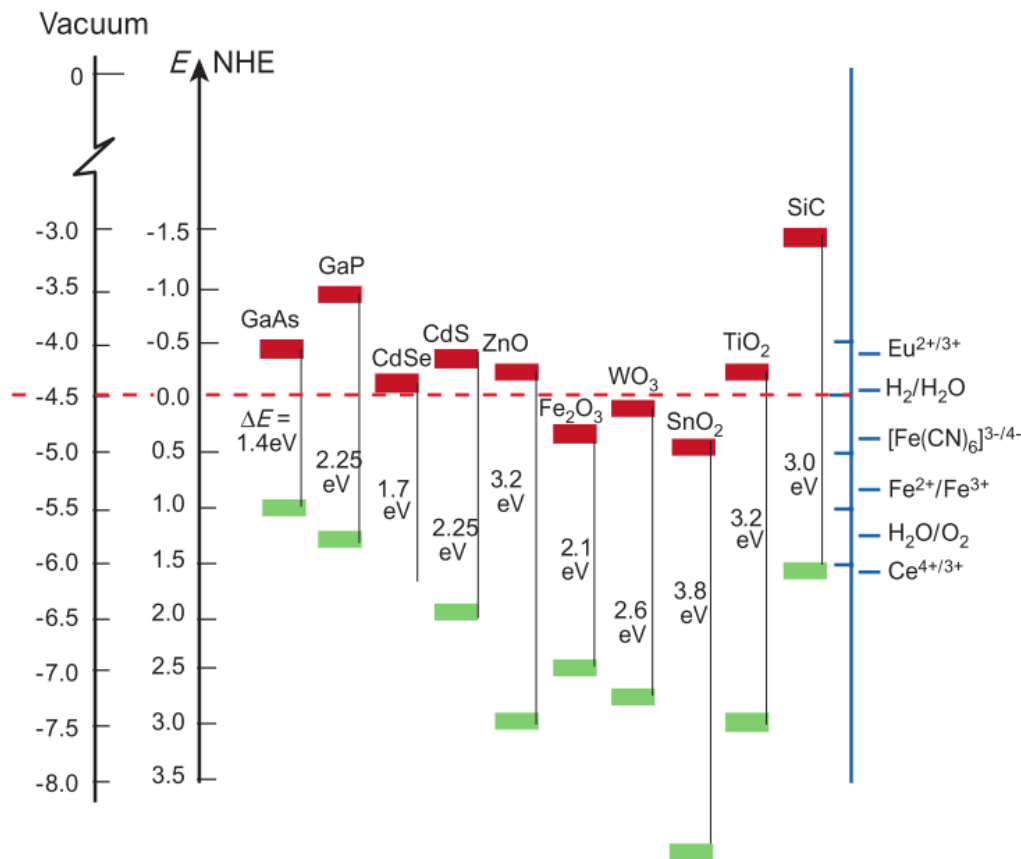


Figure 2.3 Band positions of different semiconductors in contact with aqueous electrolyte at pH 1. The conduction band (red colour) and the valence band (green colour) are presented along with the band gap in electron volts (eV) [7].

In this work, commercially available paste of TiO₂ nanoparticles is used as a metal oxide semiconductor. TiO₂ paste (18 NR-T) contains highly dispersed and stable anatase nanoparticles of 20 nm size as an active layer (Figure 2.4-2.6). The scattering paste (WER2-O) contains 150-250 nm sized anatase particles. These pastes are provided by Dyesol (Australia). TiO₂ nanoparticle paste is deposited on TCO glass substrates by the doctor blade method. Figure 2.7 shows the anode structure of the DSSC.

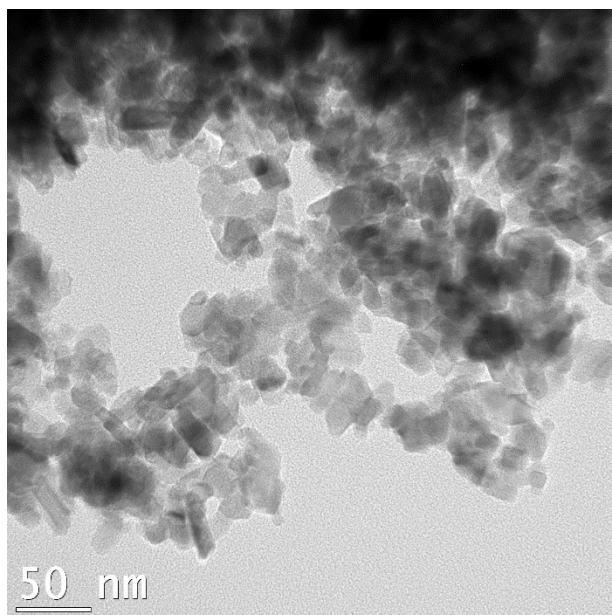


Figure 2.4 TEM image of TiO_2 anatase nanoparticles.

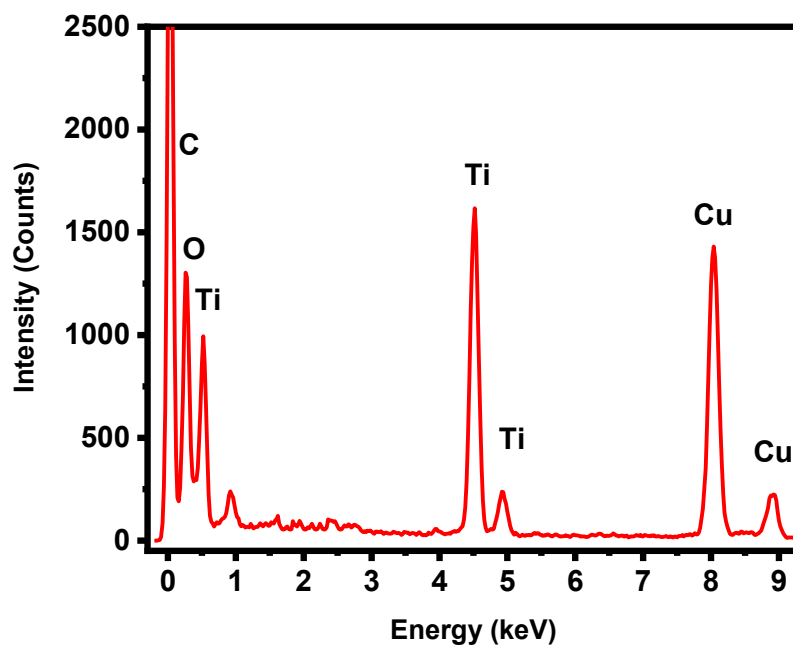


Figure 2.5 EDS spectra of the TiO_2 anatase nanoparticles.

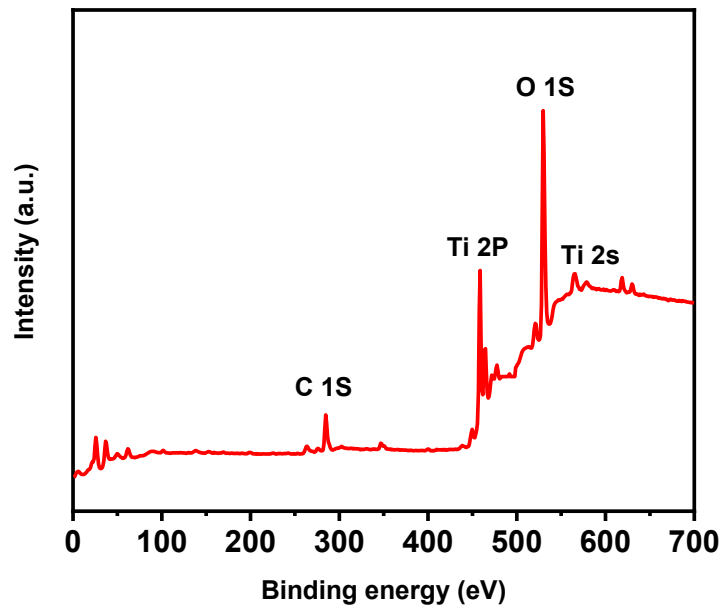


Figure 2.6 XPS spectra of the TiO₂ anatase nanoparticles.

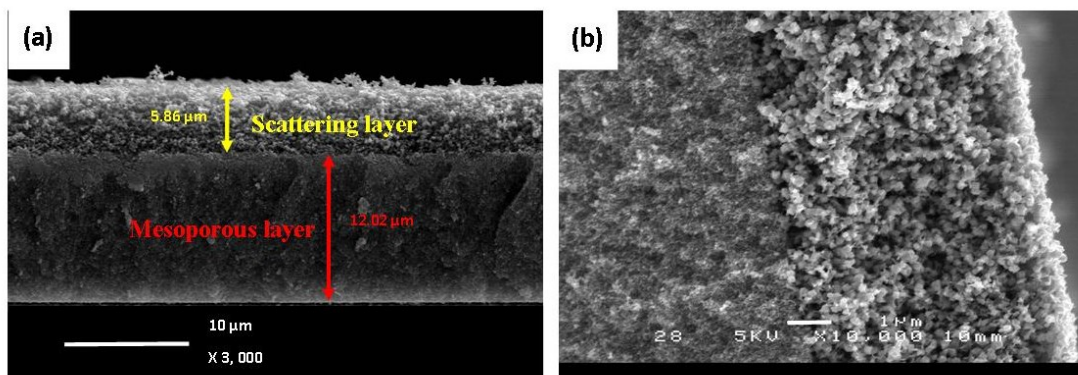


Figure 2.7 Cross-sectional SEM image of mesoporous and scattering TiO₂ layer: (a) low and (b) high magnification.

2.1.3 Sensitizers

Unfortunately, because of their wide band gap, metal oxide semiconductors absorb only the UV part of solar emission, which represents about 4-5% of the total. To optically enhance the light absorption in the visible-infrared region, dye molecules are chemically bound to the surface of the semiconductor. There are generally different kinds of adsorption modes, but for DSSCs the chemical bounding of the dye to the semiconductor

surface needs to be stable. For a strong linking of the dye to the semiconductor surface, most dyes have an anchoring group that reacts with the semiconductor surface and creates a chemical bond, over which charge transfer takes place. Usually commercially available dyes, such as N719 and black dye, have a carboxylic acid anchoring group that can coordinate to the oxide surface of the semiconductor in three different modes, namely unidentate, chelating and bridging bidentate, as shown in Figure 2.8 [67].

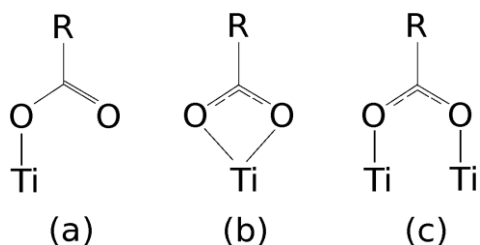


Figure 2.8 Various binding modes for a carboxylate unit on the TiO_2 surface as an example of a metal oxide semiconductor: (a) monodentate (b) bidentate chelating (c) bidentate bridging [67].

The most efficient and stable dye molecules in use are ruthenium (II) based dyes. However, they come with several drawbacks, especially a high cost and a limited amount of noble metals (Figure 2.9). The different forms of ruthenium-complex dye molecules that are commonly used in DSSCs, and which provide particularly high PCE, are shown in Figure 2.10 [55].

In this work, Ru (II) based dye coded N719 is applied as the light harvester.

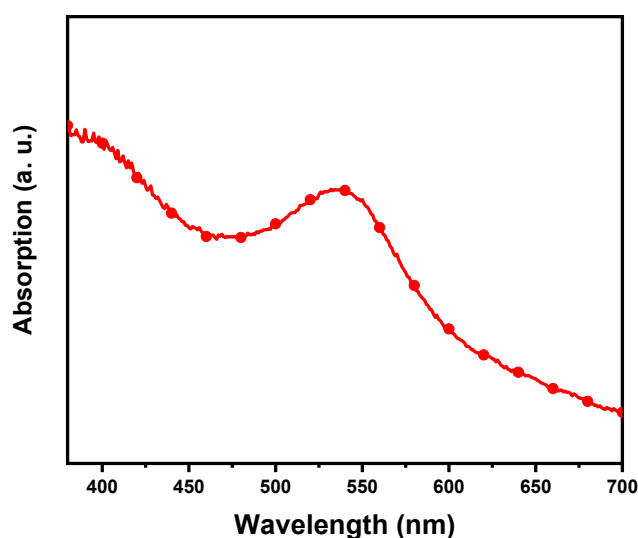


Figure 2.9 UV-visible absorption of N719 dye molecule photosensitizers for DSSCs.

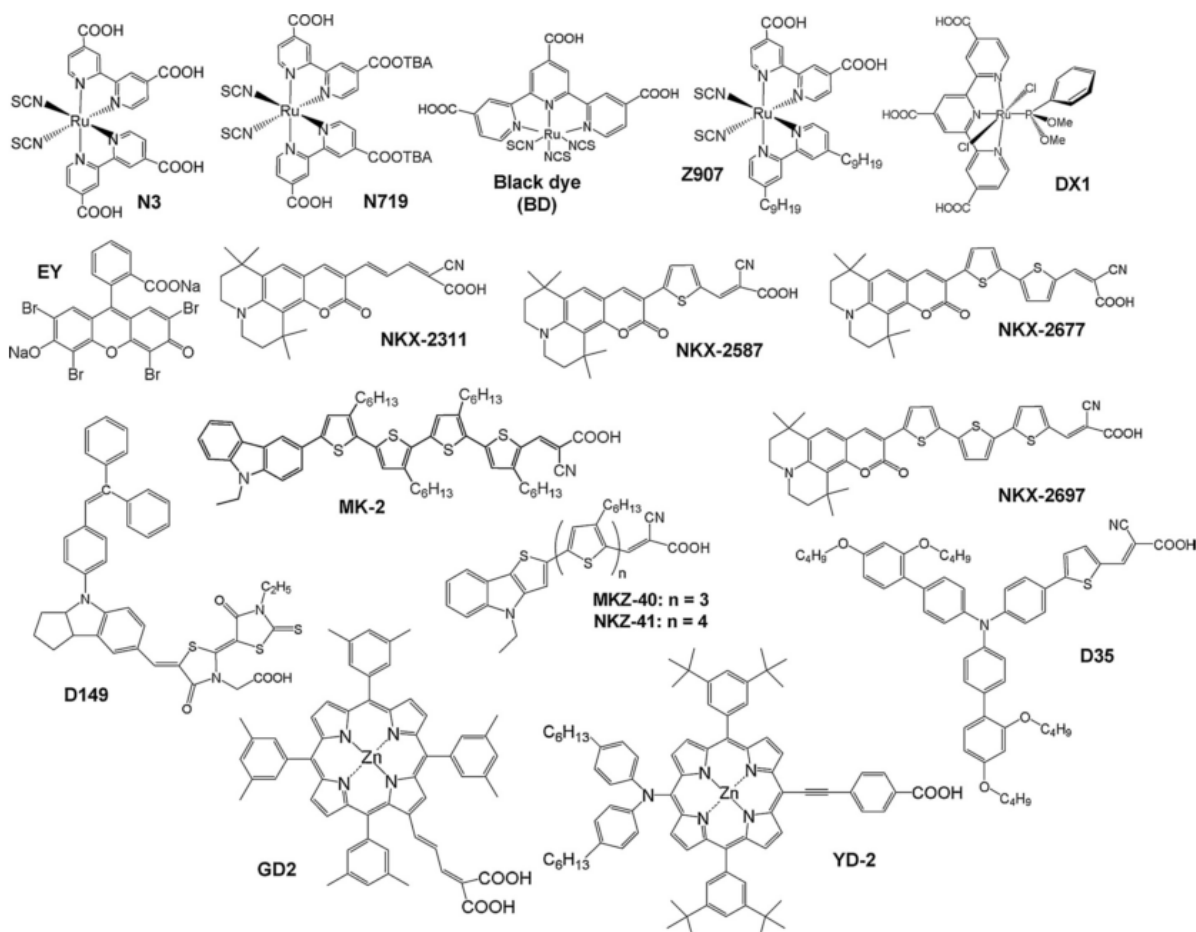


Figure 2.10 Molecular structures of different dye molecule photosensitizers for DSSCs [55].

2.1.4 Electrolytes

In DCCSs, the space between the photoanode and the CE is filled with an electrolyte that works as a hole transporting medium. In general, there are liquid, semi-solid and solid electrolytes [53,68–70]. However, liquid electrolytes, which are based on organic solvents (ethanol, acetonitrile and acetonitrile/valeronitrile), have higher stability and are the most commonly used. In addition to transferring the positive charge to the CE, the electrolyte should contain some “blocking agent” that adsorbs the nanoparticles on those surface sites not occupied by the dye molecules in order to prevent electron leakage from the electrolyte and recombination. Moreover, for dye regeneration, the electrolyte must have a more negative electrochemical potential than the oxidized dye. Since the V_{oc} in DSSCs

is determined by the difference between the quasi-Fermi level of the semiconductor and the redox potential of the electrolyte, the redox potential of the electrolyte should be as positive as possible [1,35,36]. The electrolytes must have negligible absorption in the visible spectral range. In addition, electrolytes should have good chemical and thermal stability, low viscosity, negligible vapour pressure, non-flammability, and high ionic conductivity. In terms of cell efficiency, the most commonly used electrolyte in DSSCs is the iodide/triiodide redox couple; however, attempts to use alternative redox mediators have been made [68,69,71,72]. There have also been attempts to replace the organic solvent (acetonitrile-based electrolytes) with water, since the ionic behavior makes them ideal in terms of stability. However, the problem of these electrolytes is the rather large viscosity of ionic liquids, which causes mass transport issues [36,53,68,69,71,72].

In this work, the iodide/tri-iodide redox couple in acetonitrile is used as an electrolyte.

2.1.5 Counter electrode

In DSSCs, the CE has the important task of collecting electrons from the external circuit and catalyzing the oxidized species of the redox. An ideal CE should have low electrical resistance, because the charge transfer resistance at the CE and the electrolyte interface directly affect the FF of the device [69,72]. The most common CE used for the iodide/triiodide redox system is FTO glass coated with a layer of a catalyst. The most successful trials were achieved using thermally deposited or sputtered Pt, due to high catalytic activity, chemical stability in the electrolyte and near transparency. However, Pt suffers from few limitations such as a higher production cost, high temperature sintering and resource scarcity. These limitations of Pt lead to a demand for the development of an alternative low cost, chemically stable CE with good catalytic property, including carbonaceous materials, metal sulfides (MS) and conductive polymers [49,69,72–74].

In this work, a platinized (10 nm Pt thin layer) FTO glass is used as a CE (Figure 2.11).

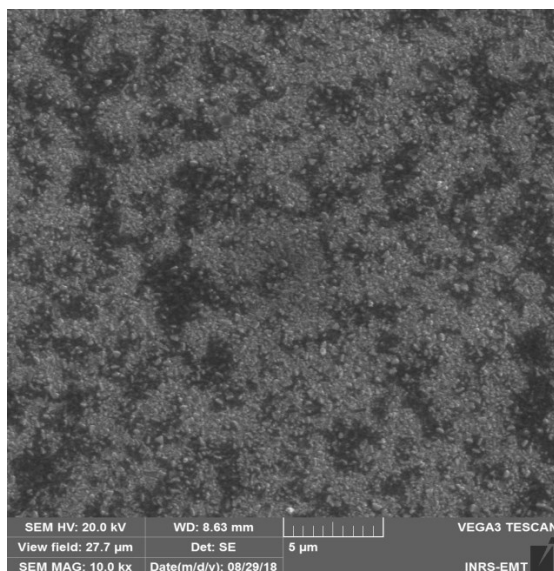


Figure 2.11 SEM image of Pt thin film layer on an FTO substrate.

2.1.6 Sealant

The DSSC sealant acts as a spacer between the photoanode and the CE. For long-term stability and large scale application, the sealing material must be: (i) chemically inert towards the corrosive liquid electrolyte; (ii) thermally stable; and (iii) able to adhere well to electrodes to prevent electrolyte leakage as well as water and gas entering from the atmosphere.

In this work, Meltonix 1170-60PF films (from Solaronix), with a thickness of 60 μm, are used as a sealant.

2.1.7 Carbon nanomaterials

Carbon has various forms, namely diamond, graphite, and nano carbon encompasses fullerenes, nanotubes and graphene. Since ancient times, diamond and graphite are well-known allotropes of carbon forms. Fullerenes was discovered in 1985 by Kroto et al. [75]. In 1991, Iijima reported experimental results of carbon nanotubes (CNTs) [76]. Geim was awarded the 2010 Nobel Prize in Physics jointly with Novoselov for groundbreaking experiments regarding the two-dimensional material graphene [77]. Graphene is a single layer of the graphite crystal, pure covalently bonded carbon in a honeycomb lattice, and of one atom thickness. Single graphene layers can be detached from graphite; however,

it is extremely strong in tension and can very easily bend. CNT can be described as a graphene layer rolled into a cylindrical shape with axial symmetry [51,78]. Depending on the number of walls, CNTs usually exist in three forms: (1) single-wall CNT (SWCNT), consisting of only one graphene layer; (2) double-wall CNT (DWCNT); and (3) multi-wall CNT (MWCNT), consisting of a nested coaxial array of SWCNTs [79]. During recent years, various forms of carbon nanomaterials have attracted a great deal of interest because of their unique structure and properties in different types of solar cells (see Figure 2.12 and Table 1) [79,80].

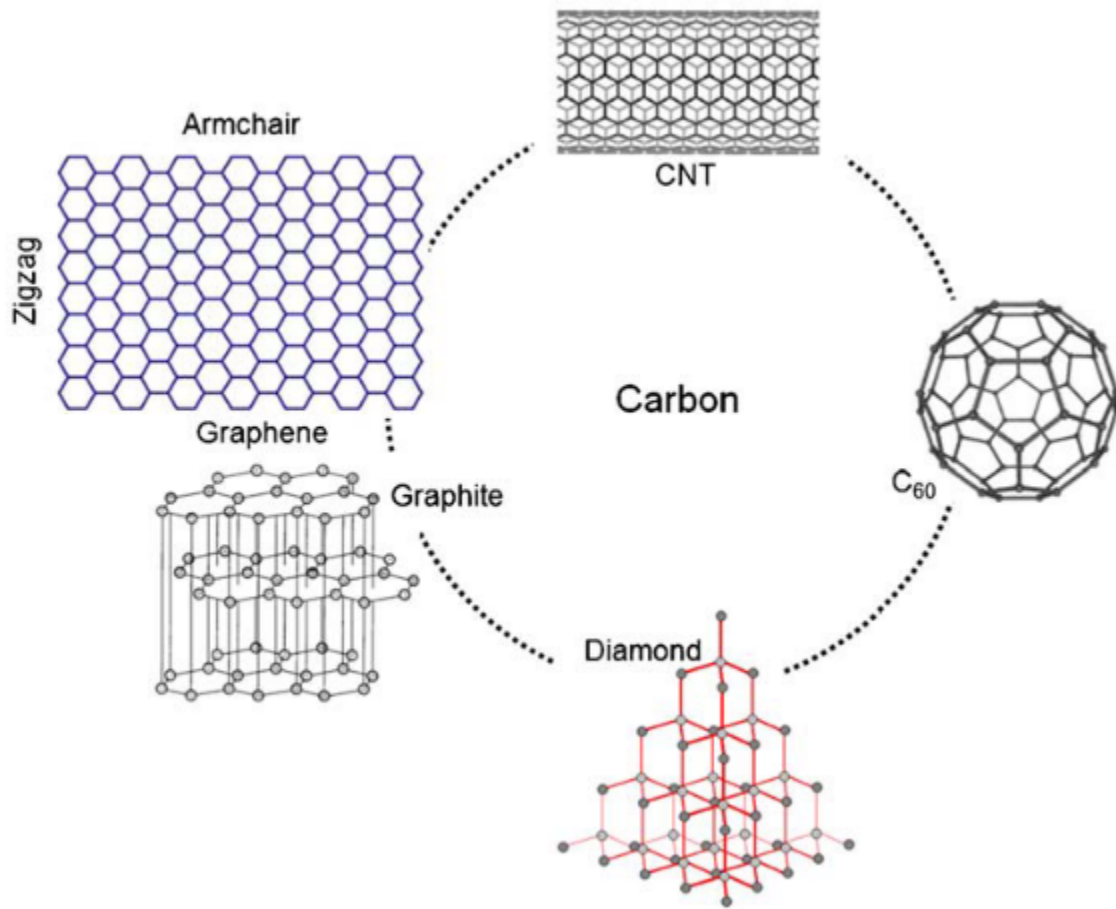


Figure 2.12 Polymorphs of carbon materials [80].

Table 2.1. Properties of carbon allotropes [80].

	Crystal structure	Hybridization	Conduction type	BG (eV)	WF (eV)
Amorphous carbon	-	sp^3+sp^2	Semiconductor	0.2-0.3	4.9
Diamond	Cubic	sp^3	Insulator	5.5	5.45
Graphite	Hexagonal	sp^2	Conductor	0	5.0
Fullerene	Cubic	sp^2+sp^3	Semiconductor	1.6	4.6-5.0
CNT	Cylindrical	sp^2+sp^3	Metallic/ Semiconductor	0.3-2.0	4.5-5.1
Graphene	-	sp^2	Semi-metallic/ Semiconductor	0-0.3	5.0

To improve performance and stability while decreasing the production cost of DSSCs, carbon nanomaterials have attracted great attention for use in various components due to their unique structure, excellent conductivity, good transparency, high catalytic activity, low cost and abundance [51,78,79,81]. The active layer of the DSSC has three main disadvantages: (i) significant recombination of the injected electrons; (ii) slow electron transport due to a large number of grain boundaries; and (iii) ineffective light harvesting [51]. During recent years, several research groups have developed composites of carbon nanomaterials, including graphene and CNT, as charge transport channels to improve cell performance (Figure 2.13) [51,78,79].

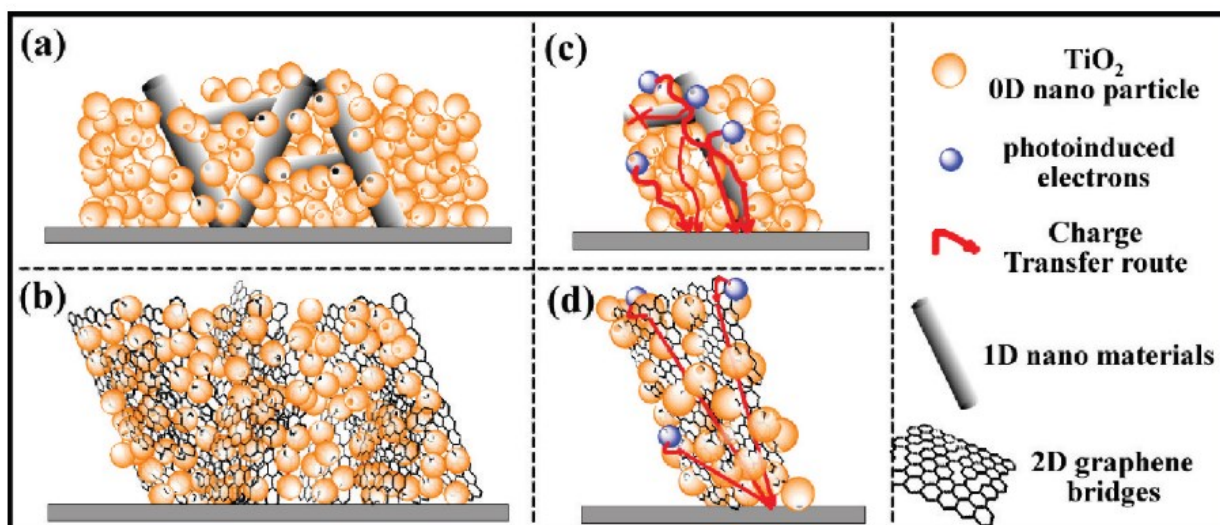


Figure 2.13 Electron transport across nanostructured semiconductor films: (a) and (c) CNT and (b) and (d) graphene composite electrodes [19].

According to various research studies, carbonaceous materials can be used to replace the platinum catalyst. Carbon nanomaterial based composites are used as a CE in DSSCs due to their high electrical conductivity, extremely large surface areas and controllable defect edges that could facilitate the electron kinetics associated with electrolyte reduction. The main advantage of using a carbonaceous material composite as a CE is that these nanomaterials (CNT and graphene) act as an active site for the electrocatalytic process as well as a spacer in the matrix, which speeds up the diffusion of the electrolyte, thus creating a brilliant electrode–electrolyte contact [1,51,78,81,82].

In this work, MWCNTs and graphene are used as composite materials in two different components of the cell: the anode and the CE (Figure 2.14).

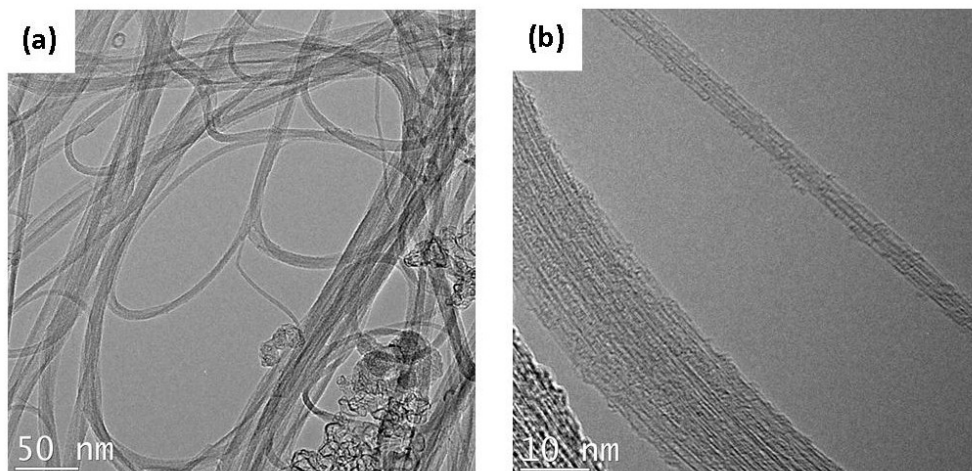


Figure 2.14 TEM images of the MWCNTs: (a) low and (b) high magnifications.

2.2 Device Fabrication

TiO₂ paste is composed of 20 nm anatase nanoparticles (18 NR-T, purchased from Dyesol). A TiO₂ blocking layer (Ti-Nanoxide) solution was purchased from Solaronix. All materials were used as received, without further purification. Prior to layer deposition, the FTO glass substrates were ultrasonically cleaned in acetone, methanol and deionized water, then dried in flowing nitrogen gas. The blocking layer was deposited onto pre-cleaned FTO substrates by spin coating in two steps: Step one at a rotation speed of 3000 rpm for 20 seconds and Step two at a rotation speed of 6000 rpm for 40 seconds, under ambient conditions, followed by annealing at 500°C for 30 minutes in air. The TiO₂ paste was then tape cast onto FTO glass substrates that were coated with the blocking layer. The photoanodes were subsequently dried for 15 minutes in an ambient atmosphere and temperature, then for 6 minutes at 120°C in an ambient atmosphere. After drying, the samples were annealed at 500°C for 30 minutes in an ambient atmosphere. Before device fabrication, the annealed samples were dye-sensitized by immersion into a 0.5 mM ethanolic solution of a commercial Ru-based complex molecular dye N719 (from Solaronix) for 24 h. After washing the samples with ethanol and drying with nitrogen, the DSSCs were fabricated by using a Pt CE and I^{3-/I⁻} redox couple electrolyte, with 60 μm thick spacers (from Solaronix) between the photoanode and the Pt CE (Figure 2.15).

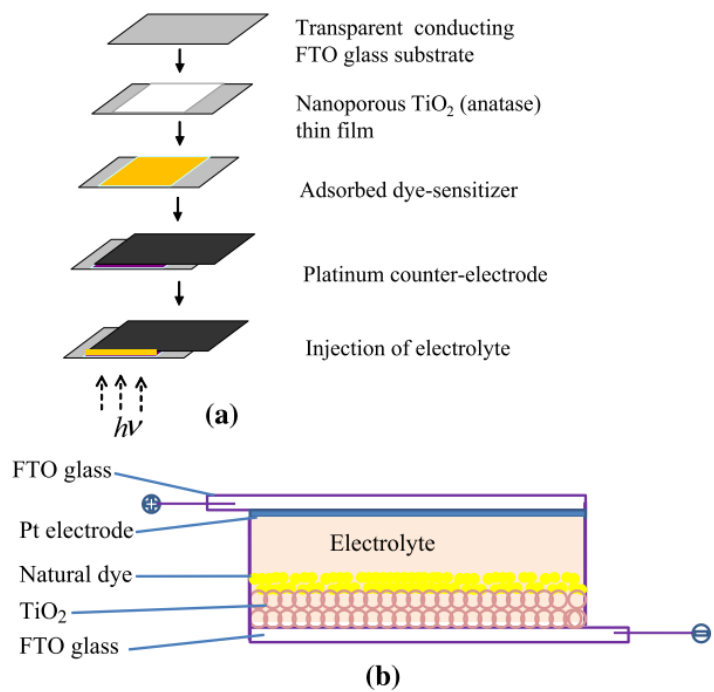


Figure 2.15 (a) DSSC fabrication steps and (b) a complete DSSC [83].

2.3 Characterization methods

2.3.1 X-ray diffraction

X-ray diffraction (XRD) is employed to determine the crystal structures and phase transformation of the material. Figure 2.16 illustrates the working principle of XRD, based on Bragg's law [84]:

$$n\lambda = 2d\sin\theta \quad \text{(Equation 2. 1)}$$

where (d) is the distance between two parallel planes periodically arranged, (λ) is the wavelength of a monochromatic X-ray source and (θ) is the diffraction angle. In this research, the crystallinity and phase transformation of the films are investigated using the X'Pert Pro MRD and a Bruker D8 Advance X-ray diffractometer equipped with Cu K α radiation.

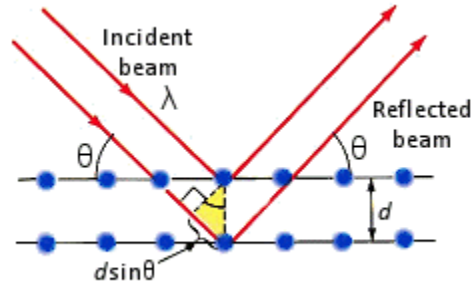


Figure 2.16 Schematics of diffraction of X-rays [84].

2.3.2 Scanning electron microscope

Scanning electron microscopy (SEM) is used for studying the morphology and structure of different electrodes. In SEM, a beam of the electron scans over the surface of the sample in a vacuum chamber to extract structural and chemical information based on the three types of electrons: secondary electrons, backscattered electrons, and elemental X-ray (Figure 2.17) [85]. For SEM measurement, the sample needs to be electrically conductive in order to prevent accumulation of electrostatic charge at the surface. In this thesis, field emission scanning electron microscopy (FESEM) using a JEOL JSM7401 F FE-SEM equipped with an energy-dispersive X-ray spectrometer (EDS), with acceleration voltage in the range of 2 to 20 KV, is used to record the images.

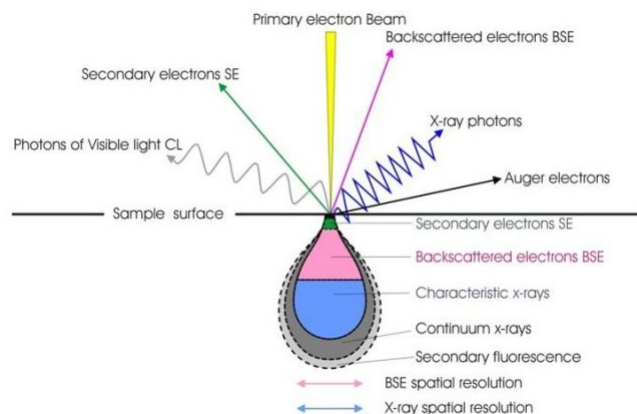


Figure 2.17 Electrons interact with a sample's atoms in the SEM [85].

2.3.3 Transmission electron microscopy

Transmission electron microscopy (TEM) was used for material analysis in the current work. In this technique, a high-energy beam of electrons is shone through a very thin sample (100 nm thick). Due to the interactions between the accelerated beams of electrons and the atoms in the sample, different information, such as the crystal structure, can be taken from materials. A rich variety of interactions takes place between the electron beams and the sample in the TEM, including directly transmitted electrons, secondary electrons, backscattered electrons, characteristic x-rays and Auger electrons (Figure 2.18) [86]. Moreover, TEM can be used to study the defects in different materials including semiconductors [87,88]. High resolution TEM has been used to study the structural properties of carbon nanomaterials (graphene and CNT), including their diameter, chirality and number of layers, as well as to detect potential defect sites within them [89]. In this research, TEM and selected area electron diffraction (SAED) are performed using a JEOL JEM-2010 TEM.

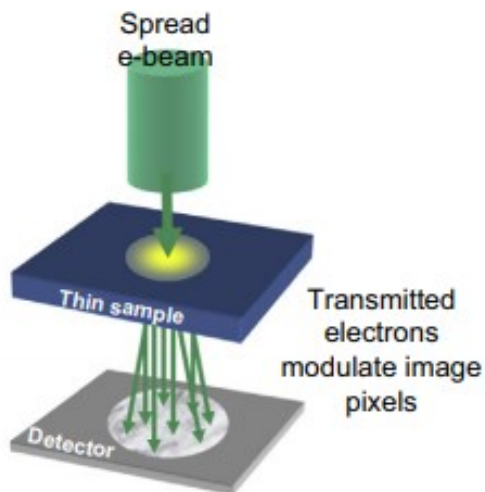


Figure 2.18 Electron beams interact with a sample's atoms in the TEM [86].

2.3.4 Atomic force microscopy

Atomic force microscopy (AFM) has three different modes of operation, namely; contact mode, non-contact mode and tapping mode. In AFM, imaging relies on the measurement of the forces, either attractive or repulsive, between a fine sharp tip attached to a flexible

cantilever [90]. An AFM probe is used to scan the specimen surface. The major difference between AFM and electron-based microscopes is that AFM does not use beam irradiation. Therefore, it does not suffer from a limitation in spatial resolution due to creating a vacuum and preparing a chamber for guiding the beam. Figure 2.19 shows the experimental setups of AFM. In this work, surface morphologies are examined by an Enviroscope AFM (Digital Instruments) operated in tapping mode at room temperature in ambient air.

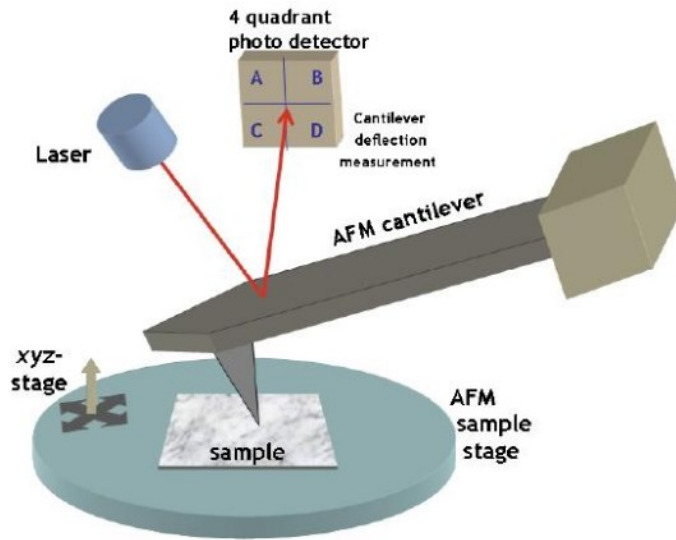


Figure 2.19 Experimental setup for a typical AFM [91].

2.3.5 X-ray Photoemission spectroscopy

XPS provides valuable quantitative and chemical state information from the surface of the material with approximately 10 nm average depth of analysis. The XPS method is used to determine the kinetic energy and number of electrons that escape from the surface of a specimen by the irradiating X-ray having a constant energy, $h\nu$, in an ultra-high vacuum [92]. The kinetic energy can be determined by the following equation:

$$E_{binding} = E_{photon} - (E_{kinetic} + \phi) \quad \text{(Equation 2.2)}$$

where $E_{binding}$ is the binding energy, E_{photon} is the photon energy of the X-ray source and ϕ is the spectrometer work function. Figure 2.20 shows an experimental XPS set-up [93].

Here, XPS was performed on a VG Escalab 220i-XL recorded for a Twin Anode X-ray Source.

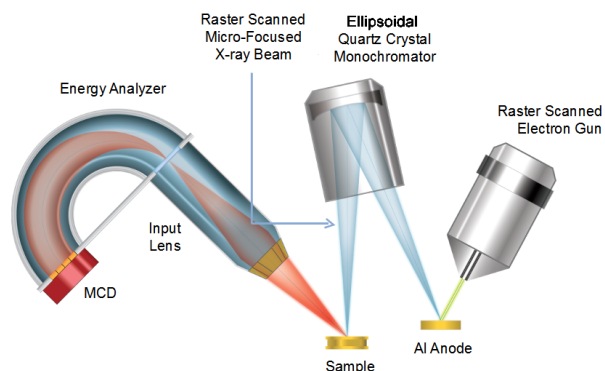


Figure 2.20 Experimental setup for a typical XPS [93].

2.3.6 Raman spectroscopy

Raman scattering is one of the most effective optical methods of studying vibrational spectrum of materials in various phases, whether solid, liquid or gas. Investigations into Raman scattering by phonons in different materials such as semiconductors allows to obtain new information on molecular vibrations and crystal structures. This technique has some unique advantages, including: (i) non-contact and non-destructive analysis; (ii) no sample preparation needed; and (iii) capacity for in situ measurements. In Raman, the laser light (in the visible, near infrared, or near ultraviolet range) interacts with molecular vibrations, resulting in the energy of the scattering laser being shifted up or down. It relies on the shift in energy that gives information about the vibrational modes in the system [94–96].

When light interacts with a molecule, it could induce a transition to a higher or virtual energy state (Figure 2.21). The first condition for the molecule relaxing to the initial ground state is Rayleigh, or elastic, scattering, which occurs in a single step by releasing the same amount of energy as that of the incoming photon. Rayleigh scattering does not yield any information about the molecules because no energy is transferred to the molecule. The second condition is Stokes scattering, where the energy can be transferred to the molecule from the incident photon. The third mode is anti-Stokes Raman scattering, when

the energy of the scattered photon is higher than that of the incident photon. Stokes and anti-Stokes are known as Raman scattering [94,97].

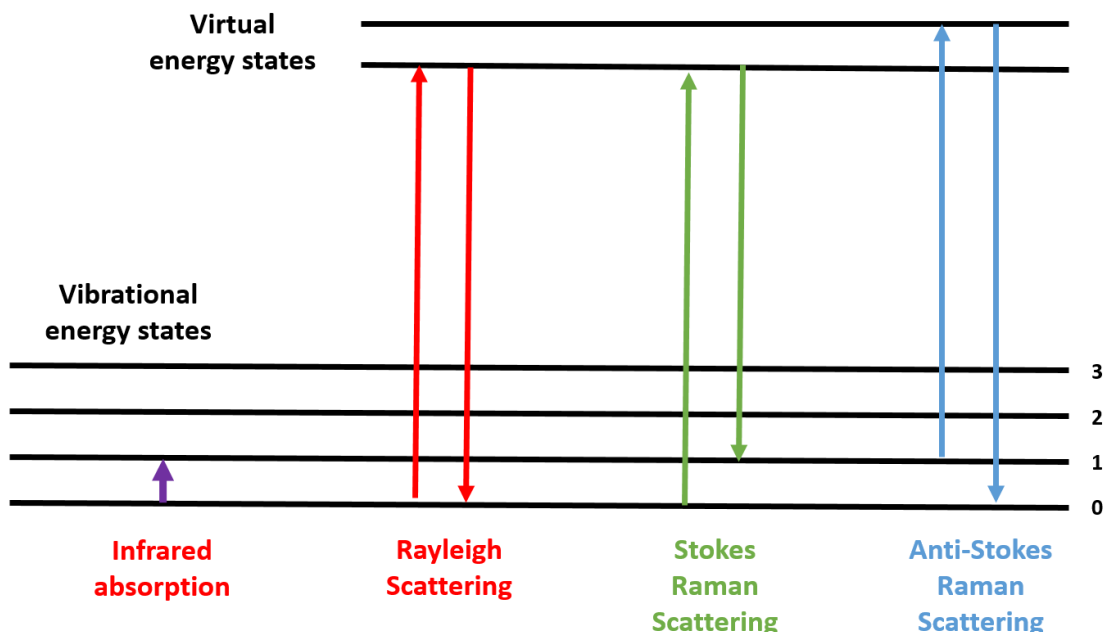


Figure 2.21 "Jablonski" style diagrams of different forms of energetic transitions in Raman scattering.

2.3.7 UV-visible (UV-vis) Spectroscopy

UV-visible (UV-vis) spectroscopy is an indispensable tool that is used to evaluate the optical properties of materials. Absorption of light with a precise amount of energy is associated with excitation of electrons from lower to higher energy levels, in both atoms and molecules. The UV-vis spectral range is approximately 190 to 900 nm. In this research, the UV-vis absorption spectrum is conducted using a Cary 5000 UV-visible-NIR spectrophotometer (Varian). During measurement, the sample is irradiated with light and the absorbance is defined as an intensity of light before and after illumination [98,99]:

$$A = \log_{10}\left(\frac{I_0}{I}\right) \quad \text{(Equation 2.3)}$$

If the sample compound absorbs the light of a given wavelength, then I is less than I_0 . However, if the sample does not absorb light, $I = I_0$.

2.3.8 Electrochemical impedance spectroscopy

Electrochemical impedance spectroscopy (EIS) is a steady-state technique for evaluating the kinetics and energetics of electron transport and recombination in DSSCs. As a non-destructive technique, an important advantage of EIS, over other techniques is the possibility of in situ measurement during and after working the device. EIS is carried out by applying an AC potential $V(\omega, t)$ with a certain frequency range ($f = \frac{\omega}{2\pi}$), then measuring the current $I(\omega, t)$ of the electrochemical system. Thus, the impedance $Z(\omega)$ of the system can be expressed according to Ohm's law [61,100]:

$$Z(\omega) = \frac{V(\omega, t)}{I(\omega, t)} \quad \text{(Equation 2.4)}$$

In this work, the EIS measurement was conducted under dark conditions and at room temperature, using a SOLARTRON 1260 A Impedance/Gain-Phase Analyzer, by applying an AC amplitude of voltages from 0 to 600 mV. The tests were recorded over a frequency range between 10 mHz and 300 kHz, and the AC signal was 10 mV in amplitude. All impedance measurements were analyzed using an appropriate equivalent circuit model with Z-View software (v3.5, Scribner Associate, Inc.) [62,101].

2.3.9 Cyclic voltammetry

Cyclic voltammetry (CV) is a type of powerful and popular electrochemical measurement that is used to investigate reduction and oxidation reactions. In DSSCs, CV is used to analyze the catalytic activities of the CE. In this present work, CV was carried out in a Solartron SI 1287 potentiostat galvanostat using a three-electrode system including a working electrode, an Ag/AgCl reference electrode and a Pt plate as CE in the electrolyte [102–105].

2.3.10 Photovoltaic characterization

To provide a controllable indoor test facility under laboratory conditions, a solar simulator is used for the testing of solar cells. A solar simulator is a device that provides illumination that approximates natural sunlight. A SS50AAA solar simulator (class AAA), which consists of a high-pressure Xenon Lamp (Xenon Short Arc) at AM 1.5G (100 mW cm^{-2}),

is used in the experiments in the present work. The current density-voltage (J-V) characteristics of the cell under both light illumination and dark conditions were obtained by applying external potential bias to the cell and measuring the generated photocurrent using a Keithley 2400 Source Meter.

2.3.11 External quantum efficiency

External quantum efficiency (EQE) refers to the incident photon to converted electron ratio. Since the energy of a photon is inversely proportional to its wavelength, EQE is the ratio of the number of charge carriers collected by the solar cell over a range of different wavelengths. Relative and arbitrary unit EQE measurements can be quite easily obtained when the user pays attention to the details of test conditions for each device, such as illumination intensity, device temperature and the effective active area [36,106].

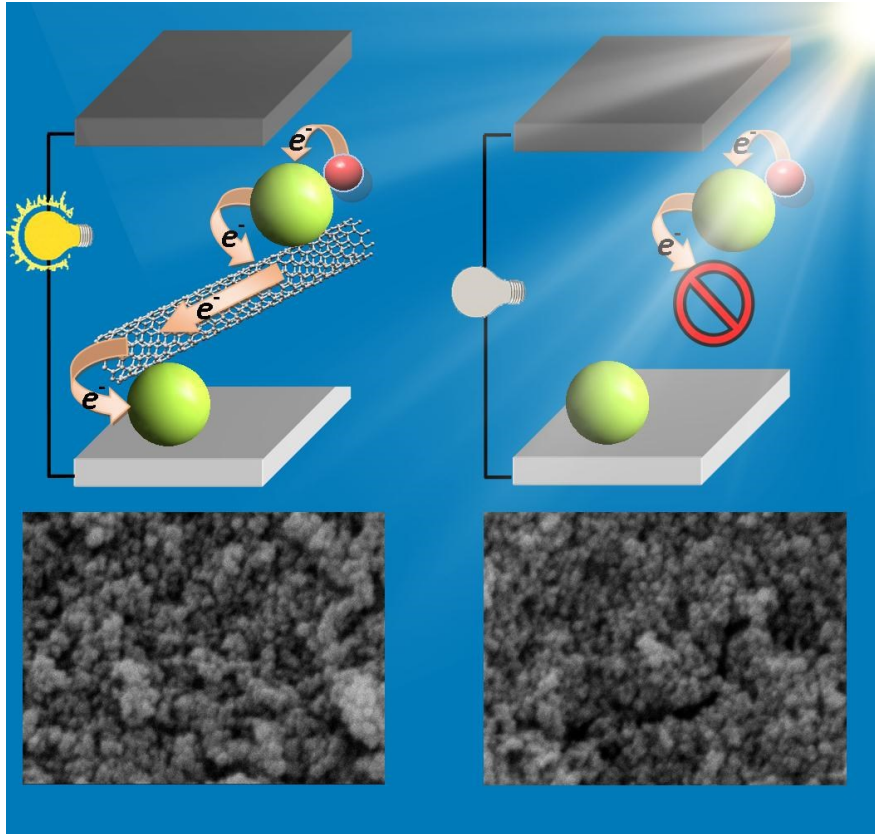
“Research is formalized curiosity. It is poking and prying with a purpose.”

Zora Neale Hurston

CHAPTER 3

Role of carbon nanotubes to enhance the long-term stability of dye-sensitized solar cells

This chapter mainly focuses on the concept that the integration of MWCNTs in commercially available TiO₂ nanoparticle paste can beneficially affect the long-term stability of DSSCs under continuous simulated one sun, indoor and UV light. To understand the degradation mechanisms that underpin these changes in device performance, both standard and composite devices were characterized using various techniques. The results indicate that the MWCNTs can act as strong conductive support and reinforcement of the TiO₂ matrix in the photoanode, which prevents a reduction of electron lifetime and a higher recombination rate. UV stability measurements indicate that MWCNTs are an efficient absorbing and blocking agent for UV light, thereby preventing degradation.



3.1 Introduction

Over the years, the world's demand for energy has sharply increased, due to the rapid development of industrialization and globalization. It is predicted that the world energy consumption rate will increase by over 50% before 2030 [4,33]. In contrast, the limited sources of fossil fuels and their related issues, including climate change and environmental pollution, dictate a transition towards renewable energy sources such as wind power, hydroelectric and solar energy [4,107]. Amongst various renewable energy sources, solar energy is one of the cleanest energy resources; it neither compromises nor adds to global warming and is considered as a viable alternative to fossil fuels [2,4,28,108].

In this context, PV converts the solar energy into electricity. Amongst all third-generation solar cells, DSSCs are considered as a promising future technology due to their appealing features, including a simple fabrication process, eco-friendly production, and low

production costs, and also offer an excellent choice for indoor applications such as windows and sunroofs [1,6].

A DSSC typically consists of: a wide band gap semiconducting oxide (e.g. ZnO, TiO₂ and SnO₂) film coated on a FTO transparent conductive glass; dye sensitizer molecules anchored to semiconductor nanoparticles as a light harvester; a redox couple electrolyte as hole transport; and a Pt coated FTO as a CE [78,79,109].

Major efforts have recently focused on improving the PCE that can be addressed using new nanomaterials. In particular, carbon-based nanomaterials such as MWCNTs and graphene are considered promising for DSSC applications, due to their unique structural and optoelectronic properties as well as low cost. Within the scientific and manufacturing communities, carbonaceous nanomaterials have been very well known due to several reasons. As examples, Young's modulus value of individual MWCNTs (0.27-0.95 TPa) is about a hundred times stronger than steel, and with about 1000 times more electric current than copper wire and carbon-based materials displays the highest measured thermal conductivity of any known material [79,110,111].

Among different components of DSSCs, the photoanode is considered as the heart of a device because it provides light absorption, charge collection and transport to FTO. The photoanode of DSSCs is generally fabricated by nanostructured mesoporous film of a wide-band gap metal oxide semiconductor with high internal surface area for chemisorptions of dye molecules. One of the main strategies used for improving electron transport and suppressing recombination is the addition of carbon nanomaterials that can work as charge carriers [78,79,111]. The effect of MWCNTs on the performance of DSSCs is reported in [15], which presents a fast and effective procedure for the preparation of hybrid MWCNT-TiO₂ photoanodes by dispersing commercial MWCNTs in a commercial TiO₂ paste. PV performance analysis indicated that the PCE of the device in the case of MWCNTs-TiO₂ (0.010% wt.) films is approximately 25% higher than that of a device based on TiO₂. Dye loading measurements confirmed that the average number of dye moles per volume unit is increased more than three-fold in the composite sample (TiO₂-MWCNTs) compared to bare TiO₂. This condition creates an optimum combination to obtain light absorption exclusively from dye molecules and higher photoelectron

excitation to semiconductor nanoparticles, resulting in improvement of photocurrent generation and overall PCE. Moreover, analysis of the transient photovoltage decay and of the corresponding electron lifetime result in increased electron collection and recombination resistance. The results of this research strongly indicate that the incorporation of MWCNTs in the TiO₂ matrix has the overall effect of favoring electron conduction and inhibiting the recombination process.

These results on the improvement of the PV performance of DSSCs with the addition of low concentration of MWCNTs raised the question of whether the composite photoanode might improve long-term stability. Various stability issues are generally associated with DSSCs, such as: the thermal stability of the dye molecules; stability of the CE; the particle bonding strength of the anode; leakage of the electrolyte; thermal stability of the sealing layer; the UV and visible light stability of the dye molecules and the electrolyte; and the mechanical stability of the photoanode and sealing layer [11,73,113,114]. Typical methods used to test the long-term stability of DSSCs involve light soaking tests, continuous UV radiation exposure and thermal stability. Under these conditions, the devices can experience several degradation mechanisms, which still remain unexplored, requires further investigation and characterization.

This chapter reports on comparative studies on the long-term stability of DSSCs based on TiO₂ nanoparticles with and without MWCNTs under continuous visible and UV light illumination. It is shown that the presence of 0.010 wt% of MWCNTs in TiO₂ nanoparticles leads to a significant improvement in the long-term stability of DSSCs under continuous simulated one sun and indoor light by 22% and 42%, respectively. The results of UV light illumination indicate that MWCNTs can successfully stabilize DSSCs for long-term operation with a 24% improvement. This observation is confirmed by various characterizations, including J-V measurements, transient photovoltage decay and EIS measurements. In addition, FESEM and Raman spectroscopy are used to investigate the anode's morphology, composition and degradation mechanism.

3.2 Experimental

Mesoporous TiO₂ photoanodes are composed of two layers: (i) TiO₂ paste, composed of 20 nm sized anatase (18 NR-T from Dyesol); and (ii) the TiO₂ scattering layer composed of 150-250 nm sized particles (WER2-O from Dyesol). MWCNTs were purchased from Sigma-Aldrich (10 μm average length and 12 nm average diameter). All materials were used as received, without further purification. The blocking layer (Ti-Nanoxide from Solaronix) was deposited onto pre-cleaned FTO substrates by spin coating in two steps: Step one, at a rotation speed of 3000 rpm for 20 seconds and Step two, at a rotation speed of 6000 rpm for 40 seconds. The prepared samples were subsequently annealed at 500°C for 30 minutes under ambient conditions. The MWCNTs-TiO₂ composite photoanodes were prepared in accordance with a previous report [15,115]. A suspension of MWCNTs was prepared by dispersing 6 mg of MWCNTs in 15 mL of ethanol followed by a three-hour bath sonication. The TiO₂-MWCNTs composite was then prepared by mixing 0.010 wt% of MWCNTs with the TiO₂ paste. The mechanically mixed TiO₂-MWCNTs composite paste was then tape casted on the blocking layer. Similarly, one batch of bare TiO₂ photoanodes was prepared as reference. After deposition, the photoanodes were dried for 15 minutes at ambient temperature and subsequently for 6 minutes at 120°C. All dried samples were annealed at 500°C for 30 minutes in an ambient atmosphere. Afterwards, the annealed samples were immersed with a 0.5 mM ethanolic solution of a commercial Ru-based complex molecular dye N719 (from Solaronix) for 24 hours. After dye sensitization, devices were fabricated by using a platinized FTO CE (a 10 nm thin film of Pt sputter-deposited on FTO), and a redox couple iodide/triiodide redox couple electrolyte, with 60 μm thick spacers (from Solaronix) between the photoanode and the Pt CE. The PV parameters of the fabricated devices were measured by a Keithley 2400 Source Meter under simulated sunlight using an ABET2000 solar simulator at M1.5G (100 mW cm⁻²).

The stability tests in this study were performed with continuous simulated sunlight, indoor light and UV light illumination over different periods at room temperature. The light source with one sun intensity was used without any additional UV filtration and a UV lamp [wavelength (λ) 365 nm] with 0.7 mW cm⁻² was also used. The morphology and structure

of the photoanodes were investigated by SEM (FE-SEM, JEOL JSM-6900 F). EIS was conducted in the dark using a SOLARTRON 1260 A Impedance/Gain-Phase Analyzer by applying a bias from 150 to 600 mV. The tests were recorded over the AC signal (10mV) in amplitude and frequency range between 10 mHz and 300 kHz. The obtained impedance spectra were fitted with Z-view software (v3.5, Scribner Associate, Inc.) and an appropriate equivalent circuit model. The completed cells were characterized by Raman spectroscopy using a 514 nm excitation source, at room temperature, in the 50-2900 cm^{-1} region.

3.3 Results and discussion

We investigated the effect of adding MWCNTs in the photoanode on the PV performance of DSSCs. Figure 3.1 displays the J-V curves obtained under simulated sunlight at AM1.5G (100 mW cm^{-2}) of DSSCs with and without MWCNTs. All PV parameters, including J_{sc} , V_{oc} , FF and PCE of both devices are reported in Table 3.1. The results show that the addition of 0.010 wt% MWCNTs to the TiO_2 nanoparticles leads to a ~30% improvement in the PCE compared to the control device, consistent with previous reports [15,115].

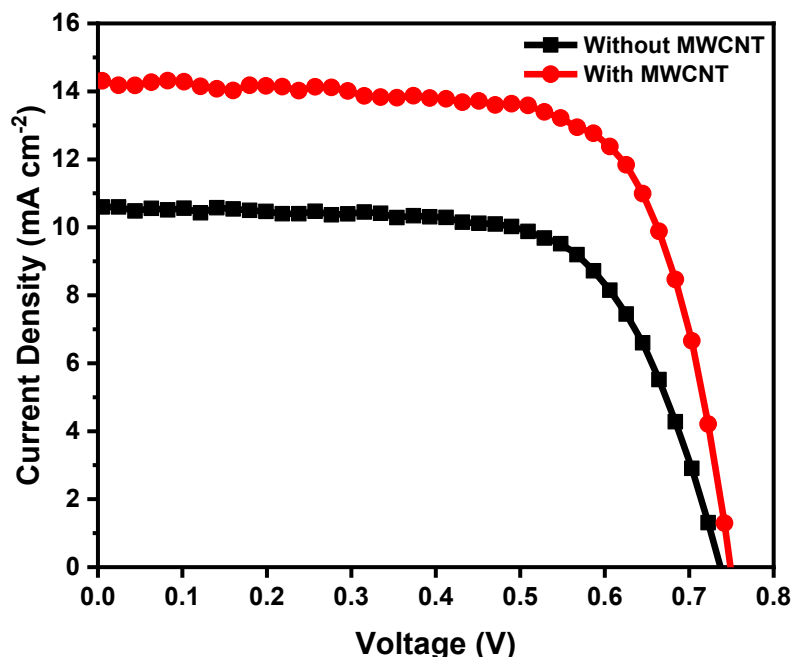


Figure 3.1 Current density-voltage curves of solar cells under simulated one sun at AM 1.5G (100 mW cm^{-2}) fabricated using TiO_2 mesoporous films with (red circles) and without MWCNTs (black squares).

Table 3.1. Functional parameters of DSSCs with and without MWCNTs.

anode structure	PCE (%)	FF (%)	V_{oc} (mV)	J_{sc} (mA cm^{-2})
TiO_2	5.3 ± 0.2	68 ± 2	718 ± 10	10.8 ± 0.3
$\text{TiO}_2 + \text{MWCNTs}$	7.0 ± 0.2	68 ± 2	738 ± 10	14.0 ± 0.3

3.3.1 Long-term stability under simulated sunlight illumination

Stability experiments were performed on two series of cells with and without the presence of MWCNTs in a TiO_2 mesoporous film, while keeping the other components identical, including the dye molecules, the redox couple electrolyte, the cathode and measurement conditions, to obtain statistically relevant information on the long-term stability of the devices. Figure 3.2 shows the variation of the PV parameters of different devices under continuous simulated sunlight at AM 1.5G (100 mW cm^{-2}) at room temperature. All PV

parameters were normalized using the initial value of the cells. The results demonstrate that the degradation rate of the PV parameters in the composite cell with MWCNTs was effectively suppressed compared to the device without MWCNTs. While the J_{sc} (mA cm^{-2}) of the composite device illustrated only 6% loss compared to its initial value, the cell without MWCNTs decreased to a larger extent (21%). Similarly, in the cell without MWCNTs, there is an 18% degradation of the V_{oc} (V), whereas the cell with MWCNTs declined by only 6%. This could be related to an increased recombination at the $\text{TiO}_2/\text{dye}/\text{electrolyte}$ interface [15,64,116,117]. The FF of both devices stayed approximately stable during the long-term test. The FF is largely responsible for the charge transfer resistance at the CE (related to the stability of the catalyst material) and the sheet resistance of the substrate (FTO). These results indicate that there are no apparent changes in the series connected resistances, hence no degradation of the FTO and Pt-catalyst layer [11,116–118]. The overall PCE of the composite device with MWCNTs decreases slowly (only 10%). However, the device without MWCNTs shows a considerable reduction (32%) under the same test period and measurement conditions, which could be mainly attributed to the simultaneous reduction of J_{sc} (mA cm^{-2}) and V_{oc} (V). Several reasons can be invoked to explain the effect of MWCNTs on the long-term stability of the DSSC.

A mesoporous photoanode film with bonding between TiO_2 nanoparticles is considered necessary for the efficient transport and collection of the photogenerated electrons. Thus decreased bonding by crack formation in the photoanode film could be one of the main reasons for the reduction of J_{sc} (mA cm^{-2}) [119,120]. Tributsch et al. [121] suggested that the fabrication of a device exhibiting high efficiency and long-term stability should be possible with increased adsorption of dye molecules because the dye molecules are the weakest component in DSSCs. It is believed that a porous photoanode with lower agglomeration of the nanoparticles is an important prerequisite for absorbing a higher number of dye molecules because their penetration is higher in mesoporous structures [109,122–124]. Alternatively, high porosity of the metal oxide could present many opportunities for charge recombination of the photo-injected electrons and electron transfer reduction [17,125]. Several reports have shown that CNTs can act as a useful dispersing agent for decreasing the agglomeration of nanoparticles in a photoanode

[15,109,122,123]. This explanation suggests that CNTs not only develop a highly porous morphology while preventing the agglomeration of TiO_2 particles that act as dye anchoring, but also work as an excellent electron transport carrier in the hybrid structure of the photoanode [15,18,109,122,123,126–128]. Previous results indicated that the dye loading increased more than three-fold in the TiO_2 -MWCNT composite sample compared to the bare TiO_2 [15]. When a higher number of dye molecules are present, the stability is expected to improve, as is referenced from (Figure 3.4 a-d). In this modified composite structure with a very large active surface area, there are sufficient dye molecules to capture photons and electron injection, therefore the ruthenium complexes have not been irreversibly destroyed and the photocurrent can be sustained [11,120,121]. These reasons could account for why the stability of DSSCs based on the MWCNT- TiO_2 /dye photoanode is higher than a standard TiO_2 /dye photoanode and how the high porosity of the anode affects stability.

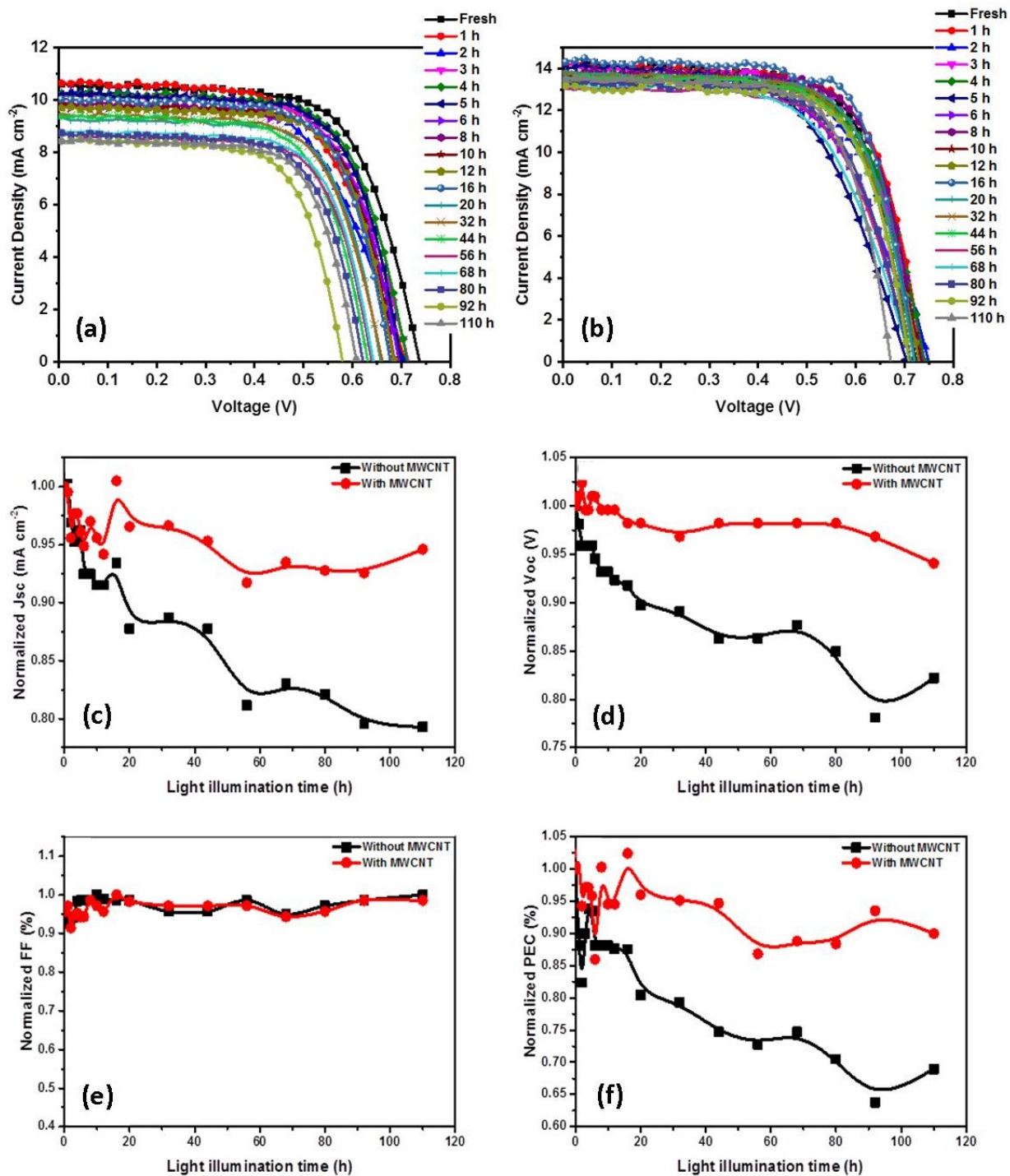


Figure 3.2 Functional properties of DSSCs in cases with and without MWCNTs under a continuous one sun light irradiation as a function of soaking time: (a) J-V curves of DSSCs without MWCNTs; (b) J-V curves of DSSCs with MWCNTs; (c) J_{sc} (mA cm^{-2}); (d) V_{oc} (V); (e) FF (%); and (f) PCE (%).

Electron recombination at the TiO₂/dye/electrolyte interfaces is another possible reason for the PV performance degradation that impacts the J_{sc} (mA cm⁻²) as well as V_{oc} (V) [63,64,129,130]. The considerable loss in efficiency during the prolonged stability test indicates that they suffer from undesirable carrier recombination [131]. It has been suggested that the optimization of the working electrode structure in order to delay interfacial charge recombination dynamics and improve electron transport is a crucial factor in improving the PCE and stability of DSSCs [132]. Bisquert et al. [64] reported that measuring the transient photovoltage decay allows monitoring of the τ_e, which can be defined as Equation (3.1) [64]:

$$\tau_e = \left(-\frac{k_B T}{e} \right) / \left(\frac{dV_{oc}}{dt} \right) \quad \text{(Equation 3.1)}$$

where *T* is the absolute temperature, *k_B* is Boltzmann's constant, and *e* is the elementary charge. The obtained photovoltage decay and τ_e curves of DSSCs in cases with and without MWCNTs, tested under continuous light irradiation, are shown in Figure 3.3. The results show that the photovoltage decay and the calculated τ_e of the device based on a TiO₂-MWCNTs hybrid photoanode remained stable under long time continuous one sun illumination, while the devices based on bare TiO₂ nanoparticles exhibit a significant loss under similar conditions. In the composite sample, the presence of MWCNTs in TiO₂ reduces the charge recombination, due to their action as excellent conducting networks inside the photoanode [109,130]. In this respect, the investigations undertaken by Belcher and coworkers [131] confirm that photo-induced electrons are transferred to the carbon nanotubes from the TiO₂ nanoparticles, then rapidly transported to the anode substrate without either recombination or a back reaction, as can be observed from (Figure 3.4 g).

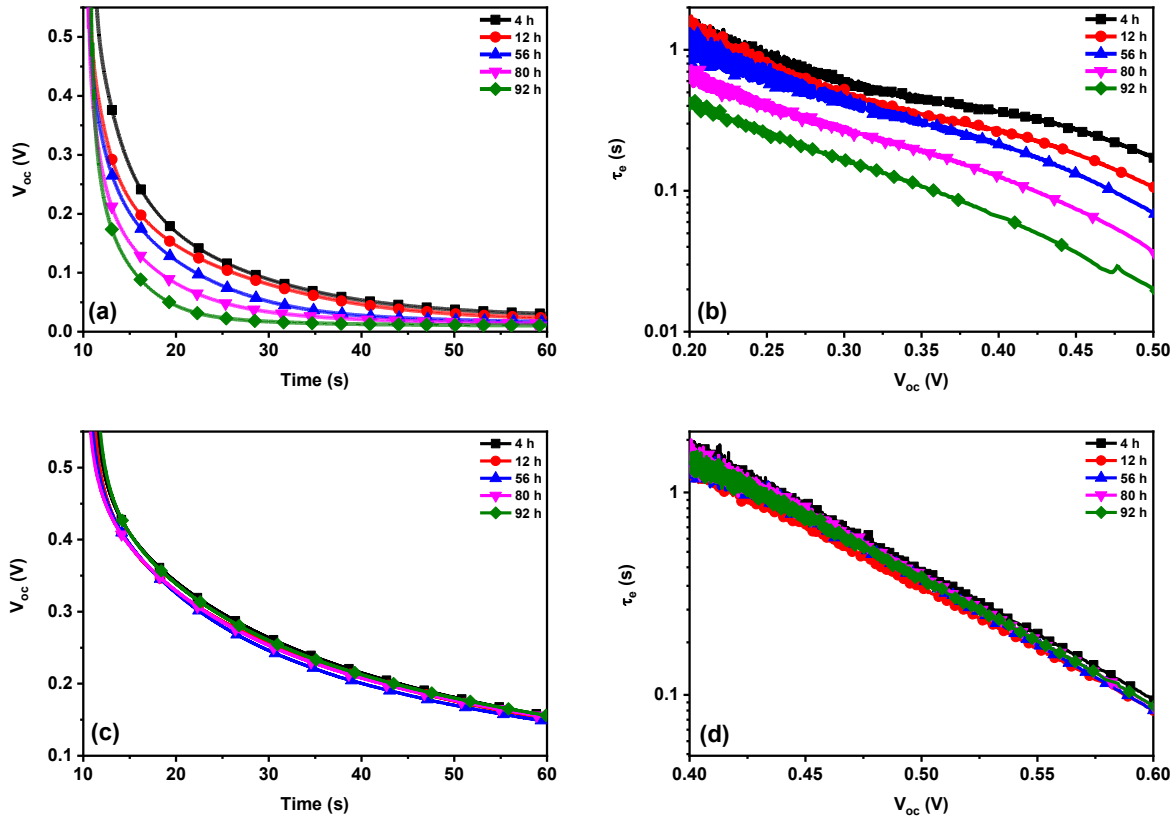


Figure 3.3 Transient V_{oc} decay and obtained electron lifetime (τ_e): for cells without MWCNTs (a) and (b) and cells with MWCNTs (c) and (d), measured at different times under one sun irradiation.

Another hypothesis to explain the degradation of DSSCs under continuous illumination is based on increasing the temperature of the device and related thermal stress. The created stress could produce some micro cracks in the photoanode and break the interconnection between the TiO_2 nanoparticles, consequently causing a decline in electron transport [Figure 3.4 (g) and (h)]. Previous studies have demonstrated that CNTs can work as a strong support among TiO_2 nanoparticles due to the formation of intimate contact with them [17,109,125,133,134]. Moreover, the addition of CNTs might improve the stability of the working electrode under thermal stress because of their excellent thermal conductivity [111,131,135]. The presence of MWCNTs could decrease the thermal stress of the photoanode and prevent its degradation [Figure 3.4 (e)].

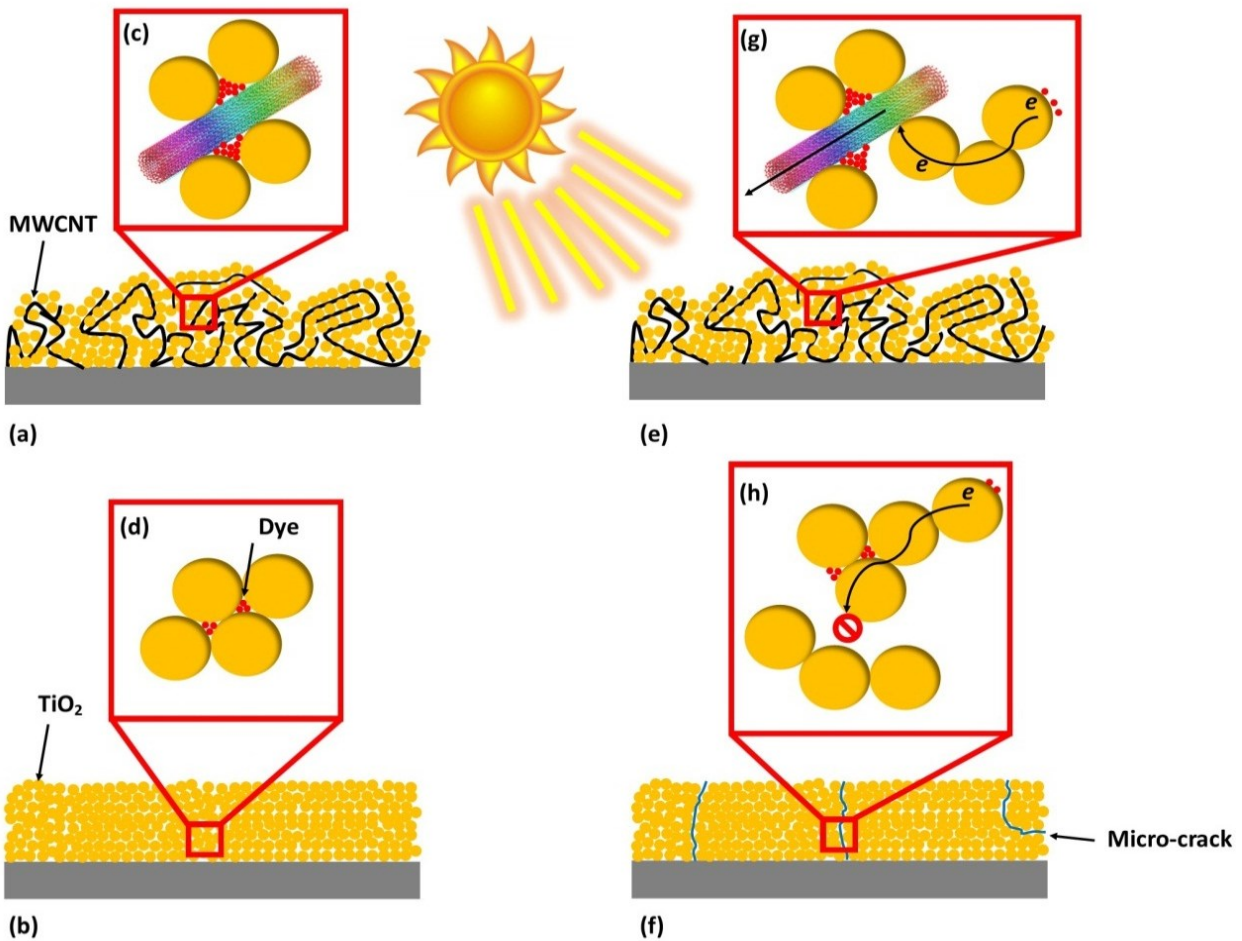


Figure 3.4 Schematic of: (a) and (b) enhanced dispersion of TiO_2 particles and preventing agglomerating with MWCNT addition; (c) and (d) greater quantity of dye molecules are adsorbed to the highly porous morphology; (e) MWCNTs act as act good support and reinforcement for TiO_2 ; (f) micro-crack formation in the photoanode because of intense light soaking and thermal stress; (g) MWCNTs act as a strong conductive network, preventing charge recombination; (h) loss of electrical contact between the TiO_2 particles and decrease in electron lifetime and recombination resistance.

3.3.2 Long-term stability under indoor light illumination

DSSCs designed especially for indoor applications and working under low light intensities. Hence, it is important to measure the stability of the device under indoor light illumination. The cells were tested for a period of 150 days under continuous artificial fluorescent light (30 mW cm^{-2}). Figure 3.5 illustrates a systematic comparison of the PV parameters of the devices based on the TiO_2 photoanode with and without MWCNTs. The results indicate that the J_{sc} (mA cm^{-2}) of standard devices sharply declines (63%), while the V_{oc} (V) decreases by only 9% over the test period, meaning that the crucial factor that determines

the degradation of the devices is the decrease of J_{sc} (mA cm^{-2}). The rapid decreasing of the J_{sc} (mA cm^{-2}) could be mainly related to the degrading of dye molecules under the test conditions [109,116,121]. On the other hand, the small reduction of V_{oc} (V) indicates a limited recombination of photo-produced electrons. As discussed in the previous section, intense illumination under simulated one sun intensity (100 mW cm^{-2}) and the related stress may be a possible reason for breaking the bond between the TiO_2 nanoparticles. However, in this test under indoor conditions, the intensity of the light is about three times lower than simulated sunlight, hence the related stress should be reduced. The PCE of the cell without MWCNTs rapidly decreases with 67%, while for the cell with MWCNTs only 25%. These results confirm that the addition of MWCNTs significantly improves cell stability, mainly by stabilizing J_{sc} (mA cm^{-2}).

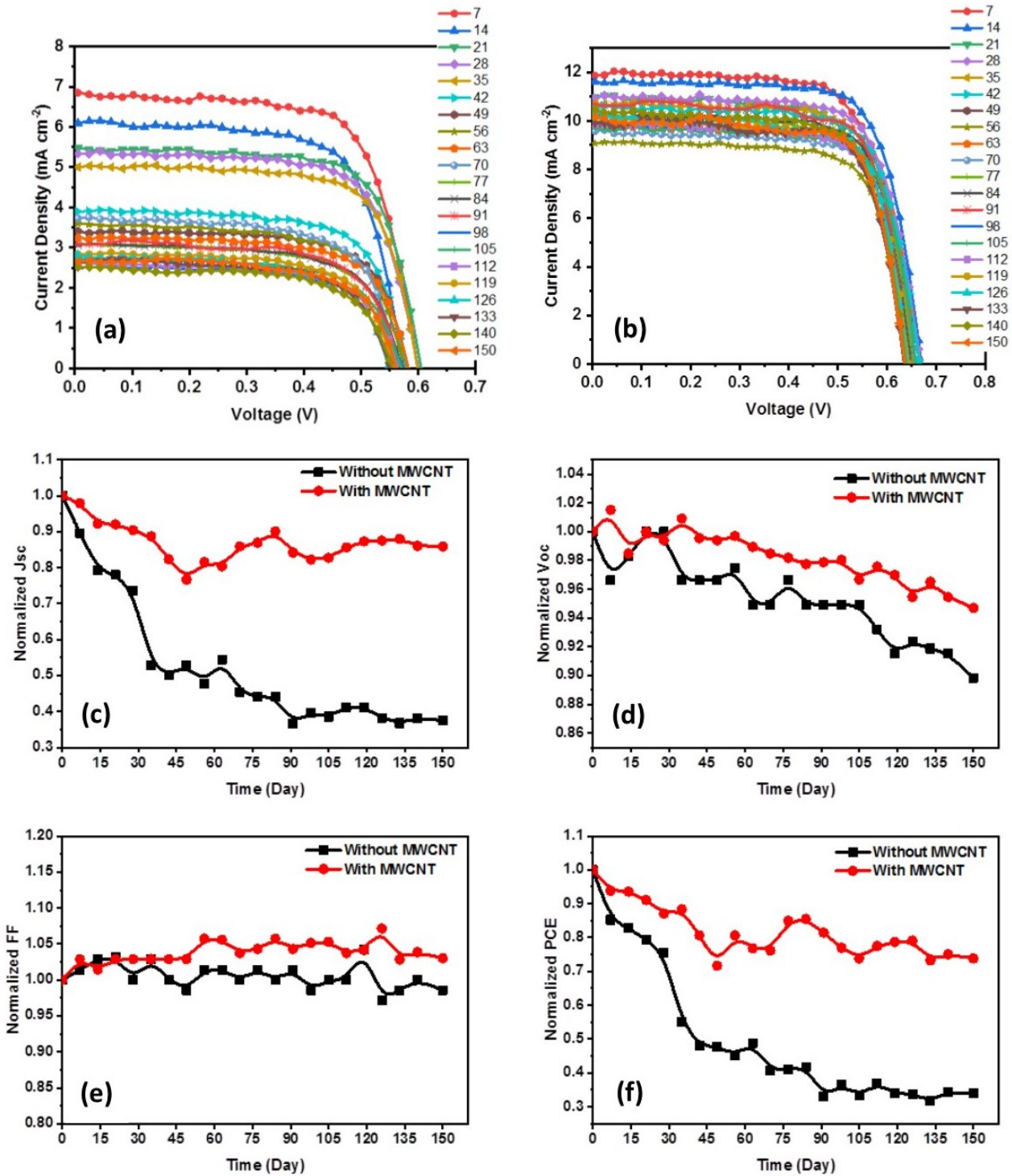


Figure 3.5 Functional properties of DSSCs in cases with and without MWCNTs under a continuous indoor light irradiation as a function of soaking time: (a) J-V curves of DSSCs without MWCNTs; (b) J-V curves of DSSCs with MWCNTs; (c) J_{sc} (mA cm⁻²); (d) V_{oc} (V); (e) FF (%); and (f) PCE (%).

3.3.3 Long-term stability under UV light

To gain more insight into the effect of MWCNTs on the long-term stability, the cells were tested under continuous UV light illumination. UV light is generally considered to be a damaging factor for DSSCs [120,121]. However, the effects of UV light over a long-term period on the functional parameters of DSSCs and related degradation mechanisms are not yet well understood because UV cut-off filters are often used to measure long-term stability [136]. Figure 3.6 illustrates the changes in functional parameters of DSSCs in cases with and without MWCNTs under UV light illumination.

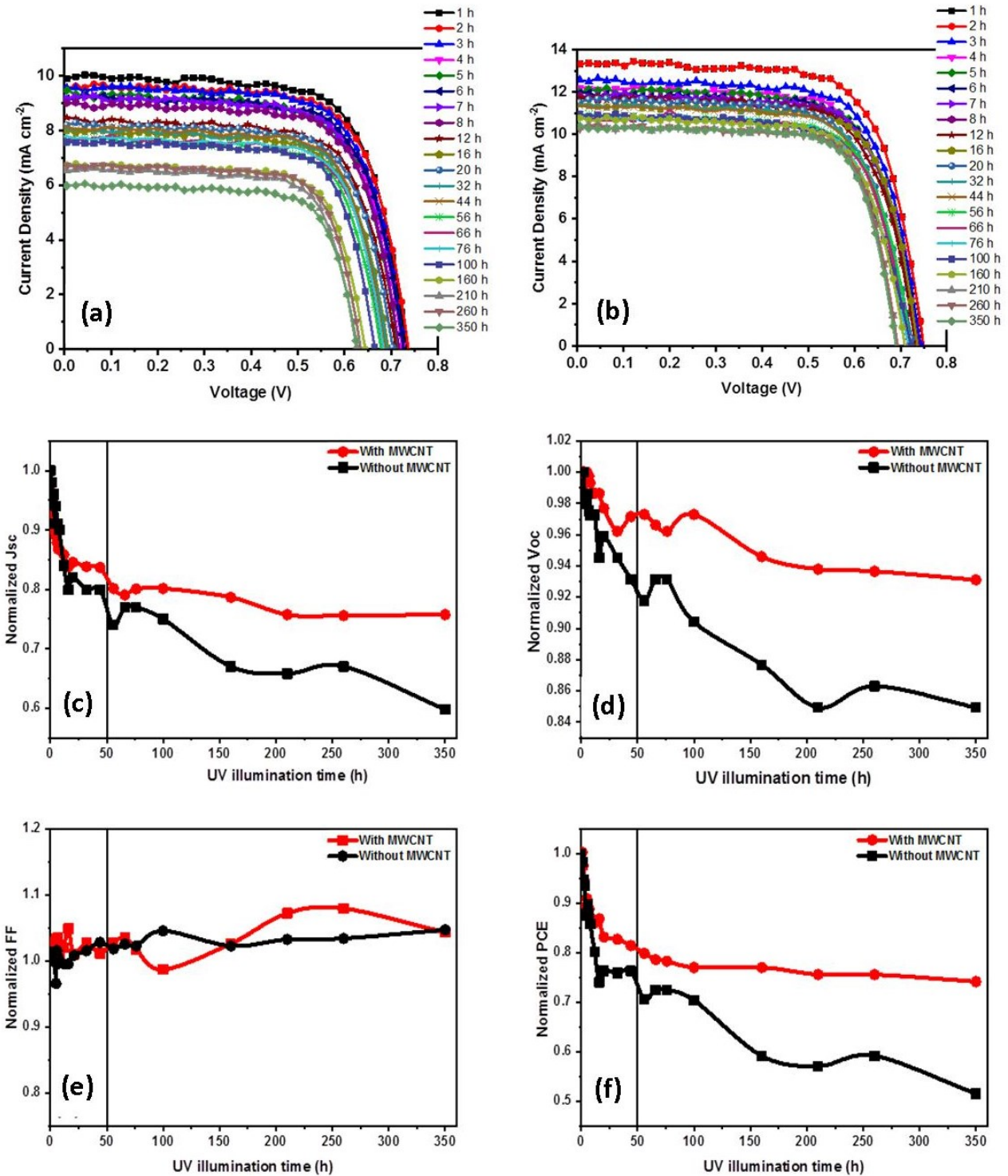


Figure 3.6 Functional properties of DSSCs in cases with and without MWCNTs under a continuous UV light irradiation as a function of soaking time: (a) J-V curves of DSSCs without MWCNTs; (b) J-V curves of DSSCs with MWCNTs; (c) J_{sc} (mA cm^{-2}); (d) V_{oc} (V); (e) FF (%); and (f) PCE (%).

As can be observed from Figure 3.6, the degradation rate of cells under UV irradiation is higher compared with simulated sunlight, which means that the components of the DSSC device are more sensitive to UV light than one sun illuminated light [9,11]. The result indicated that the PV performance of both samples (with and without MWCNTs) gradually decreased during the first 50 h of the UV illumination, which means there is a similar degradation mechanism over this test time. According to Hinsch [120], UV light soaking always has a strong negative effect on the molecular structure of the electrolyte, therefore the PV performance of the cell could decline due to electrolyte degradation. Under UV light aging, iodine in the redox couple iodide/triiodide is irreversibly consumed, which reduces the electrolyte redox cycle (oxidation/reduction) rate at the CE. Moreover, photo-oxidation of the electrolyte is another undesired side reaction under UV soaking [63,120,137]. Between 50 to 350 h of UV aging, a minor decrease (-7.9%) in the PCE of the cell with MWCNTs is shown, compared to the test results of the device without MWCNTs, which shows a considerable reduction (-30.3%). This difference demonstrates that adding MWCNTs significantly improves stability of the cell under UV light. Snaith *et al.* [136,137] reported that, upon UV light illumination, both electrons and holes are formed at the surface of TiO₂ due to the band gap excitation. However, the UV light might introduce crystalline defects (energetically deep electron traps) in the TiO₂, which was identified as a limiting factor for electron diffusion [138]. The energy level of these sites was determined approximately 1 eV below the conduction band, which means that the electrons cannot escape from them to reach the conduction band [138]. Thus, charge recombination between the trapped electrons and the electrolyte can be produced [136,137]. After electron-hole recombination, these sites tend to again trap the electrons (Figure 3.7). In addition, UV light can lead to dye desorption or dye decomposition, thus resulting in substantial deterioration of device operation [9,11,121,139]. Although DSSCs based on TiO₂ photoanodes are very sensitive to UV light, there are limited solutions to overcoming this problem: for example by preventing UV light from reaching the TiO₂ nanoparticles [136,137,140]. Previous studies have confirmed that CNTs can efficiently absorb and hence block UV light [122,128,140]. As a result, MWCNTs can increase the stability of DSSCs under UV light soaking.

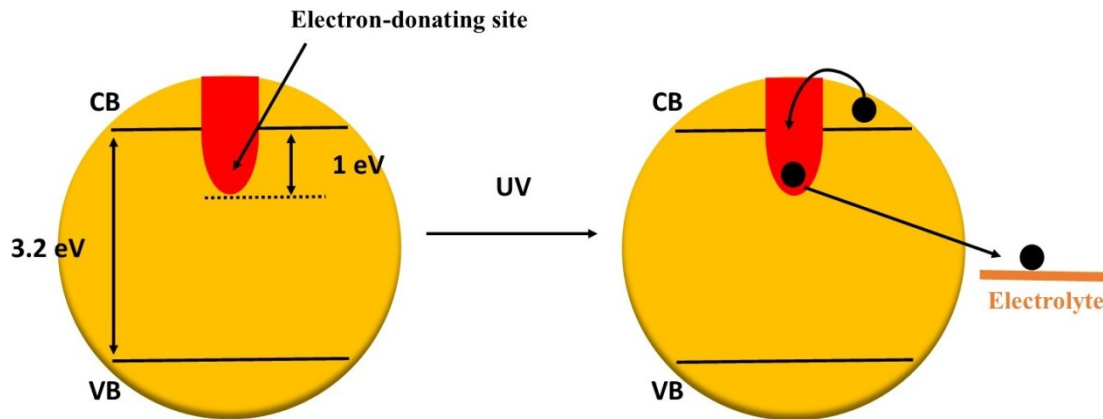


Figure 3.7 Schematic illustration of the band structure model for the TiO_2 that forms deep electronic traps. Under UV light illumination, the injected and photogenerated electron can be adsorbed through deep electron-donating sites. The electron in this site can then undergo direct recombination with a hole in the electrolyte.

3.3.4 Microstructure evaluation

In DSSCs, a good porous photoanode film with continuous bonding between TiO_2 nanoparticles and without any cracks and/or defects is necessary for efficient electron collection and transport [63,119,141]. The degradation of the PV parameters of DSSCs under illumination can be associated with some defect formation in the photoanode. Figure 3.8 shows a microstructure evaluation of the photoanode before and after 200 h of continuous simulated sunlight (100 mW cm^{-2}) soaking and 70 days storage under continuous indoor light (30 mW cm^{-2}). As shown in Figures 3.8 (a and b), the working electrodes are composed of TiO_2 nanoparticles with a porous structure, completely crack-free for electron transport. Previous reports indicated that the presence of MWCNTs in a TiO_2 matrix result in a structure with a more uniform dispersion of nanoparticles and, consequently, the formation of a more porous film [18,51,109,122]. In this study, in the composite anode, it was not possible to observe the MWCNTs due to their very low concentration and the low contrast of carbon-based materials [78]. The FESEM images of the samples after the stability tests [Figures 3.8 (c) and (d)] indicate that after the stability tests, the cell without MWCNTs shows micro-crack formation in the photoanode, which reduces electron transport and increases the charge transport resistance [51,63]. In contrast, the composite device shows a stable structure with no defects or cracks that

could be related to the interaction between the MWCNTs and the TiO₂ particles. These results highlight the role of MWCNTs in improving the mechanical and thermal properties of the photoanode [111,135].

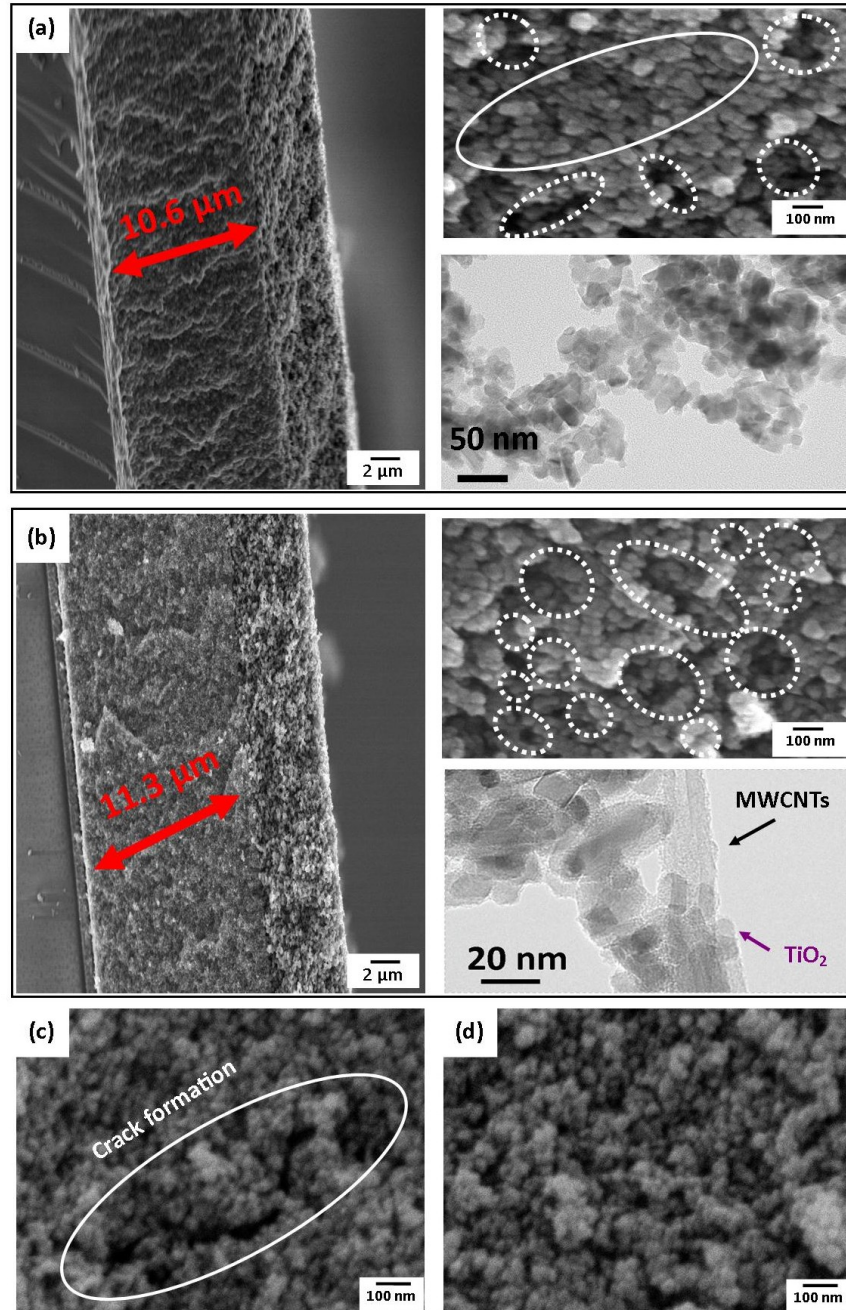


Figure 3.8 FESEM images of synthesized photoanodes: (a) without MWCNTs and (b) with MWCNTs at different magnifications before aging. Solid and dashed ovals highlight the agglomeration and porosity of the TiO₂ particles, respectively. (c) Photoanode without MWCNTs and (d) photoanode with MWCNTs after aging.

3.3.5 Raman spectroscopy measurements

The subsequent stage in the present work focuses on the effect of illumination on the degradation behaviour of the device using Raman spectroscopy. Figure 3.9 displays the Raman spectra of the assembled DSSCs, accessed from the photoanode side by focusing a laser beam at the anode/dye/electrolyte interface. A comparison of the Raman spectra from the two cells before illumination shows similar trend that can confirm the uniform distribution of MWCNTs in the anatase matrix [Figure 3.9(c)]. However, careful peak fitting allows spectral decomposition at 1605 cm^{-1} in the composite photoanode to a series of two Raman peaks at 1599 cm^{-1} and 1610 cm^{-1} . The appearance of an additional peak at 1610 cm^{-1} demonstrates the bonding between the TiO_2 and MWCNTs since, in the Raman spectra of MWCNTs, there is no peak at 1610 cm^{-1} [15,141,142]. Raman modes of the pure anatase phase of TiO_2 are found at: 144 cm^{-1} (E_{g1}), 395 cm^{-1} (B_{1g}), 514 cm^{-1} (A_{1g}), and 641 cm^{-1} (E_{g3}) [142–147]. The E_g mode at 142 cm^{-1} (vibrational mode of the anatase phase) exhibits the anatase structure of both samples. When comparing the Raman spectra recorded from both samples, it is observed that, in the composite sample, the E_g mode shifts from 142 to 150 cm^{-1} . The shift of the Raman band in the sample with MWCNTs is of particular interest because it is attributed to the adsorption of more dye molecules by the TiO_2 nanoparticles [142,146,148]. However, all the other TiO_2 peaks are absent in the observed spectra of the two samples, most likely due to the adsorption of the dye molecules on the TiO_2 surface [149–151]. Some reports previously indicated that, under light illumination, a large number of photo-produced electrons are injected into the conduction band of TiO_2 nanoparticles so that their surface charge dramatically increases [149,150]. The increase of the surface charge tends to change the interface layers from semiconducting to metallic, thus eliminating the TiO_2 bands. Under light irradiation the dye molecules degrade, so that less charge-transfer takes place from the LUMO of the dye molecules to the conduction band of TiO_2 . Therefore, the anatase phase can then recover its semiconducting nature and its peak will appear.

After aging for 200 h under continuous one sun light irradiation (100 mW cm^{-2}) and 70 days' storage under continuous indoor light (30 mW cm^{-2}), the TiO_2 line at 394 cm^{-1} is present in the spectra of both samples, but the peak intensity of the sample without

MWCNTs is more than three times higher than that of the sample containing MWCNTs, which means that the degradation of the dye is suppressed in the composite sample. In addition, the spectra after aging indicate a sharp increase in intensity and a red shift for the band at 168 cm^{-1} , which is several times higher in the sample without MWCNTs compared to the sample with MWCNTs. This transformation can be attributed to desorption of the dye molecules from the surface of nanoparticles and their interaction with the electrolyte and the formation of an oxidized form of dye, which leads to a degradation of device performance [113,149,151–153]. Previous studies have reported that two Raman peaks, including C-C at 1260 cm^{-1} and C-O at 1310 cm^{-1} , are the most important features to distinguish desorption or adsorption of the dye molecules on the TiO_2 substrate [13,151,154]. In other words, there is a direct relationship between the intensity of C-C and C-O peaks and dye desorption. As can be observed after illumination, the intensity of these peaks of the standard sample are increased compared with the initial intensities, which confirms desorption of the dye molecules. However, the composite device was stable, because the peaks show no discernable changes. As mentioned in the previous section, MWCNTs develop a larger number of attached dye molecules on the surface area of the TiO_2 .

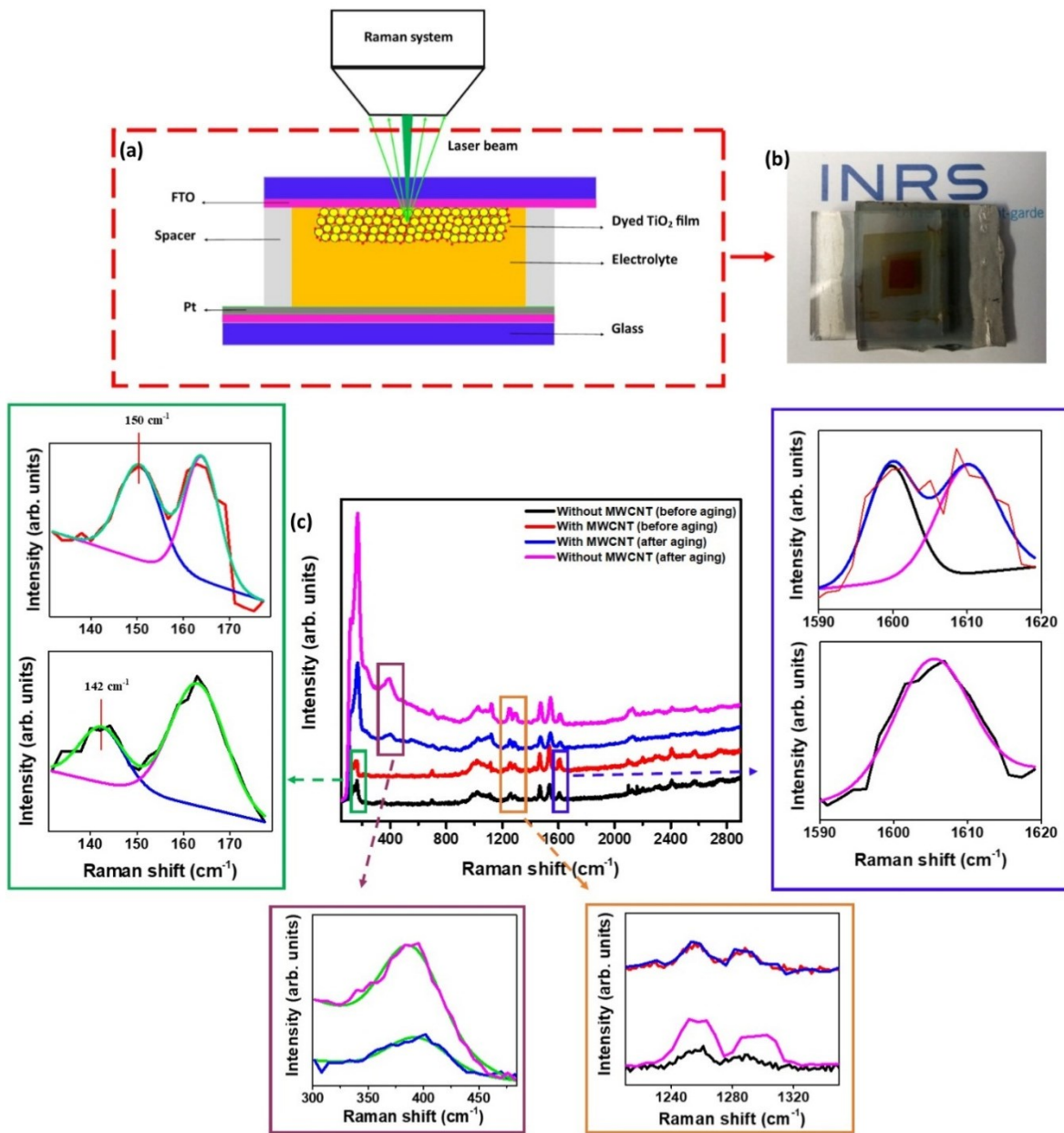


Figure 3.9 (a) Schematic overview of a DSSC under Raman setup for Raman characterization; (b) a complete fabricated DSSC for Raman measurement; and (c) Raman spectra of cells in cases with and without MWCNTs at 514.5 nm before and after aging.

3.3.6 EIS analyses

EIS is a useful technique for investigating the reasons for DSSC degradation [61,101,155]. EIS was measured for cells before and after light illumination over 100 h with continuous one sun light (100 mW cm⁻²) irradiation and 70 days storage under

continuous indoor light (30 mW cm^{-2}). Figures 3.10-12 show the Nyquist and Bode plots of the two cells in cases with and without MWCNTs, before and after aging. The results indicate that the R_s , which is mainly caused by the sheet resistance of the two conductive substrates, remains almost the same for both samples, before and after aging. The similar R_s is consistent with the stability of the FF over the test period. Therefore, both electrodes are very stable and are not responsible for any loss of PV parameters. The size of a well-defined semicircle of the cell with MWCNTs is lower than the cell without MWCNTs (Figure 3.12). This difference in semicircle size confirms that the cell with MWCNTs has lower R_{ct} than the control sample [see Figure 3.12 (b)] since the presence of MWCNTs promotes efficient electron transport and connection between the TiO_2 particles [15,17–19]. Moreover, R_{ct} increases with light aging, but the increasing rate is lower in the composite cell. The increasing of electron transport resistance in the photoanode could be related to the reduction of bonding between the TiO_2 particles due to micro-crack formation, which could be one of the main degradation mechanisms of the cell [155–157]. It has been reported that the τ_e of the device is given by: $\tau_e = 1/(2\pi f_{max})$. f_{max} is the phase angle corresponding to the maximum frequency [17,65,120]. Based on this equation, the τ_e of the cell with MWCNTs is longer than the cell without MWCNTs, in agreement with previous work [14,15,106]. In the cell without MWCNTs, the peak shifts to higher frequency with light soaking [Figure 3.10(e)], suggesting that the decrease of the τ_e is due to degradation. However, in the cell with MWCNTs, the frequency peaks remained at approximately the same position [Figure 3.11 (e)]. This result confirms that adding MWCNTs significantly improves τ_e of DSSCs. In addition, the comparison between the two devices indicates that a higher τ_e can be obtained in the composite sample than in the cell without MWCNTs [Figure 3.12 (c)-(e)], which is consistent with the τ_e obtained from transient photovoltage decay. Therefore, from the electrochemical results, the MWCNTs increase the long-term stability of DSSCs by developing a conductive network between the TiO_2 nanoparticles in the photoanode and preventing crack formation in order to improve charge transport and suppress electron recombination.

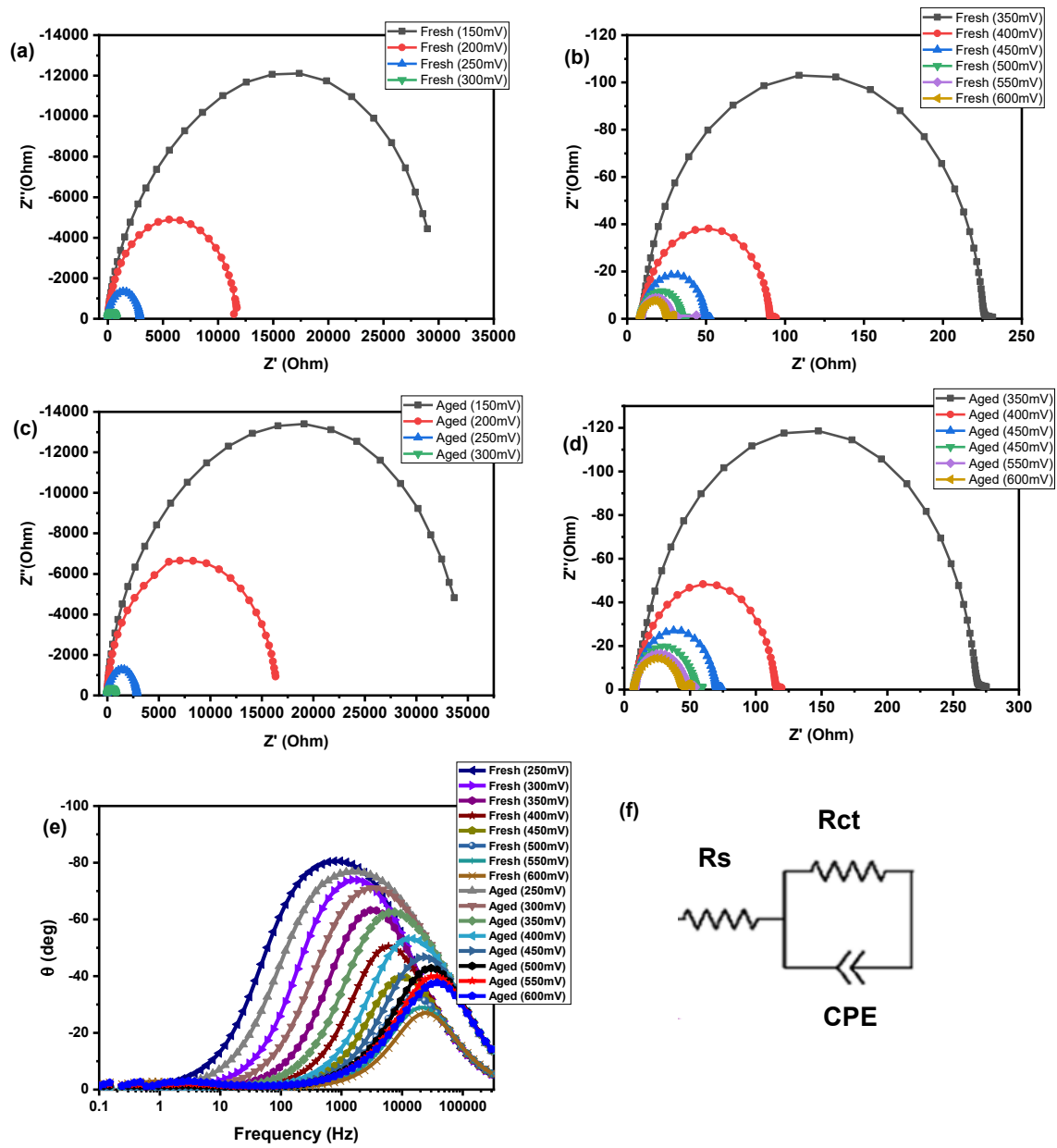


Figure 3.10 (a)-(d): Electrochemical impedance spectroscopy analysis of fresh and aged cells without MWCNTs as a function of applied biases; (e) Bode phase of fresh and aged cells without MWCNTs; and (f) equivalent circuit of the transmission model.

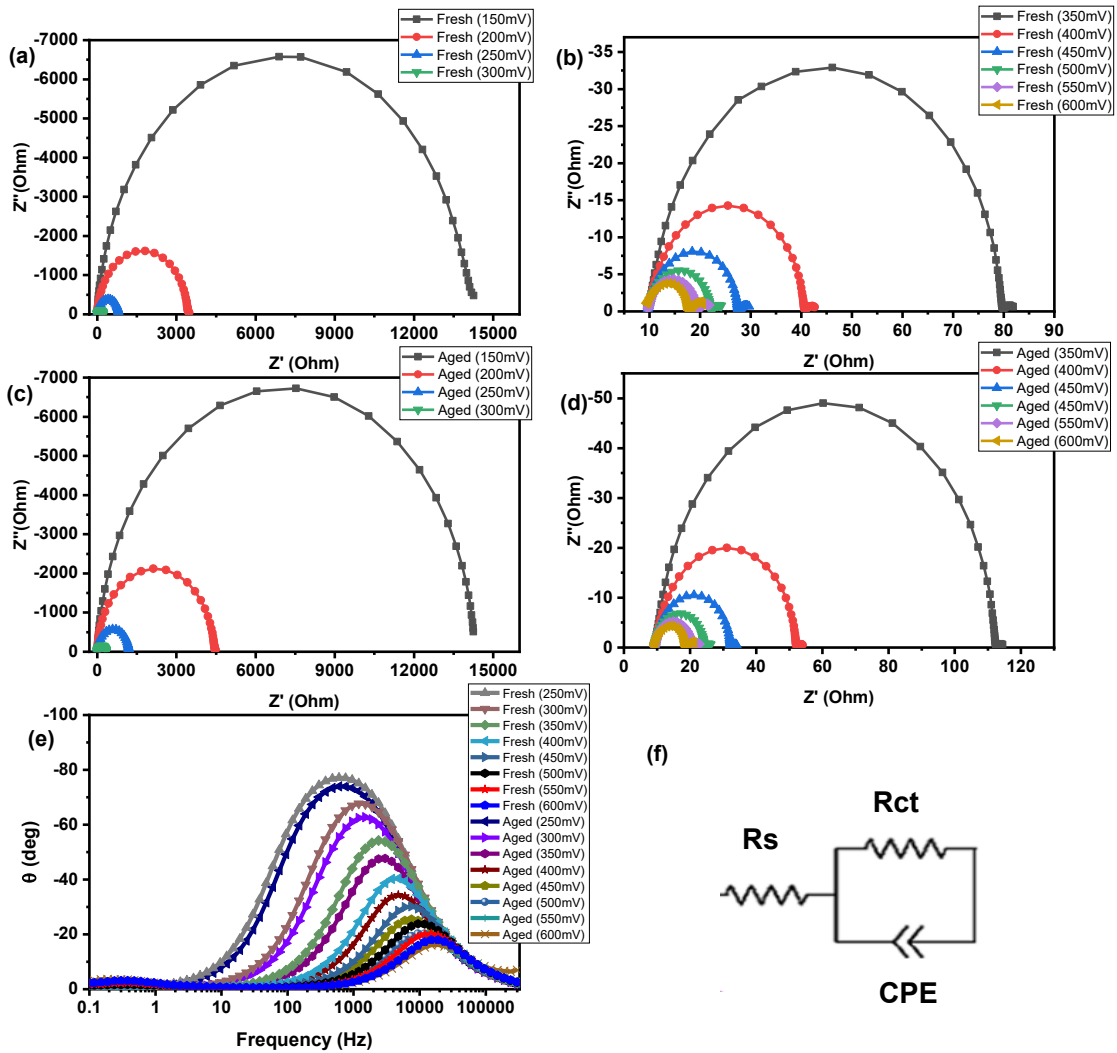


Figure 3.11 (a)-(d) Electrochemical impedance spectroscopy analysis of fresh and aged cells with MWCNTs as a function of applied biases; (e) Bode phase of the fresh and aged cells with MWCNTs; and (f) equivalent circuit of the transmission model.

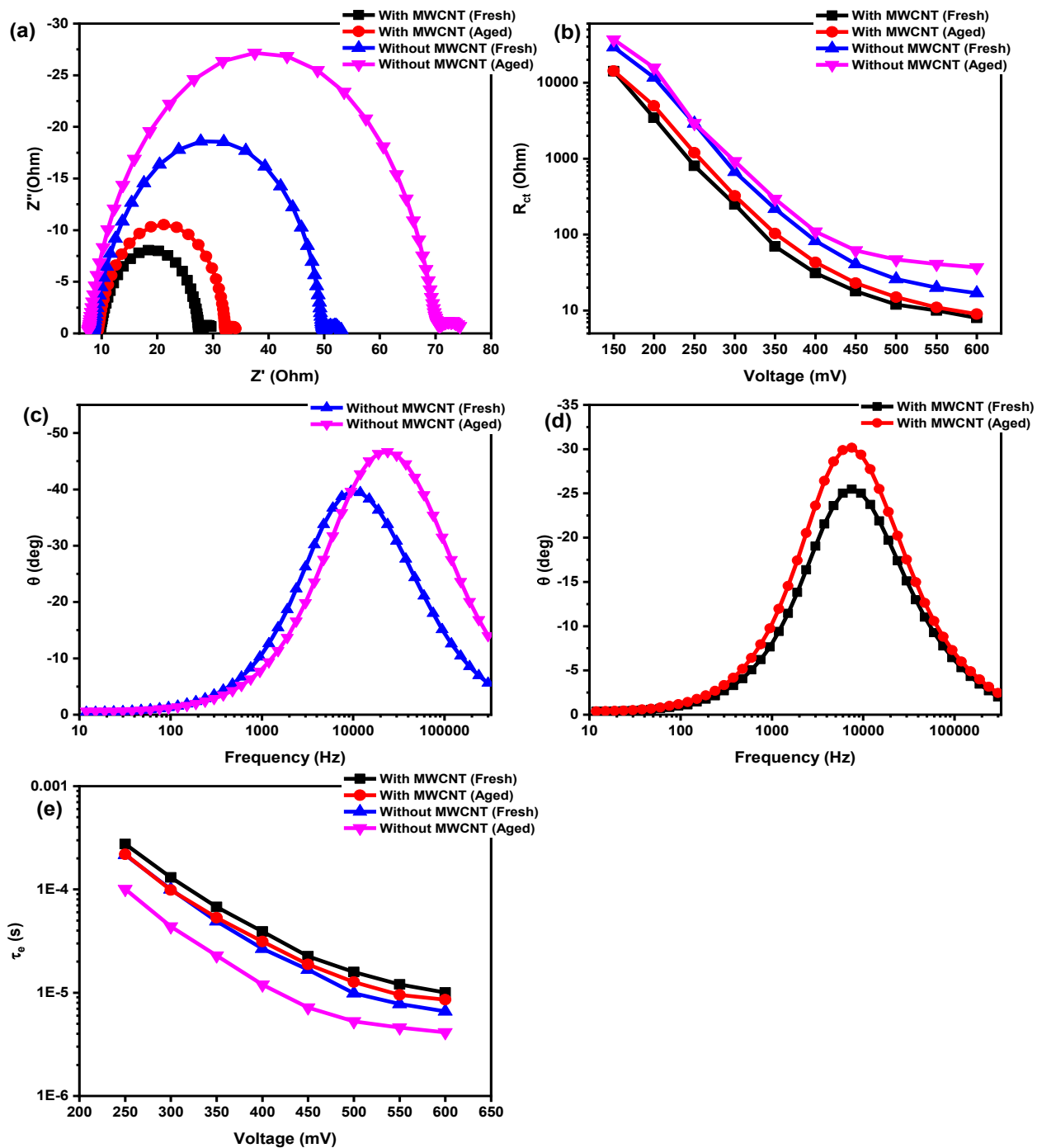


Figure 3.12 (a) Electrochemical impedance spectroscopy analysis of fresh and aged cells without MWCNTs and with MWCNTs for a bias of 450 mV; (b) charge-transfer resistance (R_{ct}) as a function of applied bias in samples with and without MWCNTs, before and after aging; (c) and (d) Bode phase of fresh and aged cells in cases without and with MWCNTs, respectively; and (e) electron lifetime (τ_e) for cells without and with MWCNTs.

3.4 Conclusions and Perspectives

This chapter presents the experimental study of the effect of MWCNTs on the long-term stability of DSSCs. Two different types of DSSCs based on TiO_2 and TiO_2 -MWCNTs nanocomposite anodes were assembled and characterized by different techniques in order to document the degradation mechanisms. The results demonstrate that a small amount of MWCNTs (0.010 wt%) can significantly improve the long-term stability of the DSSCs under continuous simulated one sun and indoor light by 22% and 42%, respectively. In addition, the results of UV light soaking indicate that MWCNTs can successfully stabilize the DSSCs for long-term operation up to 24% improvement. Transient photovoltage decay and EIS measurements confirm the higher τ_e and reduced recombination in the TiO_2 -MWCNTs composite network compared to the standard device. These results as presented in the chapter provide a low cost, simple and straightforward way to improve the long-term stability of DSSCs, which is a major challenge for this technology.

“In fact, researchers have settled on what they believe is the magic number for true expertise: ten thousand hours.”

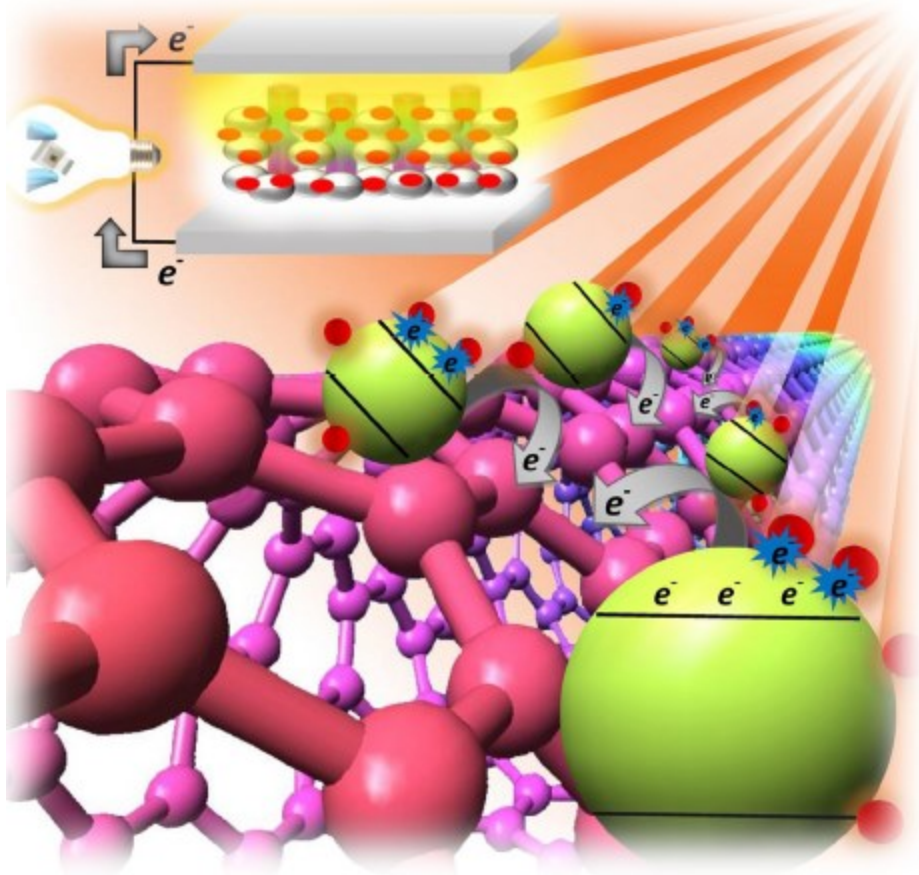
Malcolm Gladwell

CHAPTER 4

Incorporation of multi-wall carbon nanotubes to boost the long-term thermal stability of dye sensitized solar cells

*This chapter is adapted from the peer reviewed publication by Mahyar Mohammaznezhad, Gurpreet Singh Selopal, Zhiming W. Wang, Barry Stansfield, Haiguang Zhao and Federico Rosei, **ChemPlusChem**, 2018, 83, 682-690.*

In this chapter, the effect of MWCNTs on the thermal stability of DSSCs is discussed. The results of this work demonstrated that, under identical measurement conditions (aging at 80°C for 240 h in the dark), DSSCs based on a bare TiO₂ anode present a significant loss in PCE, dropping to 59% of their initial value, while DSSCs based on a TiO₂-MWCNTs nanocomposite anode attained a promising thermal stability with only 20% reduction of the initial PCE. This degradation of cell performance is mainly associated with a dramatic reduction of the J_{sc} .



4.1 Introduction

As described in Chapters 1 and 3, the world energy demand has rapidly increased; all predictions indicate that this growing trend will continue in both developed and developing nations [4,108]. Since different forms of fossil fuels, namely coal, oil and natural gas, make up 80% of the world's energy, it is extremely important to search for clean, carbon-emission-free energy sources [4,28]. In this scenario, solar cells are investigated as a solution to this situation [3,28]. During recent decades, different types of solar cells have been explored and developed. In this regard, DSSCs attract much interest and are considered as a viable alternative to silicon based solar cells due to their simple and low cost of fabrication [51,79].

Degradation analysis of DSSC is not yet well established due to fewer efforts devoted to this important subject [9, 116]. Thermal aging and related stress is one of the most important external factors that should be considered since under sun illumination devices

experience severe unavoidable thermal stress caused by increase in temperature [63, 137]. Sommeling et al. [9] reported that under one sun illumination, depending on the climate, temperatures around 80-85°C can be reached for a solar cell module. In an attempt to improve the thermal stability of DSSCs, a great deal of literature is available on the subject of thermal degradation of the electrolyte and dye molecules. Di Carlo et al. [114,158] illustrated that thermal stress strongly reduces the efficiency and the short-circuit current of DSSCs due to the degradation reaction between the dye and the electrolyte. Gratzel et al. [101] also investigated the effect of prolonged thermal aging at 80°C on dye/electrolyte interface and electron recombination. Their results indicated a large drop of photocurrent during thermal aging due to an incomplete charge carrier collection and, consequently, reduction of effective electron diffusion length. Kontos et al. [113] investigated long-term high temperature (80°C) stability of DSSCs using electrolytes with two different organic solvents, namely methoxypropionitrile and tetraglyme. The results of this research highlighted that a DSSC methoxypropionitrile based electrolyte presents a severe efficiency loss (70%) upon thermal aging, while solar cells using a tetraglyme electrolyte attains a promising stability with only 20% loss of performance. For the methoxypropionitrile electrolyte, a sharp decrease in the short-circuit photocurrent was observed due to severe triiodide loss. Kwak et al. [13] highlighted changes in the molecular structure and condition of the dye molecules of DSSCs when exposed at 85°C. The results revealed that loss of overall PCE was due to desorption of the dye molecules from the TiO₂ nanoparticles as well as dissociation of the electrolyte with the dye.

Chapter 3 of the present work demonstrates that the long-term stability of DSSCs improves under continuous simulated one sun, indoor light and UV light by 22%, 42% and 24%, respectively, with the limited addition of MWCNTs into a commercial TiO₂ anatase paste. Meanwhile, numerous studies have reported that CNTs tend to increase the mechanical properties and thermal stability of the nanocomposite structure due to their unique properties, such as high tensile strength and thermal conductivity [51,110,159]. However, as far as can be ascertained by a review of the relevant literature, no report has yet demonstrated the effect of adding MWCNTs to a TiO₂ photoanode on the durability of DSSCs under heat stress, which is directly related to outdoor performance. Since this direction demands more efforts, this chapter investigates the

effects of MWCNTs on the thermal stability of DSSCs. Two series of DSSCs were fabricated based on bare TiO₂ and composite TiO₂-MWCNTs electron transport layers, which have been exposed to thermal stress under dark conditions in order to avoid other possible effects of light illumination and related degradation mechanisms. The DSSCs based on the TiO₂ photoanode suffer from an extremely rapid decrease in PV performance under thermal stress. However, the device with MWCNTs demonstrates extremely stable performance under similar test conditions.

4.2 Experimental

TiO₂ anatase paste composed of 20 nm sized nanoparticles (18 NR-T) and anatase scattering paste (WER2-O) particles (150nm to 250nm) were purchased from DyeSol. A TiO₂ blocking layer (Ti-Nanoxide) was purchased from Solaronix. MWCNTs of 10 μm average length and a 12 nm average diameter was purchased from Sigma-Aldrich (cat. no. 698849). All materials were used as received, without further purification. The blocking layer was prepared onto ultrasonically cleaned FTO substrates in acetone, methanol and deionized water in two steps, namely Step one, at a rotation speed of 3000 rpm for 20 seconds and Step two, at a rotation speed of 6000 rpm for 40 seconds, followed by annealing at 500°C for 30 minutes under ambient conditions. A TiO₂-MWCNTs based nanocomposite was prepared according to a previously reported procedure [15,115]. MWCNTs suspension was prepared by adding 6 mg of MWCNTs to 15 mL of ethanol, followed by three h sonication in an ultrasonic bath. A TiO₂-MWCNTs nanocomposite paste was prepared by mechanically stirring 0.010 % wt of MWCNTs with the TiO₂ paste. Bare TiO₂ and the prepared TiO₂-MWCNTs nanocomposite pastes were then tape casted on the top of the blocking layer. The photoanodes were subsequently dried for 15 min at ambient atmosphere and temperature and 6 min at 120 °C. All the samples were then annealed at 500°C for 30 min before dye-sensitization by commercial Ru-based molecular complex N719 dye (from Solaronix). DSSCs were fabricated by injection of an iodide/triiodide redox couple electrolyte between the photoanode and the CE with 60 μm thick spacers (from Solaronix). The thermal stability tests in this study were performed at different temperatures and under dark conditions [101,160]. The J-V

characteristics of the cells were determined by a Keithley 2400 Source Meter under simulated sunlight using an ABET2000 solar simulator at M1.5G (100 mW cm^{-2}) after aging at different times and temperatures. Morphology of the samples was characterized by SEM (FE-SEM, JEOL JSM-6900 F). EIS was performed using a SOLARTRON 1260 A Impedance/Gain-Phase Analyzer by applying different biases under dark condition. The tests were recorded over a frequency range between 10 mHz and 300 kHz, and the AC signal was 10 mV in amplitude. All impedance measurements were analyzed using an appropriate equivalent circuit model with Z-View software (v3.5, Scribner Associate, Inc.). The Raman spectra of the complete cells were measured at 514 nm excitation sources at room temperature. Chemical bonding was determined by XPS analysis in a VG Escalab 220i-XL equipped with an Mg K α source.

4.3 Results and discussion

The results indicated that the PCE of the DSSCs improved ~30% with 0.010 % addition of MWCNTs in TiO₂ with respect to the standard device (reported in Figure 4.1 and Table 4.1).

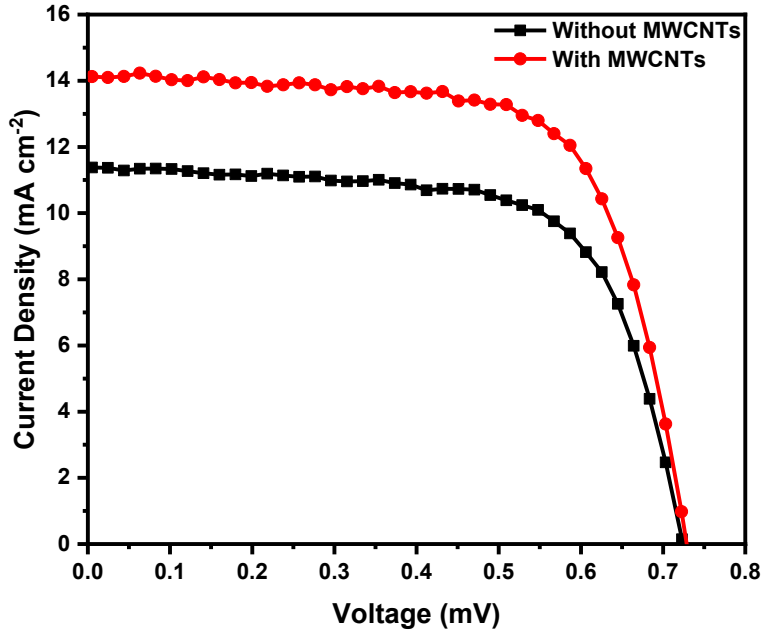


Figure 4.1 Current density-voltage curves of solar cells under simulated one sun at AM 1.5G (100 mW cm⁻²) fabricated using TiO₂ mesoporous films with (red circles) and without MWCNTs (black squares).

Table 4.1. Functional parameters of DSSCs with and without MWCNTs.

anode structure	PCE (%)	FF (%)	V _{oc} (mV)	J _{sc} (mA cm ⁻²)
TiO ₂	5.5±0.2	67±2	715±10	11.3±0.3
TiO ₂ +MWCNTs	7.0±0.2	68±2	720±10	14.1±0.3

4.3.1 Stability under different aging temperatures

There are several commonly used tests to evaluate the thermal stability of the solar cells under different stress factors. There is no exact figure mentioned in the literature, but usually the thermal stability are declared to pass by heating in dark conditions, in order to

avoid other possible effects of light soaking and related degradation mechanisms [63,157]. PV parameters of two series of DSSCs, with and without MWCNTs, were recorded before and after applying thermal stress at different temperatures in the range 40-100°C and a similar aging period (15 h), in order to obtain the critical temperature. Figure 4.2 shows the PCE of the cells as a function of the thermal aging temperature in the dark for 15 h. The drastic decline of the PCE of the DSSCs, based on the TiO₂ photoanode occurring when increasing the temperature from 40 to 80°C, is compared to the PCE of the DSSCs with MWCNTs. However, a strong reduction was identified for both cells above 80°C. A visual inspection of the cells that were aged at temperatures higher than 80°C, 90°C and 100°C indicates leakage of the electrolyte, which signifies that thermal stress at high temperatures can accelerate damage to the sealing layer and, consequently, loss of electrolyte [114,158,160]. Based on these results, it can be concluded that 80°C is the critical temperature, hence this temperature was selected in order to obtain information for a more systematic study of degradation phenomena in DSSCs during thermal aging. The following section mainly focuses on the thermal stability of DSSCs at 80°C and different aging times, without any sealing damage or apparent leakage of the electrolyte.

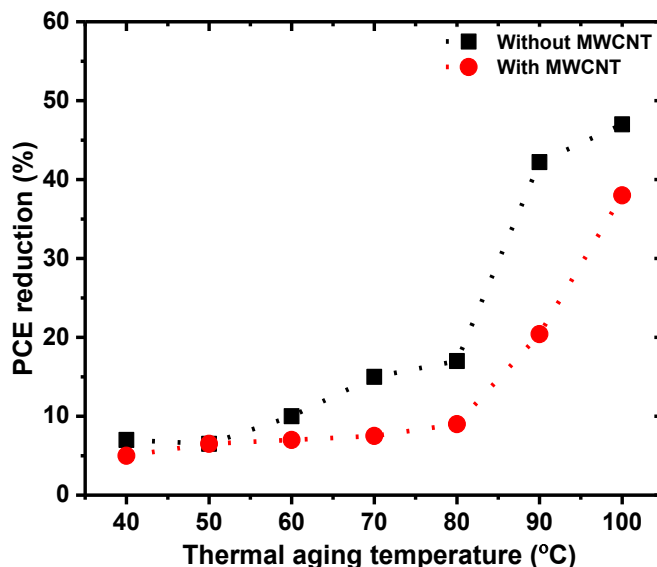


Figure 4.2 PCE reduction (%) as a function of the thermal aging temperature of the two devices: TiO₂ (black square) and TiO₂-MWCNTs (red circle).

4.3.2 Long-term thermal stability

Figure 4.3 shows the degradation of the PV parameters of the DSSCs with and without MWCNTs as a function of the thermal aging time at 80°C. All parameters are normalized to the initial value. Evidently, the functional parameters of the composite device are only moderately influenced by thermal stress, in contrast to the DSSC without MWCNTs, which is strongly affected. The J_{sc} (mA cm^{-2}) substantially decreases by 55% for the DSSC without MWCNTs, yet by only 14% for the DSSC with MWCNTs. At the same time, the V_{oc} (V) declines by 20% and 12% of their initial value for DSSCs with and without MWCNTs, respectively.

Consequently, thermal stress at 80°C over 240 h leads to a major decline of the overall PCE of the DSSCs based on the bare TiO_2 by 59%, but is limited to only 20% for the cell with the TiO_2 -MWCNTs nanocomposite anode. Moreover, the fact that the FF (%) of both cells slightly increased (~ 6%) with thermal aging suggests improved activation and better connection between the electrolyte and CE upon thermal aging [101]. This result is very important, indicating that use of a TiO_2 -MWCNTs nanocomposite anode can significantly increase thermal stability of DSSCs.

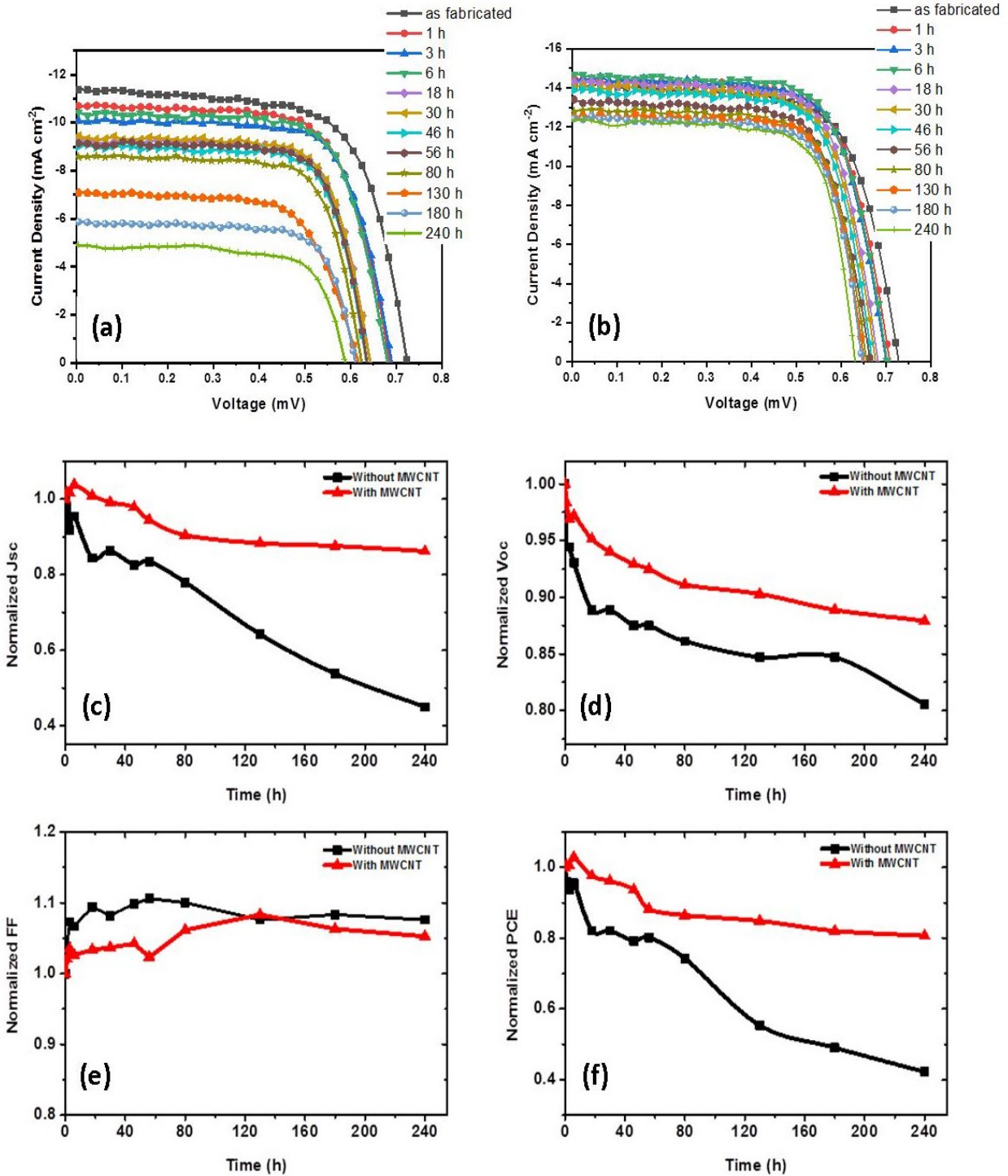


Figure 4.3 Functional properties of DSSCs in cases with and without MWCNTs as a function of thermal aging time: (a) J-V curves of DSSCs without MWCNTs; (b) J-V curves of DSSCs with MWCNTs; (c) J_{sc} (mA cm⁻²); (d) V_{oc} (V); (e) FF (%); and (f) PCE (%).

4.3.3 Microstructural characterization

The correlation between thermal stress and device degradation should also be clarified in this work. Therefore, a detailed microstructure evaluation was performed on an aged device at 80°C for 240 h, the results are shown in Figures 4.4 and 4.5. It is believed that a good porous anode is a crucial factor for electron transporting in DSSCs, and that any defect formation in this layer has significant effect on the device performance. Figure 4.4 shows cross-sectional FESEM images of the DSSCs without MWCNTs, indicating that thermal stress gives rise to long cracks and loss of connection between TiO₂ particles. However, the microstructural evaluation of the composite device indicates that there is no crack on the composite sample; since the MWCNTs are ~10 micrometers long, they can improve bond strength between large numbers of TiO₂ nanoparticles (see Figure 4.5) [134]. According to the literature [109,125,134], electron collection and transportation are directly related to the connection between TiO₂ particles, hence crack formation can adversely affect the charge transfer and consequently the J_{sc} (mA cm⁻²). CNTs have been used as a fibre reinforcement to improve mechanical strength of a TiO₂ matrix under different stresses due to their substantial contact with the particle surface [111,131,135,146,161]. Moreover, the unusual properties of CNTs, including high thermal conductivity and thermal expansion, make them one of the most promising candidate materials for thermally stable composites [31-33]. Hence, MWCNTs are able to improve the stability of DSSCs during thermal stress by preventing the degradation of the photoanode. However, the properties of the composite mainly depend on the uniform distribution of MWCNTs [127,161]. Due to the very low concentration and the low contrast of MWCNTs, it was not possible to observe the MWCNTs in the TiO₂ matrix (Figure 4.5). Hence, in order to investigate the distribution of MWCNTs between TiO₂ nanoparticles, a sample was synthesized with a higher concentration of MWCNTs (three times higher). Figure 4.6 illustrates the FESEM images of the sample with a higher concentration of MWCNTs, shows the uniform distributions of the MWCNTs on the TiO₂ matrix. In these images, the diameters of the tubes that are arranged outside of the matrix are in the range of 15-25 nm, which are consistent with single or double bundle MWCNTs. However, observation confirms that some MWCNTs are coated with TiO₂ nanoparticles. Previous work indicated that TiO₂ nanoparticles bound to the surface of the CNTs [161]. The

connection between the CNTs and TiO₂ is a result of the Ti-C bonds that form during annealing treatment at temperatures higher than 400°C [162].

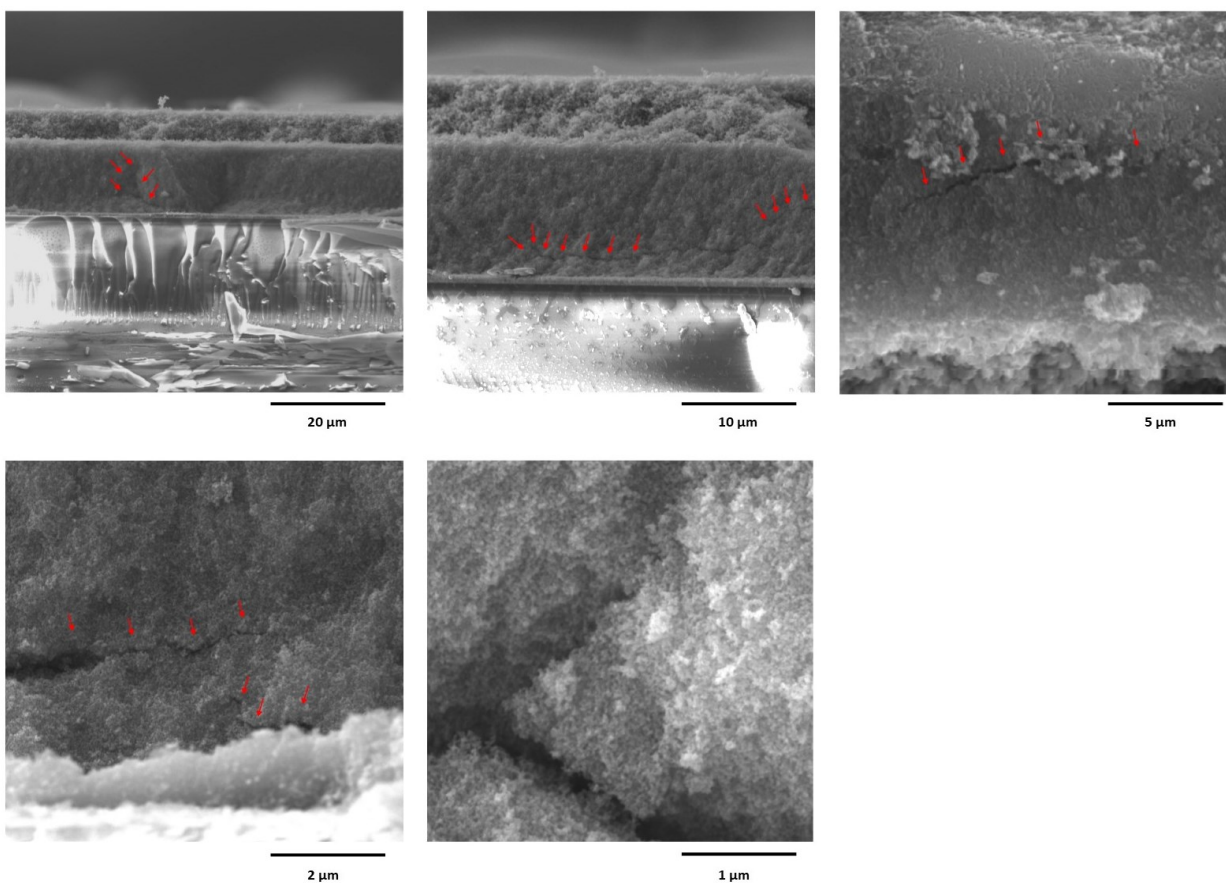


Figure 4.4 FESEM images of the photoanodes without MWCNTs in different magnifications after thermal aging. Red arrows indicate cracks in the photoanode.

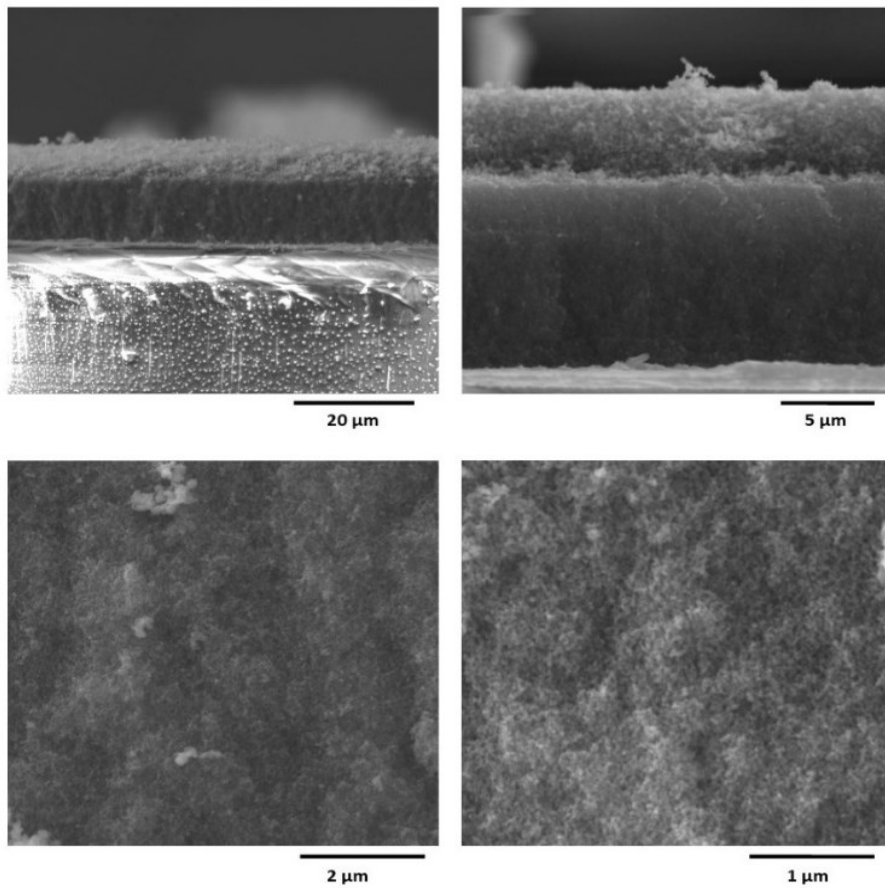


Figure 4.5 FESEM images of the photoanodes with MWCNTs in different magnifications after thermal aging.

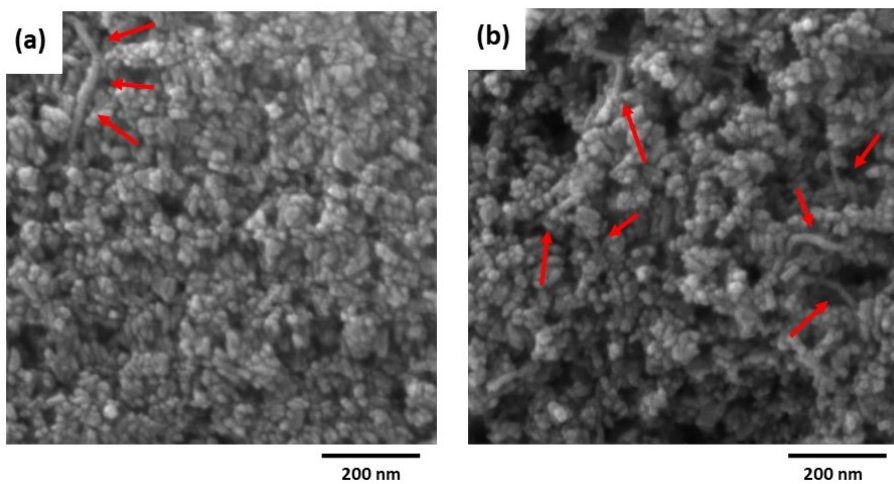


Figure 4.6 High magnification FESEM images of the photoanodes with (a) 0.01 % wt and (b) 0.03 % wt of MWCNTs. Red arrows indicate MWCNTs.

4.3.4 Electron lifetime evaluation

The characterizations of DSSCs exhibit a degradation of the V_{oc} (V) that may be due to a decrease of the electron lifetime and recombination resistance at the photoanode [15,63,64,116,130]. Previous reports indicated that optimization of the photoanode as the heart of the device that increases recombination resistance and decreases charge transport resistance is a crucial factor in improving the performance of DSSCs [131,132]. The electron lifetime and recombination resistance at the photoelectrode were measured according to the transient photovoltage decay, as represented by Equation (3.1) [64]. The photovoltage decay and calculated electron lifetime curves of DSSCs before and after thermal aging are shown in Figure 4.7. As can be seen, the rate of V_{oc} decay is slower in the device with MWCNTs than the device based on the bare TiO_2 . The electron lifetime of the cell without MWCNTs dramatically decreases after thermal aging, while the composite devices show no significant changes. In the cell without MWCNTs, degradation and crack formation of the photoanode, leading to incomplete charge transfer, are likely responsible for the reduction of electron lifetime and recombination [101,158,160]. Meanwhile, in the composite sample, the addition of MWCNTs is expected to prevent charge recombination by acting as a strong conductive network in the structure [109,130]. The related literature supports the hypothesis that electrons are transferred to the CNTs from the TiO_2 nanoparticles, followed by rapid transport to the FTO substrate without recombination [131].

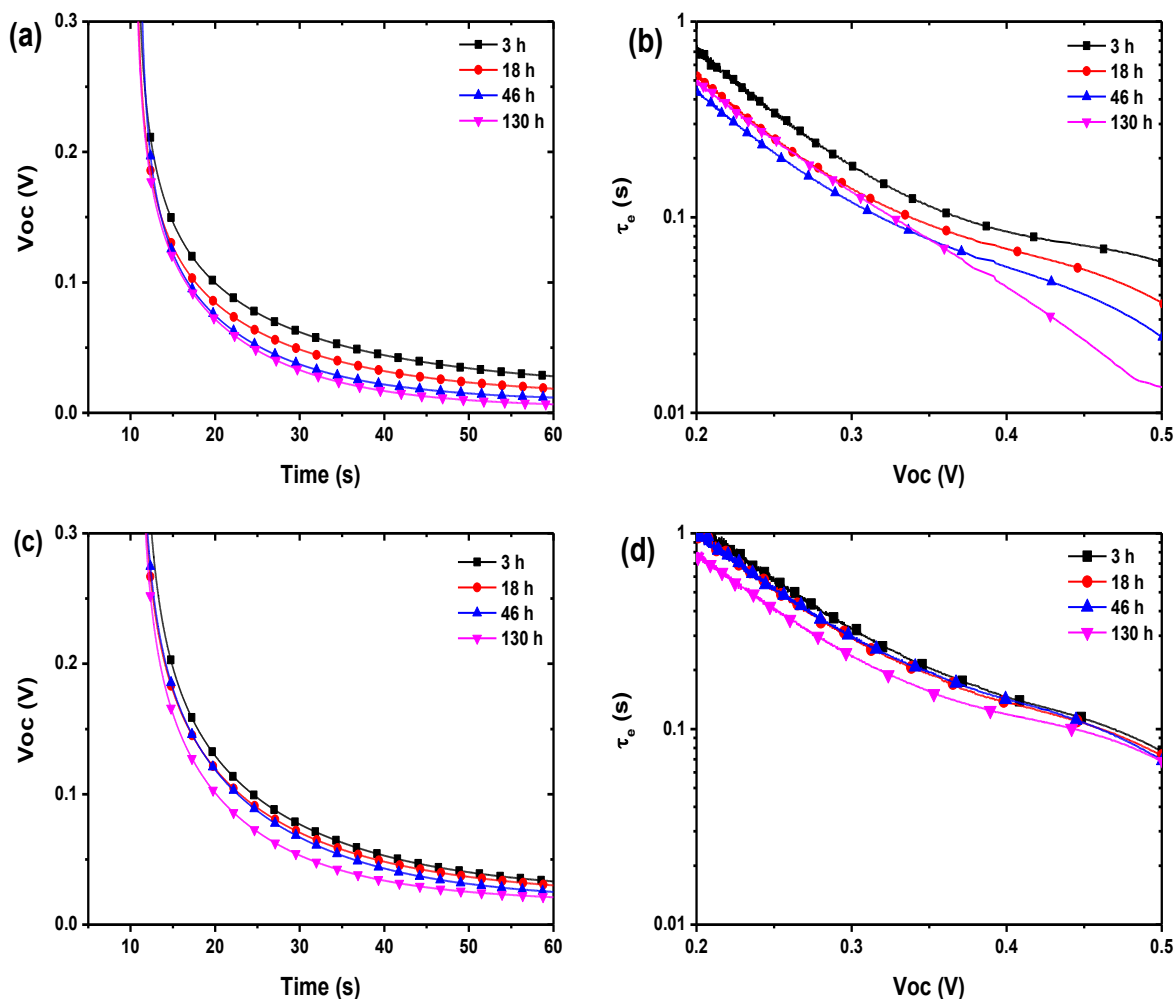


Figure 4.7 Transient V_{oc} decay and obtained electron lifetime (τ_e): for cells without MWCNTs (a) and (b) and cells with MWCNTs (c) and (d), measured after different thermal stress times.

4.3.5 Electrochemical characterization

To achieve additional insight into the effects of thermal stress on device durability, EIS measurement, which is a useful technique for investigating the reason for the degradation phenomena from a physical perspective, was taken [61,101]. Nyquist spectra of the impedance of the two devices in cases with and without MWCNTs upon thermal aging (240 h at 80°C) of different applied voltages at 300 and 450 mV indicate that, during the degradation process, the semicircle size increases [see Figure 4.8 (a) and (b)]. The results indicated that increasing the size of the semicircle is greater in the cell without MWCNTs, due to the reduction of electron transfer in the photoanode [18,19,160]. The

EIS measurements indicate that the R_{ct} of the composite cell is lower than that of the cell with bare TiO_2 , which confirmed the effect of MWCNTs as an efficient electron transport within the photoanode [18,19]. After thermal aging, the charge-transfer resistance increases; however, the increasing rate is higher in the cell without MWCNTs compared with the composite device. In DSSCs, the degradation of the device performance is often associated with an increase in electron transport resistance that is dependent on the bonding between TiO_2 particles [63]. A reduction of electron transport in the photoanode confirms the degradation of the mesoporous film with thermal stress [155,157]. The phase angle corresponding to the maximum frequency (f_{max}) is related to the electron lifetime, according to the equation: $\tau_e = 1/(2\pi \cdot f_{max})$ [17,120]. After thermal aging, the f_{max} of the standard device shifts to higher frequencies, while in the cell with MWCNTs it remains in approximately the same position. The shift of f_{max} confirms the electron lifetime reduction, which is consistent with the τ_e calculated from the transient photovoltage decay (Figure 4.7) [15,106]. Figure 4.8 (e) shows the Mott-Schottky (MS) plots calculated from EIS plots for both devices before and after thermal aging. The results indicated that the composited with MWCNTs leads to changes in the MS plots, in turn resulting in significant structural changes in the mesoporous film as well as an increase in electron transport. Therefore, there is no surprise that, in the composite device, the V_{oc} and τ_e are observed to be higher and more stable over long-term thermal aging than that of the bare TiO_2 cell.

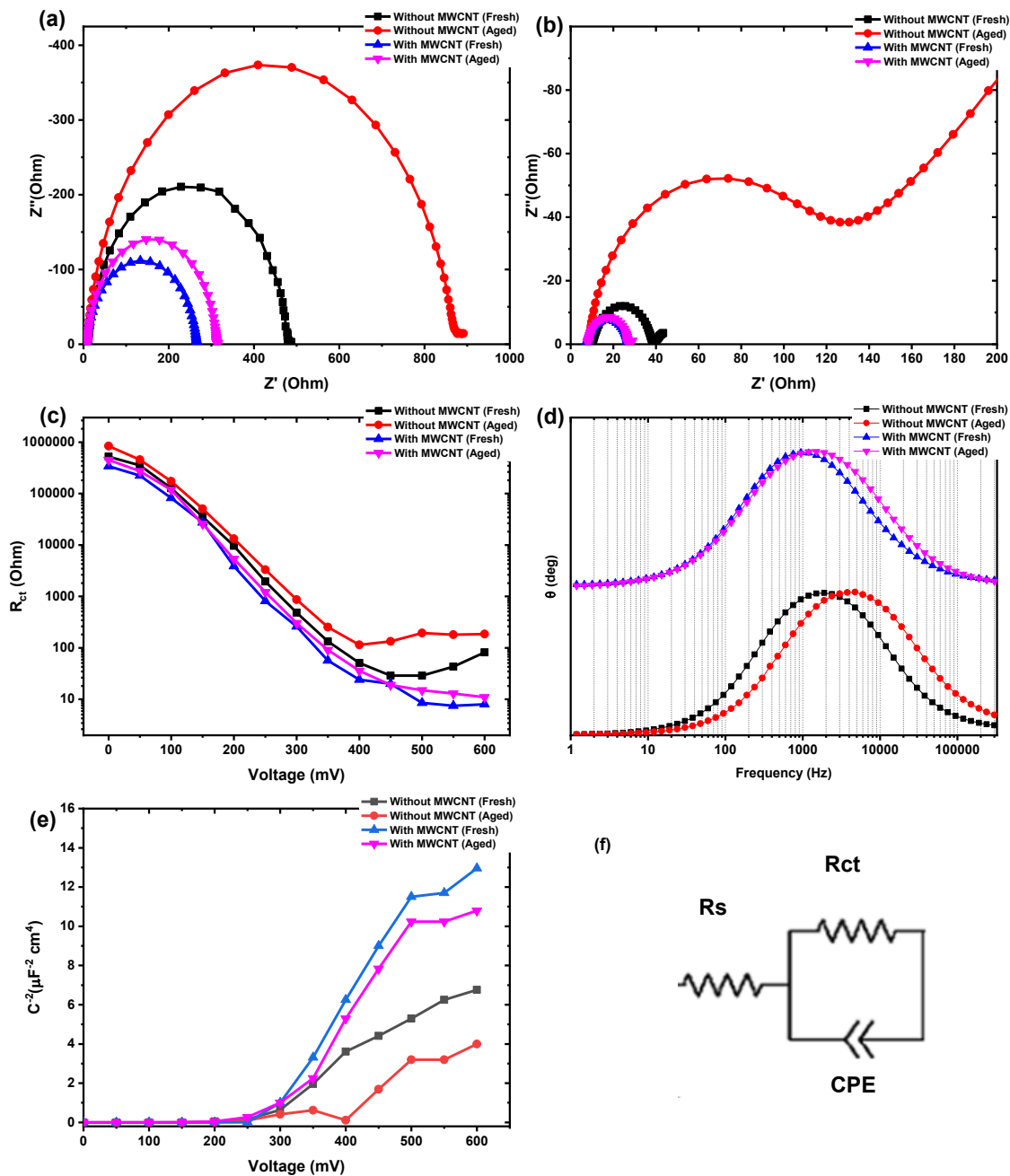


Figure 4.8 (a) and (b) EIS analysis of the fresh and aged cells without and with MWCNTs in biases at 300 and 450 mV respectively; (c) charge-transfer resistance as a function of applied biases before and after thermal aging; (d) Bode phase of the fresh and aged cells; (e) Mott-Schottky plots for fresh and aged cells without and with MWCNTs; and (f) equivalent circuit of the transmission model.

4.3.6 Raman spectroscopy analysis

Raman spectroscopy was applied for a deeper investigation into the degradation behaviour of the devices under thermal stress (Figure 4.9). The Raman spectra accessed the assembled devices by focusing the laser beam at the photoanode of the DSSCs with and without MWCNTs, before and after thermal aging. The Raman spectra from both reference cells yielded similar features and intensities since the only difference in the examined DSSCs was the presence of a low concentration of MWCNTs in the TiO₂ mesoporous film. These similar spectra could be related to two different reasons: (i) uniform distribution of MWCNTs in the TiO₂ mesoporous film; and (ii) MWCNTs covered by TiO₂ nanoparticles. However, comparisons of the Raman spectra for the fresh and thermally stressed devices exhibit variation in the TiO₂ and dye molecule Raman modes after thermal stress. Thermal stress leads to desorption of dye molecules from the surface of the TiO₂ nanoparticles, which strongly affects the degradation kinetics of the DSSCs, as discussed in recent studies [13,63,113,160]. Two Raman peaks, C-C at 1260 cm⁻¹ and C-O at 1310 cm⁻¹, are related modes for distinguishing desorption or adsorption of the dye molecules on the surface of TiO₂ nanoparticles. These Raman peaks disappear with adsorption and their intensities increase with dye desorbed [13,151,154]. The observation of the appearance of the peaks after aging in the cell without MWCNTs confirms desorption of the dye molecules from the surface of the TiO₂ nanoparticles. The corresponding Raman spectra reveals a sharp increase in the intensity of the band at 166 cm⁻¹ after thermal aging in the standard device, mostly ascribed to oxidation the dye. This marked increase is mainly related to the interaction between the desorbed dye molecules and the redox couple electrolyte, and the formation of an oxidized form of the dye, which leads to a degradation of DSSC performance [113,149,151,153].

The Raman modes of the anatase phase of the TiO₂ are observed at: 144 cm⁻¹ (E_{g1}), 395 cm⁻¹ (B_{1g}), 514 cm⁻¹ (A_{1g}), and 641 cm⁻¹ (E_{g3}). Due to the adsorption of the dye molecules on the TiO₂ surface, all peaks related to the anatase are absent in the spectra of the fresh samples [142,144,147,149,150]. However, after thermal stress, three bands are observed in the spectrum of the device without MWCNTs at about 390 cm⁻¹, 508 cm⁻¹ and 635 cm⁻¹. This is another confirmation for the heat-induced desorption of the dye

from the TiO₂ particles during the aging test [149–151]. Di Carlo and coworkers [158] suggested that thermal stress may break the bonds between dye molecules and TiO₂, which can be correlated to the strong reduction of J_{sc} (mA cm⁻²). In the composite device, the MWCNTs improve the thermal conductivity of the active layer, thus preventing the increase of temperature and dye desorption in the cell [51,110,159].

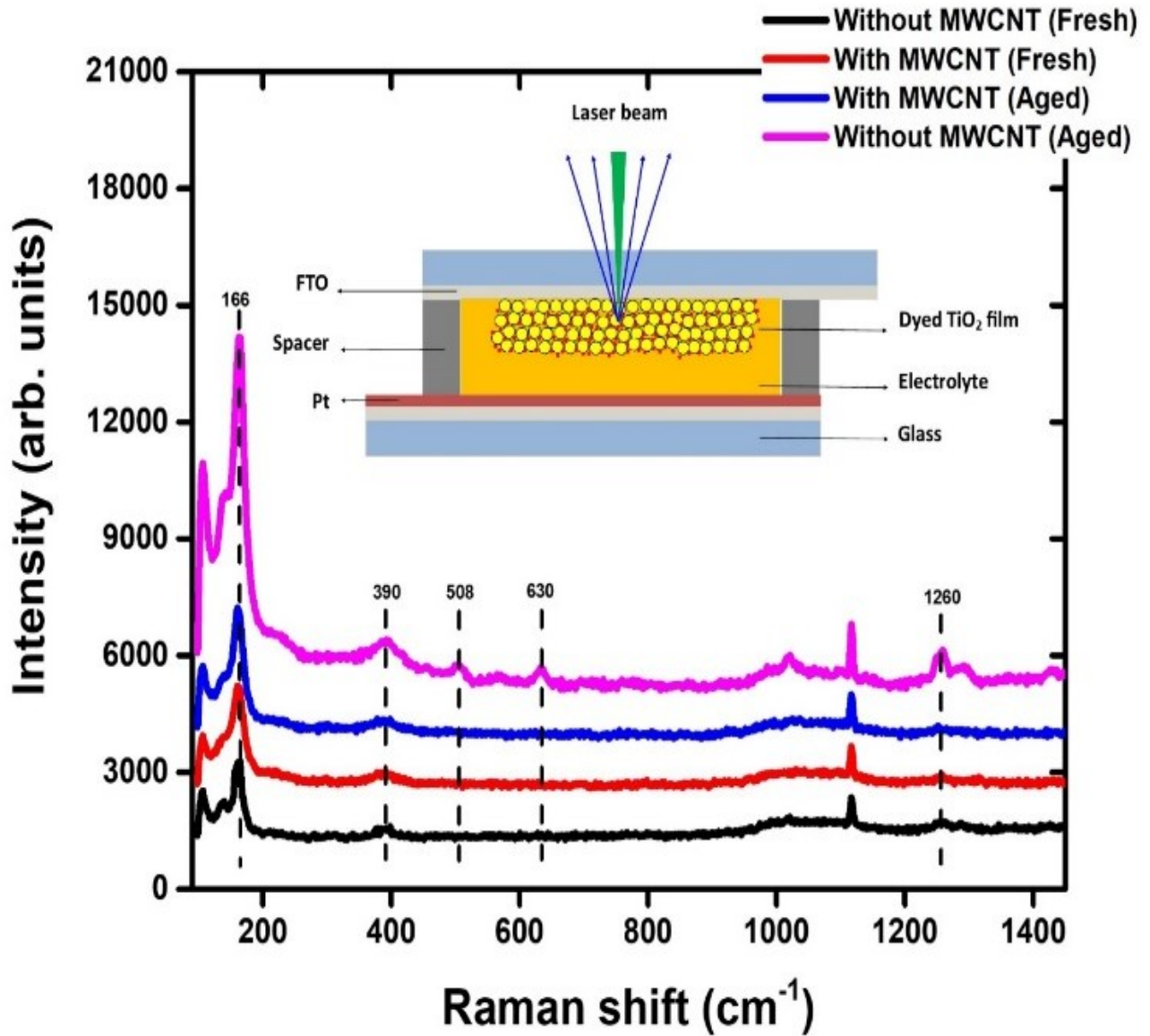


Figure 4.9 Raman spectra of cells with and without MWCNTs at 514.5 nm before and after thermal aging. The insert shows a schematic overview of a DSSC under setup for Raman measurement.

4.3.7 Chemical analysis

Further information on the adsorption of the dye molecules on the TiO₂ nanoparticles was investigated by XPS. Figure 4.10 shows the XPS results of the TiO₂ mesoporous film without and with MWCNTs, before and after dye sensitization. As is apparent from high-resolution spectra of C before dye sensitization, two peaks were observed at 284.6 and 288.4 eV. However, after dye loading, a new peak at 280.5 eV is observed and is assigned to the Ru 3d_{5/2} spectra of the N719 dye. Another peak that is related to the N719 dye, Ru 3d_{3/2}, is hidden under the major C 1s peak, so the peak at 284.6 eV is contributed by pyridine, NCS and TBA cation groups. The N 1s region of XPS spectra for the dye (N719) is composed of three peaks: (i) the peak at around 402 eV is attributed to the Nitrogen in TBA⁺ (tetrabutylammonium) cations; (ii) the peak at around 400 eV corresponds to the Nitrogen in the bipyridine ligands; and (iii) the peak at about 398 eV is ascribed to the Nitrogen in the NCS groups [163,164]. Both samples have very similar N1s intensities, which agree with the chemical formula of the dyes and adsorption of the dye molecules on the surface the TiO₂ nanoparticles. The S 2p spectrum originates from the sulfur in the NCS ligands of the dye molecules and is a clear indicator that the dye molecules are deposited on the TiO₂ nanoparticle surface [163,164]. Hence, this peak was not observed before sensitization. This XPS result implies that dye molecules are anchored on the TiO₂ surface, an observation that is consistent with previous results obtained by Raman spectroscopy.

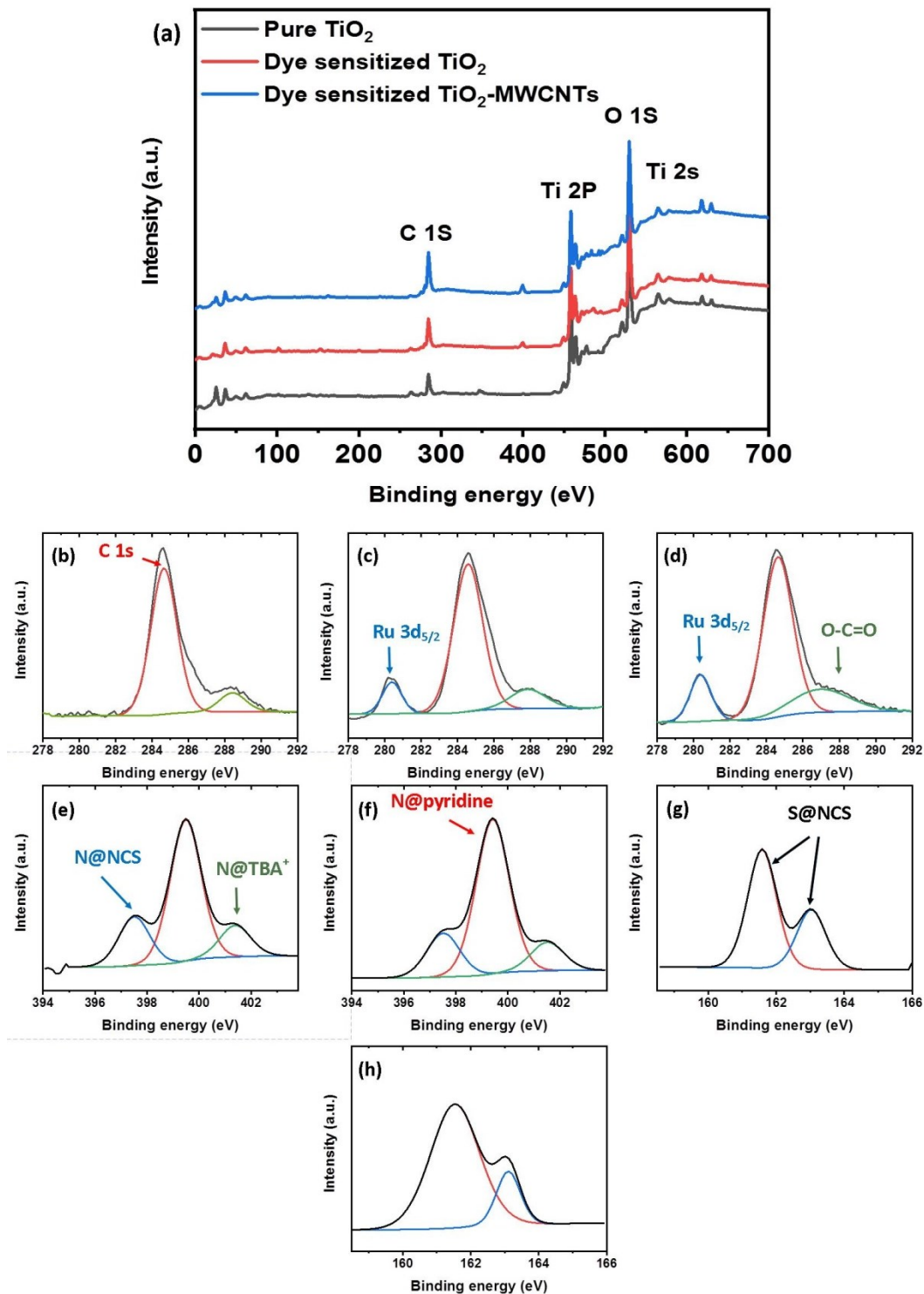


Figure 4.10 High-resolution XPS spectra of (a) TiO₂ mesoporous films with and without MWCNTs, before and after dye sensitization; (b) TiO₂ mesoporous film before dye sensitization in the C 1s region; (c) and (d) dye sensitized mesoporous film without and with MWCNTs in the C 1s region, respectively; (e) and (f) dye sensitized mesoporous film without and with MWCNTs in the N 1s region, respectively; (g) and (h) dye sensitized mesoporous film without and with MWCNTs in the S 2p region.

4.4 Conclusions and Perspectives

Prolonged thermal aging is one of the most prominent stress tests for the assessment of DSSC long term stability. In this present work, in order to improve durability of the DSSC at high temperatures, MWCNTs are employed in the anode. Moreover, the main focus is only on the thermal stability of DSSCs at 80°C and different aging times. The results show that DSSCs fabricated with a TiO₂-MWCNTs nanocomposite anode exhibit improved thermal-stability, with only a 20% loss in PCE after 240 h of continuous thermal aging at 80°C. In contrast, DSSCs fabricated with a bare TiO₂ anode exhibit worse stability performance with a 59% loss in PCE, under the same stressed conditions, mainly by a drop in J_{sc} (mA cm⁻²). The device with MWCNTs exhibit excellent microstructure stability of the photoanode with respect to the standard DSSCs due to the strong bonding between MWCNTs and TiO₂ nanoparticles. In addition, MWCNTs tend to form a strong-conductive network between TiO₂ nanoparticles, resulting in a reduction in charge recombination. This is a particularly significant result, indicating that engineering a composite photoanode can be a practical approach to improving the thermal stability of DSSCs. The results presented in this chapter provide a straightforward way to improve the stability of the DSSCs via a low cost, fast, scalable and highly reproducible process, which represents a major advance towards the exploitation of this promising technology.

“Renewables are, in fact, much more reliable than power based on extraction, since those energy models require continuous new inputs to avoid a crash, whereas once the initial investment has been made in renewable energy infrastructure, nature provides the raw materials for free.”

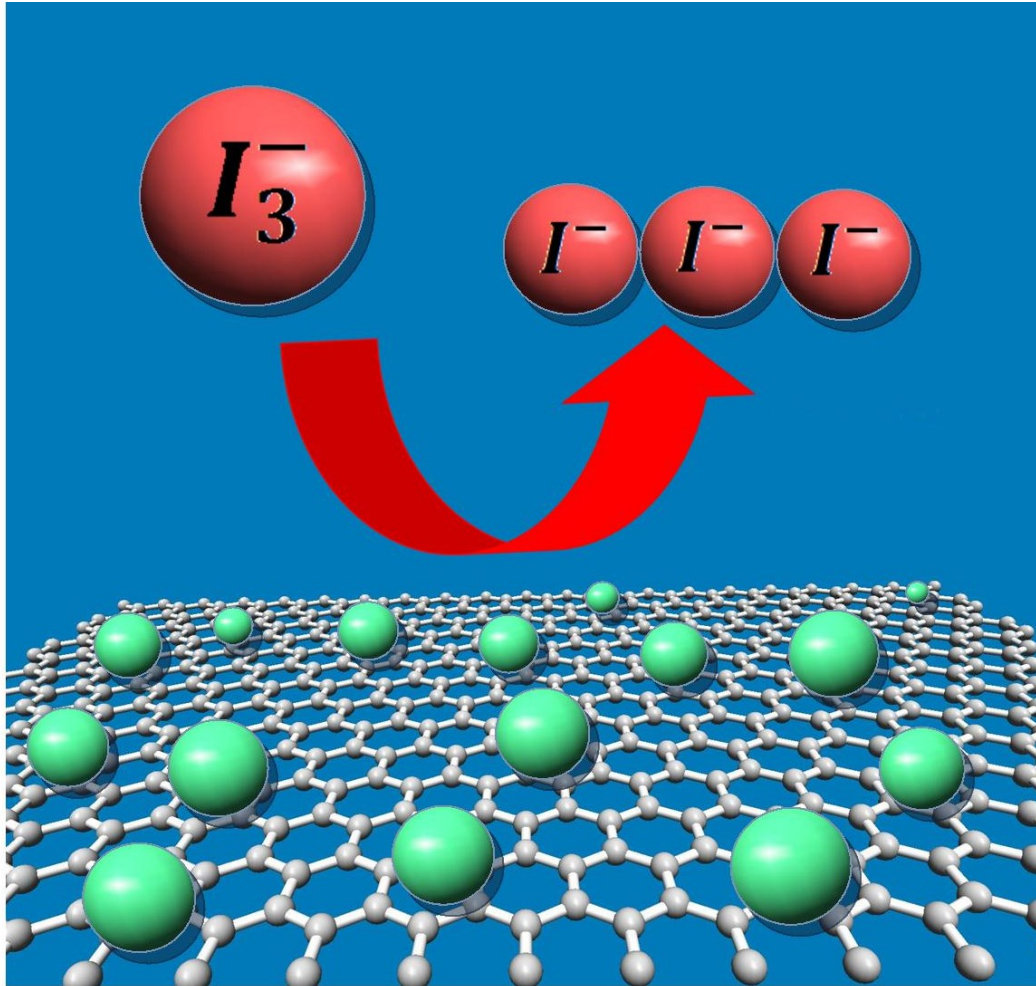
Naomi Klein

CHAPTER 5

CuS-graphene nanocomposite as a transparent conducting oxide and Pt-free counter electrode for dye-sensitized solar cells

*This chapter is adapted from the peer reviewed publication by Mahyar Mohammadnezhad, Gurpreet Singh Selopal, Nasser Alsayyari, Rusoma Akilimali, Fabiola Navarro-Pardo, Zhiming M. Wang, Barry Stansfield, Haiguang Zhao, and Federico Rosei, **Journal of The Electrochemical Society**, 2019, 166 (5) H3065-H3073.*

This chapter presents a simple, fast and highly reproducible single-step procedure for the preparation of TCO and Pt-free CE for DSSCs. Results show that the device assembled with a composite film of CuS-G yields a PCE of 4.83%, which is comparable to the 5.14% PCE of DSSCs based on platinized FTO CEs. Our results demonstrate that the addition of 3.3 vol% of graphene improves the PCE of the cell by about 12% compared with a device based on CEs made of pristine CuS. A similar performance of as-prepared nanocomposite thin film is mainly attributed to small series resistance and good catalytic performance toward the reduction of the tri-iodide electrolyte.



4.5 Introduction

A DSSC typically consists of a nano-structured semiconductor film deposited on a FTO transparent conductive glass as an electron transporter, dye molecules as a light harvester, a redox couple electrolyte as the hole transport medium, and a Pt coated FTO as a CE [20–24]. It is well known that the PV performance of DSSCs, such as J_{sc} , V_{oc} , FF and PCE are directly related to the quality of all components and processes [24]. Moreover, each part of the device heavily determines the production cost of DSSCs. Thus, during recent years, almost all research efforts have been focused on the modification of each component in order to become this commercially viable technology [52,69]. After decades of attempts, a record PCE of around 14% for DSSCs was obtained

[8]. However, the production cost and stability were not been seriously considered. Chapters 3 and 4 presented the application of a TiO₂-MWCNTs nanocomposite in order to improve the stability of DSSCs.

Among the different components of DSSCs, the CE is the most expensive part. The CE in DSSCs has the important task of collecting electrons from the external circuit and the regeneration of the oxidized iodine/iodide redox couple electrolyte. By improving the catalyst activity of the CE, the FF of the cell rises, which is mainly influenced by the R_s . R_s is related to the charge-transfer resistance at the CE and the electrolyte interface. A lower value of charge-transfer resistance at the interface of the CE and electrolyte signifies considerable electron transfer for the reduction of the electrolyte at the catalytic interfaces of the CE [25,82,165].

In this type of device, Pt coated on FTO/glass is the most common CE due to the following reasons: (i) high conductivity for charge transport; (ii) excellent stability towards the iodine/iodide redox couple electrolyte; and (iii) high catalytic activity [166,167]. Pt as a noble metal and the TCO glass accounts for more than 40% of the total device cost [25–27]. However, the corrosion behaviour of noble metals, such as Pt, Au and Ag, in a liquid electrolyte such as a cobalt redox couple is another concern [69,168]. Therefore, the design and fabrication of alternative TCO and Pt-free CEs for DSSCs without reducing electrocatalytic activity represents a major challenge for large scale commercialization of this promising solar energy conversion technology. Degradation of the catalytic activity of the CE increases the charge transfer resistance and consequent incomplete reduction of the electrolyte, thus reducing the short circuit current density and the FF [52].

In recent years, different types of materials, such as transition metal sulfides, conductive polymers, conductive fibers and carbon materials, have been tested as alternatives to the Pt/FTO CE to DSSCs [26,27,166,169,170]. Carbon nanomaterials on FTO substrate CEs show comparable device efficiency with a Pt-based CE, due to the electronic conductivity, high catalytic activity and cost-effectiveness [54,73,82,171]. Lee et al. [172] examined the possibility of bamboolike-structured MWCNTs as the CE of DSSCs. Their results showed that a CE based on these bamboo-like tubes was comparable to the Pt CE, due to the fast electron kinetics at the defect-rich edge planes along the tube. This electrode exhibits

lower R_{ct} , decreasing from $1.8 \Omega \text{ cm}^{-2}$ to $0.82 \Omega \text{ cm}^{-2}$. The SWCNTs, which have also been investigated as CE materials, have achieved excellent performance in comparison with Pt CE [24]. Several reports have recently demonstrated a facile approach for the deposition of graphene on different substrates as a CE. These approaches prove that, amongst various carbon material-based CEs, graphene is considered more promising [24,25,54,79,82,168,173,174]. However, there are still some unresolved issues for fabrication graphene-based CE, including: reduction in transparency; high deposition temperatures; electrochemical corrosion under persistent cell operation; a limited number of active sites for electrolyte electrocatalysis; and complicated fabrication processes [26,166,173,175]. To overcome these issues, facile approaches have recently focused on production composites made of graphene with functional nanoparticles, such as transition metal sulfides, in order to exploit synergistic effects [24,69,173].

Transition metal sulfides, such as NiS, CoS, CuS, WS and MoS₂, are considered promising materials for potential applications as CEs in DSSCs [25,27,165,169,173,176]. Recently, Patil et al. [177] introduced a simple and reproducible synthesis method for the fabrication of a two-dimensional MoS₂ CE using a low-temperature, wet chemical method. The obtained PCE parameters of the DSSCs based on the MoS₂ as the CE exhibited an excellent PCE of 7.01%, which is comparable to DSSCs with a Pt CE (7.31%). According to EIS characteristics, the obtained R_{ct} values of the MoS₂ and Pt CEs are 18.50 and 22.88 $\Omega \text{ cm}^{-2}$, respectively. Moreover, the R_s value decreased from 26.73 $\Omega \text{ cm}^{-2}$ (Pt) to 23.51 $\Omega \text{ cm}^{-2}$ for the MoS₂ CE. These performances are attributed to: (a) the p-type conductivity of MoS₂; (b) the nanoporous nature of the MoS₂ in contrast to the planar Pt; and (c) higher surface roughness of MoS₂ compared to Pt. Another group proposed a nanocomposite of MoS₂ and graphene (MoS₂/RGO) CE in DSSCs [178]. Their CV results indicated that the addition of graphene increases cathodic current density, due to the increased active surface area of the former. The DSSCs assembled with the MoS₂/RGO CE showed a PCE of 6.04%, which is higher than the bare MoS₂ CE (5.09%). Zhang et al. [170] designed CuS nanosheet networks on the plastic substrates as a completely transparent CE, with remarkable efficiency and mechanical stability under bending tests. DSSCs based on CuS nanosheet networks yield a PCE of 6.38%, which is even higher than Pt/FTO CEs (5.6%). Patil et al. [179] have developed a low temperature, one pot

and solution-processing method to successfully grow a uniform and dense CuS thin film on the FTO substrate as a Pt free CE. The CE based on the CuS thin film demonstrated R_{ct} value of $1.99 \Omega \text{ cm}^{-2}$, which confirmed good electrocatalytic activity towards the reduction of the tri-iodide electrolyte. The R_s of CuS is $7.68 \Omega \text{ cm}^{-2}$, which is comparable with Pt CE $7.46 \Omega \text{ cm}^{-2}$. However, the DSSCs using the CE based on the CuS/FTO thin film exhibit a low PCE compared with the DSSCs based on the Pt/FTO CE (28.2% lower), but this was the initial step to use low-cost materials and a simple processing method for Pt-free CE fabrication. In addition, despite the few reports, the literature on DSSCs with Pt/TCO free CEs is still inadequate. Therefore, it is necessary to explore a TCO and Pt-free CE for the cost-effective commercial fabrication of DSSCs. According to previous reports, fabrication of graphene composites can increase efficiency of the CE through an increase in the electron transfer rate, acting as a spacer between the matrix particles and providing active sites for the electrocatalytic process [25,54,82]. These reports raise the question of whether graphene composites might improve the performance of CuS as a CE for DSSCs. As far as can be confirmed from a review of the relevant literature, using a graphene composited CuS as the CE in DSSCs has not yet been reported.

This chapter provides a description of a synthesized CuS-G nanocomposite film with varying concentrations of graphene on non-conductive glass as a TCO and Pt-free transparent CE in DSSCs. It is shown that the presence of 3.3 vol% of graphene in a CuS matrix leads to ~12% improvement of the PCE of DSSCs compared to the bare CuS, due to the excellent electrocatalytic activity for electrolyte reduction. This observation is confirmed by various characterization techniques, including J-V, transient photovoltage decay, CV and EIS. The morphology and structure of the CEs were investigated by FESEM, XRD and Raman spectroscopy.

4.6 Experimental

Copper nitrate trihydrate (CNTH) [$\text{Cu}(\text{NO}_3)_2 \cdot 3\text{H}_2\text{O}$], thioacetamide (TAA) ($\text{C}_2\text{H}_5\text{NS}$), acetone and ethanol were obtained from Sigma-Aldrich. Graphene microplatelets were purchased from Cheaptubes. Other materials such as TiO_2 , dye and the electrolyte were

prepared as described in Chapters 2 and 3. All materials were used as received, without further purification.

CuS CEs were fabricated using a solution method. In brief, glass substrates were ultrasonically cleaned in water, acetone and isopropanol for 20 minutes each, then dried with nitrogen gas. A coating solution was prepared by dissolving 3 mmol of CNTH in 25 mL ethanol, then sonicated for 40 minutes. Additionally, 7.5 mmol of TAA was dissolved in 25 mL ethanol and sonicated for 30 minutes. In the subsequent step, two prepared solutions, TAA and CNTH, were mixed together during 2.5 hours of sonication. A graphene suspension was prepared by adding 10 mg of graphene powder to 20 mL ethanol, followed by sonication for three hours. The final solution was prepared by the addition of different volume percentages of the graphene suspension to the CuS solution: CuS-2G (2 vol%), CuS-3G (3.3 vol%), CuS-6G (6.6 vol%), CuS-10G (10 vol%). The films were grown on the surface of the pre-cleaned glass substrates that were submerged in the solution inside a glass tube that was tilted at an angle of 45-60 degrees. The glass tube was then sealed and kept in a water bath maintained at 95 °C for 2 hours. The coated film on the bottom-facing side of the glass substrates was then sintered at 100 °C for 15 minutes to ensure removal of all organic substances. The Pt CEs were prepared by 10 nm deposition of the Pt on the pre-cleaned FTO/glass substrate, using an RF magnetron sputtering system (Kurt J. Lesker, CM818) under argon atmosphere. The DSSC device was fabricated, according to the method described in Chapters 2 and 3, by using different CEs.

The morphology of the deposited films was evaluated by AFM (Veeco Enviroscope) and SEM (FE-SEM, JEOL JSM-6900 F) equipped with an EDS. The phase identification of the CuS film was analyzed using GIXRD in a Bruker D8 Advance X-ray diffractometer equipped with Cu K_{α} radiation. EIS was conducted under dark conditions using a SOLARTRON 1260 A by applying bias voltages of 0 to 200 mV. The results of the EIS were fitted and analyzed using an appropriate equivalent circuit model with Z-View software. The chemical bonding of the composite CEs was conducted by XPS using a VG Escalab 220i-XL equipped with an Al K_{α} source. CV was carried out in a Solartron SI 1287 potentiostat galvanostat using a three-electrode system (different CuS-G samples as the working electrode, an Ag/AgCl reference electrode and a Pt plate as the CE), at a

scan of 10 mVs^{-1} . The electrolyte used for this measurement was a diluted I^-/I_3^- redox couple electrolyte in acetonitrile (20 times). The J-V graph of the fabricated cells was obtained using a Keithley 2400 Source Meter under simulated sunlight with an ABET2000 solar simulator at AM 1.5G (100 mW cm^{-2}).

4.7 Results and discussion

4.7.1 Microstructure evaluation

In DSSCs, a reduction of the electrolyte takes place on the surface of the CE, therefore the formation of a uniform and dense layer of the catalyst material has an obvious effect on the electrocatalytic property. A defect-free architecture with high surface areas improves the transfer of the electron from the surface of the CE to the electrolyte. Optical transparency is one of the main aspects to be considered for CEs in DSSCs [82]. Figure 5.1(a) shows a photograph of the CuS-G composite film coated on the glass substrate, which exhibits high optical transparency of the film and highlights the film homogeneity. Figure 5.1(b)-(g) shows the SEM images of the bare CuS and CuS-G hybrid nanocomposite films on the glass substrate with different concentrations of graphene. As observed in these images, the CuS film grows homogeneously on the surface of a glass substrate that is composed of continuous and uniform crystalline grains with an average diameter of $\sim 0.34 \mu\text{m}$ and standard deviation=0.014. In the composite samples, it is quite challenging to detect graphene, due to the low contrast of carbon material as well as the very low concentration and uniform distribution of graphene sheets between the CuS nanoparticles. The microstructure of bare CuS [Figure 5.1 (b)-(c)] and CuS-3G [Figure 5.1 (d)-(e)] are similar and homogeneous, with no defect or crack. In contrast, the surface of the sample with a high concentration of graphene (CuS-10G) exhibits deep cracks and holes [Figure 5.1 (f)-(g)]. These results suggest that the high concentration of graphene causes the formation of micro-cracks, likely due to the strong Van der Waals interaction between the graphene sheets [180]. The formation of these defects in the CE can reduce the electron charge transport and electrocatalytic properties of the CE [54,73,82]. This was further verified by performing photovoltaic and carrier dynamics characterization.

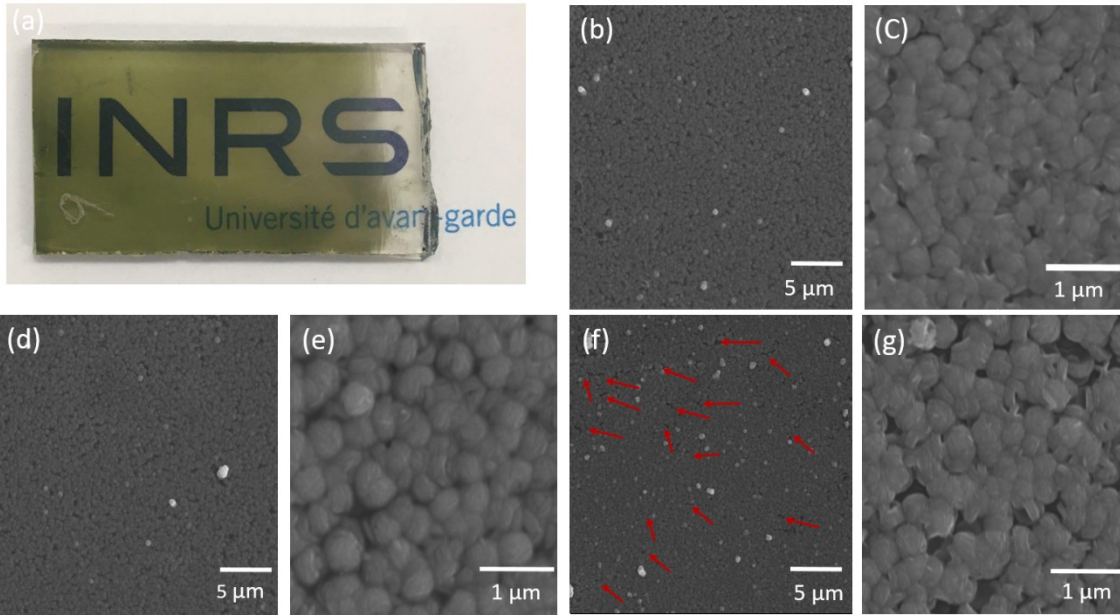


Figure 5.1 (a) Photograph of the CuS-3G composite film. SEM images of CuS film with various concentrations of graphene at different magnifications: (b)-(c) bare CuS-0G; (d)-(e) CuS-3G; (f)-(g) CuS-10G. Red arrows indicate the microcrack areas.

The chemical composition of the as-prepared CEs was further determined by the EDS, as shown in Figure 5.2. EDS analysis confirms the uniform distribution of Cu, S and C elements on the surfaces of the two samples, namely bare CuS and CuS-3G nanocomposite. The peaks of different elements in the selected zones (red square) and elemental quantitative data indicate that the copper to sulfur ratio is consistent with CuS. In addition, this measurement confirms CuS-G nanocomposite formation by the presence of the C peak that is related to the graphene. The oxygen and silicon content in the EDS spectra are related to the glass substrate.

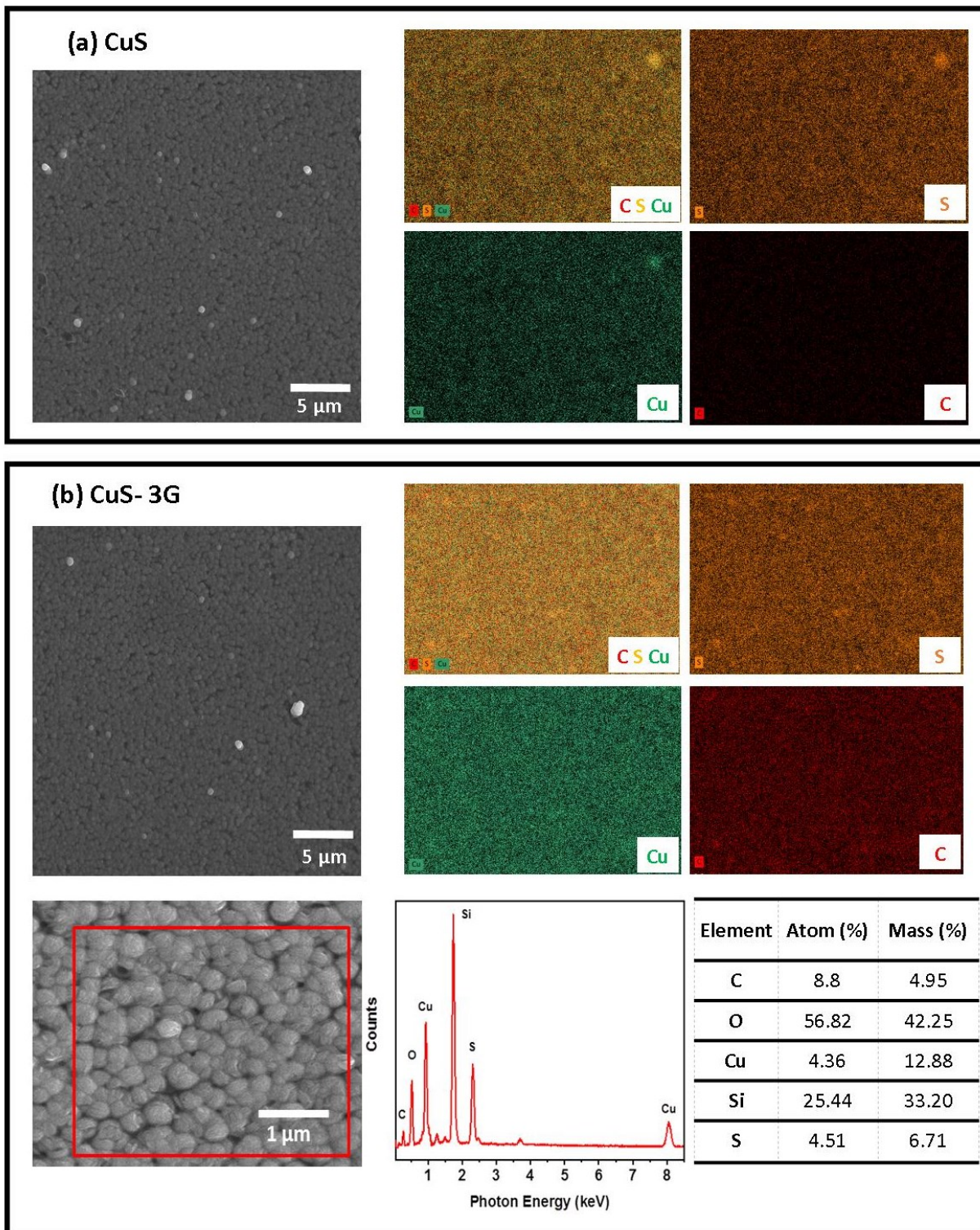


Figure 5.2 EDS mapping of as-prepared CEs, (a) CuS and (b) CuS-3G nanocomposites. EDS spectra and measurement of chemical composition are taken from the red squared zones.

4.7.2 Surface characterizations of CuS-3G nanocomposite

To identify the characteristics of the as-prepared CuS-3G nanocomposite CE sample, XRD measurements were carried out. The diffraction pattern displays eight characteristic peaks at 27° , 27.7° , 29.3° , 32.7° , 47.9° , 52.6° , 59.4° , which correspond to the crystal planes of (1 0 0), (1 0 1), (1 0 2), (1 0 3), (0 0 6), (1 1 0), (1 0 8), (1 1 6). As can be seen, no peak is related to impurities in the XRD pattern. All peaks match well with the values in the standard card of the CuS hexagonal phase (JCPDS 06-0464), as can be observed in Figure 5.3. XRD results indicated that the CuS particles are the main constituent of the CuS-3G composite film because there is no diffraction peak that corresponds to graphene [169,181]. These results confirm the excellent crystallinity of CuS and the homogeneous dispersion of graphene sheets in a CuS-3G composite CE [182,183].

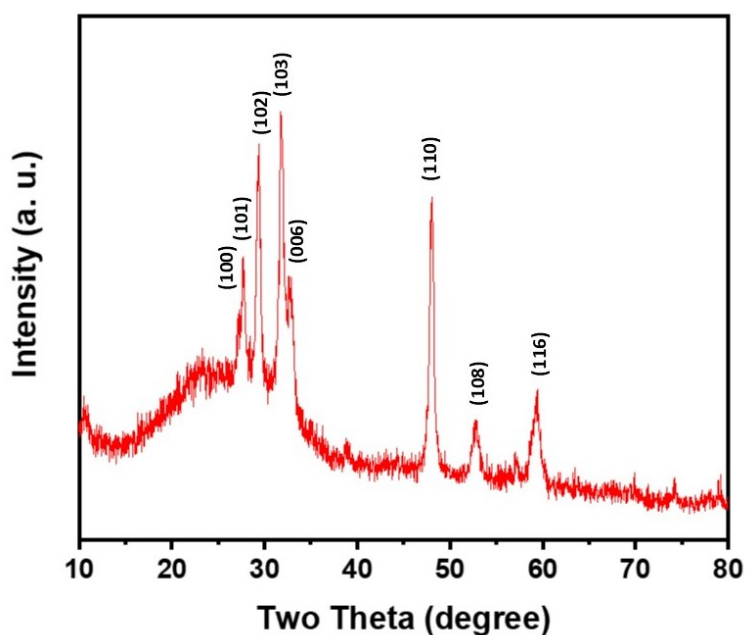


Figure 5.3 XRD pattern of as-prepared CuS-3G nanocomposites.

Important information on the surface elemental composition of the CuS-3G nanocomposite products can be further provided by XPS. As shown in Figure 5.4 (a), the survey spectrum shows the peaks of the C, O, S and Cu elements with no extra peak related to the impurities. To verify chemical composition and chemical binding of the elements, three main peaks, namely C, Cu and S, were investigated by acquiring high

resolution spectra. The C1s spectrum deconvoluted into four different peaks. The peaks at binding energies of 284.7 eV can be assigned to C-C and C=C bonds. Furthermore, three peaks at 286.5, 288.4 and 289.9 eV are attributed to bonding between carbon and oxygen atoms by a single bond and by a double bond [165,177,181,182]. High-resolution XPS spectra of Cu 2P show the binding energies of Cu 2P_{3/2} and Cu 2P_{1/2} peaks at 932.1 and 952.1 eV, respectively. The weak shake-up satellite line at approximately 942.5 eV is also visible, which indicates the paramagnetic chemical state of Cu²⁺ [181]. All Cu peaks are characteristic of Cu (II) in the composite of CuS-3G [181,184]. In Figure 5.4 (c), the Auger line of Cu at 568.3 eV, which is the typical value for CuS, indicates that there is low concentration of Cu(I) [183]. High-resolution spectrum in the S2p region can be fitted with two main peaks that are S2P_{3/2} at 162 eV and S2P_{1/2} at 163.3 eV, which is a typical value for metal sulphides, as can be observed from Figure 5.4 (e) [181,184]. All the above XPS results are well matched with the reported values and support the XRD results that a nanocomposite CuS-G has been successfully synthesized on the glass substrate [173,182–184].

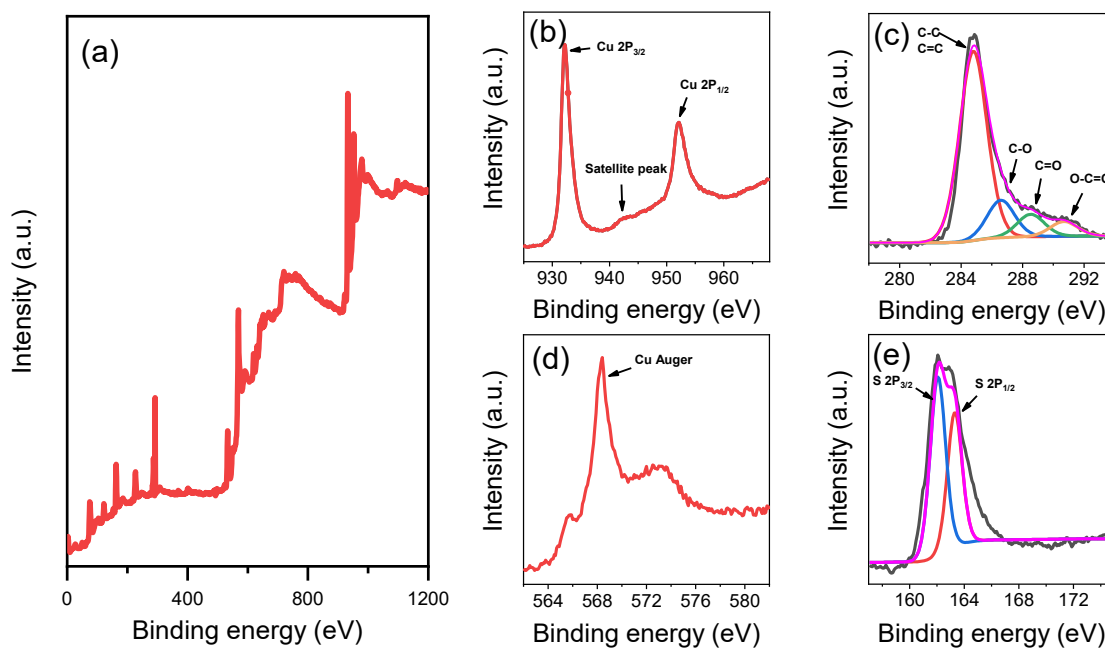


Figure 5.4 XPS plots of the CuS-3G composite film: (a) Survey; (b) Carbon; (c) Cu; (d) Auger Cu; and (e) Sulfur.

4.7.3 PV performance of the DSSC fabricated CuS-G nanocomposite CEs

To investigate the performance of CuS as a CE of DSSCs, five series of cells based on CuS-graphene nanocomposite CEs with different concentrations of graphene were fabricated as part of the present work. Figure 5.5 (a) and Table 5.1 display the J-V curves and calculated PV parameters that were obtained under one sun simulated sunlight at AM 1.5G (100 mW cm^{-2}) of DSSCs with different CEs, respectively. As presented, the device assembled with a CuS CE yields a PCE of 4.31%. The results show that the PCE of the DSSC is improved with the addition of a graphene sheet in CuS. The best PCE was found to be 4.83% for DSSCs based on the CuS-3G composite CE reaching the maximum values of 10.33 mA cm^{-2} and 708 mV for J_{sc} and V_{oc} , respectively. As displayed in Figure 5.5 (b)-(c), the moderate increase in PCE of the optimized device is mainly attributed to the increased functional parameters, including J_{sc} , V_{oc} and FF. The increase in functional parameters may be attributed to the effective dispersion of graphene within the CuS nanoparticles [25,173]. The enhancement in the CE-electrolyte interface may be another reason for improving the J_{sc} (discussed later) [25,26,165]. The high surface area and conductivity can increase the electrocatalytic activity of the CE and faster electrolyte reduction [165]. The DSSC assembled with a CuS-10G CE displays a much lower PCE (3.96%) compared to the CuS-3G (4.83%). Based on Table 5.1, this may be mainly ascribed to the lower functional parameters, which originate from the non-uniform CuS thin film on the glass substrate with different defects such as deep cracks and holes [see Figure 5.1 (f)-(g)]. In DSSCs, the CE not only serves as catalyzing electrolyte reduction, but also as conducting film toward the collection of electrons from the external circuit [54,73,82]. Therefore, in order to obtain high efficiency DSSCs, a good quality film with high surface area and without defects, especially cracks and holes, is necessary for electron transfer, catalytic reaction and fast regeneration of the electrolyte [54,171]. According to the J-V results, CuS-3G nanocomposite film exhibits the best PV performance.

Table 5.1. Functional parameters of DSSCs fabricated using different CuS-G nanocomposite CEs.

Sample	PCE (%)	FF (%)	V_{oc} (mV)	J_{sc} (mA cm^{-2})
CuS	4.3 \pm 0.15	67 \pm 2	688 \pm 10	9.4 \pm 0.2
CuS-2G	4.3 \pm 0.15	66 \pm 2	693 \pm 10	9.5 \pm 0.2
CuS-3G	4.8 \pm 0.15	66 \pm 2	708 \pm 10	10.3 \pm 0.2
CuS-6G	4.5 \pm 0.15	66 \pm 2	692 \pm 10	9.8 \pm 0.2
CuS-10G	3.9 \pm 0.15	63 \pm 2	694 \pm 10	9.0 \pm 0.2

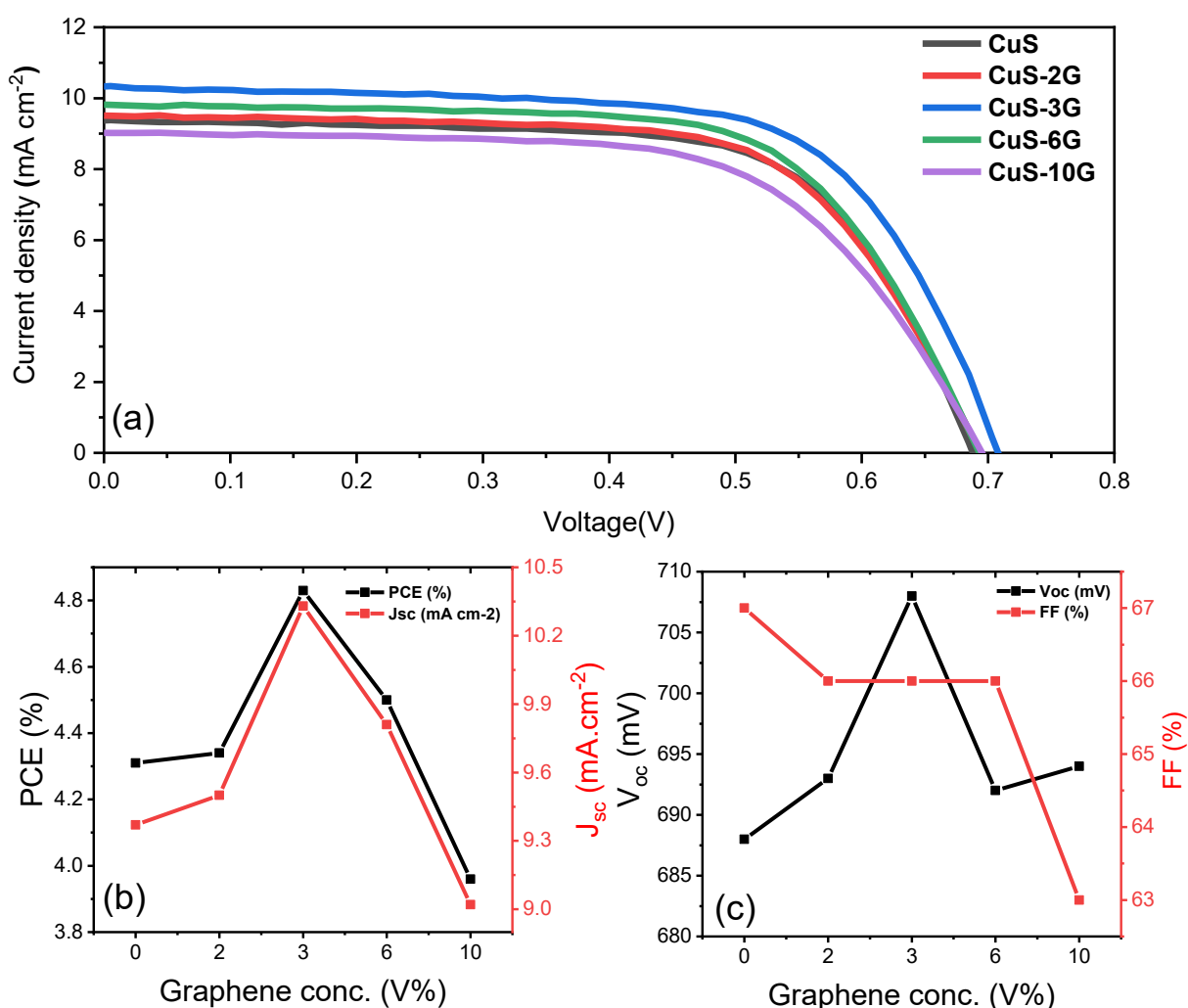


Figure 5.5 (a) Current density-voltage curves of the DSSCs under one sun simulated sunlight at AM 1.5G (100 mW cm^{-2}) fabricated using different CEs. Variation of the photovoltaic parameters of the corresponding devices: (b) PCE (%) and J_{sc} (mA cm^{-2}); (c) V_{oc} (mV) and FF (%).

According to Durrant [132], in DSSCs, optimization of the structure of the CE is a crucial factor in increasing recombination resistance and electron lifetime. The photovoltage decay of DSSCs assembled with different CEs is shown in Figure 5.6 (a). Among all the fabricated DSSCs, the photovoltage decay rate is highest for CuS-10G CEs and lowest for the device based on CuS-3G CE. The recombination process and τ_e of the DSSCs are investigated using transient photovoltage decay, as previously discussed in Chapters 2 and 3. The calculated τ_e curves of DSSCs based on different CEs are shown in Figure 5.6 (b). At a particular value of V_{oc} (0.15 V), the obtained τ_e follows the trend of CuS-3G > CuS-0G > CuS-10G, which is consistent with the obtained PV performance. This difference in photovoltage decay and τ_e is mainly attributed to the electrocatalytic activities of the prepared CEs, as all other components of the devices are similar. The highest τ_e of the DSSCs based on CuS-3G is due to the continuous, uniform and defect-free film with a high active surface area. Meanwhile, the devices based on CuS-10G CE show a shorter lifetime compared to the others, which means that the addition of a large amount of graphene causes a sharp decline in the CE performance. The reduction of the electron lifetime on the DSSC based on the CuS-10G CE can be related to defect formation that could hinder charge transfer, resulting in a very large electron recombination, in agreement with PV performance results.

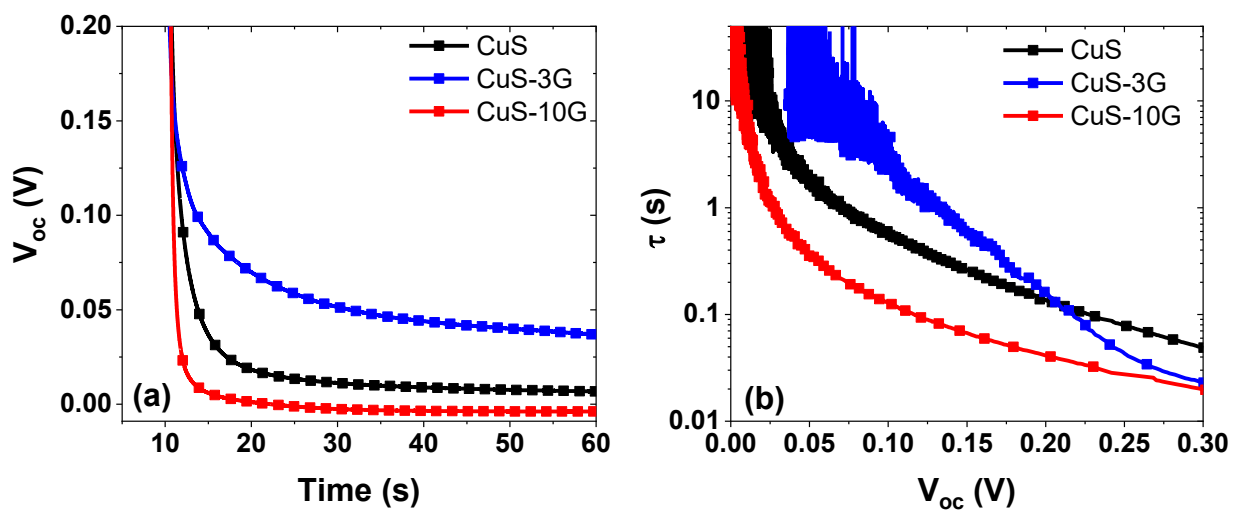


Figure 5.6 (a) Transient V_{oc} decay and (b) obtained electron lifetime (τ_e) for DSSCs fabricated using different CEs.

CV is a very powerful technique for further elucidating the catalytic activities of the prepared CEs. The CV measurements for three prepared CEs, namely CuS, CuS-3G and CuS-10G, are compared in Figure 5.7. CV characterization was obtained in the standard three-electrode system composed of a working electrode (here, CuS, CuS-3G and CuS-10G CEs), a Pt CE and a reference electrode (Ag/AgCl). The CV curves demonstrated two pairs of redox peaks. The peak at negative potential relates to the reduction reaction at electrolyte ($I_3^- + 2e^- \rightarrow 3I^-$) while the other at more positive potential corresponds to the oxidation reaction at electrolyte ($3I^- \rightarrow I_3^- + 2e^-$) [176,178]. The CuS-3G film on the glass substrate exhibited a higher current density when compared to the CuS, due to the higher electrical conductivity of the graphene composite sample [26,73,177]. The reduction of triiodide is faster with the CuS-3G nanocomposite compared with the CuS and CuS-10G, indicating excellent electrocatalytic activity of the CuS-3G composite sample [170]. Compared with the CuS and CuS-3G CEs, the current density of the CuS-10G is the lowest, which can be attributed not only to the lower electrical conductivity but also to the lesser active surface area on the non-uniform CuS thin film with some deep cracks and holes. The CE with poor electrocatalytic activity means less over potential for an electron transferring at the CE electrolyte interface, which may introduce the possibility of electron-hole recombination. This is in agreement with the results of the PV performance where the CuS-10G CE shows low-ranking electrocatalytic activity for electrolyte reduction compared to the CuS-3G CEs.

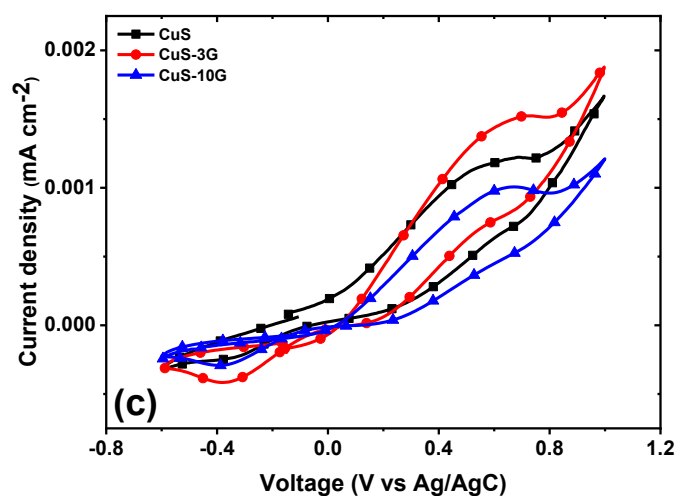


Figure 5.7 Cyclic voltammogram for the standard three-electrode system using different CEs.

4.7.4 DSSCs based on Pt and optimized CuS-3G CEs

A deeper understanding of the performance of the synthesized electrode was obtained by comparing the functional parameters of the DSSCs assembled with Pt and CuS-3G CEs. Figure 5.8 presents a comparison of the J-V curves obtained under similar conditions: one sun simulated sunlight at AM 1.5G (100 mW cm^{-2}) and 25°C , of DSSCs fabricated with Pt and CuS-3G CEs. The results show that the device with optimized CuS-3G nanocomposite on the glass substrate CE exhibited an excellent PCE of 4.83%, which is close to the PCE of DSSCs based on platinized FTO CEs (5.14%). DSSCs based on Pt and CuS CEs exhibit a similar FF, namely 67% and 66% respectively, suggesting that almost similar electrocatalytic properties are offered by the CuS CE (Table 5.2) [176]. However, the results indicate that the obtained photocurrent density for the Pt CE (10.86 mA cm^{-2}) was slightly higher than the device based CuS-3G CE (10.33 mA cm^{-2}). The CuS based CEs demonstrate a transparent behaviour while the Pt CE shows a mirror-like surface with high reflectivity. Thus, Pt CE is expected to reflect the unabsorbed portion of the incident light back to the photoanode and enhance the light-harvesting efficiency of the DSSCs [178]. This might be a possible concurring reason for the higher J_{sc} value in the DSSC assembled with Pt CE compared to the device based CuS-3G CE. The obtained V_{oc} value is approximately similar ($\sim 700 \text{ mV}$) for the two devices.

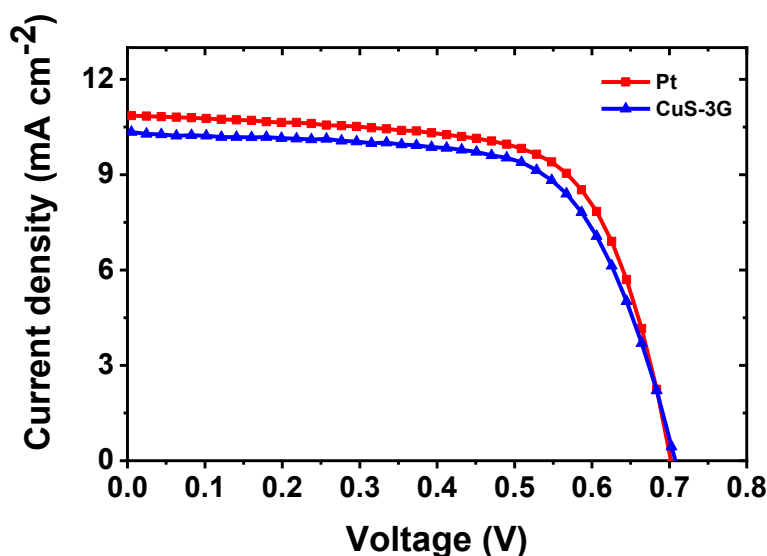


Figure 5.8 Current density-voltage curves of solar cells under one sun simulated sunlight at AM 1.5G (100 mW cm^{-2}) fabricated using Pt and CuS-3G composite CEs.

Table 5.2. Functional parameters of DSSCs with different Pt and CuS-3G CEs.

Sample	PCE (%)	FF (%)	V _{oc} (mV)	J _{sc} (mA cm ⁻²)
Pt	5.1±0.15	67±2	702±10	10.8±0.25
CuS-3G	4.8±0.15	66±2	708±10	10.3±0.25

The obtained CV curves of the Pt and CuS-3G CEs for the iodide/triiodide electrolyte are shown in Figure 5.9. The CV measurements show that the curve of the two samples exhibit two pairs of redox peaks. The anodic and cathodic peak separation of the Pt CE was slightly lower than that of the CuS-3G nanocomposite electrodes. However, the current densities in the redox peaks of the CuS-3G nanocomposite electrode are higher than those of the Pt, suggesting great electrocatalytic activity of the CuS-3G as the CE in a DSSC. This may be attributed to the higher electrical conductivity of the graphene composite electrode as well as to the improved surface area from the higher surface roughness (discussed later in more detail) [26,73,177].

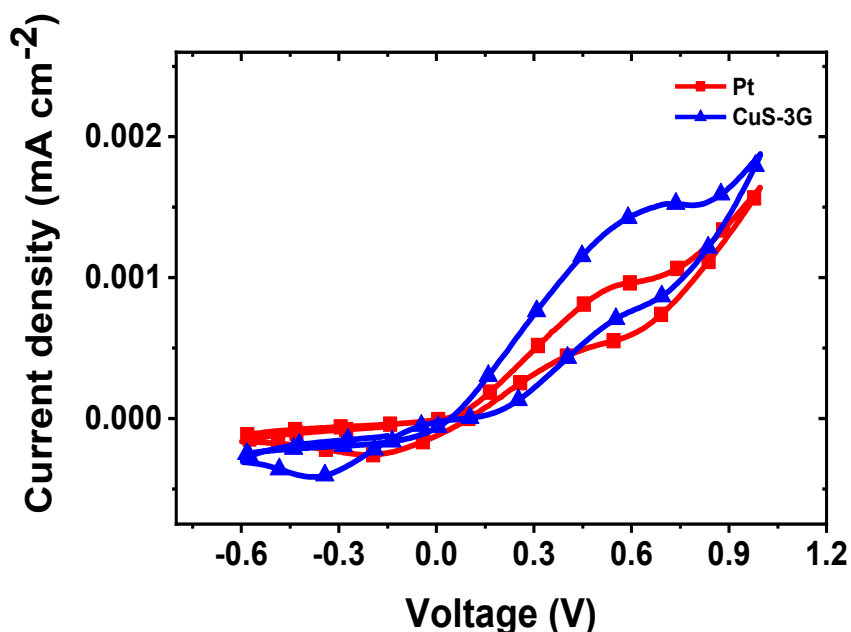


Figure 5.9 Cyclic voltammogram of Pt and CuS-3G composite CEs.

To further confirm the investigation into the electrocatalytic activity of the produced CEs from the CV results, EIS analysis was performed with a sealed symmetric cell with Pt and CuS-3G CEs. The obtained Nyquist plots and related parameters are shown in Figure 5.10 and Table 5.3. The intercept of the semicircle on the real axis is assigned to the R_s , where the value of the produced CuS-3G nanocomposite is very close to that of the sputtered Pt electrode. Moreover, the R_{ct} of the CE is another important factor that affects the PV performance of the DSSC and which can be obtained from EIS. R_{ct} can be assigned to the resistance of charge transfer at the electrode-electrolyte interface [25,177,178]. The results of the R_{ct} for the two devices with Pt and CuS-3G CEs indicate that the R_{ct} of the CuS-3G nanocomposite cell is lower than that of the cell assembled with Pt CE, which is mainly caused by the increase in the active catalytic surface area of the CuS-3G composite CE. These electrochemical measurements indicate that the CuS-3G nanocomposite CE shows superior electrocatalytic activity for electrolyte reduction, which is in good agreement with the similar values of FF. These results indicate that the CuS-3G nanocomposite CE on the glass substrate is comparable to that of the platinized FTO CEs.

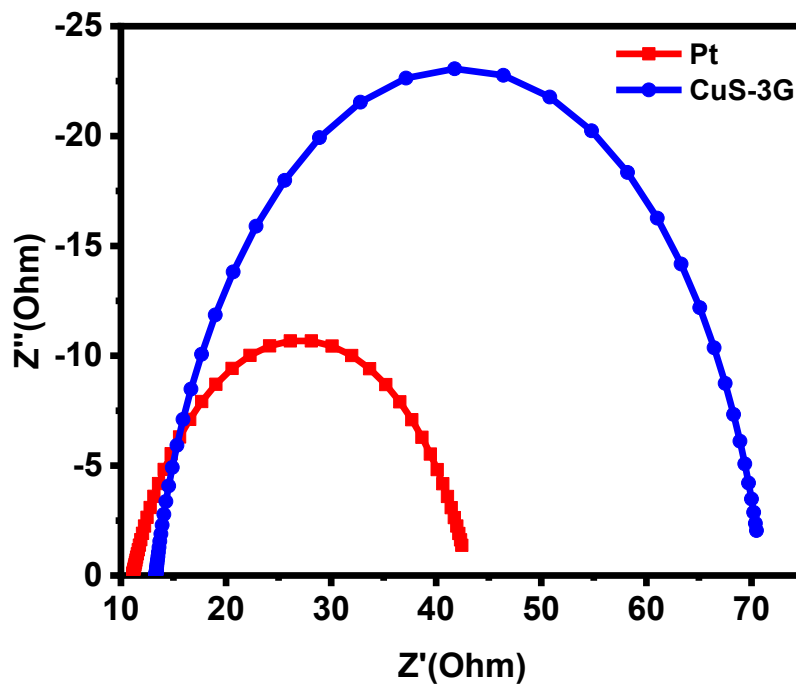


Figure 5.10 Electrochemical impedance spectroscopy analysis of the Pt and CuS-3G composite CEs.

Table 5.3. Comparison of R_s (Ω) and R_{ct} (Ω) calculated from EIS measurements of symmetric cell configuration of spin coated CuS-3G composite and Platinum CEs.

Types of CEs	CuS-3G	Pt
R_s (Ω)	13.6 \pm 0.8	11.2 \pm 0.8
R_{ct} (Ω)	68 \pm 4	25 \pm 4

Surface roughness and morphology have a crucial effect on the catalytic activities of the CEs [54]. The rough structure with a high surface area is beneficial for the catalytic reaction [73,176,178]. AFM is a powerful technique for investigating the surface morphology and topography. Figure 5.11 shows the AFM observation of the CuS-3G nanocomposite and Pt CEs. As can be observed, the surface of the CuS-3G nanocomposite is fully covered with a dense crystalline layer. The analysis of the AFM images demonstrates that the roughness of the CuS-3G nanocomposite layer on the glass substrate is 38 nm, which is more than two times higher than that of platinized FTO (17 nm). This evidence shows that the electrocatalytic activity of the CuS-3G nanocomposite as a CE for DSSCs is comparable with Pt.

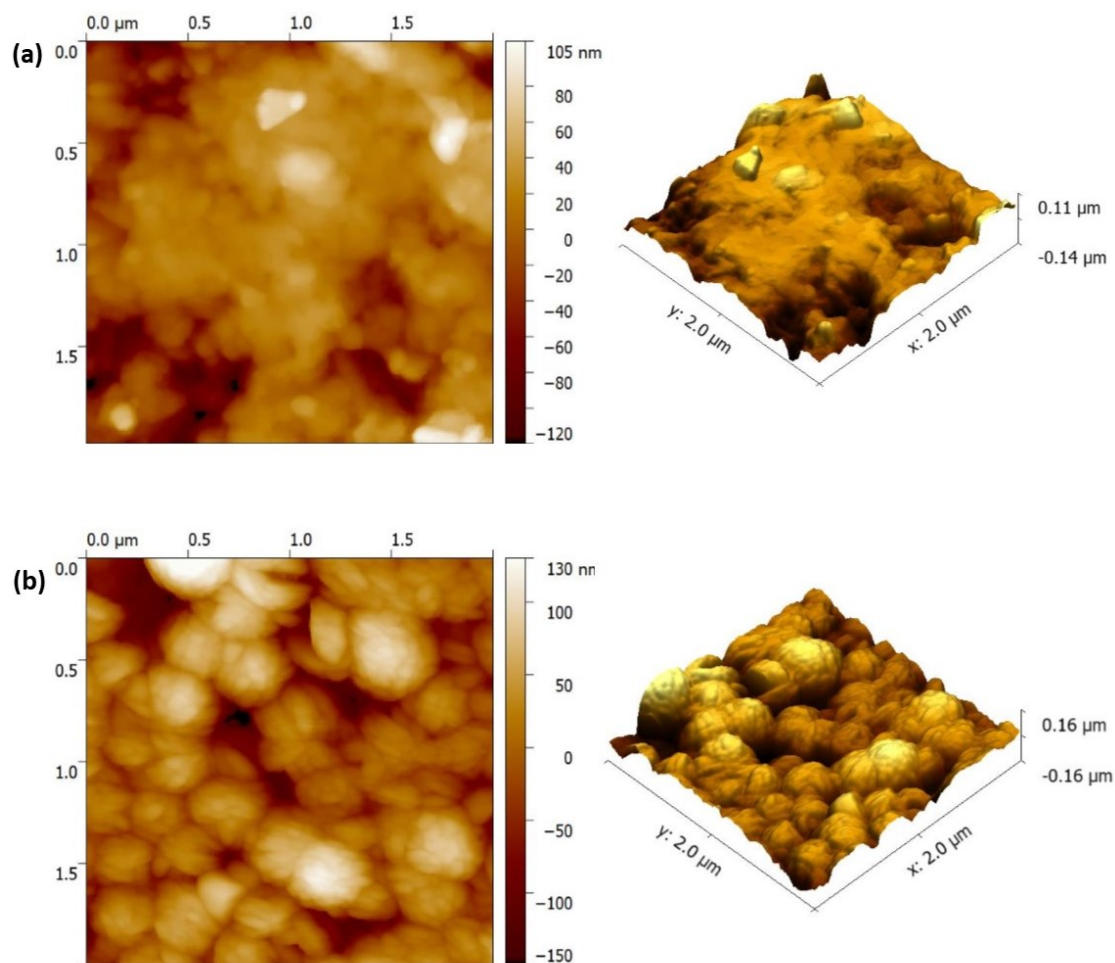


Figure 5.11 AFM images of: (a) Pt/FTO and (b) CuS-3G/Glass composite film.

One important aspect of solar cell commercialization is high reproducibility without large batch-to-batch variations. Upon reinstating the previous operating conditions for DSSCs, 12 independent cells based on the CuS-3G nanocomposite and Pt CEs were made over six different batches to ensure data manufacturability. Figure 5.12 shows the PV parameters, including, J_{sc} , V_{oc} , FF and PCE, of all tested devices. This measurement reports similar functional parameters for cells with Pt and CuS-3G CEs within the different batches, which confirms the remarkable reproducibility of the investigated solar cells.

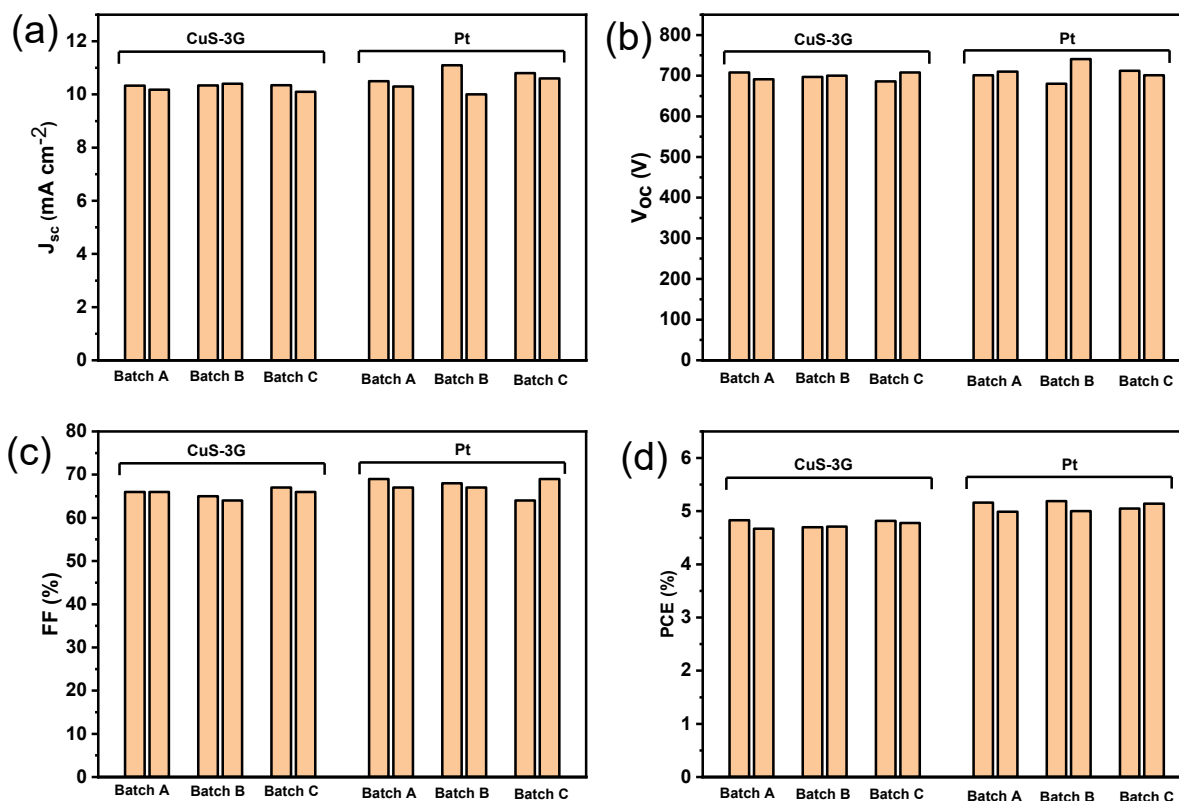


Figure 5.12 Statistics (a) J_{sc} (mA cm^{-2}); (b) V_{oc} (mV); (c) FF (%); and (d) PCE (%) of 12 devices as collected over 6 different batches.

4.8 Conclusions and Perspectives

This chapter presents a description of a fast and highly reproducible solution-processable approach to synthesizing crystalline and uniform CuS-G nanocomposite thin film on glass substrates as a CE of DSSCs. XRD, XPS and EDS measurements verify the formation of a CuS-G nanocomposite with uniform distribution of graphene sheets between CuS particles. Electrochemical analysis demonstrated that CuS-G nanocomposite thin films have good catalytic ability towards the reduction of the tri-iodide electrolyte. A PCE of 4.83% is achieved for the DSSC employing an optimized CuS-G nanocomposite with high reproducibility under one sun simulated sunlight at AM 1.5G (100 mW cm^{-2}), which is comparable to that using the Pt CE (5.14%). The results of this study provide a low cost, simple and interesting method for producing TCO and Pt free electrodes as prospective candidates to replace highly expensive platinized FTO CEs, due to their excellent

electrochemical catalytic activities and, most importantly, the ease of fabrication at low temperatures.

Conclusions and perspectives

5.1 Conclusions

DSSCs are a promising alternative to conventional silicon solar cells. However, the drive to improve stability and reduce costs is of the utmost importance for this technology. This thesis focused on the development of a carbonaceous nanomaterial composite to enhance long-term stability and decrease fabrication cost of DSSCs.

In the case of DSSCs, the processes that govern cell operation are quite well understood as a result of more than two decades of scientific research. However, there remain many questions regarding the degradation of this device under different environmental stimuli. Chapters 3 and 4 focus on the effect of the addition of MWCNTs to a TiO_2 anode on the long-term stability of DSSCs. It has been demonstrated that PV performance of DSSCs sharply declines under continuous light illumination that is mainly attributed to increased recombination and charge transfer resistance. In contrast, the results demonstrate that the presence of MWCNTs effectively suppresses the degradation of the PV parameters in DSSCs, without any considerable reduction of the electron lifetime. The microstructure evaluation indicates that, after stability tests, the cell without MWCNTs shows micro-crack formation in the photoanode, which could be the main reason for increased charge transport resistance. The composite device shows a stable anode structure during the test with no cracks or any defects that could be related to the interaction between the MWCNTs and the TiO_2 particles. In the device based TiO_2 -MWCNT nanocomposite anode, the MWCNTs provide a conductive network to improve charge transport and suppress electron recombination. The results of this work indicate that the degradation rate of DSSCs is high under UV irradiation because the components of the device are very sensitive to UV light. MWCNTs can increase the stability of the cells under UV light

exposure because they can partially absorb and block UV light. The UV light may introduce crystalline defects (energetically deep electron traps) in the surface of the TiO₂ nanocrystals, which are identified as a limiting factor for electron transport.

The present work also reports the effect of incorporating MWCNTs on the thermal stability of DSSCs. The microstructural observation indicates that thermal stress gives rise to long cracks and loss of connection between TiO₂ nanoparticles. Thermal stress leads to desorption of dye molecules from the surface of the TiO₂ nanoparticles, which can be considered as one of the most critical reasons for the degradation of DSSCs upon thermal aging. However, the addition of MWCNTs offers an approximate three-fold improvement to the stability of DSSCs under thermal stress. MWCNTs also improve bond strength between TiO₂ nanoparticles. MWCNTs are able to prevent the degradation of the photoanode during thermal stress due to the unusually high thermal conductivity that makes them one of the most promising candidate materials for thermally stable composites.

Chapter 5 provided a synthesis of a CuS-G nanocomposite film on a glass substrate as the TCO and Pt-free CE in DSSCs. A CE made of Pt coated on a FTO/glass substrate, which is still the most widely used, accounts for more than 40% of the total device cost. Therefore, the design and fabrication of TCO and Pt-free CEs for DSSCs represents a major challenge for the commercial deployment of this technology. This work demonstrates that the PV performance and electrocatalytic activity of a CuS-G CE grown on a glass substrate with a low temperature and solution-processable approach is comparable to that obtained using “standard” Pt CEs. A microstructure evaluation displays the formation of continuous, uniform crystalline grains and a completely crack-free composite film. An investigation of the PV performance of DSSCs based on a CuS-G nanocomposite CE shows that the PCE improves about 12% with the addition of graphene concentration, which is comparable to the PCE of DSSCs based on platinized FTO CEs. The synthesized composite electrode exhibits excellent electrocatalytic activity as the CE in a DSSC system, mainly attributed to the increased high surface area and conductivity of the CE by graphene addition.

5.2 Perspectives

Although this work rigorously investigates degradation mechanisms and physical properties of the photoanode and CE, there is still scope for further fruitful exploration and improvement.

Chapter 3 describes the degradation mechanisms of bare and composite DSSCs. However, regeneration of DSSCs is a potentially interesting topic. MWCNTs and other carbon nanomaterials may increase the regeneration of DSSCs. A composite blocking layer with carbonaceous nanomaterials also offers an interesting study topic in terms of obtaining high UV stability due to their properties as an efficient absorbing and blocking agent for UV light. Replacement of the electrolyte with solid-state hole transporting materials may further improve the stability of DSSCs based on the MWCNTs-TiO₂ nanocomposite anode.

Chapter 4 provides a description of the effect of MWCNTs on the thermal stability of DSSCs. Under real conditions, solar cells simultaneously experience two types of stimuli (thermal and light). The combination of light and thermal stress alters the physical and chemical properties of material systems and therefore impacts device behavior. Hence, it is important to study light and elevated temperature induced degradation of DSSCs composited with MWCNTs.

Chapter 5 describes the electrocatalytic activity of the CuS-G nanocomposite as a CE for DSSCs. The results show great potential for the development of a TCO and Pt free electrodes in electrochemical reactions for DSSCs, which in turn will pave the way towards the development of a new low cost and efficient CE. Although the superior PEC performance in fabricated devices is illustrated in this work, the effect of film thickness and grain size, which could be optimized to improve device performance, are not discussed. A study of the degradation mechanisms of the CuS-G nanocomposite film could be a useful contribution for the future design of an efficient CE.

References

- [1] J. Gong, K. Sumathy, Q. Qiao, Z. Zhou, Review on dye-sensitized solar cells (DSSCs): Advanced techniques and research trends, *Renew. Sustain. Energy Rev.* 68 (2017) 234–246. doi:10.1016/J.RSER.2016.09.097.
- [2] G.R. Timilsina, L. Kurdgelashvili, P.A. Narbel, Solar energy: Markets, economics and policies, *Renew. Sustain. Energy Rev.* 16 (2012) 449–465. doi:10.1016/j.rser.2011.08.009.
- [3] R. Banos, F. Manzano-Agugliaro, F.G. Montoya, C. Gil, A. Alcayde, J. Gomez, Optimization methods applied to renewable and sustainable energy: A review, *Renew. Sustain. Energy Rev.* 15 (2011) 1753–1766. doi:10.1016/j.rser.2010.12.008.
- [4] L. Suganthi, A.A. Samuel, Energy models for demand forecasting-A review, *Renew. Sustain. Energy Rev.* 16 (2012) 1223–1240. doi:10.1016/j.rser.2011.08.014.
- [5] B. O'Regan, M. Gratzel, A Low-Cost, High-Efficiency Solar-Cell Based on Dye-Sensitized Colloidal TiO₂ Films, *Nature.* 353 (1991) 737–740. doi:10.1038/353737a0.
- [6] J. Gong, J. Liang, K. Sumathy, Review on dye-sensitized solar cells (DSSCs): Fundamental concepts and novel materials, *Renew. Sustain. Energy Rev.* 16 (2012) 5848–5860. doi:10.1016/j.rser.2012.04.044.
- [7] M. Gratzel, Photoelectrochemical cells, *Nature.* 414 (2001) 338–344. doi:10.1038/35104607
- [8] K. Kakiage, Y. Aoyama, T. Yano, K. Oya, J. Fujisawa, M. Hanaya, Highly-efficient dye-sensitized solar cells with collaborative sensitization by silyl-anchor and carboxy-anchor dyes, *Chem. Commun.* 51 (2015) 15894–15897. doi:10.1039/C5CC06759F.
- [9] P.M. Sommeling, M. Spath, H.J.P. Smit, N.J. Bakker, J.M. Kroon, Long-term stability testing of dye-sensitized solar cells, *J. Photochem. Photobiol. A Chem.* 164 (2004) 137–144. doi:10.1016/j.jphotochem.2003.12.017.

- [10] H. Pettersson, T. Gruszecki, Long-term stability of low-power dye-sensitized solar cells prepared by industrial methods, *Sol. Energy Mater. Sol. Cells*. 70 (2001) 203–212. doi:10.1016/S0927-0248(01)00025-3.
- [11] R. Harikisun, H. Desilvestro, Long-term stability of dye solar cells, *Sol. Energy*. 85 (2011) 1179–1188. doi:10.1016/j.solener.2010.10.016.
- [12] E. Leonardi, S. Penna, T.M. Brown, A. Di Carlo, A. Reale, Stability of dye-sensitized solar cells under light soaking test, *J. Non. Cryst. Solids*. 356 (2010) 2049–2052. doi:10.1016/j.jnoncrysol.2010.05.072.
- [13] C.H. Kwak, J.H. Baeg, I.M. Yang, K. Giribabu, S. Lee, Y.S. Huh, Degradation analysis of dye-sensitized solar cell module consisting of 22 unit cells for thermal stability: Raman spectroscopy study, *Sol. Energy*. 130 (2016) 244–249. doi:10.1016/j.solener.2016.02.017.
- [14] K.T. Dembele, G.S. Selopal, R. Milan, C. Trudeau, D. Benetti, A. Soudi, M.M. Natile, G. Sberveglieri, S. Cloutier, I. Concina, F. Rosei, A. Vomiero, Graphene below the percolation threshold in TiO₂ for dye-sensitized solar cells, *J. Mater. Chem. A*. 3 (2015) 2580–2588. doi:10.1039/C4TA04395B.
- [15] K.T. Dembele, G.S. Selopal, C. Soldano, R. Nechache, J.C. Rimada, I. Concina, G. Sberveglieri, F. Rosei, A. Vomiero, Hybrid Carbon Nanotubes–TiO₂ Photoanodes for High Efficiency Dye-Sensitized Solar Cells, *J. Phys. Chem. C*. 117 (2013) 14510–14517. doi:10.1021/jp403553t.
- [16] M.E. Yeoh, K.Y. Chan, Recent advances in photo-anode for dye-sensitized solar cells: a review, *Int. J. Energy Res.* 41 (2017) 2446–2467. doi: 10.1002/er.3764.
- [17] S. Sun, L. Gao, Y. Liu, Enhanced dye-sensitized solar cell using graphene-TiO₂ photoanode prepared by heterogeneous coagulation, *Appl. Phys. Lett.* 96 (2010) 083113. doi:10.1063/1.3318466.
- [18] M.Y. Yen, M.C. Hsiao, S.H. Liao, P.I. Liu, H.M. Tsai, C.C.M. Ma, N.W. Pu, M. Der Ger, Preparation of graphene/multi-walled carbon nanotube hybrid and its use as photoanodes of dye-sensitized solar cells, *Carbon N. Y.* 49 (2011) 3597–3606. doi:10.1016/j.carbon.2011.04.062.

- [19] N. Yang, J. Zhai, D. Wang, Y. Chen, L. Jiang, Two-dimensional graphene bridges enhanced photoinduced charge transport in dye-sensitized solar cells, *ACS Nano*. 4 (2010) 887–894. <http://dx.doi.org/10.1021/nn901660v>.
- [20] K. Basu, H. Zhang, H. Zhao, S. Bhattacharya, F. Navarro-Pardo, P.K. Datta, L. Jin, S. Sun, F. Vetrone, F. Rosei, Highly stable photoelectrochemical cells for hydrogen production using a SnO₂-TiO₂/quantum dot heterostructured photoanode, *Nanoscale*. 10 (2018) 15273–15284. doi:10.1039/C8NR02286K.
- [21] K. Basu, D. Benetti, H. Zhao, L. Jin, F. Vetrone, A. Vomiero, F. Rosei, Enhanced photovoltaic properties in dye sensitized solar cells by surface treatment of SnO₂ photoanodes, *Sci. Rep.* 6 (2016) 1–10. <http://dx.doi.org/10.1038/srep23312>.
- [22] S.K. Matta, K. Kakiage, S. Makuta, A. Veamatahau, Y. Aoyama, T. Yano, M. Hanaya, Y. Tachibana, Dye-Anchoring Functional Groups on the Performance of Dye-Sensitized Solar Cells: Comparison between Alkoxysilyl and Carboxyl Groups, *J. Phys. Chem. C*. 118 (2014) 28425–28434. doi:10.1021/jp5088338.
- [23] T. Daeneke, A.J. Mozer, Y. Uemura, S. Makuta, M. Fekete, Y. Tachibana, N. Koumura, U. Bach, L. Spiccia, Dye Regeneration Kinetics in Dye-Sensitized Solar Cells, *J. Am. Chem. Soc.* 134 (2012) 16925–16928. doi:10.1021/ja3054578.
- [24] S. Yun, Y. Liu, T. Zhang, S. Ahmad, Recent advances in alternative counter electrode materials for Co-mediated dye-sensitized solar cells, *Nanoscale*. 7 (2015) 11877–11893. doi:10.1039/c5nr02433a.
- [25] G. Yue, J. Lin, S. Tai, Y. Xiao, J. Wu, A catalytic composite film of MoS₂/graphene flake as a counter electrode for Pt-free dye-sensitized solar cells, *Electrochim. Acta*. 85 (2012) 162–168. doi:10.1016/j.electacta.2012.08.040.
- [26] H. Kim, G. Veerappan, J.H. Park, Conducting Polymer Coated Non-woven Graphite Fiber Film for Dye-Sensitized Solar Cells: Superior Pt-and FTO-Free Counter Electrodes, *Electrochim. Acta*. 137 (2014) 164–168. doi:10.1016/j.electacta.2014.06.012.
- [27] Z. Xu, T. Li, Q. Liu, F. Zhang, X. Hong, S. Xie, C. Lin, X. Liu, W. Guo, Controllable and large-scale fabrication of rectangular CuS network films for indium tin oxide-

- and Pt-free flexible dye-sensitized solar cells, *Sol. Energy Mater. Sol. Cells.* 179 (2018) 297–304. doi:10.1016/j.solmat.2017.12.024.
- [28] K.H. Solangi, M.R. Islam, R. Saidur, N.A. Rahim, H. Fayaz, A review on global solar energy policy, *Renew. Sustain. Energy Rev.* 15 (2011) 2149–2163. doi:10.1016/j.rser.2011.01.007.
- [29] L. Pérez-Lombard, J. Ortiz, C. Pout, A review on buildings energy consumption information, *Energy Build.* 40 (2008) 394–398. doi:10.1016/j.enbuild.2007.03.007.
- [30] N.S. Lewis, D.G. Nocera, Powering the planet: Chemical challenges in solar energy utilization, *Proc. Natl. Acad. Sci.* 103 (2006) 15729–15735. doi:10.1073/pnas.0603395103.
- [31] R. Eisenberg, D.G. Nocera, Overview of the Forum on Solar and Renewable Energy, *Inorg. Chem.* 44 (2005) 6799–6801. doi:10.1021/ic0580083.
- [32] A. Kumar, G. Richhariya, A. Sharma, Solar Photovoltaic Technology and Its Sustainability, in: *Green Energy Technol.*, 2015. doi:10.1007/978-81-322-2337-5.
- [33] M.S. Dresselhaus, I.L. Thomas, Alternative energy technologies, *Nature.* 414 (2001) 332–337. <https://doi.org/10.1038/35104599>.
- [34] A.E. Becquerel, Mémoire sur les effets électriques produits sous l'influence des rayons solaires, *Comptes Rendus l'Academie Des Sci.* 9 (1839) 561–567.
- [35] P. Werfel, *Physics of Solar Cells*, WILEY-VCH Verlag GmbH, 2005.
- [36] A. Luque, S. Hegedus, *Handbook of Photovoltaic Science and Engineering*, John Wiley & Sons, Ltd., 2011.
- [37] C.E. Fritts, On a new form of selenium cell, and some electrical discoveries made by its use, *Am. J. Sci.* 26 (1883) 465–472.
- [38] D.M. Chapin, C.S. Fuller, G.L. Pearson, A New Silicon p-n Junction Photocell for Converting Solar Radiation into Electrical Power, *J. Appl. Phys.* 25 (1954) 676–677. doi:10.1063/1.1721711.
- [39] M.A. Green, Third Generation Photovoltaics: Ultra-high Conversion Efficiency at Low Cost, *Prog. Photovoltaics Res. Appl.* 9 (2001) 123–135. doi:10.1002/pip.360.

- [40] Y. Kuang, M. Di Vece, J.K. Rath, L. Van Dijk, R.E.I. Schropp, Elongated nanostructures for radial junction solar cells, *Reports Prog. Phys.* 76 (2013) 106502. doi:10.1088/0034-4885/76/10/106502.
- [41] M.T. Kibria, A. Ahammed, S.M. Sony, F. Hossain, Shams-UI-Islam, A Review : Comparative studies on different generation solar cells technology, *Int. Conf. Environ. Asp. Bangladesh.* (2014) 51–53.
- [42] M. Gratzel, Dye-Sensitized Solar Cells, *J. Photochem. Photobiol. C Photochem. Rev.* 110 (2010) 6595–6663. doi:10.1016/S1389-5567(03)00026-1.
- [43] N.R.E.L. (NREL), Best Research-Cell Efficiencies, 2020.
- [44] H.T. H. Gerischer, M.E. Michel-Beyerle, F. Rebertus, Sensitization of charge injection into semiconductors with large band gap, *Electrochim. Acta.* 13 (1968) 1509–1515.
- [45] U.B. R. Memming, F. Schröppel, Sensitized oxidation of water by tris (2,2'-bipyridyl) ruthenium at SnO₂ electrodes, *J. Electroanal. Chem. Interfacial Electrochem.* 100 (1979) 307–318.
- [46] R. Memming, Photochemical processes in monomolecular dye layers on SnO₂, *Faraday Discuss. Chem. Soc.* 58 (1974) 261–270. doi:10.1039/DC9745800261.
- [47] R. Memming, F. Schröppel, Electron transfer reactions of excited ruthenium (II) complexes in monolayer assemblies at the SnO₂-water interface, *Chem. Phys. Lett.* 62 (1979) 207–210.
- [48] H. Tsubomura, M. Matsumura, Y. Nomura, T. Amamiya, Dye sensitised zinc oxide: aqueous electrolyte: platinum photocell, *Nature.* 261 (1976) 402–403. doi:10.1038/261402a0.
- [49] S. Yun, P.D. Lund, A. Hinsch, Stability assessment of alternative platinum free counter electrodes for dye-sensitized solar cells, *Energy Environ. Sci.* 8 (2015) 3495–3514. doi:10.1039/c5ee02446c.
- [50] M. Gratzel, Dye-sensitized solar cells, *J. Photochem. Photobiol. C Photochem. Rev.* 4 (2003) 145–153. doi:10.1016/S1389-5567(03)00026-1.

- [51] M. Batmunkh, M.J. Biggs, J.G. Shapter, Carbon Nanotubes for Dye-Sensitized Solar Cells, *Small*. 11 (2015) 2963–2989. doi:10.1002/sml.201403155.
- [52] G. Syrokostas, A. Siokou, G. Leftheriotis, P. Yianoulis, Degradation mechanisms of Pt counter electrodes for dye sensitized solar cells, *Sol. Energy Mater. Sol. Cells*. 103 (2012) 119–127. doi:10.1016/j.solmat.2012.04.021.
- [53] Y. Huang, G. Luo, M. Huang, J. Wu, Z. Lan, L. Fan, J. Lin, Electrolytes in Dye-Sensitized Solar Cells, *Chem. Rev.* 115 (2015) 2136–2173. doi:10.1021/cr400675m.
- [54] M.Z. Iqbal, S. Khan, Progress in the performance of dye sensitized solar cells by incorporating cost effective counter electrodes, *Sol. Energy*. 160 (2018) 130–152. doi:10.1016/j.solener.2017.11.060.
- [55] R. Katoh, A. Furube, Electron injection efficiency in dye-sensitized solar cells, *J. Photochem. Photobiol. C Photochem. Rev.* 20 (2014) 1–16. doi:10.1016/j.jphotochemrev.2014.02.001.
- [56] A. Vogler, H. Kunkely, Photochemistry induced by metal-to-ligand charge transfer excitation, *Coord. Chem. Rev.* 208 (2000) 321–329. doi:10.1016/S0010-8545(99)00246-5.
- [57] A. Vogler, H. Kunkely, Photoreactivity of metal-to-ligand charge transfer excited states, *Coord. Chem. Rev.* 177 (1998) 81–96. doi:10.1016/S0010-8545(98)00131-3.
- [58] T. Marinado, K. Nonomura, J. Nissfolk, M.K. Karlsson, D.P. Hagberg, L. Sun, S. Mori, A. Hagfeldt, How the Nature of Triphenylamine-Polyene Dyes in Dye-Sensitized Solar Cells Affects the Open-Circuit Voltage and Electron Lifetimes, *Langmuir*. 26 (2010) 2592–2598. doi:10.1021/la902897z.
- [59] F. Fabregat-Santiago, J. Bisquert, E. Palomares, L. Otero, D. Kuang, S.M. Zakeeruddin, M. Gratzel, Correlation between Photovoltaic Performance and Impedance Spectroscopy of Dye-Sensitized Solar Cells Based on Ionic Liquids, *J. Phys. Chem. C*. 111 (2007) 6550–6560. doi:10.1021/jp066178a.
- [60] D. Gentilini, D. D’Ercole, A. Gagliardi, A. Brunetti, A. Reale, T. Brown, A. Di Carlo,

- Analysis and simulation of incident photon to current efficiency in dye sensitized solar cells, *Superlattices Microstruct.* 47 (2010) 192–196. doi:10.1016/J.SPMI.2009.10.005.
- [61] M. Adachi, M. Sakamoto, J. Jiu, Yukio Ogata, S. Isoda, Determination of Parameters of Electron Transport in Dye-Sensitized Solar Cells Using Electrochemical Impedance Spectroscopy, *J. Phys. Chem. B.* 110 (2006) 13872–13880. doi:10.1021/JP061693U.
- [62] J. Bisquert, Theory of the Impedance of Electron Diffusion and Recombination in a Thin layer, *J. Phys. Chem. B.* 106 (2002) 325–333. doi:10.1021/jp011941g.
- [63] M.I. Asghar, K. Miettunen, J. Halme, P. Vahermaa, M. Toivola, K. Aitola, P. Lund, Review of stability for advanced dye solar cells, *Energy Environ. Sci.* 3 (2010) 418–426. doi:10.1039/b922801b.
- [64] A. Zaban, M. Greenshtein, J. Bisquert, Determination of the electron lifetime in nanocrystalline dye solar cells by open-circuit voltage decay measurements, *ChemPhysChem.* 4 (2003) 859–864. doi:10.1002/cphc.200200615.
- [65] C. Xiang, C.A. Okonkwo, Q. Xiong, L. Wang, L. Jia, A novel TiO₂ film photoanode decorated with spirulina-derived residual groups for enhanced photocurrent in dye-sensitized solar cells, *Sol. Energy.* 134 (2016) 461–467. doi:10.1016/j.solener.2016.05.020.
- [66] J. Poortmans, V. Arkhipov, *Thin Film Solar Cells Fabrication, Characterization and Applications*, JohnWiley & Sons Ltd, 2006.
- [67] A. Akbari, J. Hashemi, J. Niskanen, S. Huotari, M. Hakala, Identification of the dye adsorption modes in dye-sensitized solar cells with X-ray spectroscopy techniques: a computational study, *Phys.Chem.Chem.Phys.* 17 (2015) 10849–10855. doi:10.1039/c4cp05980h.
- [68] B. Li, L. Wang, B. Kang, P. Wang, Y. Qiu, Review of recent progress in solid-state dye-sensitized solar cells, *Sol. Energy Mater. Sol. Cells.* 90 (2006) 549–573. doi:10.1016/J.SOLMAT.2005.04.039.
- [69] M. Ye, X. Wen, M. Wang, J. Iocozzia, N. Zhang, C. Lin, Z. Lin, Recent advances in

- dye-sensitized solar cells: from photoanodes, sensitizers and electrolytes to counter electrodes, *Mater. Today*. 18 (2015) 155–162. doi:10.1016/J.MATTOD.2014.09.001.
- [70] E. Figgemeier, A. Hagfeldt, Are dye-sensitized nano-structured solar cells stable? An overview of device testing and component analyses, *Int. J. Photoenergy*. 6 (2004) 127–140. doi:10.1155/S1110662X04000169.
- [71] Y. Bai, Y. Cao, J. Zhang, M. Wang, R. Li, P. Wang, S.M. Zakeeruddin, M. Gratzel, High-performance dye-sensitized solar cells based on solvent-free electrolytes produced from eutectic melts, *Nat. Mater.* 7 (2008) 626–630. <https://doi.org/10.1038/nmat2224>.
- [72] S. Shalini, R. Balasundara prabhu, S. Prasanna, T.K. Mallick, S. Senthilarasu, Review on natural dye sensitized solar cells: Operation, materials and methods, *Renew. Sustain. Energy Rev.* 51 (2015) 1306–1325. doi:10.1016/J.RSER.2015.07.052.
- [73] S. Yun, P.D. Lund, A. Hinsch, Stability assessment of alternative platinum free counter electrodes for dye-sensitized solar cells, *Energy Environ. Sci.* 8 (2015) 3495–3514. doi:10.1039/c5ee02446c.
- [74] K. Miettunen, I. Asghar, X. Ruan, J. Halme, T. Saukkonen, P. Lund, Stabilization of metal counter electrodes for dye solar cells, *J. Electroanal. Chem.* 653 (2011) 93–99. doi:10.1016/j.jelechem.2010.12.022.
- [75] H.W. Kroto, J.R. Heath, S.C. O'Brien, R.F. Curl, R.E. Smalley, C60: Buckminsterfullerene, *Nature*. 318 (1985) 162–163. doi:10.1038/318162a0.
- [76] S. Iijima, Helical microtubules of graphitic carbon, *Nature*. 354 (1991) 56–58. doi:10.1038/354056a0.
- [77] <https://www.nobelprize.org/prizes/physics/2010/summary/>
- [78] M. Janani, P. Srikrishnarka, S. V. Nair, A.S. Nair, An in-depth review on the role of carbon nanostructures in dye-sensitized solar cells, *J. Mater. Chem. A*. 3 (2015) 17914–17938. doi:10.1039/C5TA03644E.

- [79] L.J. Brennan, M.T. Byrne, M. Bari, Y.K. Gun'ko, Carbon nanomaterials for dye-sensitized solar cell applications: A bright future, *Adv. Energy Mater.* 1 (2011) 472–485. doi:10.1002/aenm.201100136.
- [80] H. Zhu, J. Wei, K. Wang, D. Wu, Applications of carbon materials in photovoltaic solar cells, *Sol. Energy Mater. Sol. Cells.* 93 (2009) 1461–1470. doi:10.1016/j.solmat.2009.04.006.
- [81] J. Chen, B. Li, J. Zheng, J. Zhao, Z. Zhu, Role of Carbon Nanotubes in Dye-Sensitized TiO₂-Based Solar Cells, *J. Phys. Chem. C.* 116 (2012) 14848–14856. doi:10.1021/jp304845t.
- [82] S. Thomas, T.G. Deepak, G.S. Anjusree, T.A. Arun, S. V. Nair, A.S. Nair, A review on counter electrode materials in dye-sensitized solar cells, *J. Mater. Chem. A.* 2 (2014) 4474–4490. doi:10.1039/c3ta13374e.
- [83] I.C. Maurya, P. Srivastava, L. Bahadur, Dye-sensitized solar cell using extract from petals of male flowers *Luffa cylindrica* L. as a natural sensitizer, *Opt. Mater. (Amst).* 52 (2016) 150–156. doi:10.1016/J.OPTMAT.2015.12.016.
- [84] <https://www.chemistryviews.org>.
- [85] K. John, *Electron Microscopy*, Humana Press Inc., 2007.
- [86] B.J. Inkson, Scanning electron microscopy (SEM) and transmission electron microscopy (TEM) for materials characterization, *Materials Characterization Using Nondestructive Evaluation (NDE) Methods.* (2016) 17-43.
- [87] D.B. Williams, C.B. Carter, *Transmission Electron Microscopy*, Springer US, Boston, MA, 1996. doi:10.1007/978-1-4757-2519-3_1.
- [88] K. van Benthem, S.J. Pennycook, A.Z. Mohammad Saliqur Rahman, Atomic Resolution Characterization of Semiconductor Materials by Aberration-Corrected Transmission Electron Microscopy, *Ref. Modul. Mater. Sci. Mater. Eng.* (2017). doi:10.1016/B978-0-12-803581-8.10405-9.
- [89] P. Linkov, M. Artemyev, A.E. Efimov, I. Nabiev, Comparative advantages and limitations of the basic metrology methods applied to the characterization of

- nanomaterials, *Nanoscale*. 5 (2013) 8781–8798. doi:10.1039/C3NR02372A.
- [90] C. Zeng, C. Vitale-Sullivan, X. Ma, In Situ Atomic Force Microscopy Studies on Nucleation and Self-Assembly of Biogenic and Bio-Inspired Materials, *Minerals*. 7 (2017) 1–18. doi:10.3390/min7090158.
- [91] <https://phys.libretexts.org>.
- [92] F. Kang, H. Konno, X-ray Photoelectron Spectroscopy, in: *Mater. Sci. Eng. Carbon*, Butterworth-Heinemann, 2016: pp. 153–171. doi:10.1016/B978-0-12-805256-3.00008-8.
- [93] <https://www.phii.com/surface-analysis-techniques/xps-esca.html>.
- [94] A.G. Milekhin, L.L. Sveshnikova, T.A. Duda, N.A. Yeryukov, E.E. Rodyakina, A.K. Gutakovskii, S.A. Batsanov, A.V. Latyshev, D.R.T. Zahn, Surface-enhanced Raman spectroscopy of semiconductor nanostructures, *Phys. E Low-Dimensional Syst. Nanostructures*. 75 (2016) 210–222. doi:10.1016/J.PHYSE.2015.09.013.
- [95] M. Fan, G.F.S. Andrade, A.G. Brolo, A review on the fabrication of substrates for surface enhanced Raman spectroscopy and their applications in analytical chemistry, *Anal. Chim. Acta*. 693 (2011) 7–25. doi:10.1016/J.ACA.2011.03.002.
- [96] E. V. Efremov, F. Ariese, C. Gooijer, Achievements in resonance Raman spectroscopy: Review of a technique with a distinct analytical chemistry potential, *Anal. Chim. Acta*. 606 (2008) 119–134. doi:10.1016/J.ACA.2007.11.006.
- [97] K.J.I. Ember, M.A. Hoeve, S.L. McAughtrie, M.S. Bergholt, B.J. Dwyer, M.M. Stevens, K. Faulds, S.J. Forbes, C.J. Campbell, Raman spectroscopy and regenerative medicine: a review, *Npj Regen. Med*. 2 (2017) 1–12. doi:10.1038/s41536-017-0014-3.
- [98] R.A. Viscarra Rossel, R.N. McGlynn, A.B. McBratney, Determining the composition of mineral-organic mixes using UV–vis–NIR diffuse reflectance spectroscopy, *Geoderma*. 137 (2006) 70–82. doi:10.1016/J.GEODERMA.2006.07.004.
- [99] S.G. Kumar, L.G. Devi, Review on Modified TiO₂ Photocatalysis under UV/Visible Light: Selected Results and Related Mechanisms on Interfacial Charge Carrier

- Transfer Dynamics, *J. Phys. Chem. A.* 115 (2011) 13211–13241. doi:10.1021/jp204364a.
- [100] M. Mahbuburrahman, N. Chandradebnath, J.J. Lee, Electrochemical Impedance Spectroscopic Analysis of Sensitization-Based Solar Cells, *Isr. J. Chem.* 55 (2015) 990–1001. doi:10.1002/ijch.201500007.
- [101] Q. Wang, M. Gratzel, Electrochemical Impedance Spectroscopic Analysis of Dye-Sensitized Solar Cells, *J. Phys. Chem. B.* 109 (2005) 14945–14953.
- [102] N. Elgrishi, K.J. Rountree, B.D. McCarthy, E.S. Rountree, T.T. Eisenhart, J.L. Dempsey, A Practical Beginner's Guide to Cyclic Voltammetry, *J. Chem. Educ.* 95 (2018) 197–206. doi:10.1021/acs.jchemed.7b00361.
- [103] H. Ren, H. Shao, L. Zhang, D. Guo, Q. Jin, R. Yu, L. Wang, Y. Li, Y. Wang, H. Zhao, D. Wang, A New Graphdiyne Nanosheet/Pt Nanoparticle-Based Counter Electrode Material with Enhanced Catalytic Activity for Dye-Sensitized Solar Cells, *Adv. Energy Mater.* 5 (2015) 1–6. doi:10.1002/aenm.201500296.
- [104] L. Yi, Y. Liu, N. Yang, Z. Tang, H. Zhao, G. Ma, Z. Su, D. Wang, One dimensional CuInS₂–ZnS heterostructured nanomaterials as low-cost and high-performance counter electrodes of dye-sensitized solar cells, *Energy Environ. Sci.* 6 (2013) 835–840. doi:10.1039/c3ee24176a.
- [105] K.S. Lee, W.J. Lee, N.-G. Park, S.O. Kim, J.H. Park, Transferred vertically aligned N-doped carbon nanotube arrays: use in dye-sensitized solar cells as counter electrodes, *Chem. Commun.* 47 (2011) 4264+4266. doi:10.1039/c1cc10471c.
- [106] D. Benetti, K.T. Dembele, J. Benavides, H. Zhao, S. Cloutier, I. Concina, A. Vomiero, F. Rosei, Functionalized multi-wall carbon nanotubes/TiO₂ composites as efficient photoanodes for dye sensitized solar cells, *J. Mater. Chem. C.* 4 (2016) 3555–3562. doi:10.1039/C6TC00800C.
- [107] R. Saidur, M.R. Islam, N.A. Rahim, K.H. Solangi, A review on global wind energy policy, *Renew. Sustain. Energy Rev.* 14 (2010) 1744–1762. doi:10.1016/j.rser.2010.03.007.
- [108] P. V. Kamat, Meeting the clean energy demand: Nanostructure architectures for

- solar energy conversion, *J. Phys. Chem. C.* 111 (2007) 2834–2860. doi:10.1021/jp066952u.
- [109] C.Y. Yen, Y.F. Lin, S.H. Liao, C.C. Weng, C.C. Huang, Y.H. Hsiao, C.C.M. Ma, M.C. Chang, H. Shao, M.C. Tsai, C.K. Hsieh, C.H. Tsai, F.B. Weng, Preparation and properties of a carbon nanotube-based nanocomposite photoanode for dye-sensitized solar cells, *Nanotechnology.* 19 (2008) 1–9. doi:10.1088/0957-4484/19/37/375305.
- [110] J. Hone, M. Whitney, C. Piskoti, A. Zettl, Thermal conductivity of single-walled carbon nanotubes, *Phys. Rev. B.* 59 (1999) 2514–2516. doi:10.1103/PhysRevB.59.R2514.
- [111] A. Moisala, Q. Li, I.A. Kinloch, A.H. Windle, Thermal and electrical conductivity of single- and multi-walled carbon nanotube-epoxy composites, *Compos. Sci. Technol.* 66 (2006) 1285–1288. doi:10.1016/j.compscitech.2005.10.016.
- [112] J.D. Roy-Mayhew, I.A. Aksay, Graphene Materials and Their Use in Dye-Sensitized Solar Cells, *Chem. Rev.* 114 (2014), 6323–6348. doi:10.1021/cr400412a.
- [113] A.G. Kontos, T. Stergiopoulos, V. Likodimos, D. Milliken, H. Desilvesto, G. Tulloch, P. Falaras, Long-Term Thermal Stability of Liquid Dye Solar Cells, *J. Phys. Chem. C.* 117 (2013) 8636–8646. doi:10.1021/jp400060d.
- [114] S.K. Yadav, S. Ravishankar, S. Pescetelli, A. Agresti, F. Fabregat-Santiago, A. Di Carlo, Stability of dye-sensitized solar cells under extended thermal stress, *Phys. Chem. Chem. Phys.* 19 (2017) 22546–22554. doi:10.1039/C7CP04598K.
- [115] K.T. Dembele, R. Nechache, L. Nikolova, A. Vomiero, C. Santato, S. Licoccia, F. Rosei, Effect of multi-walled carbon nanotubes on the stability of dye sensitized solar cells, *J. Power Sources.* 233 (2013) 93–97. doi:10.1016/j.jpowsour.2013.01.075.
- [116] M.I. Asghar, K. Miettunen, S. Mastroianni, J. Halme, H. Vahlman, P. Lund, In situ image processing method to investigate performance and stability of dye solar cells, *Sol. Energy.* 86 (2012) 331–338. doi:10.1016/j.solener.2011.10.006.
- [117] N. Kato, K. Higuchi, H. Tanaka, J. Nakajima, T. Sano, T. Toyoda, Improvement in

- long-term stability of dye-sensitized solar cell for outdoor use, *Sol. Energy Mater. Sol. Cells.* 95 (2011) 301–305. doi:10.1016/j.solmat.2010.04.019.
- [118] P.D. Lund, G. Hashmi, Y. Ma, J. Patakangas, Y. Jing, Degradation and stability of nanostructured energy devices, *Microelectron. Eng.* 126 (2014) 49–53. doi:10.1016/j.mee.2014.05.002.
- [119] K.M. Lee, W.H. Chiu, M. De Lu, W.F. Hsieh, Improvement on the long-term stability of flexible plastic dye-sensitized solar cells, *J. Power Sources.* 196 (2011) 8897–8903. doi:10.1016/j.jpowsour.2011.06.049.
- [120] A. Hinsch, J.M. Kroon, R. Kern, I. Uhlendorf, J. Holzbock, A. Meyer, J. Ferber, Long-term stability of dye-sensitised solar cells, *Prog. Photovoltaics Res. Appl.* 9 (2001) 425–438. doi:10.1002/pip.397.
- [121] R. Grünwald, H. Tributsch, Mechanisms of Instability in Ru-Based Dye Sensitization Solar Cells, *J. Phys. Chem. B.* 101 (1997) 2564–2575. doi:10.1021/jp9624919.
- [122] S. Zhang, H. Niu, Y. Lan, C. Cheng, J. Xu, X. Wang, Synthesis of TiO₂ Nanoparticles on Plasma-Treated Carbon Nanotubes and Its Application in Photoanodes of Dye-Sensitized Solar Cells, *J. Phys. Chem. C.* 115 (2011) 22025–22034. doi:10.1021/jp206267x.
- [123] C.Y. Yen, Y.F. Lin, C.H. Hung, Y.H. Tseng, C.C.M. Ma, M.C. Chang, H. Shao, The effects of synthesis procedures on the morphology and photocatalytic activity of multi-walled carbon nanotubes/TiO₂ nanocomposites., *Nanotechnology.* 19 (2008) 1–11. doi:10.1088/0957-4484/19/04/045604.
- [124] C.J. Barbe, F. Arendse, P. Comte, M. Jirousek, F. Lenzmann, V. Shklover, M. Gra, Nanocrystalline Titanium Oxide Electrodes for Photovoltaic Applications, *J. Am. Ceram. Soc.* 80 (1997) 3157–3171. doi:10.1111/j.1151-2916.1997.tb03245.x.
- [125] L. Hu, S. Dai, J. Weng, S. Xiao, Y. Sui, Y. Huang, S. Chen, F. Kong, X. Pan, L. Liang, K. Wang, Microstructure Design of Nanoporous TiO₂ Photoelectrodes for Dye-Sensitized Solar Cell Modules, *J. Phys. Chem. B.* 111 (2007) 358–362. doi:10.1021/jp065541a.
- [126] W. Wang, P. Serp, P. Kalck, J.L. Faria, Photocatalytic degradation of phenol on

- MWNT and titania composite catalysts prepared by a modified sol-gel method, *Appl. Catal. B Environ.* 56 (2005) 305–312. doi:10.1016/j.apcatb.2004.09.018.
- [127] Y. Yao, G. Li, S. Ciston, R.M. Lueptow, K. a. Gray, Photoreactive TiO₂/Carbon Nanotube Composites: Synthesis and Reactivity, *Environ. Sci. Technol.* 42 (2008) 4952–4957. doi:10.1021/es800191n.
- [128] W. Wang, P. Serp, P. Kalck, J.L. Faria, Visible light photodegradation of phenol on MWNT-TiO₂ composite catalysts prepared by a modified sol-gel method, *J. Mol. Catal. A Chem.* 235 (2005) 194–199. doi:10.1016/j.molcata.2005.02.027.
- [129] K. Miettunen, J. Halme, P.D. Lund, Segmented Cell Design for Improved Factoring of Aging Effects in Dye Solar Cells, *J. Phys. Chem. C.* 113 (2009) 10297–10302. doi:10.1021/jp902974v.
- [130] J. Bisquert, A. Zaban, M. Greenshtein, I. Mora-Serot, Determination of Rate Constants for Charge Transfer and the Distribution of Semiconductor and Electrolyte Electronic Energy Levels in Dye-Sensitized Solar Cells by Open-Circuit Photovoltage Decay Method, *J. Am. Chem. Soc.* 126 (2004) 13550–13559. doi:10.1021/ja047311k.
- [131] X. Dang, H. Yi, M. Ham, J. Qi, D.S. Yun, R. Ladewski, M.S. Strano, P.T. Hammond, A.M. Belcher, Virus-templated self-assembled single-walled carbon nanotubes for highly efficient electron collection in photovoltaic devices, *Nat. Nanotechnol.* 6 (2011) 377–384. doi:10.1038/nnano.2011.50.
- [132] E. Palomares, J.N. Clifford, S. a Haque, T. Lutz, J.R. Durrant, Control of Charge Recombination Dynamics in Dye Sensitized Solar Cells by the Use of Conformally Deposited Metal Oxide Blocking Layers, *J. Am. Chem. Soc.* 125 (2003) 475–482. doi:10.1021/ja027945w.
- [133] A. Jitianu, T. Cacciaguerra, R. Benoit, S. Delpeux, F. Béguin, S. Bonnamy, Synthesis and characterization of carbon nanotubes-TiO₂ nanocomposites, *Carbon N. Y.* 42 (2004) 1147–1151. doi:10.1016/j.carbon.2003.12.041.
- [134] W. Jarernboon, S. Pimanpang, S. Maensiri, E. Swatsitang, V. Amornkitbamrung, Effects of multiwall carbon nanotubes in reducing microcrack formation on

- electrophoretically deposited TiO₂ film, *J. Alloys Compd.* 476 (2009) 840–846. doi:10.1016/j.jallcom.2008.09.157.
- [135] R.S. Ruoff, D.C. Lorents, Mechanical and thermal properties of carbon nanotubes, *Carbon N. Y.* 33 (1995) 925–930. doi:10.1016/0008-6223(95)00021-5.
- [136] T. Leijtens, G.E. Eperon, S. Pathak, A. Abate, M.M. Lee, H.J. Snaith, Overcoming ultraviolet light instability of sensitized TiO₂ with meso-superstructured organometal tri-halide perovskite solar cells, *Nat. Commun.* 4 (2013) 1–8. doi:10.1038/ncomms3885.
- [137] S.K. Pathak, A. Abate, P. Ruckdeschel, B. Roose, K.C. Godel, Y. Vaynzof, A. Santhala, S.I. Watanabe, D.J. Hollman, N. Noel, A. Sepe, U. Wiesner, R. Friend, H.J. Snaith, U. Steiner, Performance and Stability Enhancement of Dye-Sensitized and Perovskite Solar Cells by Al Doping of TiO₂, *Adv. Funct. Mater.* 24 (2014) 6046–6055. doi:10.1002/adfm.201401658.
- [138] I. Nakamura, N. Negishi, S. Kutsuna, T. Ihara, S. Sugihara, K. Takeuchi, Role of oxygen vacancy in the plasma-treated TiO₂ photocatalyst with visible light activity for NO removal, *J. Mol. Catal. A Chem.* 161 (2000) 205–212. doi:http://dx.doi.org/10.1016/S1381-1169(00)00362-9.
- [139] X. u. Zhao, Z. Li, Y. Chen, L. Shi, Y. Zhu, Solid-phase photocatalytic degradation of polyethylene plastic under UV and solar light irradiation, *J. Mol. Catal. A Chem.* 268 (2007) 101–106. doi:10.1016/j.molcata.2006.12.012.
- [140] R. Asahi, T. Morikawa, T. Ohwaki, Y. Taga, Visible-Light Photocatalysis in Nitrogen-Doped Titanium Oxides, *Science.* 293 (2001) 269–271. doi:10.1126/science.1061051.
- [141] Y. Yu, J.C. Yu, C.Y. Chan, Y.K. Che, J.C. Zhao, L. Ding, W.K. Ge, P.K. Wong, Enhancement of photocatalytic activity of mesoporous TiO₂ by using carbon nanotubes, *Appl. Catal. A Gen.* 289 (2005) 186–196. doi:10.1016/j.apcatb.2005.03.008.
- [142] A. Saha, A. Moya, A. Kahnt, D. Iglesias, S. Marchesan, R. Wannemacher, M. Prato, J. Vilatela, D.M. Guldi, Interfacial Charge Transfer in Functionalized Multi-walled

- Carbon Nanotube@TiO₂ nanofibres, *Nanoscale*. 9 (2017) 7911–7921. doi:10.1039/C7NR00759K.
- [143] S. Muduli, W. Lee, V. Dhas, S. Mujawar, M. Dubey, K. Vijayamohanan, S.H. Han, S. Ogale, Enhanced conversion efficiency in dye-sensitized solar cells based on hydrothermally synthesized TiO₂-MWCNT nanocomposites, *ACS Appl. Mater. Interfaces*. 1 (2009) 2030–2035. doi:10.1021/am900396m.
- [144] T. Stergiopoulos, M.C. Bernard, A. Hugot-Le Goff, P. Falaras, Resonance micro-Raman spectrophotocatalysis on nanocrystalline TiO₂ thin film electrodes sensitized by Ru(II) complexes, *Coord. Chem. Rev.* 248 (2004) 1407–1420. doi:10.1016/j.ccr.2004.03.023.
- [145] A. Agresti, S. Pescetelli, A. Quatela, S. Mastroianni, T.M. Brown, A. Reale, C.A. Bignozzi, S. Caramori, A. Di Carlo, Micro-Raman analysis of reverse bias stressed dye-sensitized solar cells, *RSC Adv.* 4 (2014) 12366–12375. doi:10.1039/c3ra47797e.
- [146] D. Eder, A.H. Windle, Carbon-inorganic hybrid materials: The carbon-nanotube/TiO₂ interface, *Adv. Mater.* 20 (2008) 1787–1793. doi:10.1002/adma.200702835.
- [147] A. De Morais, L.M.D. Loiola, J.E. Benedetti, A.S. Gonc, C.A.O. Avellaneda, J.H. Clerici, M.A. Cotta, A.F. Nogueira, Enhancing in the performance of dye-sensitized solar cells by the incorporation of functionalized multi-walled carbon nanotubes into TiO₂ films: The role of MWCNT addition, *J. Photochem. Photobiol. A Chem.* 251 (2013) 78–84. doi:10.1016/j.jphotochem.2012.09.016.
- [148] W.S. Li, Z.X. Shen, H.Y. Li, D.Z. Shen, X.W. Fan, Blue shift of Raman peak from coated TiO₂ nanoparticles, *J. Raman Spectrosc.* 32 (2001) 862–865. doi:10.1002/jrs.773.
- [149] H. Greijer, J. Lindgren, A. Hagfeldt, Resonance Raman Scattering of a Dye-Sensitized Solar Cell: Mechanism of Thiocyanato Ligand Exchange, *J. Phys. Chem. B*. 105 (2001) 6314–6320. doi:10.1021/jp011062u.
- [150] C. Pe, L. Kador, B. Peng, M. Thelakkat, Characterization of the Adsorption of Ru-

- bpy Dyes on Mesoporous TiO₂ Films with UV-Vis, Raman, and FTIR Spectroscopies, *J. Phys. Chem. B.* 110 (2006) 8723–8730.
- [151] T. Stergiopoulos, A.G. Kontos, V. Likodimos, D. Perganti, P. Falaras, Solvent effects at the photoelectrode/electrolyte interface of a DSC: A combined spectroscopic and photoelectrochemical study, *J. Phys. Chem. C.* 115 (2011) 10236–10244.
- [152] A. Agresti, L. Cinà, S. Pescetelli, B. Taheri, A. Di Carlo, Stability of dye-sensitized solar cell under reverse bias condition: Resonance Raman spectroscopy combined with spectrally resolved analysis by transmittance and efficiency mapping, *Vib. Spectrosc.* 84 (2016) 106–117. doi:10.1016/j.vibspec.2016.03.008.
- [153] V. Likodimos, T. Stergiopoulos, P. Falaras, R. Harikisun, J. Desilvestro, G. Tulloch, Prolonged light and thermal stress effects on industrial dye-sensitized solar cells: A micro-roman investigation on the long-term stability of aged cells, *J. Phys. Chem. C.* 113 (2009) 9412–9422. doi:10.1021/jp901185f.
- [154] C.T. Shoute, G.R. Loppnow, Excited-State Metal-to-Ligand Charge Transfer Dynamics of a Ruthenium (II) Dye in Solution and Adsorbed on TiO₂ Nanoparticles from Resonance Raman Spectroscopy, *J. Am. Chem. Soc.* 125 (2003) 15636–15646. doi:Review.
- [155] X.L. He, G.J. Yang, C.J. Li, M. Liu, S.Q. Fan, Failure mechanism for flexible dye-sensitized solar cells under repeated outward bending: Cracking and spalling off of nano-porous titanium dioxide film, *J. Power Sources.* 280 (2015) 182–189. doi:10.1016/j.jpowsour.2015.01.088.
- [156] X.L. He, M. Liu, G.J. Yang, H.L. Yao, S.Q. Fan, C.J. Li, Photovoltaic performance degradation and recovery of the flexible dye-sensitized solar cells by bending and relaxing, *J. Power Sources.* 226 (2013) 173–178. doi:10.1016/j.jpowsour.2012.10.056.
- [157] G. Xue, Y. Guo, T. Yu, J. Guan, X. Yu, J. Zhang, J. Liu, Z. Zou, Degradation mechanisms investigation for long-term thermal stability of dye-sensitized solar cells, *Int. J. Electrochem. Sci.* 7 (2012) 1496–1511.

- [158] D. Bari, N. Wrachien, R. Tagliaferro, S. Penna, T.M. Brown, A. Reale, A. Di Carlo, G. Meneghesso, A. Cester, Thermal stress effects on Dye-Sensitized Solar Cells (DSSCs), *Microelectron. Reliab.* 51 (2011) 1762–1766. doi:10.1016/j.microrel.2011.07.061.
- [159] E.T. Thostenson, C. Li, T.W. Chou, Nanocomposites in context, *Compos. Sci. Technol.* 65 (2005) 491–516. doi:10.1016/j.compscitech.2004.11.003.
- [160] W. Yang, Y. Hao, P. Ghamgosar, G. Boschloo, Thermal Stability Study of Dye-Sensitized Solar Cells with Cobalt Bipyridyl-based Electrolytes, *Electrochim. Acta.* 213 (2016) 879–886. doi:10.1016/j.electacta.2016.07.112.
- [161] D. Eder, A.H. Windle, Morphology control of CNT-TiO₂ hybrid materials and rutile nanotubes, *J. Mater. Chem.* 18 (2008) 2036–2043. doi:10.1039/b800499d.
- [162] A. Moya, N. Kemnade, M.R. Osorio, A.S. Cherevan, D. Granados, D. Eder, J. Vilatela, Large area photoelectrodes based on hybrids of CNT fibres and ALD-grown TiO₂, *J. Mater. Chem. A.* 5 (2017) 24695–24706. doi:10.1039/C7TA08074C.
- [163] K.E. Lee, M.A. Gomez, T. Regier, Y. Hu, G.P. Demopoulos, Further understanding of the electronic interactions between N719 Sensitizer and Anatase TiO₂ films: A combined X-ray absorption and X-ray photoelectron spectroscopic study, *J. Phys. Chem. C.* 115 (2011) 5692–5707. doi:10.1021/jp109869z.
- [164] E.M.J. Johansson, M. Hedlund, H. Siegbahn, H. Rensmo, Electronic and molecular surface structure of Ru(tcterpy)(NCS)₃ and Ru(dcbpy)₂(NCS)₂ adsorbed from solution onto nanostructured TiO₂: A photoelectron spectroscopy study, *J. Phys. Chem. B.* 109 (2005) 22256–22263. doi:10.1021/jp0525282.
- [165] S. Tai, C. Liu, S. Chou, F.S. Chien, J. Lin, T.-W. Lin, Few-layer MoS₂ nanosheets coated onto multi-walled carbon nanotubes as a low-cost and highly electrocatalytic counter electrode for dye-sensitized solar cells, *J. Mater. Chem.* 22 (2012) 24753–24759. doi:10.1039/c2jm35447k.
- [166] Q. Tang, J. Duan, Y. Duan, B. He, L. Yu, Recent advances in alloy counter electrodes for dye-sensitized solar cells. A critical review, *Electrochim. Acta.* 178 (2015) 886–899. doi:10.1016/j.electacta.2015.08.072.

- [167] K.S. Lee, K. Lee, H. Wang, N. Park, Y. Lee, O.O. Park, J. Hyeok, Dye-sensitized solar cells with Pt-and TCO-free counter electrodes, *Chem. Commun.* 46 (2010) 4505–4507. doi:10.1039/c0cc00432d.
- [168] X. Huang, Z. Zeng, Z. Fan, J. Liu, H. Zhang, Graphene-Based Electrodes, *Adv. Mater.* 24 (2012) 5979–6004. doi:10.1002/adma.201201587.
- [169] S.A. Patil, N. Mengal, A. Ali, S. Hoon, H. Kim, CuS thin film grown using the one pot , solution-process method for dye-sensitized solar cell applications, *J. Alloy. Compd.* J. 708 (2017) 568–574. doi:10.1016/j.jallcom.2017.03.026.
- [170] X. Zhang, W. Guo, C. Pan, Transparent conducting oxide-free and Pt-free CuS-nanosheet networks as counter electrodes, *J. Mater. Chem. A.* 4 (2016) 6569–6576. doi:10.1039/C6TA01353H.
- [171] J. Wu, Z. Lan, J. Lin, M. Huang, Y. Huang, L. Fan, G. Luo, Y. Lin, Y. Xie, Y. Wei, Counter electrodes in dye-sensitized solar cells, *Chem. Soc. Rev.* 46 (2017) 5975–6023. doi:10.1039/c6cs00752j.
- [172] W.J. Lee, E. Ramasamy, D.Y. Lee, J.S. Song, Efficient Dye-Sensitized Solar Cells with Catalytic Multiwall Carbon Nanotube Counter Electrodes, *ACS Appl. Mater. Interfaces.* 1 (2009) 1145–1149. doi:10.1021/am800249k.
- [173] X. Miao, K. Pan, G. Wang, Y. Liao, L. Wang, W. Zhou, Well-Dispersed CoS Nanoparticles on a Functionalized Graphene Nanosheet Surface : A Counter Electrode of Dye-Sensitized Solar Cells, *Chem. A Eur. J.* 20 (2014) 474–482. doi:10.1002/chem.201303558.
- [174] X. Huang, Z. Zeng, Z. Fan, J. Liu, H. Zhang, Graphene-Based Electrodes, *Adv. Mater.* 24 (2012) 5979–6004. doi:10.1002/adma.201201587.
- [175] F. Navarro-Pardo, D. Benetti, H. Zhao, V. Castano, A. Vomiero, F. Rosei, Platinum /Palladium hollow nanofibers as high-efficiency counter electrodes for enhanced charge transfer, *J. Power Sources* 335 (2016) 138–145. doi:10.1016/j.jpowsour.2016.10.011.
- [176] Z. Shi, K. Deng, L. Li, Pt-free and efficient counter electrode with nanostructured CoNi₂S₄ for dye-sensitized solar cells, *Sci. Rep.* 5 (2014) 1–6.

doi:10.1038/srep09317.

- [177] S.A. Patil, P.Y. Kalode, R.S. Mane, D. V Shinde, A. Doyoung, C. Keumnam, M.M. Sung, S.B. Ambade, S. Han, Highly efficient and stable DSSCs of wet-chemically synthesized MoS₂ counter electrode, *Dalt. Trans.* 43 (2014) 5256–5259. doi:10.1039/c3dt53356e.
- [178] C. Liu, S. Tai, S. Chou, Y. Yu, K. Chang, S. Wang, F.S.-S. Chien, J.-Y. Lin, T.-W. Lin, Facile synthesis of MoS₂/graphene nanocomposite with high catalytic activity toward triiodide reduction in dye-sensitized solar cells, *J. Mater. Chem.* 22 (2012) 21057–21064. doi:10.1039/c2jm33679k.
- [179] S.A. Patil, N. Mengal, A.A. Memon, S.H. Jeong, H.S. Kim, CuS thin film grown using the one pot, solution-process method for dye-sensitized solar cell applications, *J. Alloys Compd.* 708 (2017) 568–574. doi:10.1016/j.jallcom.2017.03.026.
- [180] W. Jareerboon, S. Pimanpang, S. Maensiri, E. Swatsitang, V. Amornkitbamrung, Effects of multiwall carbon nanotubes in reducing microcrack formation on electrophoretically deposited TiO₂ film, *J. Alloys Compd.* 476 (2009) 840–846. doi:10.1016/j.jallcom.2008.09.157.
- [181] Y. Zhang, J. Tian, H. Li, L. Wang, X. Qin, A.M. Asiri, A.O. Al-youbi, X. Sun, Biomolecule-Assisted, Environmentally Friendly, One-Pot Synthesis of CuS/Reduced Graphene Oxide Nanocomposites with Enhanced Photocatalytic Performance, *Langmuir.* 28 (2012) 12893–12900.
- [182] C. Ding, D. Su, W. Ma, Y. Zhao, D. Yan, J. Li, Design of hierarchical CuS/graphene architectures with enhanced lithium storage capability, *Appl. Surf. Sci.* 403 (2017) 1–8.
- [183] G. Nie, L. Zhang, X. Lu, X. Bian, W. Sun, C. Wang, A one-pot and in situ synthesis of CuS-graphene nanosheet composites with enhanced peroxidase-like catalytic activity, *Dalt. Trans.* 42 (2013) 14006–14013. doi:10.1039/c3dt51489g.
- [184] K. Huang, J. Zhang, Y. Liu, Y. Liu, Synthesis of reduced graphene oxide wrapped-copper sulfide hollow spheres as electrode material for supercapacitor, *Int. J. Hydrogen Energy.* 40 (2015) 10158–10167. doi:10.1016/j.ijhydene.2015.05.152.

Appendix B: Résumé (in French)

Introduction

Au cours des deux dernières décennies, avec le développement rapide de l'industrialisation et de la mondialisation, la demande énergétique mondiale a considérablement augmenté et toutes les prévisions indiquent que cette croissance se poursuivra à plus de 50% d'ici 2030 [3,4]. Selon le rapport de l'Agence internationale de l'énergie (AIE), la consommation d'énergie des pays à économies émergentes telles que l'Asie du Sud-Est, le Moyen-Orient, l'Amérique du Sud et l'Afrique augmentera à un taux annuel moyen de 3,2%. L'Europe, le Japon, l'Australie et la Nouvelle-Zélande connaîtront une croissance moyenne de 1,1% [28,29]. Différentes formes de combustibles fossiles, dont le charbon, le pétrole et le gaz naturel, contribuent à 80% de la consommation énergétique mondiale, mais elles ont généré du CO₂ et d'autres gaz dangereux dans l'atmosphère, qui ont des effets néfastes sur la qualité de la vie humaine. [3]. Une série de mesures des niveaux de CO₂ dans l'atmosphère montre cette augmentation constante, année après année. La concentration atmosphérique en CO₂ se situe entre 210 et 300 ppm depuis 420 000 ans. Cependant, au cours des 50 dernières années, la concentration de CO₂ a augmenté en raison de la consommation de combustibles fossiles et dépasse désormais 380 ppm. Cette augmentation inacceptable du niveau de CO₂ atmosphérique augmente la température de la Terre, ce qui a des effets sur le climat mondial, tels que des niveaux plus élevés de vapeur d'eau atmosphérique, la modification des régimes climatiques et l'élévation du niveau de la mer résultant de la fonte des calottes polaires [30,31].

D'autre part, la disponibilité décroissante des combustibles fossiles en tant que source d'énergie non renouvelable et la pollution croissante de l'environnement obligent la société à gérer l'énergie de manière durable, car l'énergie est le facteur déterminant le plus important [3,4]. La gestion de l'énergie a conduit les décideurs et les industriels à identifier des moyens efficaces de passer de l'énergie à l'utilisation de sources d'énergie renouvelables. Les sources d'énergie renouvelables présentent plusieurs avantages, tels

que la durabilité, le respect de la nature et la réduction des émissions de carbone dans l'atmosphère [3,4]. Une décision importante pour les gouvernements et les entreprises est de décider quelle source d'énergie renouvelable est le meilleur choix, car le monde futur dépend de la décision d'aujourd'hui. En ce sens, différents indicateurs de durabilité doivent être évalués et comparés, notamment la disponibilité de sources renouvelables, l'efficacité de la conversion d'énergie, les besoins en terrains, la consommation d'eau et les impacts sociaux [3,4]. Parmi les différentes sources d'énergie renouvelables, notamment l'énergie solaire, éolienne, hydroélectrique, de la biomasse, géothermique, de l'hydrogène et des océans, l'énergie solaire est l'une des ressources énergétiques les plus propres qui présente le moins de risques pour l'environnement et l'environnement associés à sa production [2,28]. La quantité d'énergie solaire atteignant la surface de la Terre par seconde est supérieure à l'énergie totale consommée depuis le début des temps [28]. La technologie d'énergie solaire passive ne fait que capter l'énergie du soleil sans se convertir en d'autres formes, par exemple en optimisant l'utilisation de la lumière et de la chaleur grâce à la conception de bâtiments écologiques. Tandis que la technologie d'énergie solaire active fait référence à la conversion de l'énergie solaire en d'autres formes d'énergies pouvant être classées en trois groupes: (i) photovoltaïque (PV), (ii) énergie chimique et (iii) énergie solaire thermique [2,28,33].

Les dispositifs photovoltaïques exploitent principalement des matériaux semi-conducteurs à large bande interdite qui agissent comme un absorbeur de lumière. La région située entre 400 et 1100 nm présente la densité de photons la plus élevée du spectre solaire. Par conséquent, un absorbeur de lumière idéal (semi-conducteur) est un matériau capable d'absorber la lumière du soleil entre 400 et 1 000 nm. Lors de l'absorption de photons dont l'énergie est égale ou supérieure à la bande interdite du semi-conducteur ($h\nu \geq E_g$), une paire électron / trou est générée. Ensuite, électron et trou peuvent être efficacement séparés et diffusés vers le semi-conducteur de type n et le semi-conducteur de type p, respectivement (Figure 1) [32]. Les électrons circulent dans un circuit externe et produisent un courant électrique.

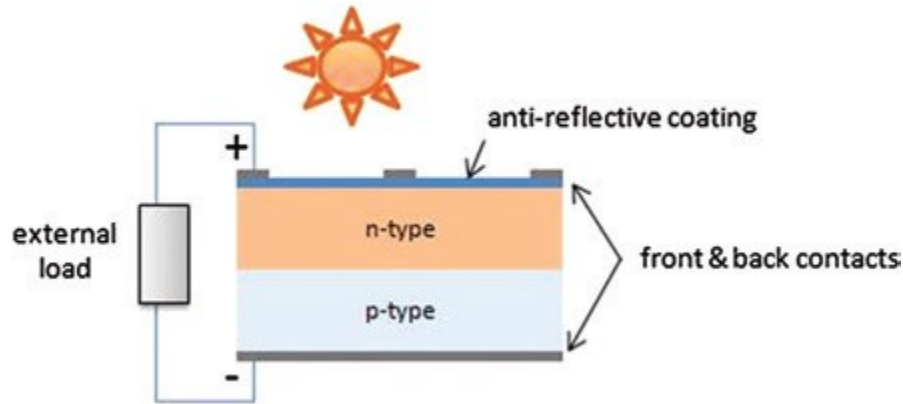


Figure 1 Schéma d'une cellule solaire à jonction p-n [32].

Depuis 1991, à la suite des travaux révolutionnaires d'O'Regan et de Gratzel, les cellules solaires à sensibilisation aux colorants (DSSC) ont suscité un vif intérêt de la part de l'industrie et de la communauté scientifique travaillant dans le domaine des cellules solaires. Ils ont introduit la structure mésoporeuse du dioxyde de titane (TiO_2) et un colorant tris (2, 2'-bipyridyle 4, 4'-carboxylate) ruthénium (II) en tant que collecteur de lumière, ce qui a permis d'obtenir un rendement de conversion énergétique significatif d'environ 8% [5]. Après ce travail de pionnier, les chercheurs se sont efforcés d'améliorer encore l'ECP et la stabilité des DSSC pour une commercialisation à grande échelle en optimisant les différents composants (oxyde de métal, colorant, électrolyte et contre-électrode) de l'appareil (Figure 2) [49]. Récemment, une ECP supérieure à 14% a été rapportée pour les DSSC [8]; c'est toujours inférieur au PCE des cellules solaires à base de silicium ($\sim 25\%$) [2]. Cependant, il a un avantage sur eux à certains points (i) l'efficacité du DSSC est presque indépendante de la température (ii) montre une efficacité encore meilleure que dans des conditions de lumière solaire diffuse ou nuageuse (iii) les performances sont moins sensibles à l'angle d'incidence du rayonnement lumineux [6,42].

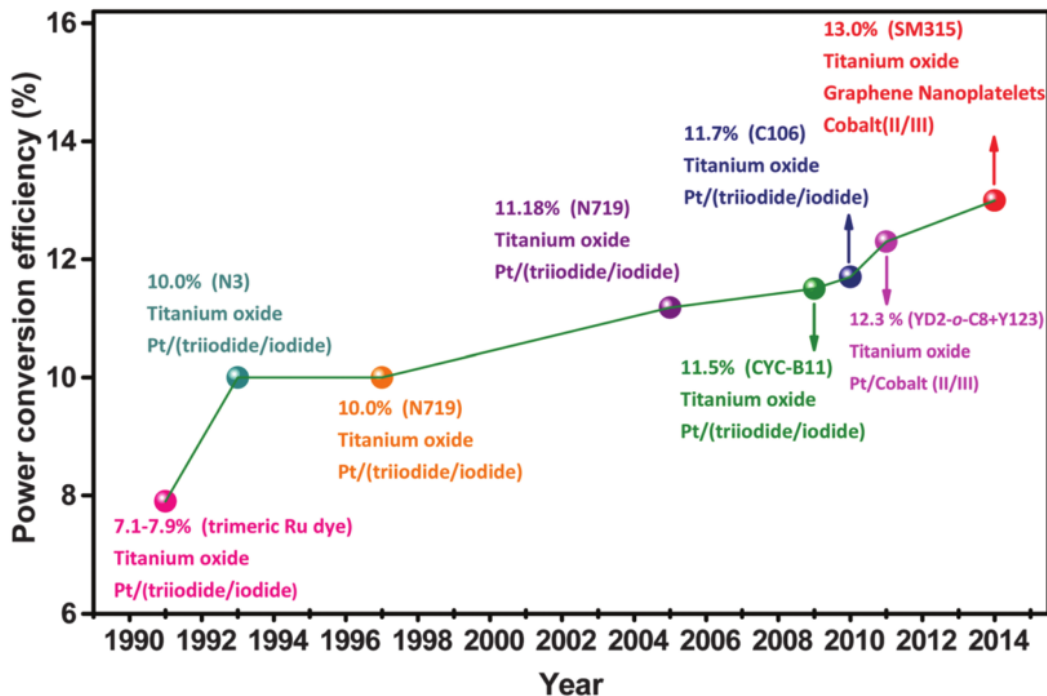


Figure 2 Sélection de points de repère PCE dans les DSSC [49].

Les DSSC ont attiré l'attention de la communauté scientifique en tant qu'alternative possible aux cellules solaires classiques à silicium cristallin et à couche mince, en raison des arguments de vente suivants [6,42]:

- Coûts d'investissement nettement inférieurs aux technologies PV conventionnelles et traditionnelles
- Faible coût de production (temps de retour d'énergie réduit (<1 année))
- Performances relativement meilleures que celles de la concurrence dans des conditions extérieures réelles à une lumière diffuse et à des températures plus élevées
- Options de conception, telles que la transparence et les opportunités multicolores
- Surpasse ses concurrents pour les applications intérieures
- Flexibilité et légèreté

Les DSSC sont fabriqués dans une configuration en sandwich de différents matériaux qui sont piégés entre deux morceaux de verre conducteur. Le schéma d'une cellule complète est présenté à la Figure 3. Les principaux composants du DSSC sont les suivants: semi-

conducteur, colorant, électrode transparente, électrolyte et une contre-électrode. La photoanode est constituée d'une couche de 10 à 20 μm d'épaisseur d'un semi-conducteur à base d'oxyde métallique à large bande (généralement du TiO_2 , du ZnO et du SnO_2) déposé sur un substrat conducteur transparent en oxyde. Parmi les différents types de semi-conducteurs, la nanostructure de TiO_2 est le matériau le plus efficace à utiliser comme photoanode. La photoanode de TiO_2 est composée de deux couches différentes: (i) un film mésoporeux de nanoparticules de TiO_2 d'une taille de 20 nm appelé "couche active" de 8-14 μm et (ii) une couche de 4-6 μm de nanoparticules d'une taille de 200 nm à 400 nm appelée "couche de diffusion". Les molécules de colorant servent d'antennes pour capter la lumière du soleil (photons). La lumière pénètre dans l'appareil du côté du photoanode, de sorte que la bonne transparence du substrat est nécessaire. La contre-électrode est généralement réalisée avec un verre conducteur transparent platiné (couche mince de 5-10 nm). L'espace entre la photoanode sensibilisée au colorant et la contre-électrode est rempli par un électrolyte liquide [5,50–52].

Le principe de fonctionnement des DSSC est très différent des cellules solaires classiques à jonction p-n par sa construction de base et les processus physiques à la base de son fonctionnement. La configuration typique des DSSC combine deux phases solide et liquide, tandis que d'autres cellules solaires sont basées sur la phase solide. [5,6,36,50–52]. Tous les composants et un cycle complet de conversion de la lumière en électrons dans les DSSC sont présentés dans Figure 3. l'efficacité de conversion de photo (PCE) global des DSSC peut être exprimé comme le produit des trois termes clés ($\eta = \eta_{\text{abs}} + \eta_{\text{inj}} + \eta_{\text{coll}}$) [53]. En règle générale, un cycle d'opérations DSSC se termine en cinq étapes, répertoriées ci-dessous:

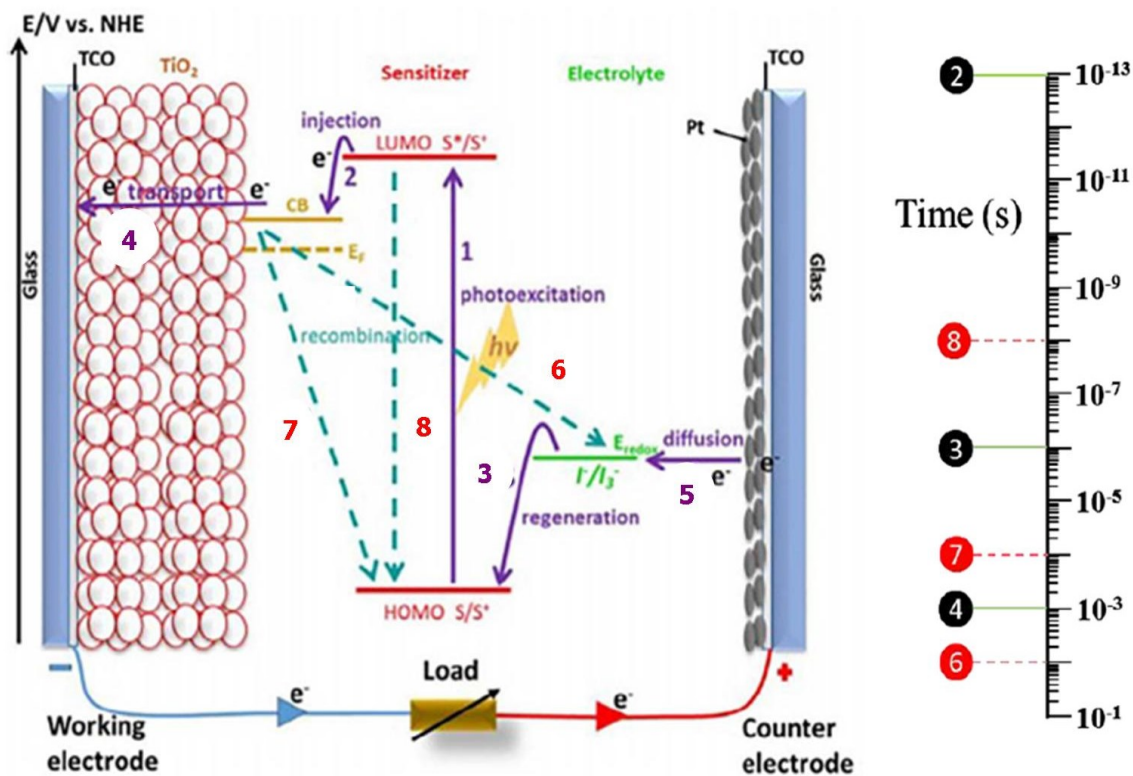


Figure 3 Schéma du principe de fonctionnement d'un DSSC et échelle de temps des processus au sein d'un appareil [54].

Les DSSC doivent surmonter trois défis principaux: efficacité, stabilité et coût de production pour une commercialisation à grande échelle. Au cours des dernières années, la communauté des chercheurs a réalisé des avancées significatives sur différents composants du DSSC, notamment la photoanode, l'électrode, le colorant et l'électrolyte, afin d'améliorer le PCE. [1,6,7]. Grâce aux progrès de la conception d'architectures nouvelles et modifiées, la production de cellules stables et reproductibles a été activée et a contribué à renforcer le PCE jusqu'à $\sim 14.7\%$ [8]. Cependant, il reste des améliorations à apporter, telles que la stabilité à long terme et la réduction des coûts de production, qui constituent des défis cruciaux pour la commercialisation à grande échelle.

En général, divers problèmes de stabilité associés aux DSSC, tels que la stabilité thermique, la stabilité aux ultraviolets (UV) et à la lumière visible de la photoanode, comme coeur d'appareil [9–13]. Il existe déjà des rapports intéressants sur l'amélioration des performances PV des DSSC avec l'ajout de nanomatériaux au carbone [14–19].

Cependant, des questions ont été soulevées quant à savoir si ces matériaux composites à base de carbone ont un effet sur la stabilité des DSSC.

La contre-électrode (CE) est un autre composant important des DSSC généralement constitué de fibres synthétiques revêtues de platine (Pt) [20–24]. Alors que le coût global de fabrication des DSSC est comparativement faible, le Pt et le verre à conductivité transparente (TCO) représentent plus de 40% du coût total des dispositifs [25–27]. Par conséquent, la conception et la fabrication de CE sans TCO et sans Pt pour les DSSC sans réduire son activité électrocatalytique est un sujet de recherche important dans le domaine des DSSC.

La motivation et les objectifs

Dans ce travail de recherche, les DSSC ont été fabriqués dans différentes configurations, incorporant une structure composite à base de nanomatériaux en carbone pour améliorer la stabilité et réduire le coût de production du dispositif.

La thèse commence par un chapitre d'introduction intitulé Énergie solaire et cellules solaires, utile pour comprendre les idées de base de la capture de l'énergie solaire et de sa transformation en électricité. Ensuite, le principe de fonctionnement de base de PV et son développement sont discutés. En outre, une discussion en profondeur sur la structure du dispositif et une description théorique des phénomènes dans la cellule sont présentées. La dernière section de ce chapitre fournit les bases nécessaires aux méthodes d'investigation du dispositif.

Dans le deuxième chapitre, matériaux et techniques expérimentales, tous les matériaux et techniques expérimentaux utilisés pour la fabrication et la caractérisation de dispositifs sont décrits en détail.

Au chapitre 3, la contribution des nanotubes de carbone à parois multiples (MWCNT) dans l'anode en TiO_2 est examinée. La présente section est consacrée à la comparaison de la stabilité à long terme de deux dispositifs constitués d'une anode composite à base de TiO_2 nanocristallin et de (ii) nanotubes de carbone à parois multiples (MWCNT)- TiO_2 , exposés à une exposition continue visible et ultraviolette (UV) irradiation lumineuse.

Le chapitre 4 met l'accent sur la stabilité thermique à long terme, en tant que défi majeur à relever pour que cette technologie devienne commercialement viable. Le sujet principal de cette section porte sur l'effet de l'incorporation de MWCNT sur la stabilité thermique des DSSC.

Le chapitre 5 décrit une approche simple permettant de préparer un film composite de sulfure de cuivre / graphène (CuS-G) en solution à base d'oxyde conducteur transparent (TCO) et de platine (Pt) pour les DSSC.

Chapitre 3. Rôle des MWCNT dans l'amélioration de la stabilité à long terme des cellules solaires sensibilisées au colorant

Nous avons d'abord étudié l'effet de l'ajout de MWCNT dans le photoanode sur les performances PV des DSSC. La Figure 4 montre les courbes J-V obtenues sous un soleil simulé à 1,5 G (100 mW cm^{-2}) de DSSC avec et sans MWCNT. Les résultats montrent que l'ajout de 0,010% en poids de MWCNT aux nanoparticules de TiO_2 entraîne une amélioration d'environ 30% du PCE par rapport au dispositif de contrôle, conformément aux rapports précédents [15,115].

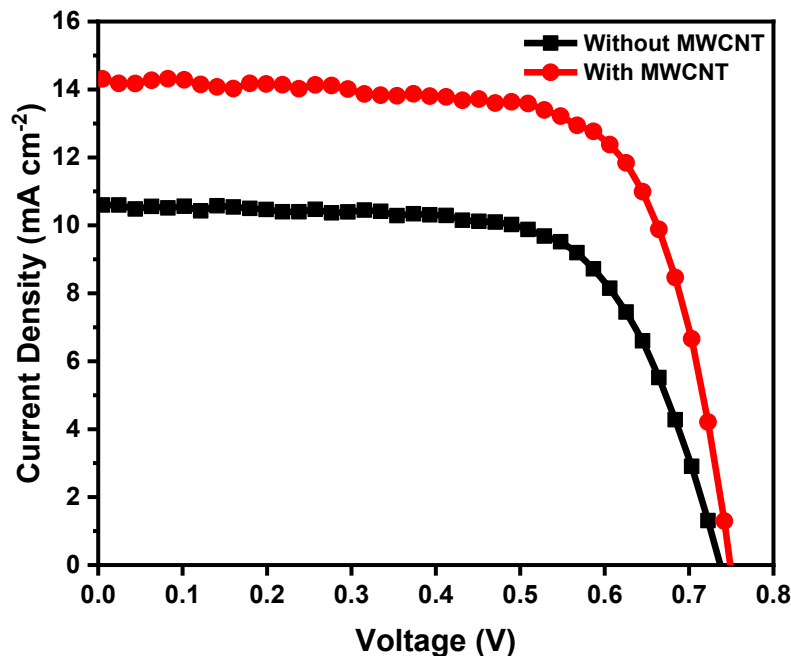


Figure 4 Courbes densité / tension actuelles de cellules solaires sous un soleil simulé à AM 1,5G (100 mW cm⁻²) fabriquées à l'aide de films mésoporeux de TiO₂ avec (cercles rouges) et sans MWCNT (carrés noirs).

Des expériences de stabilité ont été effectuées sur deux séries de cellules avec et sans la présence de MWCNT dans un film mésoporeux de TiO₂ sous une lumière solaire simulée continue afin d'obtenir des informations statistiquement pertinentes sur la stabilité à long terme. La figure 5 montre la variation des paramètres PV de différents dispositifs sous une lumière solaire simulée continue à AM 1,5 G (100 mW cm⁻²) à la température ambiante. Les résultats démontrent que la cellule composite avec MWCNT a une stabilité impressionnante sur une aussi longue période de test comparée au dispositif sans MWCNT. Alors que le Jsc (mA cm⁻²) du dispositif composite ne montre qu'une perte de 6% par rapport à sa valeur initiale, la cellule sans MWCNT a diminué dans une plus large mesure (21%). Dans la cellule sans MWCNT, il y a une dégradation de Voc (V) de 18%, alors que dans le DCCS composite, elle n'a diminué que de 6% au cours des 110 h de trempage léger continu. Ceci pourrait être lié à une recombinaison accrue à l'interface TiO₂/colorant/électrolyte [15,64,116,117]. Le FF des deux dispositifs est resté à peu près stable pendant le test à long terme. Le FF est en grande partie responsable de la résistance au transfert de charge au niveau de la contre-électrode (liée à la stabilité du matériau catalyseur) et de la résistance en couche du substrat (FTO). Ces résultats indiquent qu'il n'y a pas de changements apparents dans les résistances connectées en série et donc pas de dégradation de FTO et de la couche de catalyseur Pt [11,116–118]. Le PCE global du dispositif composite avec MWCNT décroît lentement (seulement 10%); cependant, le dispositif sans MWCNT a montré une réduction considérable (32%) au cours de la même période de test et des mêmes conditions de mesure que l'on pouvait attribuer principalement à la réduction simultanée de Jsc (mA cm⁻²) et de Voc (V). Plusieurs raisons peuvent être invoquées pour expliquer l'effet des MWCNT sur la stabilité à long terme du DSSC.

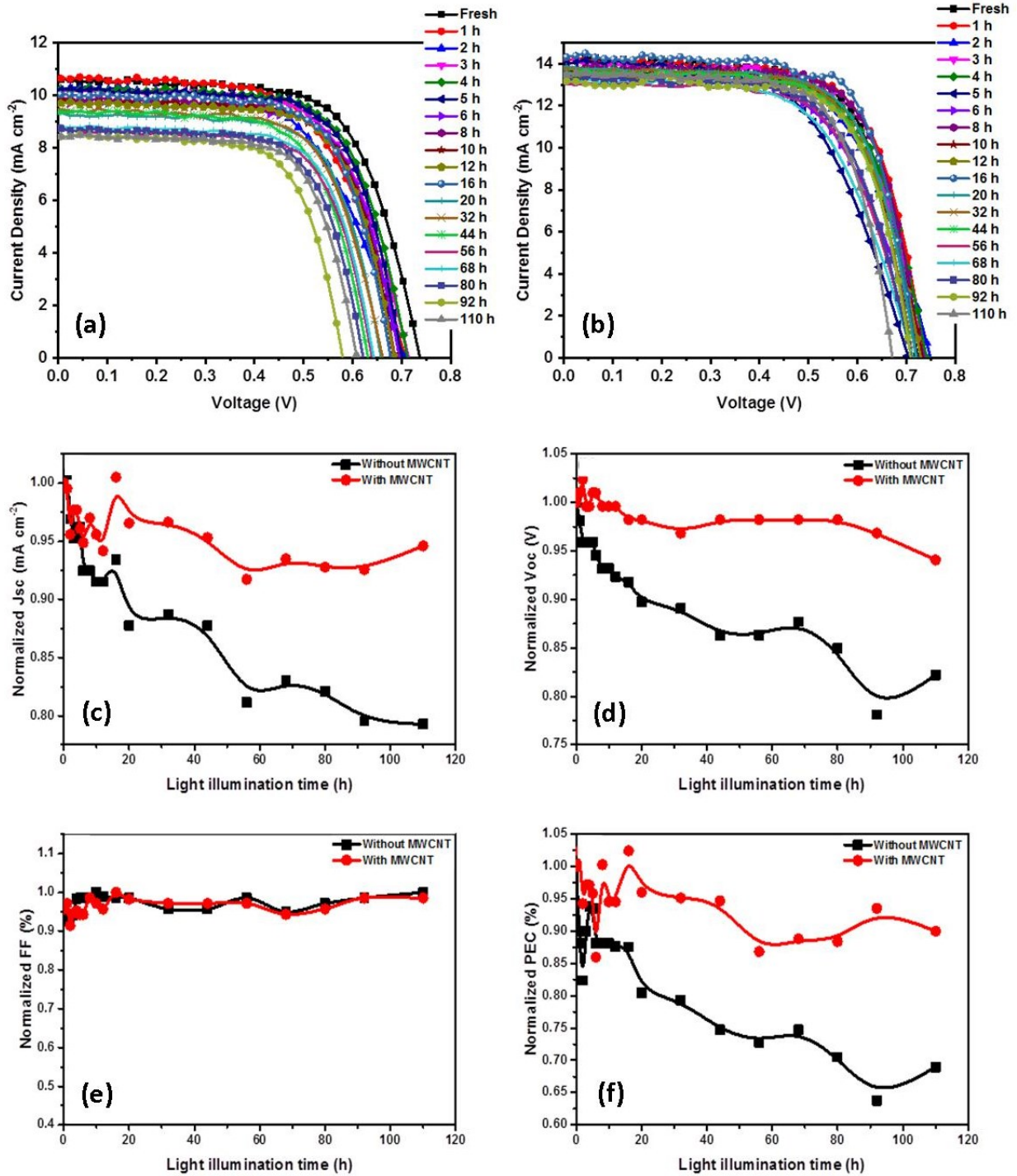


Figure 5 Propriétés fonctionnelles des DSSC dans les cas avec et sans MWCNT sous irradiation continue d'un rayonnement solaire en fonction du temps de trempage (a) Courbes J-V des DSSC sans MWCNT, (b) Courbes J-V des DSSC avec MWCNT, (c) J_{sc} (mA cm^{-2}); (d) V_{oc} (V); (e) FF (%) and (f) PCE (%).

Dans les DSSC, un bon film de photoanode poreux avec une liaison continue entre les nanoparticules de TiO_2 et sans aucune fissure et/ou défaut est nécessaire pour une collecte et un transport efficaces des électrons [63,119,141]. La dégradation des paramètres PV des DSSC sous illumination pourrait être associée à la formation de défauts dans la photoanode. La Figure 6 montre l'évaluation de la microstructure de la photoanode avant et après 200 h de trempage simulé par la lumière solaire continue (100 mW cm^{-2}) et par stockage pendant 70 jours sous une lumière intérieure continue (30 mW cm^{-2}). Comme le montrent les Figures 6 (a et b), les électrodes de travail sont composées de nanoparticules de TiO_2 à structure poreuse, totalement exemptes de fissures pour le transport d'électrons. Des rapports antérieurs indiquaient que la présence de MWCNT dans une matrice de TiO_2 donne une structure avec une dispersion plus uniforme des nanoparticules et par conséquent la formation d'un film plus poreux [18,51,109,122]. Dans l'anode composite, nous n'avons pas pu voir les MWCNT en raison de leur très faible concentration et du faible contraste des matériaux à base de carbone [78]. Les images FESEM des échantillons après les tests de stabilité (Figures 6 c et d) indiquent que la cellule sans MWCNT présente une formation de micro-fissures dans la photoanode, ce qui pourrait être une raison pour la réduction du transport d'électrons et l'augmentation de la résistance au transport de charge [51,63]. En revanche, le dispositif composite présente une structure stable sans défauts ni fissures pouvant être liés à l'interaction entre les MWCNT et les particules de TiO_2 . Ces résultats mettent en évidence le rôle des MWCNT dans l'amélioration des propriétés mécaniques et thermiques du photoanode [111,135].

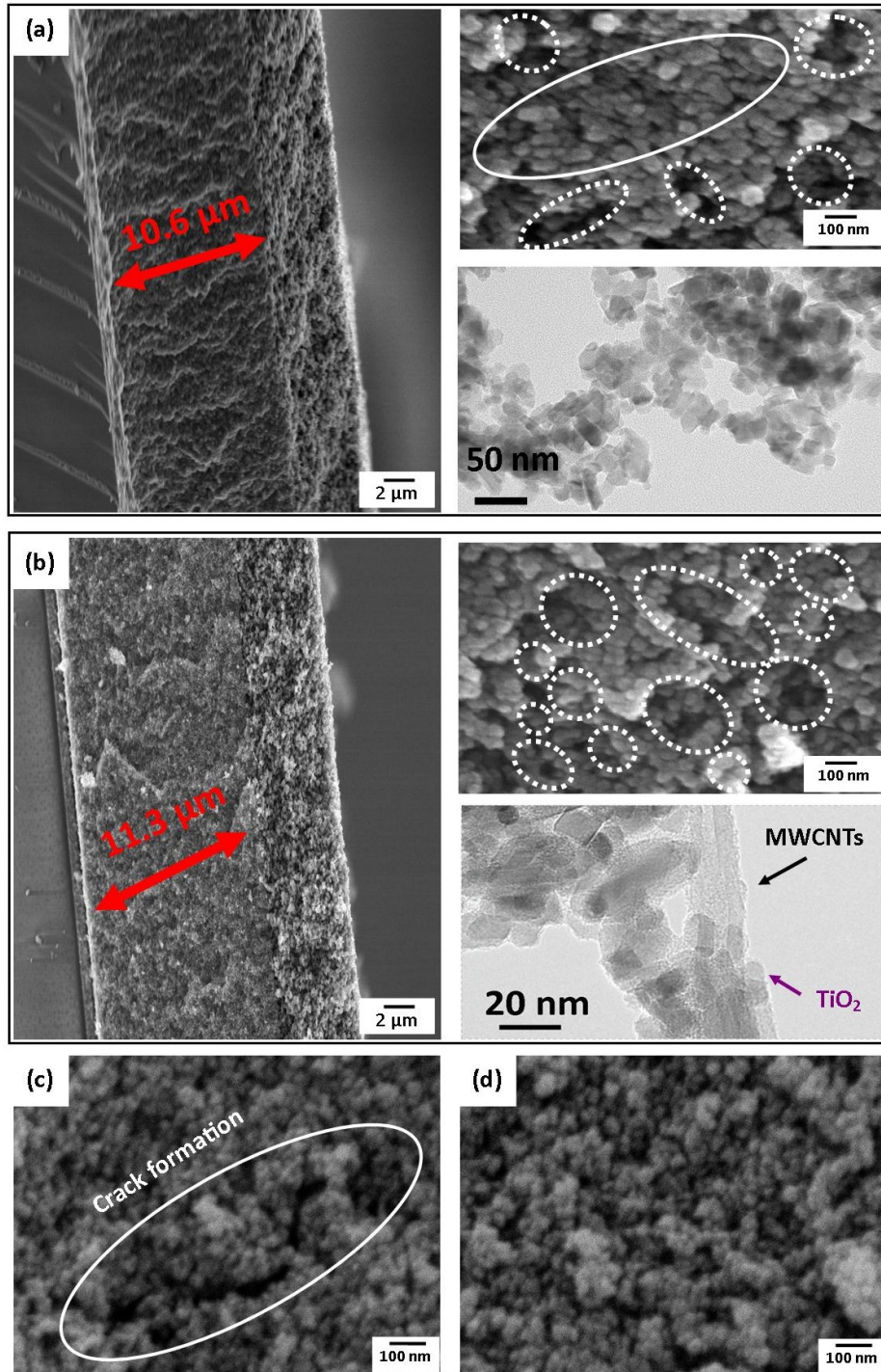


Figure 6 Images FESEM de photoanodes synthétisées: (a) sans MWCNT et (b) avec des MWCNT à un grossissement différent avant vieillissement. Les ovales solides et en pointillés mettent en évidence l'agglomération et la porosité des particules de TiO₂, respectivement. (c) photoanode sans MWCNT et (d) photoanode avec MWCNT après vieillissement.

Pour mieux comprendre l'effet des MWCNT sur la stabilité à long terme, les cellules ont été testées sous un éclairage UV continu. La lumière UV est généralement considérée comme un facteur dommageable pour les DSSC [120,121]. Cependant, les effets des rayons ultraviolets sur une longue période sur les paramètres fonctionnels des DSSC et les mécanismes de dégradation associés ne sont pas encore bien compris car les filtres anti-UV sont souvent utilisés pour mesurer la stabilité à long terme [136].

Après 350 h de vieillissement UV, une diminution mineure (-7,9%) du PCE de la cellule avec MWCNT est présentée, par rapport aux résultats de test du dispositif sans MWCNT, qui a montré une réduction considérable (-30,3%). Cette différence démontre que l'ajout de MWCNT améliore considérablement la stabilité de la cellule sous lumière UV. Snaith *et al.* [136,137] a rapporté que lors de l'illumination par la lumière UV, des électrons et des trous sont formés à la surface de TiO_2 en raison de l'excitation de la bande interdite. D'autre part, la lumière UV pourrait introduire des défauts cristallins (pièges à électrons énergétiquement profonds) dans le TiO_2 identifié comme facteur limitant de la diffusion des électrons [138]. Le niveau d'énergie de ces sites a été déterminé à environ 1 eV sous la bande de conduction, ce qui signifie que les électrons ne peuvent pas s'en échapper pour atteindre la bande de conduction [138]. Ainsi, une recombinaison de charge entre les électrons piégés et l'électrolyte peut être produite [136,137]. Après recombinaison électron-trou, ces sites ont tendance à piéger à nouveau les électrons (Figure 7). En outre, les rayons ultraviolets peuvent entraîner une désorption ou une décomposition du colorant, entraînant ainsi une détérioration sensible du fonctionnement du dispositif [9,11,121,139]. Bien que les DSSC basés sur des photoanodes de TiO_2 soient très sensibles aux rayons ultraviolets, il existe des solutions limitées pour résoudre ce problème, par exemple en empêchant les rayons ultraviolets d'atteindre les nanoparticules de TiO_2 [136,137,140]. Des études antérieures ont confirmé que les NTC peuvent efficacement absorber et donc bloquer la lumière UV [122,128,140]. En conséquence, les MWCNT peuvent augmenter la stabilité des DCCS sous immersion dans des rayons ultraviolets.

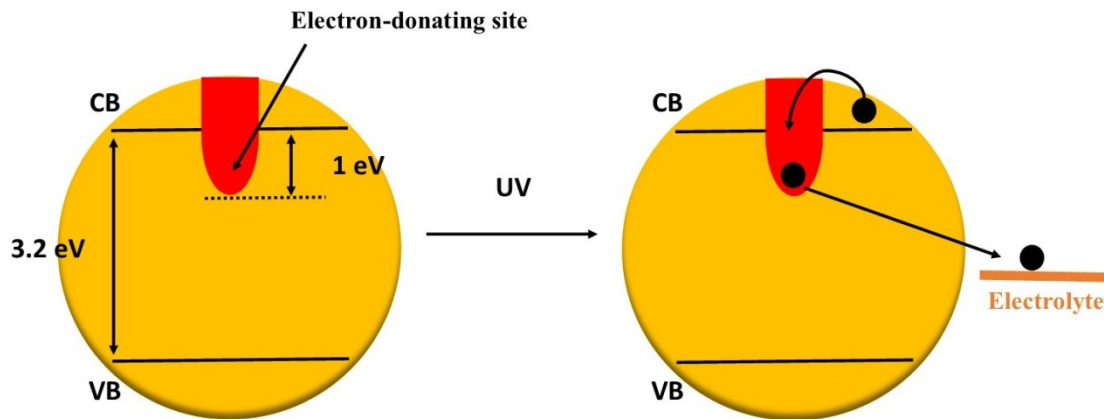


Figure 7 Illustration schématique du modèle de structure de bande du TiO_2 formant des pièges électroniques profonds. Sous illumination UV, les électrons injectés et photogénérés peuvent être adsorbés via des sites de donneurs d'électrons profonds. Ensuite, l'électron dans ce site peut subir une recombinaison directe avec un trou dans l'électrolyte.

Chapitre 4. Incorporation de MWCNT pour renforcer la stabilité thermique à long terme du DSSC

Le vieillissement thermique et les contraintes qui en résultent sont l'un des facteurs externes les plus importants à prendre en compte, car les appareils d'éclairage sous le soleil sont soumis à de fortes contraintes thermiques inévitables causées par une augmentation de la température [63,137]. Sommeling et al. [9] ont signalé que sous une seule illumination solaire, en fonction du climat, les températures autour de 80-85°C peuvent être atteintes par le module de cellule solaire. Dans ce chapitre, nous étudions les effets des MWCNT sur la stabilité thermique des DSSC. Deux séries de DSSC basées sur les couches de transport d'électrons composites neutres de TiO_2 et composites de TiO_2 -MWCNT ont été exposées à des contraintes thermiques dans l'obscurité afin d'éviter les autres effets possibles de l'éclairage et les mécanismes de dégradation correspondants. Les DSSC basés sur la photoanode au TiO_2 souffrent d'une diminution extrêmement rapide des performances PV sous contrainte thermique. Cependant, les appareils dotés de MWCNT présentent des performances extrêmement stables dans des conditions de test similaires. La Figure 8 montre la dégradation des paramètres PV des DSSC avec et sans MWCNT en fonction du temps de vieillissement thermique à 80°C.

Les contraintes thermiques sur 240 h entraînent une baisse importante de 59% du PCE global des DSSC basé sur le TiO_2 , mais elles ne sont limitées qu'à 20% pour la cellule à anode nanocomposite TiO_2 -MWCNT. De plus, le FF (%) des deux cellules a légèrement augmenté (~ 6%) avec le vieillissement thermique, ce qui suggère une activation améliorée et une meilleure connexion entre l'électrolyte et la contre-électrode lors du vieillissement thermique [101]. Ce résultat est très important car il indique que l'utilisation de l'anode nanocomposite TiO_2 -MWCTN peut augmenter de manière significative la stabilité thermique des DSSC.

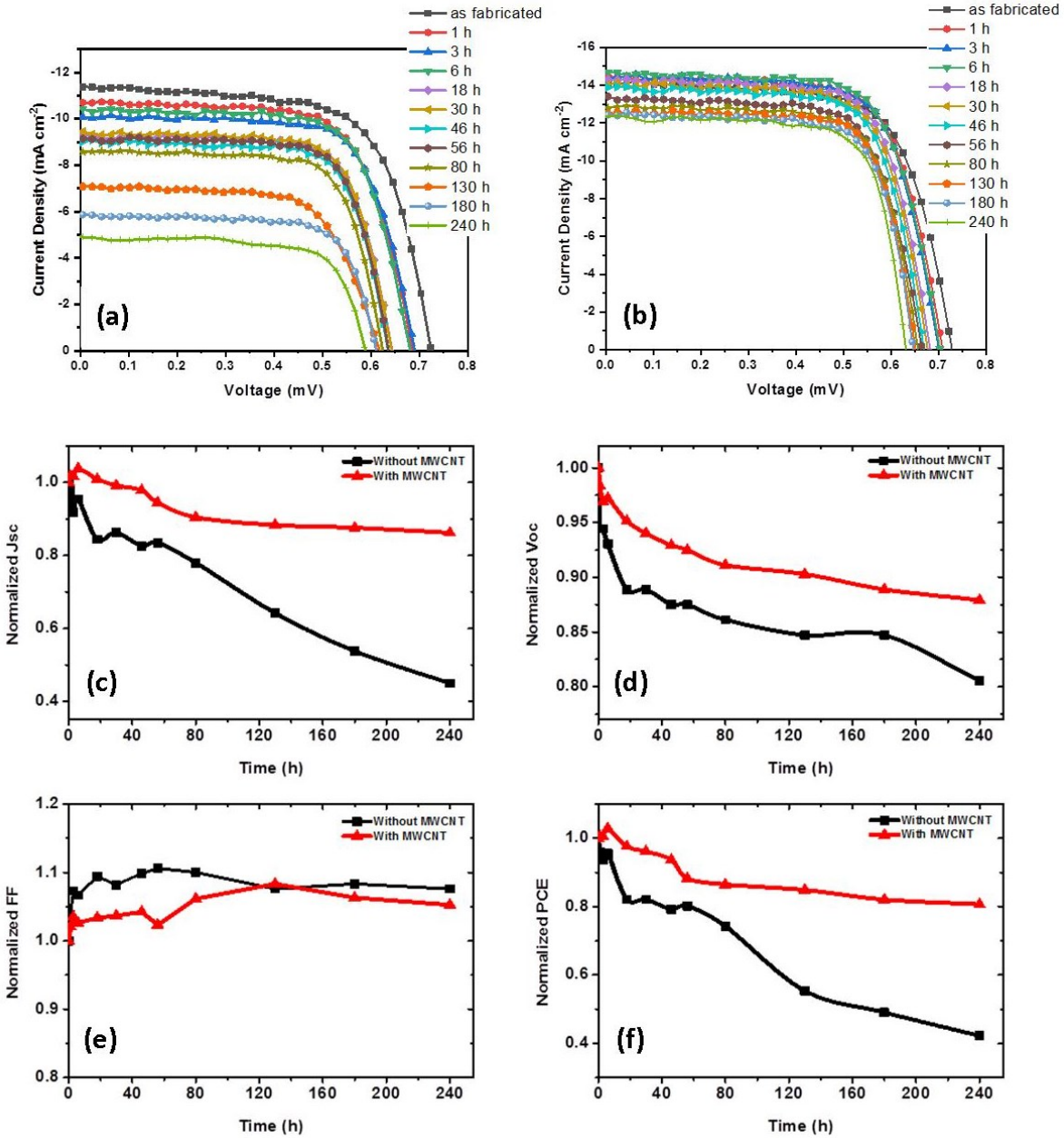


Figure 8 Propriétés fonctionnelles des DSSC dans les cas avec et sans MWCNT en fonction du temps de vieillissement thermique (a) courbes J-V des DSSC sans MWCNT, (b) courbes J-V des DSSC avec MWCNT, (c) J_{sc} (mA cm^{-2}); (d) V_{oc} (V); (e) FF (%) and (f) PCE (%).

Les caractérisations des DSSC présentent une dégradation du V_{oc} (V) pouvant être due à une diminution de la durée de vie des électrons et de la résistance à la recombinaison au niveau de la photoanode [15,63,64,116,130]. La durée de vie des électrons et la résistance de recombinaison au niveau de la photoélectrode ont été mesurées en

fonction de la décroissance transitoire de la photovoltage (équation (3.1)) [64]. Comme on peut le constater, le taux de décroissance de la Voc est plus lent dans l'appareil équipé de MWCNT que dans l'appareil à base de TiO₂. La durée de vie des électrons de la cellule sans MWCNT diminue considérablement après le vieillissement thermique, tandis que les dispositifs composites ne montrent pas de changements considérables. Dans la cellule sans MWCNT, la dégradation et la formation de fissures de la photoanode, conduisant à un transfert de charge incomplet, sont probablement responsables de la réduction de la durée de vie des électrons et de la recombinaison. [101,158,160]. D'autre part, dans l'échantillon composite, l'addition de MWCNT devrait empêcher la recombinaison de charge en agissant comme un réseau fortement conducteur dans la structure [109,130]. Cette hypothèse est confortée dans la littérature selon laquelle les électrons sont transférés aux CNT à partir des nanoparticules de TiO₂; suivi d'un transport rapide sur le substrat FTO sans recombinaison [131].

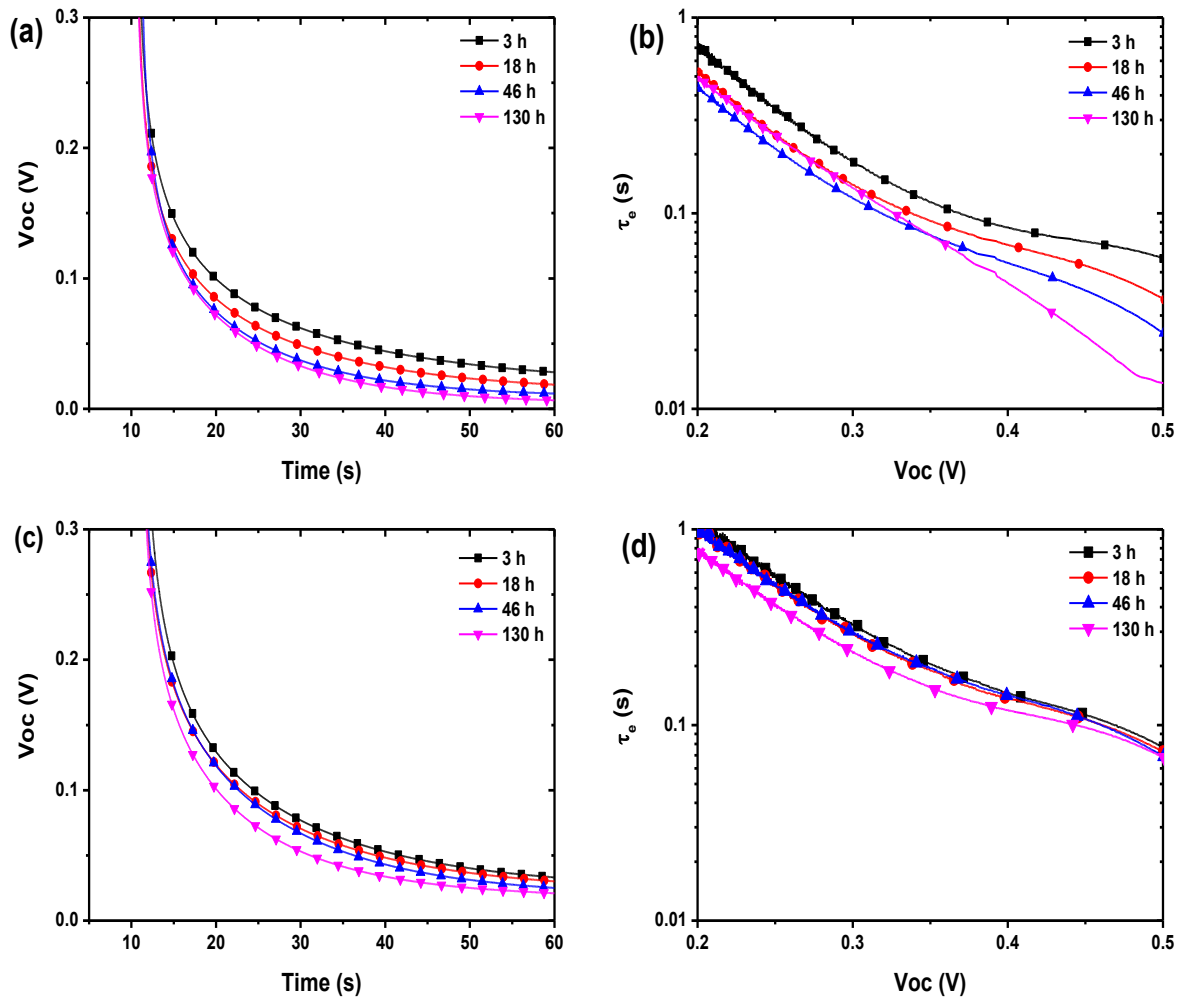


Figure 9 Décomposition transitoire de Voc et durée de vie électronique obtenue (τ_e): pour les cellules sans MWCNT (a et b) et les cellules avec MWCNT (c et d) mesurées après différents temps de contrainte thermique.

Chapitre 5. Nanocomposite CuS-graphène en tant qu'oxyde conducteur transparent et contre-électrode sans platine pour cellules solaires à colorant

Parmi les différents composants des DSSC, CE est la partie la plus chère. La CE dans les DSSC a pour tâche importante de collecter les électrons du circuit externe et de régénérer l'électrolyte oxydé à couple redox iodine/iodide. En améliorant l'activité catalytique de la CE, le FF de la cellule augmente, ce qui est principalement influencé par la résistance en série (R_s). R_s est liée à la résistance de transfert de charge à la CE et à l'interface électrolyte. Une valeur inférieure de résistance de transfert de charge à

l'interface de la CE et de l'électrolyte signifie un transfert d'électrons considérable pour la réduction de l'électrolyte aux interfaces catalytiques de la CE [25,82,165].

Dans ce type d'appareil, le Pt revêtu sur le FTO / verre est le plus largement CE pour les raisons suivantes: (i) haute conductivité pour le transport de charge, (ii) excellente stabilité vis-à-vis du couple électrolyte rédox iode/iodure et (iii) activité catalytique élevée [166,167]. Le Pt en tant que métal noble et le verre conducteur transparent (TCO) représentent plus de 40% du coût total de l'appareil [25–27]. D'autre part, le comportement à la corrosion de métaux nobles tels que le Pt, l'Ag et l'Au dans des électrolytes liquides tels que le couple rédox au cobalt est une autre préoccupation [69,168]. Par conséquent, la conception et la fabrication de solutions de remplacement, sans réduction de l'activité électrocatalytique, de CE sans Pt et sans platine pour les DSSC représentent un défi majeur pour la commercialisation à grande échelle de cette technologie prometteuse de conversion de l'énergie solaire. La dégradation de l'activité catalytique du CE augmente la résistance au transfert de charge et par conséquent la réduction incomplète de l'électrolyte, réduisant ainsi la densité de courant de court-circuit et le facteur de remplissage [52].

Dans ce chapitre, nous avons synthétisé un film nanocomposite CuS-graphène avec une concentration variable de graphène sur du verre non conducteur sous la forme de CE transparents sans TCO ni Pt dans des DSSC.

Dans les DSSC, une réduction de l'électrolyte a lieu à la surface du CE; par conséquent, la formation d'une couche uniforme et dense du matériau catalyseur a un effet évident sur la propriété électrocatalytique. Une architecture sans défaut avec de grandes surfaces améliore le transfert d'électron de la surface de la CE à l'électrolyte. La transparence optique est l'un des principaux aspects à prendre en compte pour les CE dans les DSSC [82]. La Figure 10 (a) montre une photographie du film composite de CuS-G déposé sur le substrat de verre, qui présente une transparence optique élevée du film et met en évidence l'homogénéité du film. La Figure 10 (b-g) montre les images au MEB des films nanocomposites hybrides CuS et CuS-G nus sur le substrat de verre avec différentes concentrations de graphène. Comme observé sur ces images, le film CuS s'est développé de manière homogène sur la surface d'un substrat en verre composé de

grains cristallins continus et uniformes. La surface de l'échantillon à forte concentration de graphène (CuS-10G) présente des fissures et des trous profonds, Figure 10 (f-g). Ces résultats suggèrent que la concentration élevée de graphène provoque la formation de microfissures, probablement en raison de la forte interaction de Van der Waals entre les feuilles de graphène [180]. La formation de ces défauts dans le CE peut réduire le transport de charge d'électrons et les propriétés électrocatalytiques du CE [54,73,82].

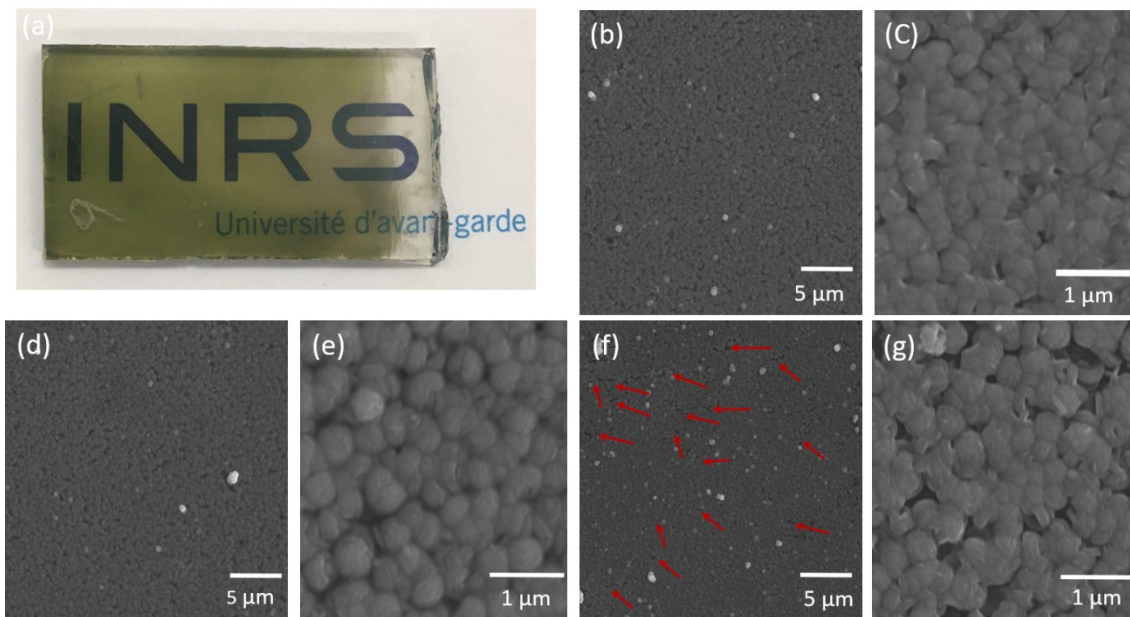


Figure 10 (a) Photographie du film composite CuS-3G. Images au MEB d'un film de CuS avec diverses concentrations de graphène à différents grossissements: (b)-(c) CuS-0G; (d)-(e) CuS-3G; (f)-(g) CuS-10G. Les flèches rouges indiquent les zones de microfissures.

Une compréhension des performances de l'électrode synthétisée a été obtenue en comparant les paramètres fonctionnels des DSSC assemblés avec des CE Pt et CuS-3G. Les résultats montrent que le dispositif avec nanocomposite de CuS-3G optimisé sur le substrat de verre CE présentait un excellent PCE de 4,83%, ce qui est proche du PCE des DSSC basé sur des CE FTO platinées (5.14%). Les DSSC basés sur les CE de Pt et de CuS présentent un FF similaire, de 67% et 66% respectivement, ce qui suggère que des propriétés électrocatalytiques presque similaires sont offertes par le CuS CE (Tableau 5.2) [176]. Cependant, les résultats ont indiqué que la densité de photocourant obtenue pour le Pt CE (10,86 mA cm⁻²) était légèrement supérieure à celle du dispositif CuS-3G CE (10.33 mA cm⁻²). Les CE basés sur CuS démontrent un comportement

transparent; tandis que Pt CE présente une surface semblable à un miroir avec une réflectivité élevée. Ainsi, Pt CE devrait refléter la partie non absorbée de la lumière incidente vers le photoanode et améliorer l'efficacité de la collecte de lumière des DSSC [178]. Ceci pourrait être une raison concourante possible pour la valeur J_{sc} plus élevée dans le DSSC assemblé avec Pt CE par rapport au système CuS-3G CE basé sur un appareil. La valeur de V_{oc} obtenue était approximativement similaire (~ 700 mV) pour les deux dispositifs.

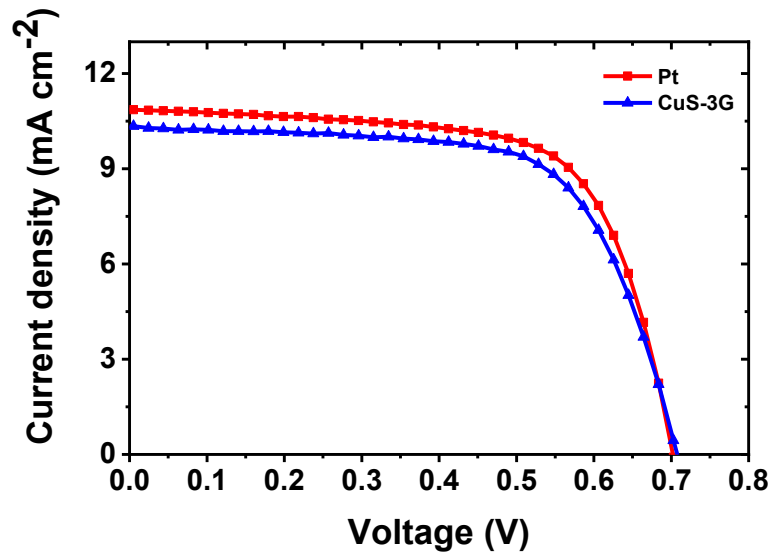


Figure 11 Courbes densité / tension actuelles de cellules solaires sous une lumière solaire simulée à une AM 1,5G (100 mW cm^{-2}) simulées à l'aide de CE composites Pt et CuS-3G.

Pour étudier l'activité électrocatalytique des CE de Pt et de CuS-3G, des analyses CV ont été effectuées. Les courbes de CV obtenues des CE Pt, CuS-3G pour l'électrolyte iodure / triiodure sont illustrées à la Figure 12. Les mesures de CV montrent que la courbe de deux échantillons présente deux paires de pics rédox. La séparation des pics anodique et cathodique du Pt CE était légèrement inférieure à celle des électrodes nanocomposites de CuS-3G. Cependant, les densités de courant dans les pics rédox de l'électrode nanocomposite CuS-3G sont supérieures à celles du Pt, suggérant la grande activité électrocatalytique du CuS-3G en tant que CE dans un DSSC. Ceci peut être attribué à la conductivité électrique plus élevée de l'électrode composée en graphène, ainsi qu'à la surface améliorée de la rugosité de surface plus élevée (voir plus loin de manière plus détaillée) [26,73,177].

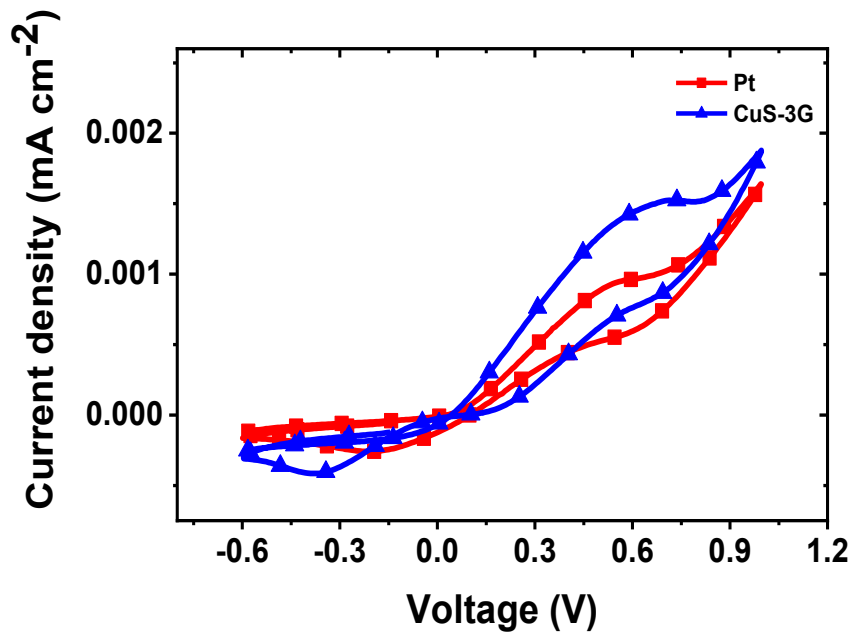


Figure 12 Voltamogramme cyclique de CE composites Pt et CuS-3G.

Les conclusions

Dans le cas des DSSC, les processus régissant le fonctionnement des cellules sont assez bien compris à la suite de plus de deux décennies de recherche scientifique. Cependant, il reste encore beaucoup de questions sur la dégradation de cet appareil sous différentes contraintes environnementales. Dans les chapitres 3 et 4, nous nous sommes concentrés sur l'effet de l'ajout de MWCNT dans une anode en TiO₂ sur la stabilité à long terme des DSSC. Nous avons montré que la performance photovoltaïque (PV) des DSSC diminuait fortement sous l'éclairage continu, principalement en raison de l'augmentation de la recombinaison et de la résistance au transfert de charge. Au contraire, les résultats démontrent que la présence de MWCNT supprime efficacement la dégradation des paramètres PV dans les DSSC, sans réduction considérable de la durée de vie des électrons. L'évaluation de la microstructure a indiqué qu'après les tests de stabilité, la cellule sans MWCNT montre une formation de micro-fissures dans la photoanode, ce qui pourrait être la raison principale de l'augmentation de la résistance au transport de charge. Le dispositif composite présente une structure d'anode stable pendant le test, sans fissures ni défauts pouvant être liés à l'interaction entre les MWCNT

et les particules de TiO_2 . Dans l'anode nanocomposite en TiO_2 -MWCNT à base de dispositif, les MWCNT fournissent un réseau conducteur pour améliorer le transport de charge et supprimer la recombinaison d'électrons. Les résultats de ces travaux indiquent que le taux de dégradation des DSSC est élevé sous irradiation UV, ce qui signifie que les composants de l'appareil sont très sensibles à la lumière UV. Les MWCNT peuvent augmenter la stabilité des cellules sous exposition aux rayons ultraviolets, car ils peuvent partiellement les absorber et donc les bloquer.

En continu, nous avons rapporté l'effet de l'incorporation de MWCNT dans TiO_2 sur la stabilité thermique des DSSC. La dégradation des paramètres PV a démontré la stabilité à long terme sous contrainte thermique du DSSC. L'observation microstructurale a indiqué que le stress thermique provoque de longues fissures et une perte de connexion entre les nanoparticules de TiO_2 . Le stress thermique entraîne la désorption des molécules de colorant à la surface des nanoparticules de TiO_2 , ce qui peut être considéré comme l'une des causes les plus critiques de la dégradation des DSSC lors du vieillissement thermique. Cependant, l'ajout des MWCNT améliore environ trois fois la stabilité des DSSC sous contrainte thermique. Les MWCNT améliorent la force de liaison entre les nanoparticules de TiO_2 . Les MWCNT sont capables d'empêcher la dégradation de la photoanode lors de contraintes thermiques grâce à leur conductivité thermique exceptionnellement élevée, ce qui en fait l'un des matériaux candidats les plus prometteurs pour les composites thermiquement stables.

Au chapitre 5, nous avons synthétisé un film nanocomposite de sulfure de cuivre / graphène (CuS/G) sur le substrat de verre sous forme de TCO et de CE sans Pt dans les DSSC. Le CE constitué de Pt revêtu sur le substrat FTO / verre est toujours le plus largement utilisé, représentant plus de 40% du coût total de l'appareil. Par conséquent, la conception et la fabrication de CE sans TCO et sans Pt pour les DSSC représentent un défi majeur pour le déploiement commercial de cette technologie. Nous avons démontré que les performances PV et l'activité électrocatalytique du CuS-G CE développé sur le substrat de verre par une approche à basse température et pouvant être traitée en solution sont comparables à celles obtenues avec des CE "standard" Pt. L'évaluation de la microstructure a montré la formation de grains cristallins uniformes et continus et d'un film composite totalement exempt de film. L'étude des performances PV

des DSSC basées sur le CE nanocomposite CuS-G montre que le PCE s'améliore d'environ 12% grâce à l'ajout de la concentration en graphène, ce qui est comparable au PCE des DSSC basés sur des CE platinés. L'électrode composite synthétisée présente une excellente activité électrocatalytique en tant que CE dans un système DSSC, principalement due à l'augmentation de la surface et de la conductivité élevées de la CE par addition de graphène.

Les composites de nanomatériaux carbonés en tant que matériau actif dans les DSSC ont été étudiés et ont découvert leurs énormes potentiels dans la conversion de l'énergie solaire verte. Bien que les mécanismes de dégradation et les propriétés physiques du photoanode et du CE aient été étudiés de manière rigoureuse, il reste encore des possibilités d'amélioration dans les directions suivantes qui pourraient être plus intéressantes et fructueuses à l'avenir.

Dans les chapitres 3, nous avons décrit les mécanismes de dégradation des DSSC nus et composites. Cependant, la régénération de DSSC pourrait être un sujet intéressant. Les MWCNT et autres nanomatériaux en carbone peuvent augmenter la régénération des DSSC. En outre, la couche de blocage composite avec des nanomatériaux carbonés pourrait être un sujet intéressant à étudier en termes d'obtention d'une stabilité élevée aux UV du fait de ses propriétés d'agent d'absorption et de blocage efficaces de la lumière UV. Le remplacement de l'électrolyte par des matériaux de transport de trous à l'état solide pourrait améliorer encore la stabilité des DSSC basés sur l'anode nanocomposite MWCNT-TiO₂.

Au chapitre 4, nous avons décrit l'effet des MWCNT sur la stabilité thermique des DSSC. Dans les conditions réelles, les cellules solaires subissent deux contraintes (thermique et lumineuse) simultanément. La combinaison de la lumière et du stress thermique modifie les propriétés physiques et chimiques des systèmes de matériaux et affecte donc le comportement du dispositif. Par conséquent, il est important d'étudier la dégradation induite par la lumière et la température élevée des DSSC composés avec les MWCNT.

Au chapitre 5, nous avons décrit l'activité électrocatalytique du nanocomposite CuS-G en tant que CE pour DSSC. Les résultats montrent de grands potentiels pour le développement d'électrodes libres de TCO et de Pt dans les réactions électrochimiques pour DSSC, ce qui ouvrira la voie au développement de nouvelles technologies CE à

faible coût et efficaces. Bien que nous ayons décrit les performances PEC supérieures dans les dispositifs fabriqués, l'épaisseur du film à effet et la taille des grains n'ont pas été discutées, ce qui pourrait être intéressant à optimiser pour améliorer les performances du dispositif. De plus, étudier les mécanismes de dégradation du film dans le cadre de cette application pourrait être utile à l'avenir pour concevoir un CE efficace.